ULTRASTRUCTURAL CHARACTERIZATION OF NATIVELY PRESERVED EXTRACELLULAR MATRIX BY CRYO-ELECTRON TOMOGRAPHY

by

Bettina Zens

January, 2023

A thesis submitted to the
Graduate School
of the
Institute of Science and Technology Austria
in partial fulfillment of the requirements
for the degree of
Doctor of Philosophy

Committee in charge:
Prof. Dr. Beatriz Vicoso, Chair
Prof. Dr. Wanda Kukulski
Prof. Dr. Florian Schur
Prof. Dr. Michael Sixt

The thesis of Bettina Zens, titled *Ultrastructural characterization of natively preserved extracellular matrix by cryo-electron tomography*, is approved by:

Supervisor: Prof. Dr. Florian Schur, ISTA, Klosterneuburg, Austria

Signature: _____

Committee Member: Prof. Dr. Michael Sixt, ISTA, Klosterneuburg, Austria

Signature: _____

Committee Member: Prof. Dr. Wanda Kukulski, University of Bern, Switzerland

Signature: _____

Defense Chair: Prof Dr. Beatriz Vicoso, ISTA, Klosterneuburg, Austria

Signature: _____

Signed page is on file

ISTA Thesis, ISSN: 2663-337X

ISBN: 978-3-99078-027-5

I hereby declare that this thesis is my own work and that it does not contain other people's work without this being so stated; this thesis does not contain my previous work without this being stated, and the bibliography contains all the literature that I used in writing the dissertation.

I declare that this is a true copy of my thesis, including any final revisions, as approved by my thesis committee, and that this thesis has not been submitted for a higher degree to any other university or institution.

I certify that any republication of materials presented in this thesis has been approved by the relevant publishers and co-authors.

Signature: _____

Bettina Zens

January, 2023

Signed page is on file

ABSTRACT

The extracellular matrix (ECM) is a hydrated and complex three-dimensional network consisting of proteins, polysaccharides, and water. It provides structural scaffolding for the cells embedded within it and is essential in regulating numerous physiological processes, including cell migration and proliferation, wound healing, and stem cell fate.

Despite extensive study, detailed structural knowledge of ECM components in physiologically relevant conditions is still rudimentary. This is due to methodological limitations in specimen preparation protocols which are incompatible with keeping large samples, such as the ECM, in their native state for subsequent imaging. Conventional electron microscopy (EM) techniques rely on fixation, dehydration, contrasting, and sectioning. This results in the alteration of a highly hydrated environment and the potential introduction of artifacts. Other structural biology techniques, such as nuclear magnetic resonance (NMR) spectroscopy and X-ray crystallography, allow high-resolution analysis of protein structures but only work on homogenous and purified samples, hence lacking contextual information. Currently, no approach exists for the ultrastructural and structural study of extracellular components under native conditions in a physiological, 3D environment.

In this thesis, I have developed a workflow that allows for the ultrastructural analysis of the ECM in near-native conditions at molecular resolution. The developments I introduced include implementing a novel specimen preparation workflow for cell-derived matrices (CDMs) to render them compatible with ion-beam milling and subsequent high-resolution cryo-electron tomography (ET).

To this end, I have established protocols to generate CDMs grown over several weeks on EM grids that are compatible with downstream cryo-EM sample preparation and imaging techniques. Characterization of these ECMs confirmed that they contain essential ECM components such as collagen I, collagen VI, and fibronectin I in high abundance and hence represent a *bona fide* biologically-relevant sample. I successfully optimized vitrification of these specimens by testing various vitrification techniques and cryoprotectants.

In order to obtain high-resolution molecular insights into the ultrastructure and organization of CDMs, I established cryo-focused ion beam scanning electron microscopy (FIBSEM) on these challenging and complex specimens. I explored different approaches for the generation of thin cryo-lamellae by FIB milling and succeeded in optimizing the cryo-lift-out technique, resulting in high-quality lamellae of approximately 200 nm thickness.

High-resolution Cryo-ET of these lamellae revealed for the first time the architecture of native CDM in the context of matrix-secreting cells. This allowed for the *in situ* visualization of fibrillar matrix proteins such as collagen, laying the foundation for future structural and ultrastructural characterization of these proteins in their near-native environment.

In summary, in this thesis, I present a novel workflow that combines state-of-the-art cryo-EM specimen preparation and imaging technologies to permit characterization of the ECM, an important tissue component in higher organisms. This innovative and highly versatile workflow will enable addressing far-reaching questions on ECM architecture, composition, and reciprocal ECM-cell interactions.

ACKNOWLEDGMENTS

This work was supported by the Niederösterreich Fond, the Federation of European Biochemical Societies (FEBS), and ISTA. Especially the Scientific Service Units (SSU) of ISTA supported my work through resources provided by Scientific Computing (SciComp), the Miba Machine Shop, the Lab Support Facility (LSF), the Imaging and Optics Facility (IOF), and the Electron Microscopy Facility (EMF).

I would like to thank Flo for giving me the opportunity to complete my doctoral studies in his laboratory and for critically supervising my progress. His everlasting optimism and constructive feedback throughout this project have helped me through the more challenging phases of my studies. Especially in the face of obstacles that seemed unsurmountable at times, his enthusiasm and readiness to let me explore different ideas were greatly appreciated. The constant supply of chocolate certainly did not hurt either! Thank you, Flo, for all your support throughout the last years!

I would also like to thank my other Ph.D. committee members – Wanda Kukulski and Michael Sixt – for their scientific input throughout my studies and their enthusiasm for this project, which always gave me a boost of motivation. Thank you, Wanda, for hosting me in your lab to show me the basics of cryo-FIB milling! This week laid the foundation for all my FIB milling work!

I am immensely grateful to all the members of the Schur group, both current and former: Florian, Julia, Dario, Andreas, Georgi, Martin, Jesse, Manjunath, Mathias, Darya, Rahmah, and Benedikt. The cheerful and open atmosphere we have created is crucial to enjoying even a 16-hour workday to some extent. Work is never dull like this, and there's at least one lame joke per day that will make one of you groan while at least Julia and I laugh.
Especially Florian, Julia, and Dario have aided me time and again by listening to my outbursts of indignation when my lamellae would not behave and cheering me up when I was done ranting and raving. Florian, I want to express my immense gratitude to you at this point - all your input, our discussions about my results, and your never-ending patience with all my many questions will never be forgotten! Thank you for everything!
A big thanks also go to Vanessa and Valentin, who have been a great support for all things EM with their experience and willingness to always help wherever they could!

Words cannot describe how thankful I am to Verena, who has been a great friend, board game partner, and provider of fun, calm, and fluff, whenever needed. Thank you, Verena, for even helping me out with this thesis with your wonderful artwork!
A special thanks also go to Daniel, who is at least in part responsible for my enrolling in graduate school and taking on this challenge. Thank you for believing in me, for supporting me wherever you could, and for pushing me to keep going wherever you couldn't.

Lastly, my heartfelt thanks go to my friends and family, whose support has made it possible for me to pursue my interest in life sciences, even in different countries and on different continents at times. My deepest gratitude goes to my mother, who has always been there for me when I needed her and who never once did not have an open ear, a kind word, and a moment of her time for me. I also want to thank my grandmother and great-grandmother, who have taught me one of the most important lessons: Der Muss ist gar ein großer Herr!
Lastly, I want to thank my late grandfather, who - despite never quite understanding why looking at tiny things in a microscope was quite that important to me – was an unwavering rock in my life; from driving me to the train station every day just so I could go to the school I thought best for me, to teaching me how to drive, and eating my terrible cooking (mostly) without complaint. Thank you for everything, Opa.

ABOUT THE AUTHOR

Bettina Zens completed a BSc in Medical and Pharmaceutical Biotechnology at the IMC Krems (Austria) and an MSc in Molecular Biosciences at the University of Heidelberg (Germany). She then worked as a laboratory manager at the Max Perutz Labs Vienna (Austria). During her scientific journey, she worked on research projects focusing on auditory nerve cells in the mouse brain, the hematopoietic stem cell niche, and autophagy and contributed to a number of publications in different journals.
Bettina joined ISTA in September 2017 and joined the Schur group in summer 2018. During her Ph.D. studies, she worked on a project that reflected her interest and motivation to learn and develop new methods. The results of one part of her project were published in 2020 in the *Journal of Structural Biology*. Bettina also helped to establish two new microscopes and techniques at ISTA in close collaboration with the Electron Microscopy Facility.
In the course of Bettina's Ph.D. studies, she presented her results at the 9th Electron Tomography Congress in Egmond aan Zee (Netherlands). She also took part as an assistant teacher at the *Advanced Workshop on Cryo-Electron Tomography* in Vienna (Austria) and the *Workshop on Advanced Correlative Light and Electron Microscopy (CLEM) methods* in Umeå (Sweden).

LIST OF CONTRIBUTORS AND PUBLICATIONS

PUBLICATIONS

I am shared first-author on a paper published in the Journal of Structural Biology by Elsevier. Section 3.1.1 summarizes this publication and details the role it played in this Ph.D. thesis work.

Fäßler, F.*; **Zens, B.***, Hauschild, R., Schur, FKM. (2020). *3D printed cell culture grid holders for improved cellular specimen preparation in cryo-electron microscopy*. Journal of Structural Biology. 212(3). doi:10.1016/J.JSB.2020.107633
*Equal contribution

CONTRIBUTORS

Florian Fäßler (Schur group)
Shared first-author of the publication outlined in section 3.1.1. Florian also provided technical support for the adaptation of grid holders and their printing, as well as for tomogram reconstruction.

Julia Stanger (Schur group)
Julia performed IsoNet processing of selected tomograms. Some of these tomograms are shown in section 3.6.

Jesse Hansen (Schur group)
Jesse performed Amira filament tracing of actin and intermediate filaments and segmentation model rendering and visualization, as shown in Figure 60.

Andreas Thader (Schur group)
Andreas expressed and purified CNA35-EGFP, used in this thesis for live collagen staining, as shown in Figure 18.

Vanessa Zheden (Electron Microscopy Facility)
Vanessa performed sample preparation for conventional electron microscopy (EM) techniques following CDM growth, including contrasting, resin embedding, and sectioning. She also acquired the SEM images shown in Figure 19 and Figure 52.

Victor-Valentin Hodirnau (Electron Microscopy Facility)
Valentin provided technical support at the Titan Krios G3i for the implementation of new scripts and data acquisition.

Armel Nicolas (Lab Support Facility)
Armel and his team performed sample preparation for Mass Spectrometry (MS) analysis following CDM growth and decellularization, followed by MS and data analysis. The results are shown in Table 4.

TABLE OF CONTENTS

LIST OF FIGURES

LIST OF TABLES

LIST OF ABBREVIATIONS

Abbreviation	Full Term
°C	Degree Celsius
µm	Micrometer
2D	Two-Dimensional
3D	Three-Dimensional
Å	Ångström
AFM	Atomic Force Microscopy
Au	Gold
BM	Basement Membrane
BMP-1	Bone Morphogenic Protein-1
BSA	Bovine Serum Albumin
BSE	Back-Scattered Electrons
CCD	Charge-Coupled Device
CDM	Cell-derived matrix
CEMOVIS	Cryo-Electron Microscopy Of Vitreous Sections
CLEM	Correlative Light and Electron Microscopy
cm	Centimeter
CS	Cross-Section
CSC	Cross-Section-Cleaning
D	Day
DAPI	4′,6-diamidino-2-phenylindole
DDD	Direct electron Detection Device
DIC	Differential Interference Contrast
e.g.	exempli gratia
ECM	ExtraCellular Matrix
EFTEM	Energy-Filtered Transmission Electron microscopy Mode
EGFP	Enhanced Green Fluorescent Protein
EM	Electron Microscopy/Microscope
EMF	Electron Microscopy Facility
ER	Endoplasmatic Reticulum
ET	Electron Tomography
ETD	Everhart-Thornley electron Detector
FACITs	Fibril-Associated Collagens with Interrupted Triple helices
FEG	Field Emission Gun
FGF	Fibroblast Growth Factor
FIB	Focused Ion Beam
FIBSEM	Focused Ion Beam Scanning Electron Microscope
FM	Fluorescence Microscopy
FN	Fibronectin
FWD	Free Working Distance
GAG	GlycosAminoGlycan
GB	Gigabyte
GFP	Green Fluorescent Protein
GIS	Gas Injection System

Gly	Glycine
h	hour(s)
HC	Holey Carbon
HPF	High Pressure Freezing
HPLC	High Performance Liquid Chromatography
i.e.	id est
IgG	Immunoglobulin G
IOF	Imaging and Optics Facility
ISTA	Institute of Science and Technology
keV	Kilovolt
LC	Liquis Chromatography
LM	Light Microscopy
LN2	Liquid Nitrogen
LOX	Lysyl Oxidase
LSF	Lab Support Facility
M	Molar
MACITs	Membrane-Associated Collagens with Interrupted Triple helices
MB	Megabyte
min	minute(s)
mm	Milimeter
MMP	Matrix MetalloProteinase
MS	Mass Spectrometry
MSC	Mesenchymal Stem Cell
nA	Nanoampere
NAD	Nonlinear Anisotropic Diffusion
NIH	National Institutes of Health
nm	Nanometer
NMR	Nuclear Magnetic Resonance
pA	Picoampere
PACE-tomo	Parallel Acquisition of Cryo-Electron Tomograms
PB	Phosphate Buffer
PBS	Phosphate Buffered Saline
PFA	Paraformaldehyde
PG	ProteoGlycan
PM	Plasma Membrane
PVP	Polyvinylpyrrolidone
px	Pixel
REF	Rat embryo fibroblasts
ROI	Region Of Interest
RPM	Rounds Per Minute
RT	Room Temperature
s	second(s)
SE	Secondary Electrons
SEM	Scanning Electron Microscopy/Microscope
SiO_2	Silicone Oxide
SIRT	Simultaneous Iterative Reconstruction Technique

SNR	Signal-to-Noise Ratio
TAMRA	5-Carboxytetramethylrhodamine
TCEP	Tris(2-carboxyethyl)phosphine hydrochloride
TEAB	Triethylammonium bicarbonate
TEM	Transmission Electron Microscopy/Microscope
TFS	Thermo Fisher Scientific
Ti	Titanium
TIFF	Telomerase Immortalized Foreskin Fibroblasts
TIMP	Tissue Inhibitors of MetalloProteinases
TSP	Thromospondin domain
UV	Ultra-Violet light
V	Volt
WBP	Weighted Back Projection
WD	Working Distance

1. INTRODUCTION

1.1. The extracellular matrix

The extracellular matrix (ECM) is a hydrated three-dimensional network composed mainly of proteins, polysaccharides, and water. This complex and highly dynamic supramolecular network provides structural scaffolding for the cells embedded within it. The development of the ECM as the non-cellular component of all multicellular eukaryotes, from plants to fungi and animals, was crucial in the transition from single autonomous cells to cohesive multicellular organisms (Kloareg et al., 2021). In this work, the ECM will be discussed in the context of vertebrate physiology specifically.
The structure and physical properties of the ECM are determined by the cells embedded within it and its precise composition, which varies from tissue to tissue and reflects the specific tissue's requirements and functions. In the vertebrate body, ECMs of the same tissue type are often very distinct. For example, the liver is comprised almost exclusively of cells to fulfill its metabolic function, which relies on clearly defined structures to a much lesser extent and consequently has only a low proportion of ECM (Martinez-Hernandez and Amenta, 1993; Nyström, 2021). Cartilage or bone, on the other hand, have a relatively high proportion of ECM to cells, and while they both are connective tissue, their ECMs drastically differ in their make-up and function. Bone is the most rigid organ in vertebrate animals and provides structure and support for the whole body while also protecting other organs. Its ECM is defined by thick fibers of filamentous proteins that are mineralized to provide rigidity and strength (Lin et al., 2020). Cartilage, in contrast, contains similar filamentous proteins to ensure high resilience but also remains elastic and flexible to serve its purpose (Muir, 1995).
These differences account for specialized topography, rigidity, porosity, stiffness, and other biomechanical properties which impact the biological function of the cells residing in the respective matrices (Mouw et al., 2014; Theocharis et al., 2016). The properties of the ECM influence a multitude of cellular processes, ranging from cell division to cell migration and tissue polarity and differentiation.
The ECM not only acts as a structural support for the cells embedded within it but also plays a vital role in signaling by directly interacting with cells through adhesion receptors such as integrins. Various chemokines, cytokines, and growth factors are deposited within the ECM and can bind to various ECM molecules. Both the binding and the release of these factors is tightly regulated and crucial for tissue homeostasis, cell migration, immunity, and many more physiological processes (Frantz et al., 2010; Theocharis et al., 2019, 2016).
It is important to note that there are two main types of ECMs that differ in their general composition and arrangement: Pericellular and interstitial matrices.
Pericellular matrices are narrow, cell-adjacent structures and play an essential role in tissue shape and buffer mechanical stress to protect the overlaying cells (Theocharis et al., 2016). The best-known and most researched example is the basement membrane which separates epithelial, endothelial, muscle, or Schwann cells from connective tissue. These sheet-like networks of basement membranes typically anchor adjacent cells through cross-junctions with ECM-cell binding proteins such as integrins. Basement membranes contain several types of fibrous proteins and high amounts of different proteoglycans (PGs). These proteins form interconnected networks that give the basement membrane its ability to anchor the overlaying cells through the formation of hemidesmosomes (Theocharis et al., 2016).

In contrast, interstitial matrices have a three-dimensional rather than a sheet-like architecture and are tightly connected to basement membranes to provide tissue integrity (Frantz et al., 2010). They typically have a high content of PGs and sequestered water to form a hydrated gel and have cells embedded within them. The examples given above – bone and cartilage – belong to this type of ECM and exemplify the wide variety and adaptability of interstitial matrices. Interstitial matrices contain a different set of fibrous proteins than pericellular matrices (Frantz et al., 2010; Theocharis et al., 2019).
In both types of matrices, the interplay between the different components and the adjacent and embedded cells is highly intricate and is vital in many physiological processes in both health and disease.
Almost all cell types produce and secrete matrix molecules and participate in the formation of the ECM throughout the life cycle of an organism (Frantz et al., 2010; Theocharis et al., 2016). Among these cell types are epithelial cells, endothelial cells, mesenchymal cells, and even immune cells. Among mesenchymal cells, fibroblasts are of particular importance for the ECM. They specialize in synthesizing ECM proteins, specifically structural components, such as fibrous proteins like collagen. They are among the most common cells in connective tissue and tend to align parallel when crowded locally. Fibroblasts have been shown to organize collagen fibrils by exerting tension on the matrix, thereby influencing collagen alignment (Theocharis et al., 2016).
The ECM is continuously synthesized and undergoes a constant remodeling process crucial for maintaining normal tissue function. This highly dynamic process is tightly controlled by a multitude of growth factors that are bound to the different ECM components and are part of a controlled feedback loop. One aspect of this feedback loop is the rigorously regulated secretion of matrix metalloproteinases (MMPs) and simultaneous synthesis of tissue inhibitors of metalloproteinases (TIMPs) as a counterbalance (Cruz-Munoz and Khokha, 2008; Mott and Werb, 2004).
On another level, the cross-linking and therefore stiffening of the ECM is controlled through enzymes such as lysyl oxidases (LOXs). ECM remodeling is even able to modulate cell growth and migration through the release of bound growth factors such as fibroblast growth factor 2 (FGF-2) (Frantz et al., 2010; Lucero and Kagan, 2006; Wilgus, 2012). Technological advancements have helped to build our understanding of the ECM and the processes regulating it, but even so, we are only just beginning to see the complete picture.

The matrisome

The major components of the ECM, also termed the “core matrisome”, consist of approximately 300 proteins that can roughly be separated into two types: fibrous proteins and proteoglycans (Frantz et al., 2010).

The matrisome: Proteoglycans

Proteoglycans (PGs) are classified based on their core proteins, their localization, and the glycosaminoglycan (GAG) chains covalently linked to their protein core (Frantz et al., 2010; Theocharis et al., 2016). The GAG chains are linear, anionic polysaccharides and are separated into four groups: hyaluronic acid, keratin sulfate, chondroitin/dermatan sulfate, and heparan sulfate. PGs are exceptionally well suited for generating hydrogels such as ECMs because of their extremely hydrophilic nature and ability to adopt highly extended formations. Matrices formed with PGs can resist high compressive forces and are known to interact with growth factors, cell surface

receptors, and chemokines. Through this, they are heavily involved in a number of cellular processes (Frantz et al., 2010; Theocharis et al., 2016).

The matrisome: Fibrous proteins

The group of fibrous ECM proteins is mainly composed of collagen, fibronectin, and laminin (Alberts et al., 2022). These molecules are the major structural components of the ECM and do not only act as substrates for cell adhesion and migration but also provide high tensile strength and are vital in tissue topography (Frantz et al., 2010; Theocharis et al., 2016). Collagen is the most abundant protein in vertebrates and accounts for up to 30% of the total protein mass. As such, they are of particular interest and have been the focus of many studies from as early as the 1960s. This group of proteins will be discussed in detail in **1.1.1. The Collagen Family.**

In my thesis, the focus rests on the ultrastructural characterization of extracellular matrix using novel tools, visualizing the fibrous components of the interstitial matrix, their arrangement, and their context with other proteins, such as PGs.

1.1.1. The Collagen Family

In vertebrates, the family of collagens consists of 28 different types of collagen, numbered from collagen type I to collagen type XXVIII (Ricard-Blum, 2011). Collagen type I is the most abundant among these and has a molecular weight of ~300kDa (León-López et al., 2019).

All collagens consist of three polypeptide chains that come together in a right-handed triple helix arrangement and have a characteristic repeating Gly-X-Y motif. The collagen conformation differs from most other proteins in that glycine is a fixed residue in every third position and generates a distinct pattern. Proline and hydroxyproline make up a high proportion of the other residues, with up to 20%. A one-residue stagger between adjacent polypeptide chains, along with interchain hydrogen bonds and electrostatic interactions, stabilizes the tripe helix (Fischer Verlag et al., 1997; Holmes et al., 2018; Persikov et al., 2005).

The single polypeptide chains comprising each collagen are called α-chains and are distinguished between distinct collagen molecules by a denotation with Roman numerals. For example, type I collagen usually is a heterotrimer of two α1(I) chains and one α2(I) chain, each composed of ~1014 amino acids (León-López et al., 2019), so it is a collagen consisting of $[\alpha1(I)]_2$, α2(I). Type II collagen, in contrast, usually occurs as a homotrimer with three α1(II) chains (Holmes et al., 2018).

Overall, collagens are categorized into several classes according to their common homology and function, as summarized in Table 1.

Fibrillar collagens represent the most abundant and ubiquitous type and include collagen I, II, III, V, XI, XXIV, and XXVII. They are characterized by their uninterrupted collagenous domains, their C-terminal propeptide, and their ability to self-assemble into heterotypic fibrils (Gelse et al., 2003; Ricard-Blum, 2011) (see Figure 1). The general composition of collagen fibers differs from tissue to tissue. Heterotypic fibrils with collagen II as their main component are typically associated with cartilage. In contrast, heterotypic fibrils of collagen I, also containing collagen III and V, are found in the skin, tendons, bones, and dermis (Amirrah et al., 2022; Ricard-Blum, 2011; Theocharis et al., 2019).

Another class, comprised of collagens IV, VIII, and X, are network-forming collagens. In contrast to fibrillar collagens, they have no propeptide domain and are more typically found in basement membranes (see Figure 1)(Ricard-Blum, 2011). Collagen IV is the most well-studied among these and is a major component of basement membranes, while collagen VIII is found in subendothelial matrices, and collagen X is associated with cartilage. Network-forming collagens are arranged into extended networks and interact with each other and other matrix components to create large supramolecular structures (Holmes et al., 2018; Kadler et al., 2007; Ricard-Blum, 2011).

Collagens IX, XII, XIV, XVI, XIX, XX, XXI, and XXII belong to the group of **fibril-associated collagens with interrupted triple helices (FACITs)** and are short collagen molecules with, as the name suggests, multiple interruptions of their collagenous domains that usually associate with fibrillar collagens and other ECM components, such as fibronectin. They are thought to be crucial in regulating collagen fibrillogenesis and functionality (Holmes et al., 2018; Ricard-Blum, 2011; Theocharis et al., 2019) (see Figure 1).

The group of membrane-associated collagens with interrupted triple helices (MACITs) contains collagens XIII, XVII, XXIII, and XXV. All of these collagens are type II transmembrane proteins with a long extracellular C-terminal domain containing collagenous and non-collagenous regions and a short cytoplasmic N-terminal domain (see Figure 1). They function as cell surface receptors and often play a role in cell adhesion and motility (Holmes et al., 2018; Kadler et al., 2007; Ricard-Blum, 2011).

Collagen XV and XVIII are termed **multiplexins** and are characterized by their multiple triple helix domains with interruptions in their chondroitin sulfate and heparan sulfate chains, respectively. They play a role in the interconnection of the basement membrane with underlying connective tissue and are also able to interact with various growth factors and cytokines (see Figure 1)(Holmes et al., 2018; Kadler et al., 2007; Ricard-Blum, 2011).

The remaining collagens, VI, VII, XXVI, and XXVIII, make up a rather diverse group of collagens. All these collagens are assembled into beaded filaments and are usually found in concert with other collagens. Collagen VII is thought to function as an anchoring fibril in the basement membrane of epithelial tissues (Frantz et al., 2010; Ricard-Blum, 2011; Shoulders and Raines, 2009). A hallmark of this class of collagens is the high amount of von Willebrand factor A domains and, to a lesser extent, fibronectin type III repeats (see Figure 1). Both of these are important for protein-protein interactions in the ECM (Ricard-Blum, 2011).

Table 1: A summary of 28 types of collagen.
This overview of the different classes and distribution of collagen is based on (Holmes et al., 2018; Kadler et al., 2007; Ricard-Blum, 2011; Shoulders and Raines, 2009).

Class	Type	Distribution examples
Fibrillar collagens	I	Connective tissues, i.e., dermis, bone
	II	Cartilage, intervertebral disc
	III	Connective tissues, i.e., skin, blood vessels
	V	Co-distribution with type I
	XI	Co-distribution with type II
	XXIV	Bone, cornea
	XXVII	Cartilage, eye
Network-forming collagens	IV	Basement membranes
	VIII	Subendothelial tissue, i.e., in brain, skin
	X	Cartilage
FACITs	IX	Co-distribution with type II
	XII	Co-distribution with type I
	XIV	Co-distribution with type I
	XVI	Dermis, kidney
	XIX	Basement membranes
	XX	Connective tissues, i.e., cornea
	XXI	Kidney, stomach
	XXII	Cartilage, tissue junctions
MACITs	XIII	Dermis, eyes
	XVII	Hemidesmosomes in epithelia
	XXIII	Heart, retina
	XXV	Heart, testis, brain
Multiplexins	XV	Basement membranes
	XVIII	Basement membranes
Beaded-filaments	VI	Connective tissues, i.e., dermis, muscle
	VII	Skin, bladder, known as anchoring fibrils
	XXVI	Testis, ovary
	XXVIII	Basement membranes

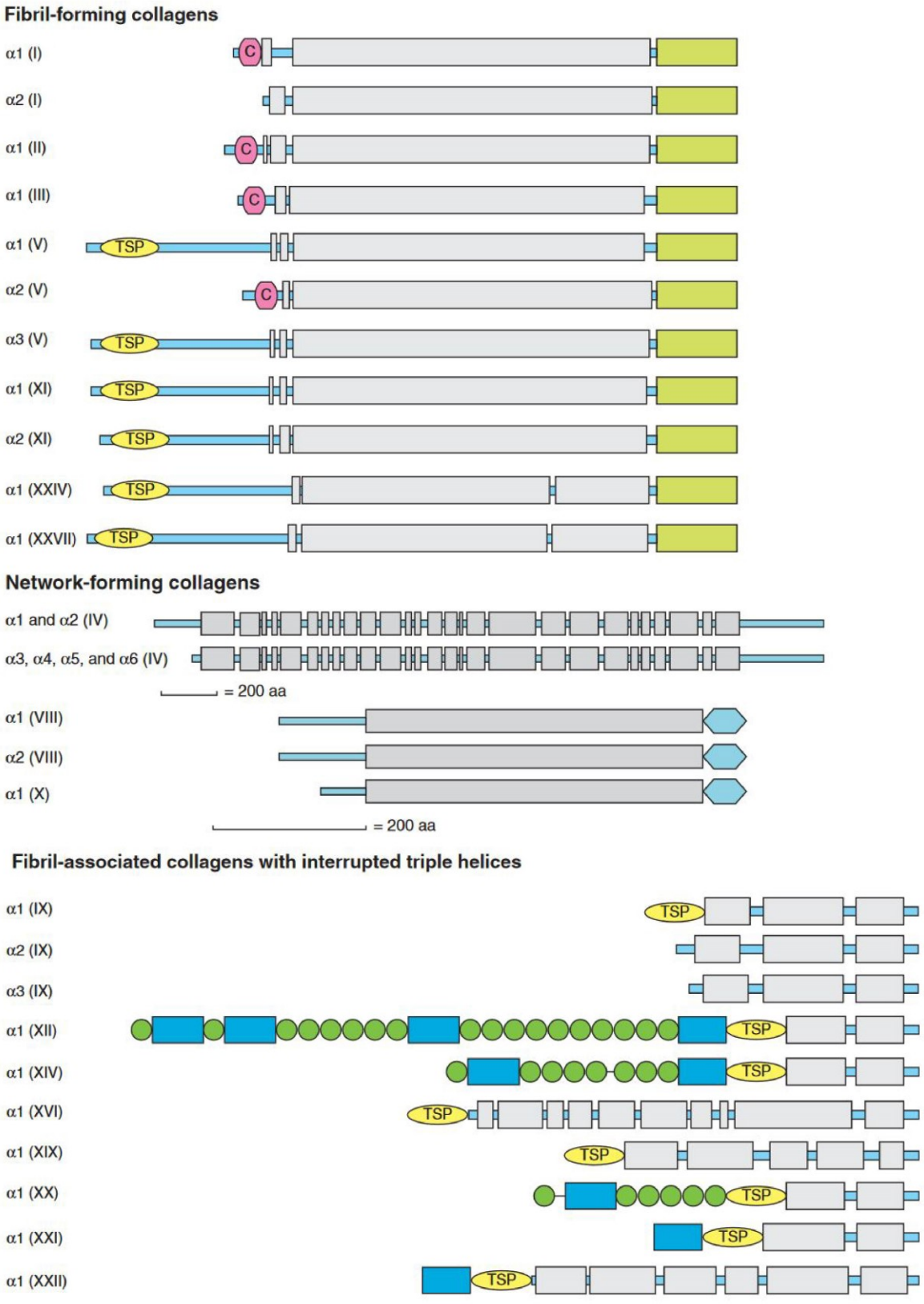

Figure 1: Structural organization of collagens.
An overview of the six different classes of collagens and the individual types of collagen belonging to them. The different domains composing each collagen are marked as explained in the legend. This figure was obtained and adapted from (Ricard-Blum, 2011), with permission from Cold Spring Harbor Laboratory Press. **Figure continued on next page.**

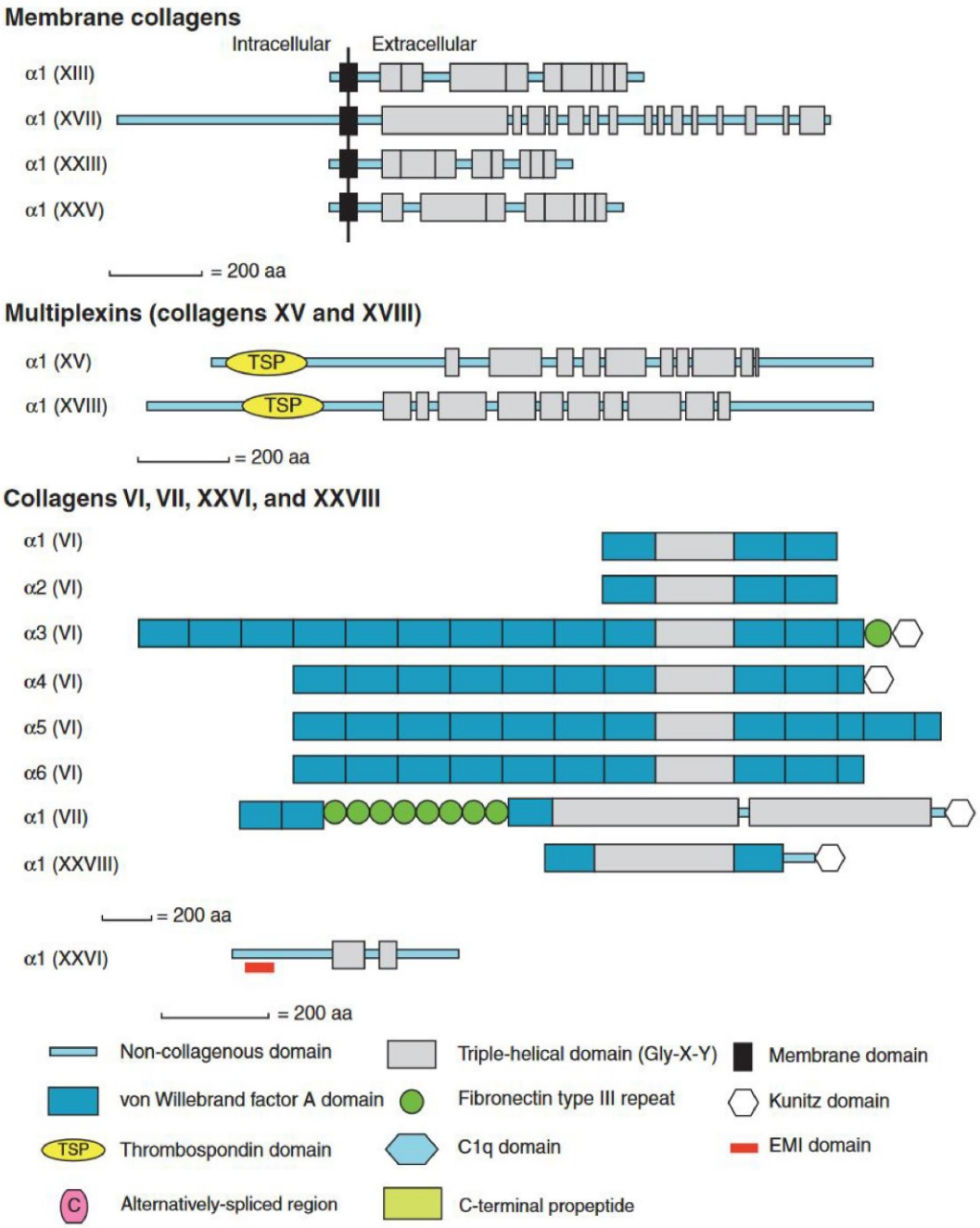

Figure 1 continued.

Fibrillar collagens are not only the most abundant type of collagen but also the best-studied ones, specifically collagen type I, which accounts for ~90% of all collagen (Gelse et al., 2003). This is owed to the fact that they can self-assemble *in vitro* and are easily isolated from tissues such as tendons and cartilage, i.e., from a rat tail (Piez, 1997). They are one of the main structural elements of all interstitial matrices in connective tissues such as the dermis and provide tensile strength, stiffness, and other biomechanical properties adapted for each tissue. Fibrillar collagens, and collagen type I, as the best-studied of this class, will be the primary focus in the subsequent chapter, but the generation of collagen fibrils depends on the collagenous domains of proteins. This means that collagen fibrillogenesis highly similar within this class.

Collagen synthesis

All fibrillar collagens are synthesized through soluble precursor molecules called procollagen. To this end, the pro-α-chains are synthesized on membrane-bound ribosomes and co-translationally translocated into the rough endoplasmatic reticulum (ER) via a signal peptide (Brownell and Veis, 1976). The pro-α-chains have three domains: the collagenous α-chain, the amino-terminal propeptide, and the carboxy-terminal propeptide. In the ER, they undergo various cotranslational modifications such as glycosylation as well as the hydroxylation of lysines and proline residues into hydroxylsyine and hydroxyproline, respectively (P. Bornstein, 1967; Paul Bornstein, 1967; Brownell and Veis, 1976). The auto assembly of the pro-α-chains into procollagen trimers is initiated through the formation of disulfide bonds of the C-termini of the individual chains and subsequent inter-chain disulfide bond formation. This serves as a nucleation reaction to the collagenous domains, which then form the triple helix in a zipper-like action from the C-terminus to the N-terminus (Brownell and Veis, 1976).

It has been suggested that this process occurs while the pro-α-chains are still associated with the rough ER (Beck et al., 1996). The three chains coming together are staggered by one residue relative to each other. The glycine in every third position is in the center of the helix, and the bulkier amino acids, such as hydroxyproline, occupy the outer positions. This is quintessential for the close packing along the central axis of this molecule and characterizes the typical collagenous domains of all collagens. Moreover, the bulkier amino acids on the outside are free to interact with other molecules (Gelse et al., 2003).

At the end of this process, the formed triple helix molecule still contains propeptides on both the C-terminus and the N-terminus and is still soluble. This molecule, termed procollagen, has a length of roughly 300 nm and a diameter of 1.5 nm (Gelse et al., 2003; Orgel et al., 2001). Procollagen is transported through the Golgi complex to the plasma membrane and processed further through the removal of both propeptides by MMPs in a tightly controlled fashion. Where precisely this processing step takes place in the cell remains unclear, albeit the trans-Golgi network has been suggested as a potential site, at least in the embryonic tendon (Canty et al., 2004). Canty-Laird *et al*. (Canty-Laird et al., 2012) propose that the N-propeptides are removed in the first step either at the ER-Golgi intermediate compartment or the Golgi. In a subsequent step, the C-propeptides are cleaved in the post-Golgi compartment. They could show that the C-propeptides are crucial for transport from the ER to the Golgi. Lee *et al.* (Lee et al., 1997), however, proposed that at least the C-propeptide cleavage can also occur in the extracellular space rather than the intracellular space as one of the main peptidases responsible for this process is localized close to the cell surface and has been shown to interact with another important ECM component, fibronectin (Saunders and Schwarzbauer, 2019).

Collagen fibrillogenesis has been extensively studied *in vitro* due to its self-assembly properties but also in tendons, which can relatively easily be isolated from a specimen and prepared for analysis by various methods. However, the exact location and mechanism of collagen fibrillogenesis *in vivo* have remained ambiguous until this point as supporting evidence for two models has been put forward (Birk and Trelstad, 1984; Gelse et al., 2003; Lee et al., 1997; Ploetz et al., 1991; Ricard-Blum, 2011; Saunders and Schwarzbauer, 2019).

One model hypothesizes that procollagen is released from the trans-Golgi network in secretory vacuoles of around 500nm diameter that appear to be electron-dense and associate with microtubules that transport them to the plasma membrane (PM) (Birk

and Trelstad, 1984). Somewhere along this path, the vacuoles mature into compartments. The procollagen molecules are then processed into collagen molecules and begin to assemble into collagen fibrils, as several studies could show the presence of short collagen fibrils within such compartments (Birk and Trelstad, 1984; Canty et al., 2006; Canty and Kadler, 2005). When these vesicles partially or fully fuse with the PM, narrow cellular invaginations are formed, termed fibripositors. From there, short collagen fibrils are secreted into the ECM and assembled into bigger structures (Birk and Trelstad, 1984; Canty et al., 2006; Canty and Kadler, 2005).
The other model suggests that collagen is secreted from the cell as procollagen, and all processing steps to collagen molecules and, finally, collagen fibrils take place in the ECM. This model will be discussed in more detail in section 1.1.2 Fibronectin.
It is important to note that the studies that support each of these models have been performed both *in vitro* and *in situ*, as well as in different developmental stages and tissue types. It is, therefore, entirely possible that the mode of collagen fibrillogenesis differs depending on the tissue, developmental stage, and other factors.
Regardless of whether the fibril assembly of collagen takes place during or following the secretion of procollagen into the ECM, the removal of the C-propeptide and generation of collagen from procollagen is the primary regulatory step to trigger the spontaneous self-assembly process (Hulmes, 2002). Until the removal of the C-propeptide, procollagen remains highly soluble. In contrast, the presence of the N-propeptide does not inhibit the formation of collagen fibers. The C-propeptide domain is highly conserved across all fibrillar collagens, while the N-propeptide domain has a higher variability and is thought to be involved in the regulation of fibril length (Hulmes, 2002).
Once the C-propeptide has been removed, five collagen molecules align longitudinally with an overlap of roughly three-quarters of the total molecular length and a gap of roughly 40 nm to the next collagen in line in the form of a hollow cylindrical filament. In this way, a collagen microfibril is formed, and this exact alignment of the single procollagens results in the characteristic D-period of ~67 nm with a distinct banding pattern of fibrillar collagens (Smith, 1968) (see Figure 2).

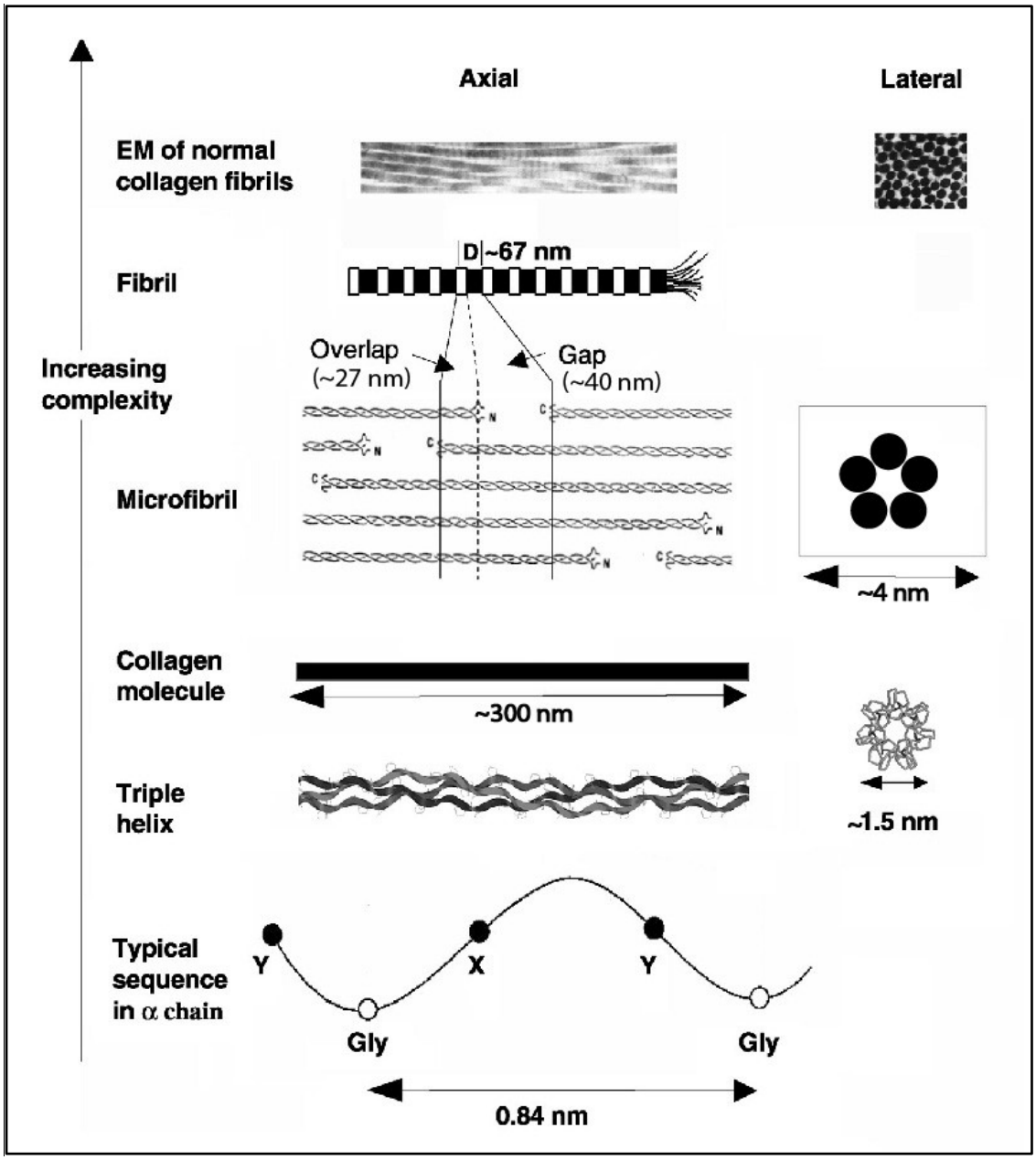

Figure 2: The known structural hierarchy of collagen type I.
The base unit of the collagen fibril is the triple helix, which consists of three α chains. After the removal of the propeptide domains, multiple collagen molecules assemble into a collagen microfibril. These microfibrils in turn then assemble into bigger fibrils that show the typical banding pattern due to their spatial arrangement. An EM image of collagen I fibers is shown at the top in axial and lateral views. This figure was adapted from Orgel *et al*. (Orgel et al., 2001) with permission from Elsevier.

The collagen microfibrils are then assembled into collagen fibrils that typically range in thickness from around 35 to 500nm, and from these fibrils, thicker fibers can be formed. Covalent cross-linking between lysine residues of the single collagen molecules by LOX strengthens the fibrils and influences the biomechanical properties of the ECM (Myllyharju and Kivirikko, 2004; Robins, 2007).
While it has become evident that the combination of different fibrils, as well as their orientation and arrangement to form ordered structures, is tissue-specific, we still understand very little about the mechanisms controlling fiber thickness, length, and arrangement (Cui et al., 2007). However, it has been shown that other matrix proteins

are important regulators of these processes. For example, collagen fibrils in connective tissues consist primarily of collagen I, with other collagens such as collagen V accounting only for a much smaller fraction (Theocharidis and Connelly, 2017). Despite its much lower abundance, collagen V still plays a crucial role in regulating the diameter and organization of collagen fibrils. As illustrated in Figure 1, it possesses a non-collagenous domain that projects outwards when incorporated into collagen I fibrils. This non-collagenous domain results in a steric hindrance that limits the lateral growth of the fibrils and has been suggested to help regulate their diameter as shown in Figure 3 (Theocharidis and Connelly, 2017; Wenstrup et al., 2004). Interestingly, collagen XI seems to serve much the same purpose. It has been shown that in cartilage, collagen I fibrils containing collagen V have a diameter of 40 nm, while those containing collagen XI have a diameter of 16 nm (Keene et al., 2017).

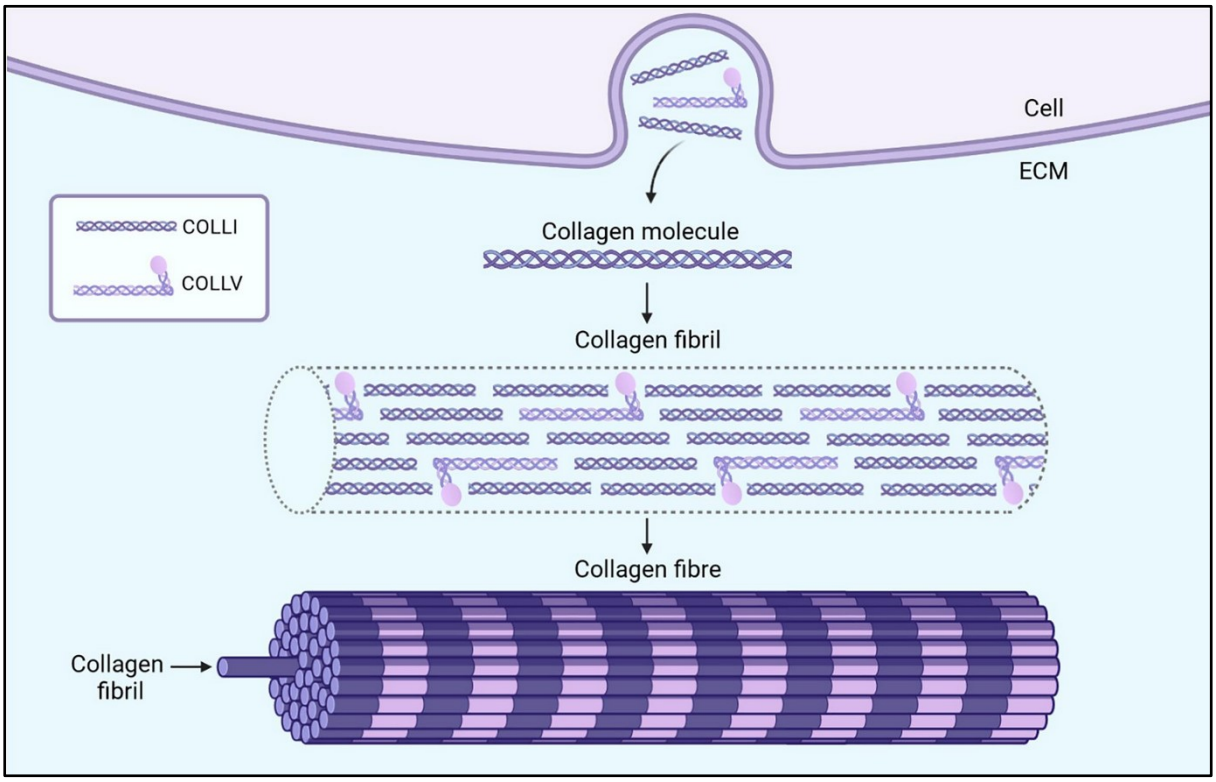

Figure 3: The formation of a collagen fiber in connective tissue.
Cells secrete collagen molecules into the extracellular space, where they are assembled into collagen fibrils that are subsequently bundled into collagen fibers. The collagen fibrils consist mainly of collagen I. Collagen V comprises only a small fraction of the total collagen but is thought to be essential in regulating fibril and fibre diameter through steric hindrance. This figure was obtained from Malek and Köster, 2021 (Malek and Köster, 2021) under the Creative Commons Attribution License (CC BY).

Numerous other proteins have been shown to influence the size, assembly rate, and structure of collagen fibrils *in vitro*, ranging from the N-propeptides of collagen I to cross-linking enzymes such as LOX, tenascin-X, perlecan, and many more (Holmes et al., 2018; Lethias et al., 2006). Nevertheless, all of this details that there is still a significant gap in our understanding of the ECM component secretion and assembly.

1.1.2. Fibronectin

Fibronectin (FN) is one of the main fibrillar proteins in the ECM and interacts with many proteins that have specific fibronectin-binding sites, such as collagens or trans-membrane proteins like integrins. There are two types of FN in vertebrates (Alberts et al., 2022):
1) soluble plasma FN that acts as a major component of blood plasma and is produced explicitly in the liver by hepatocytes.
2) insoluble cellular FN that is one of the main constituents of most interstitial ECMs and plays a role in a multitude of processes such as cell-matrix interaction, cell growth and differentiation, cell migration, and also collagen fibrillogenesis. As an important factor in most ECMs, insoluble cellular FN will be the focus of the following passage.
There is a single fibronectin gene that, once transcribed and translated, results in the synthesis of a high molecular weight monomer of ~250kDa that consists of three types of repeating units termed FN repeats: type I, type II, and type III. Together they account for about 90% of the whole amino acid sequence. Even though there is only a single FN gene, alternative splicing of its mRNA accounts for as many as 20 different variants of FN in humans.
Fibronectin is synthesized by multiple cell types and usually exists as a dimer (Singh et al., 2010). Two monomers are covalently linked at their C-termini via a pair of disulfide bonds. The still soluble dimer is folded in a compact conformation and is secreted to the cell surface, where it binds to FN-specific integrins. Integrins begin to cluster, reversibly bind to FN, and unfold it into a linearized structure. This extended morphology exposes its FN-FN polymerization domains, and another FN dimer can be deposited at the site to get unfolded in an iterative, continuous process (Singh et al., 2010; Williams et al., 1982; Zhong et al., 1998).
Interestingly, at least in some tissues and certain cell types, a reciprocal dependence of collagen fibril assembly and FN fibril assembly has been observed. Several studies have reported a co-localization of freshly assembled FN fibrils and freshly assembled collagen fibrils, at least in cultured fibroblasts and smooth muscle cells (Kadler et al., 2008). Additionally, it was found that blocking of the collagen-binding site on FN via an antibody inhibited collagen fibrillogenesis, and the knockdown of collagen I resulted in a reduced FN network (Dzamba et al., 1993; Kadler et al., 2008; McDonald et al., 1982).
The exact mechanism and site of fibronectin-collagen fibrillogenesis likely depend on developmental stage, tissue, and cell type, as different mechanisms have been proposed and are supported by findings in independent studies. While collagen can self-assemble, as many *in vitro* studies have shown (Cui et al., 2007; Shoulders and Raines, 2009), it seems only reasonable that such a fundamental process is tightly controlled *in vivo* through multiple mechanisms to produce the specific collagen fibers needed for each tissue.
Ledger *et al.* (Ledger et al., 1980) could show that in cultured fibroblasts, procollagen and FN co-localize already in the secretory pathway and potentially already interact before they are secreted into the extracellular space (Kadler et al., 2008). This, together with the possible processing of procollagen to collagen within the cell, could result in FN-collagen complexes forming already before binding to integrins at the plasma membrane.
In contrast, Saunders and Schwarzbauer (Saunders and Schwarzbauer, 2019) have shown that FN fibril assembly precedes collagen fibril assembly and propose the following mechanism: Both the collagen C-propeptidase Bone Morphogenic Protein-1

(BMP-1), and procollagen co-localize to FN fibrils at the cell surface. If the FN fibril assembly is inhibited, no proteolytic cleavage of the collagen C-propeptide occurs, and no collagen fibrillogenesis can take place. Saunders and Schwarzbauer could show that BMP-1 binds to FN at multiple sites, increasing the local concentration of the propeptidase and thus the chance for C-propeptide cleavage on adjacent FN-bound procollagen molecules. In addition, the ECM protein called heparin can bind not only FN and BMP-1 but also collagen. It is therefore thought that it helps to locally concentrate all three proteins in one location, thereby facilitating the process of collagen fibrillogenesis on top of the FN fibrils. Heparin has also been shown to induce conformational changes in FN upon binding, opening up additional binding sites for BMP-1 (Saunders and Schwarzbauer, 2019). However, whether fibripositors are involved in FN and collagen fibril assembly remains open.

1.1.3. The ECM in Health and Disease

The structural and functional integrity of the ECM is controlled and maintained by a plethora of different mechanisms, such as the coordinated secretion of MMPs and TIMPs, the controlled activity of enzymes such as LOX, and the release or sequestration of various growth factors that are bound to the ECM. The ECM is highly dynamic and continuously undergoes remodeling to guarantee tissue homeostasis. Imbalances in any of these mechanisms can lead to serious illnesses (Theocharis et al., 2019).

When an acute injury is inflicted on a tissue, the fibrogenic machinery is activated, and wound healing is induced. After the initial immune response by immune cells, fibroblasts are recruited to the site and begin to express and secret large quantities of ECM proteins, including collagens and fibronectin (Kisseleva and Brenner, 2008; Wilgus, 2012). The mechanical stress associated with these immense levels of ECM deposition often induces transdifferentiation of fibroblasts and other cells into myofibroblasts. These myofibroblasts have an elevated capacity for synthesizing ECM components and are highly contractile. They often promote the formation of large collagen bundles that then get cross-linked and lead to a stiffening of the tissue, adding mechanical strength to the ECM. This change in the microenvironment often disrupts adjacent basement membranes (BMs) and compromises tissue integrity through destabilized cell-matrix and cell-cell adhesions. The stiffened and remodeled ECM promotes cell migration toward the wound site, and more (myo)fibroblasts accumulate at the site, adding to the effect. This whole process is termed fibrosis (Frantz et al., 2010).

In healthy tissue with intact feedback mechanisms, tissue homeostasis is restored once the wound site has been repopulated and healed, thereby resolving the fibrosis. However, if erroneous feedback mechanisms or detrimental conditions such as repeated injury occur, a return to homeostasis cannot take place. The continuous ECM synthesis and deposition and increased ECM cross-linking eventually result in aberrant wound healing, where the tissue has reduced elasticity and altered mechanical properties. The final outcome of such dysregulation is tissue scarring (Kisseleva and Brenner, 2008; Schultz and Wysocki, 2009).

Similarly, these finely tuned dynamic processes can be more easily disrupted or even fail as an organism ages. A well-known pathology is the loss of PGs in the aging intervertebral disc, thereby decreasing hydration, compressibility, and buffering (Iozzo and Gubbiotti, 2018). These factors increase the probability of disc herniation, which can cause back pain and reduced mobility, and affects almost every person at some

point in their life (Iozzo and Gubbiotti, 2018). Moreover, resident fibroblasts often become senescent and resistant to apoptotic cues with increased age and produce high amounts of reactive oxygen species, fibronectin, cytokines, and other products that result in a chronic inflammation-like state (Untergasser et al., 2005). The combination of these products is detrimental to the stability of other fibrillar components of the ECM, such as elastin, and modifies collagen filaments. An increase in the cross-linking of collagen fibers leads to a stiffening of the ECM and, thereby, a reduction in elasticity and an increase in rigidity, not entirely unlike fibrosis. Such a drastic change in the biomechanical properties of an ECM may affect the spatial organization of cells, cell migration, and proliferation, and thereby potentially promote pathologies such as cancer (Frantz et al., 2010; Robins, 2007).

A hallmark of many cancers is indeed the aberrant behavior of ECM components and a loss of tissue organization. Tumor stroma can look very similar to acute injury: the ECM is stiffer and more rigid when compared to healthy tissue. This is induced by increased deposition and cross-linking of ECM components (Bonnans et al., 2014; Theocharis et al., 2019). Cancer cells have been reported to secrete chemokines and growth factors, leading to fibroblast activation and transdifferentiation into myofibroblasts, further promoting the generation and remodeling of ECM components. In this context, these fibroblasts are called cancer-associated fibroblasts (CAFs). Collagen fibers and other fibrillar structural elements are realigned and further cross-linked, resulting in further stiffening of the matrix. Increased expression of MMPs leads to the release of growth factors that result in enhanced vascular permeability and new blood vessel growth, thereby increasing the chance of metastasis (Frantz et al., 2010). Studies have shown that the increased expression of collagen-stabilizing enzymes such as LOX is a hallmark of many cancers (Mohan et al., 2020; Theocharis et al., 2019). The use of LOX inhibitors and thereby blocking at least one cross-linking mechanism together with cancer therapeutics increases the efficiency of the treatment and helps to reduce the tumor burden. However, these inhibitors only reduce further cross-linking of collagen fibers but cannot remove already existing cross-links. ECM that has been altered to resemble a fibrosis-like state can even prevent drug delivery and reduce treatment efficiency. Understanding the different cross-linking processes will be an important step in developing better cancer treatments. Normalizing fibrotic ECM may improve drug efficiency targeted at tumors and significantly increase recovery rates (Mohan et al., 2020).

Even genetic disorders arising from a single mutation in only one molecule related to ECM synthesis, signaling, or structure can have devastating effects (Iozzo and Gubbiotti, 2018). A wide range of diseases in virtually all tissues of the body is rooted at least partially in ECM abnormalities. For example, Ehlers-Danlos syndrome stems from mutations in collagen or proteins regulating collagen organization, such as MMPs. Patients with this syndrome display over-elastic skin, hyper-flexible joints, and valvular heart disease (Iozzo and Gubbiotti, 2018).

Another skin disorder is triggered by collagen VII mutations that result in aberrant anchoring of the dermis to the epidermis and, consequently, in tremendously fragile skin that easily develops wounds resembling severe burns. This disease is termed epidermolysis bullosa and often leads to a high cellular turnover and, in turn, increases the risk of cancer (Iozzo and Gubbiotti, 2018).

Moving inwards to the skeleton, defects in collagen synthesis can affect many ECM structures negatively. Osteogenesis imperfecta, for instance, is a heritable collagen disorder with a range of severity. It is usually caused by mutations in collagen I that replace glycine in the collagenous sequence with bulkier amino acids, thereby leading

to a loss of the triple helix structure (Iozzo and Gubbiotti, 2018). Consequently, collagen fibril formation is aberrant. The resulting faulty fibrils are often degraded, resulting in a critical decrease in bone strength. In severe cases, the condition is embryonically lethal, and less severe phenotypes may still have a strong negative impact on the life quality of those suffering from this disorder.
Like bone, cartilage is also a type of tissue that relies heavily on the proper alignment of fibers and healthy morphology in the ECM. Collagen IX disorders, for example, are detrimental to cartilage integrity and can result in a severe degenerative joint disease similar to osteoarthritis. Another well-known ECM-driven disease affecting cartilage and skin is Marfan syndrome. Affected patients typically present increased height and prolonged digits, flexible joints, and an increased risk of aortic aneurysms and fatal vessel rupture (Iozzo and Gubbiotti, 2018).
In short, the list of known pathologies connected to ECM dysregulation is long and ever-growing and encompasses all tissues in the body. An understanding of a healthy, balanced ECM is crucial to be able to simultaneously further our understanding of such pathologies and develop treatments for them in the future.

1.1.4. (Ultra)-Structural Biology of ECM

The discovery of the ECM preceded the discovery of cells, strictly speaking. Already in the 18th century, scientists could observe fibers upon closer inspection of tissues; at that point, most likely thick collagen fibers in tendons or similar structures (Ockenga, 2015). Back then, it was thought that tissues were composed of fibers which are the basis for life. Not until the advancement of light microscopy and the more detailed investigation of plant and animal tissues was the eukaryotic cell discovered and studied more closely. It took until 1855 that the common belief that tissues consist of fibers was adapted to the “cellular theory”, stipulating that cells are the basis of life and produce other cells as well as the fibrillar structures observed (Ockenga, 2015; Piez, 1997). While the light microscopes back then had already reached a sufficient resolution to visualize single cells and thick ECM fibers, it took the advancement of histology and the use of newly developed stains to help visualize different components of tissues, such as different cell types or ECM components. Prior to that, descriptions of tissues had been primarily based on rough dissections rather than any imaging techniques (Alberts et al., 2002; Piez, 1997).
The very first ECM protein described was collagen, which was defined as fibers found in almost all tissues that produce gelatin and glue upon boiling – the term collagen comes from the Greek language and means “glue producing”. It was at the end of the 19th century that the intercellular space was first seen to contain also much smaller fibers and a homogenous background that was referred to as “Grundsubstanz” (ground substance)(Piez, 1997) – most likely the PGs making up the hydrogel into which cells and fibers are embedded.
By the early 20th century, the dominating techniques in the research of cells and the ECM were histology and light microscopy, and the general make-up and layers of tissues were described. Once the concept of proteins was starting to be formulated in the 1920s/1930s, it was once again collagen fibrils that were the first ECM components described in their approximate appearance with light microscopy (Piez, 1997).
The first ultrastructural images of ECM components appeared in the 1940s, not long after the first commercial electron microscopes became available (Gross and Schmitt, 1948). Collagen fibrils, in particular, were uniquely suited as electron microscopy (EM) samples: they could be easily extracted from tissue using only forceps. After

contrasting by low-angle evaporation of platinum or similar materials or staining with uranyl acetate or phosphotungstic acid, they could be visualized at an unprecedented resolution. The acquired images were astonishingly detailed and already showed the D-periodicity of fibrillar collagen (Gross and Schmitt, 1948; Keene and Tufa, 2018) (see Figure 4).

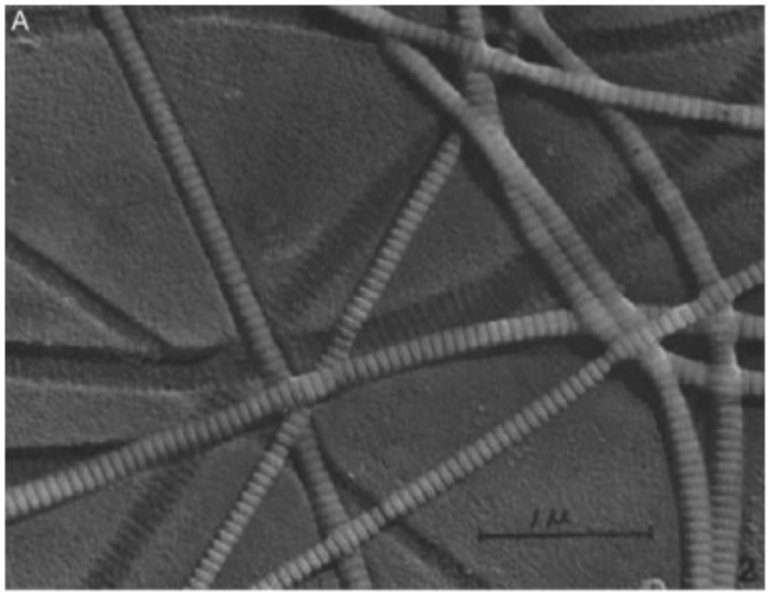

Figure 4: Collagen fibrils imaged by EM.
Collagen fibrils were teased from human skin and imaged with an EM after chromium-shadowing. The typical banding pattern of fibrillar collagens is visible. The scale bar represents 1µm. The image was sourced from the publication of Gross, J. and Schmitt, F.O. (1948), with permission from the Journal of Experimental Medicine.

By the 1960s, several important technical advances had been made, such as using chemical fixatives like glutaraldehyde, epon-based embedding media, new contrasting methods, and reliable ultramicrotomes with diamond knives. These could then be employed to create contrast-rich, ultrathin sections of tissues that allowed the investigation of intact cells and matrices by EM for the first time. This allowed descriptions of the ultrastructure of cells, basement membranes, and the ECM at a detail than previously possible (Farquhar and Palade, 1965; Keene and Tufa, 2018).
By the 1970s, X-ray crystallography had been immensely improved in terms of sample preparation and experimental conditions. It was the method of choice for the structural analysis of larger biological macromolecules, such as extracted collagen fibers. At that point, most research was probably focused on collagen I, the main component of tendon ECM; the existence of different types of collagen had not yet been discovered. However, thanks to the aforementioned technological advancement in X-ray crystallography, the structure and packing of collagen I microfibrils could be solved. It was found that five collagen I microfibrils make up the structural unit and further confirmed the 67nm or 234 amino acid residues periodicity and the 40nm gaps leading to the banding pattern (see Figure 2 and Figure 4)(Miller and Parry, 1973; Miller and Wray, 1971).
Little by little, the different ECMs were described employing methods such as microscopy, chromatography, electrophoresis, and X-ray crystallography. The importance of ECM in both health and disease became more and more evident, and every discovery was another puzzle piece that helped to achieve our modern understanding of many physiological processes.

For example, in the early 2000s, X-ray crystallography helped to uncover the arrangement of single collagen molecules into a quasihexagonal lattice in tendons after various other models had been proposed previously (see Figure 5)(Orgel et al., 2001; Wess et al., 1995).

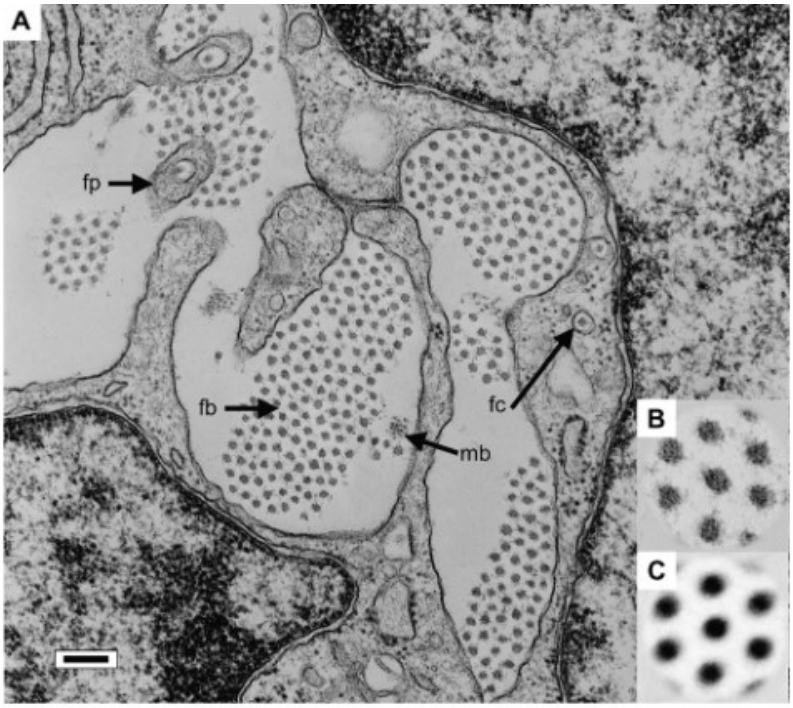

Figure 5: A TEM image of a transverse section of an embryonic mouse tail tendon.
A) Collagen fibril bundles (fb) are visible in the extracellular space. Frequently structures called fibripositors (fp) which consist of a plasma membrane encasing collagen fibrils, could be observed outside the main cell body. If these structures appear in the main cell body, they are termed fibricarriers (fc). Bundles of fibrillin microfibrils (mb) could also be observed in proximity to collagen fibril bundles. B) Collagen fibrils typically have a near-hexagonal arrangement in bundles. Here an example of the fibril arrangement is shown. C) An average of 10 regions similar to the one shown in B) is depicted. The figure was obtained from (Starborg et al., 2008) with permission from Elsevier.

At roughly the same time, atomic force microscopy (AFM) in combination with EM was used to confirm that collagen fibrils are indeed wound around their axis in a fashion similar to a classically laid rope (Bozec et al., 2007). Later, AFM was used to observe the proteolysis of collagen I by collagenase and played a crucial role in discovering MMP-9's preferential binding to already fragmented collagen (Zeug et al., 2014).
The last couple of decades has seen immense technological progress in both traditional methods and new techniques that have led to many discoveries regarding the structure and function of the ECM and its single components. While early studies often focused on single, extracted proteins and experimental *in vitro* set-ups, over time, the same techniques were utilized to study proteins in a more physiological context.
The combination of immunohistochemistry and light microscopy has been an essential factor in the observation of dynamic processes and the localization of specific proteins and their interactions. In combination with bioinformatics, mass spectrometry (MS) helped to analyze the core matrisome (ECM and ECM-associated proteins) of different tissues, and cell types, in health and disease. Moreover, cross-linking MS has furthered our understanding of protein-protein interactions between ECM components and ECM/cell surface proteins (Naba et al., 2012).

Nuclear magnetic resonance (NMR) spectroscopy of proteins is one of the pillars of structural biology and was initially used for molecules smaller than ~40kDa in solution (Huster, 2008). Of course, the size limitation was a significant setback when studying the ECM as its proteins are often bigger than 40kDa, and the technique does not allow for an *in situ* approach and instead requires the protein to be in solution. This limitation was overcome with the advent of solid-state NMR as it does not rely on molecular mobility, and there is no intrinsic limit on the molecular mass of the investigated sample. For several decades, solid-state NMR has been used to study immobile molecules of biological tissues such as cartilage, bone, or skin. Once again, collagen, in particular, has been the subject for many NMR studies that added to our understanding and painted a more complete picture of collagen and its interactions with other proteins on an atomic level (Huster, 2008; Schiller and Huster, 2012; Torchia, 1982). The measurements of different tissues showed that the motional amplitudes of collagen were larger in non-crosslinked and non-mineralized collagen (i.e., in skin) than in highly cross-linked or mineralized collagen (i.e., in bone), just as one would expect (Schiller and Huster, 2012). In short, NMR is not only a valuable tool in determining the chemical composition of tissues but also in studying the structure and dynamics of selected molecules, even in intact, hydrated tissues. However, its main drawbacks are comparably low sensitivity and the requirement of relatively large sample amounts (Murgoci and Duer, 2021).
Both MS and NMR are capable of detecting all molecules without any alteration to the sample through dyes or antibodies, which can be an immense benefit. The combination of these two techniques is especially advantageous, as it can provide important information on molecular conformations and dynamics, post-translational modifications, and non-enzymatic chemical changes (Schiller and Huster, 2012).
Besides light microscopy, EM has also been continuously employed to study the (ultra)structure of ECM and its components – from isolated single molecules, such as the different collagens, to 3D tissue volumes. The different EM techniques and recent developments in this field, also in context with the ECM, will be discussed in section 1.2. Cryo-Electron Microscopy.
Elucidating the full complexity of the ECM *in vivo* remains a significant scientific challenge to this day. Only by viewing the methods available to us as complementary rather than alternative will we succeed in better understanding the structure and functions of the single molecules making up the ECM.

1.1.5. Cell-derived matrices (CDMs)

Studying a microenvironment as complex and intricate as the ECM has been a challenge due to a multitude of factors: its three-dimensionality and diversity in both composition and structure, among the foremost ones. Studying ECMs *in vivo* would be the most desirable scenario to retain the full physiological context and relevance. However, specimen preparation workflows for certain techniques are often incompatible with such a set-up and would be detrimental to the study's success.
For example, cell migration and morphology were initially often studied *in vitro* using artificial non-physiological substrates that were traditionally stiff two-dimensional surfaces such as glass or plastic. While such approaches have given us immense insight into many biological mechanisms, they cannot fully recapitulate a native, physiological process. With an increase in our understanding of the ECM and technological advances, several *in vitro* models have been established that mimic the physiological environment of cells in the body. In the 1950s, the first attempt was to

coat cell culture substrates with particular ECM components before cell seeding. Back then, George Gey used rat tail collagen to coat his cell culture surfaces to facilitate cell attachment (Curtis et al., 1983). By the mid-1980s, most laboratories were using treated polystyrene instead of glass as it showed a much higher rate of cell attachment and survival: the laboratories also coated the polysterene with different materials to increase efficiency further (Curtis et al., 1983; Raey et al., 1984). The ECM proteins used were already known to play a role in cell adhesion and migration, such as fibronectin, laminin, or collagen. With this method, the effects of different proteins on cell adhesion, proliferation, differentiation, or migration could be studied. However, while these studies have granted us insight into these cellular processes, the created microenvironment still differed drastically from the complex 3D environment the ECM offers (Cheng et al., 2020).

The mimic of a native matrix can be further improved by using synthetic, porous materials and coating them with one or more of these ECM components to mimic the physiological situation better (Cheng et al., 2020; Ho et al., 2005). This method works best with small peptides that can diffuse through the porous structures. For example, an Arg-Gly-Asp peptide that mimics an important binding site of fibronectin for various other proteins is often used. However, cells seeded into these 3D materials tend to distribute very inhomogenously within the scaffold, and they are not suited for some sample preparation workflows.

A step closer to a physiological set-up is the use of hydrogels forming three-dimensional structures. These provide a highly hydrated environment and can consist solely of ECM proteins (Cheng et al., 2020). For example, hydrogels consisting of collagen I, collagen II, or fibronectin alone can be assembled quite easily and then seeded with cells. Their main advantage is that their composition is known, and they are easy and quick to assemble. However, depending on the questions posed, they are not a good mimic of the complex ECM that consists of over 300 different components (Cheng et al., 2020). An alternative to these single-protein-hydrogels is the use of Matrigel®, a commercially available extract of a specific type of tumor (Benton et al., 2014). Matrigel® resembles an early developmental basement membrane in composition and is often used in angiogenesis assays. It contains several growth factors inducing new vessel formation, laminin, collagen IV, and other structural components. Over time, different variations of this hydrogel have been generated and allow for a broader range of use. However, it has to be considered that a basement membrane has a very specific function and differs considerably in function, composition, and structure from interstitial ECMs (Benton et al., 2014).

A top-down approach that has been used for over a decade is the use of tissues that have been decellularized to remove most of the cellular and nuclear material (Cheng et al., 2020). This results in an excellent replica of native ECM with all its components but comes with the caveat that the process usually uses chemical, enzymatical and thermal steps that can alter the mechanical integrity of the ECM. While structural components such as fibers are likely retained, components such as PGs or other soluble factors could be lost in the process (Cheng et al., 2020). Therefore, whether this model is suitable depends strongly on the question posed. There are commercially available decellularized skin matrices, such as AlloDerm®, although they are traditionally used for medical purposes to support wound healing rather than in basic research. Similarly, other decellularized ECMs are used in medicine, such as decellularized heart valves seeded with autologous cells for implantation (Bello et al., 2012; Cheng et al., 2020).

More recently, the use of ECM-producing cells such as fibroblasts, endothelial cells, chondrocytes, or differentiated mesenchymal stem cells has found more and more applications (Hakkinen et al., 2011; Jacquemet et al., 2015; Kaukonen et al., 2017; Petrie and Yamada, 2016; Rubi-Sans et al., 2020). These cells can be cultured *in vitro* and will synthesize and secrete matrix components and, given enough time, will build a so-called cell-derived matrix (CDM) that can be either decellularized or used as-is. CDMs have the enormous advantage that their composition will resemble the ECM native to the cells producing them and can additionally be tweaked in terms of composition and properties by adapting growth conditions or even genetically modifying the CDM-producing cells. Thus, CDMs can recreate a variety of microenvironments to study different biological questions and applications (Jacquemet et al., 2015; Kaukonen et al., 2017; Rubi-Sans et al., 2020). In medicine, CDMs are used as coatings for synthetic scaffolds (Fitzpatrick and McDevitt, 2015), and in research and medicine for both the biomimetic microenvironment to induce stem cell differentiation (Fitzpatrick and McDevitt, 2015) and in the investigation of 3D cell migration (Kaukonen et al., 2017).

The main trade-off of CDMs compared to *ex vivo* tissue-derived matrices is their poorer mechanical properties, making them unsuitable for some applications. Moreover, one has to consider that the ECM is produced by a range of cells rather than just one cell type. This can be mimicked to some degree by co-culturing cells but has to date never been fully recapitulated (Cheng et al., 2020).

There are three main considerations when generating CDMs: cell source, culture method, and processing method. Cells derived from specific tissues typically generate matrices that mimic the relative composition of the natural tissue matrix. Fibroblasts, for example, will produce collagen-rich ECM. On the other hand, mesenchymal stem cells (MSCs) can be influenced by changes in their culture condition to produce ECM that resembles various tissues such as bone, cartilage, or adipose tissue. Several studies compared CDMs derived from different cell types under different culture conditions, and showed that they differ in composition (Cheng et al., 2020; Fitzpatrick and McDevitt, 2015; Lu et al., 2011).

CDMs can be synthesized by both primary cells and cell lines, and both have advantages and disadvantages. Primary cells sourced from tissue will recapitulate the native ECM with higher reliability as they have not undergone numerous rounds of proliferation and potentially accumulated mutations. It is, however, difficult to acquire a high number of cells. Hence, experiments may have to be downscaled, and culturing conditions may be challenging. Cell lines, in contrast, can be easily cultured to yield large cell numbers, and different cell lines can be co-cultured. They are often well characterized and will reproducibly produce CDMs of identical composition under the same conditions. It is important to note the source of the cell lines as they often derive from tumor tissue, which could drastically alter the CDM composition compared to healthy cells (Fitzpatrick and McDevitt, 2015).

Another factor that must be considered for the production of CDM is the culturing method, which will depend on the planned use of the CDM. Commonly, adherent cells are cultured for an extended period of time in monolayers, as multicellular aggregates, or on degradable carriers for medical purposes (Assunção et al., 2020; Fitzpatrick and McDevitt, 2015). Additionally, the environmental conditions can be adjusted to the *in vivo* conditions to mimic the physiological state more closely, e.g., by adjusting the O_2 content depending on tissue vascularization.

The process of CDM generation can take several days to weeks (Kaukonen et al., 2017). Once sufficient ECM has been deposited, the CDM can be either used as is or

decellularized through chemical, physical, and/or enzymatic treatments. Typically, such a process involves the use of alkaline or acidic reagents such as ammonium hydroxide and/or detergents such as Triton X-100. Lyophilization and freeze-thaw cycles can be used on their own or in addition to remove cellular components (Fitzpatrick and McDevitt, 2015). It should be noted that these processing steps can lead to a loss of PGs and disrupt the ECM structure, much like in the decellularization of tissue.
Nevertheless, CDMs are used more and more often in both research and medicine. For instance, scaffolds coated with mineralized CDM were shown to aid in bone regeneration and osteogenesis (Fitzpatrick and McDevitt, 2015). An added benefit of CDMs is the potential use of patient cells for matrix synthesis, significantly reducing the chance of pathogen contamination and immunogenicity (Fitzpatrick and McDevitt, 2015; Rubi-Sans et al., 2020). In basic research, CDMs have been used for over a decade now to further our understanding of physical and chemical interactions between cells and the ECM, mainly by employing light microscopy (Kutys et al., 2013). In the last years, the development of 3D substrates compatible with light microscopy set-ups has vastly increased our understanding of cancer invasion, cell motility, adhesion, and adaptation to different environmental factors (Doyle et al., 2015; Duval et al., 2017; Even-Ram and Yamada, 2005). This has offered many new insights and highlighted substantial differences in cellular behavior between 2D and 3D cultures (Friedl and Wolf, 2010; Hakkinen et al., 2011).
However, so far, such 3D environments have not been used in combination with high-resolution electron microscopy under native conditions, i.e., without employing chemical fixation, sectioning, and contrasting. Such a non-destructive approach can only be achieved by employing cryo-electron microscopy (cryo-EM), where the specimen is vitreously frozen (i.e., without forming ice crystals, a process called vitrification). By vitreous freezing, cells are fixed in a native, hydrated state for imaging. Cryo-EM has been successfully used to visualize the structure of single, purified components of cells and the ECM, and even the ultrastructure of the cellular periphery of single cells. However, due to limitations in specimen preparation and imaging of voluminous structures in micrometer size, there currently exists no approach that allows for the ultrastructural analysis of cellular and extracellular structures under native conditions in a 3D environment.

1.2. Cryo-electron microscopy (Cryo-EM)

Electron microscopy (EM) is a powerful method in cell and structural biology and is used to visualize samples at a wide range of magnifications. EM uses a beam of accelerated electrons as an illumination source. Since the wavelength of an electron is considerably smaller than that of visible light photons, electron microscopes have a drastically higher resolving power than light microscopes, enabling imaging from low magnifications to very high magnifications.
For a long time, one main disadvantage of using traditional EM for imaging of biological samples was sample preparation procedures: To withstand the vacuum within the electron microscope, biological samples such as single cells or tissues needed to be chemically fixed, dehydrated, and contrasted prior to imaging. This method offers high-resolution insights but potentially introduces artifacts and distortions, shrinks the specimens during fixation and contrasting (Gusnard and Kirschner, 1977), and does not preserve the native hydrated state of biological material. The loss of nativity is especially detrimental for highly hydrated samples such as the ECM. Despite these

restraints, traditional EM has been of great importance for our current understanding of the organization of proteins in the ECM.
The advent of modern cryo-electron microscopy (cryo-EM) started with the introduction of a new sample preparation method by Dubochet and colleagues in the 1980s(Dubochet et al., 1982). Instead of chemical fixation, their method relies on fixation by rapid freezing at cooling rates of about 10^4 K/s or more (Cheng et al., 2012). If the specimen is frozen at such cooling rates, single water molecules cannot rearrange into crystals and instead form amorphous, non-crystalline ice. This process is called vitrification, a term deriving from the Latin word *vitreum,* which means “glass”, and, indeed, perfectly vitrified water takes on a glass-like appearance (see Figure 6).

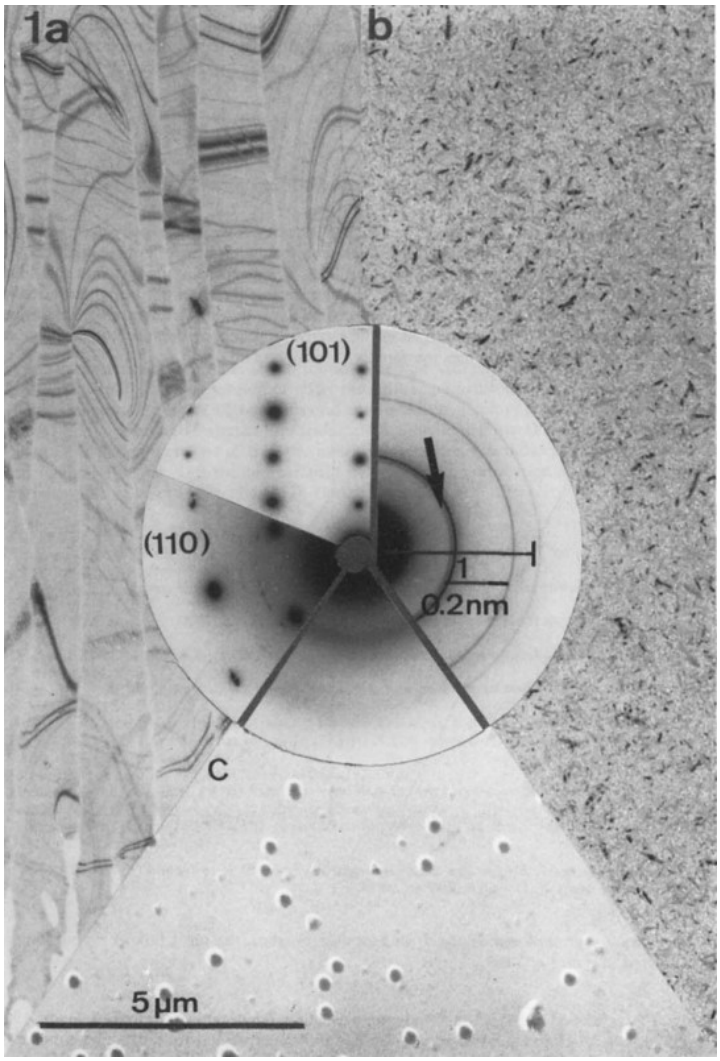

Figure 6: The three forms of ice and their electron-diffractograms.
a) Hexagonal ice and its electron diffraction pattern. Hexagonal ice crystals are relatively large (in the range of microns) and show visible structures; they typically form at low freezing rates (Bhella, 2019). b) Cubic ice and its electron diffraction pattern. They are typically relatively small (~100 nm) and show a grainy appearance. Cubic ice typically forms when the sample warms up and devitrifies (Cyrklaff and Kühlbrandt, 1994). c) This figure was obtained from (Dubochet et al., 1982), with permission from the Journal of Microscopy.

Cryo-EM retains specimens in their fully hydrated state without introducing artifacts. Depending on the thickness and complexity of the sample, two different vitrification techniques can be used. Plunge-freezing is commonly used for individual molecules,

cells, or cell clusters, and high-pressure freezing (HPF) is used for thicker specimens such as multicellular organisms and tissues. The thickness that reliably can be vitrified by plunge-freezing strongly depends on the sample composition and can be in the range of several microns (Harapin et al., 2015; Mader et al., 2010). Typically, the specimen is placed on a grid that acts as an EM sample carrier. Different grid materials (e.g., gold, titanium, copper) and surface coatings (e.g., carbon, gold, formvar) are available, which are selected according to the requirements of the sample. As copper is cytotoxic, cells are typically seeded on gold or titanium grids. Before vitrification, excess liquid is blotted away with filter paper, and the grid with the specimen is then plunged into a small vessel containing cryogen. The cryogen is typically ethane, propane, or a mix thereof and is cooled to temperatures of -180 to -190°C with liquid nitrogen (LN_2)(Cheng et al., 2012). In contrast to ethane and propane, LN_2 is subject to the Leidenfrost effect due to its significantly lower boiling point and heat transfer rate. This makes ethane and propane far better suited plunge-freezing cryogens (Cheng et al., 2012). There are multiple commercially available plunge-freezing devices, such as the Vitrobot from Thermo Fisher Scientific or the GP2 from Leica.
However, any sample that exceeds a thickness of several microns cannot be vitrified by plunge-freezing, and HPF has to be used instead, which is suited for the vitrification of samples up to 200µm and more.
HPF relies on applying high pressure during the vitrification process (Dahl and Staehelin, 1989). Ice-crystal growth starts when water is cooled below its melting point and can be slowed down considerably by applying high pressure that lowers the melting point and, thereby, the nucleation temperature for the crystallization process. Due to this shift, lower freezing rates are required for vitrification using HPF, and even thicker specimens can be vitrified.
Currently, different HPF machines are commercially available that all have the same basic mechanism and only differ slightly in their individual designs. Typically, the sample is inserted into an HPF machine in a specimen holder, such as metal carriers, and frozen with a pressurized stream of LN_2 while the specimen is subjected to a pressure of ~2100 bar. After this process, the specimen can be recovered and processed further with methods such as freeze-substitution. In this method, the water in the specimen is gradually replaced with organic solvent at higher temperatures after HPF, returned to room temperature, and subjected to conventional EM sample preparation methods, such as heavy metal staining. While this process is much better suited to retain native structures, it still subjects the specimen to a series of chemical treatments and potentially introduces artifacts.
For cryo-EM, the specimen must stay at cryogenic temperatures of -150°C or lower to remain vitrified during sample processing and EM imaging.
EM can be divided into two main methods: Transmission electron microscopy (TEM) and scanning electron microscopy (SEM). Both are widely used in biological and material sciences and have been vital in advancing our understanding of the topography, morphology, and composition of many different materials.

1.2.1. Transmission Electron Microscopy (TEM)

In TEM, a projection image is created by transmitting a beam of electrons through a sample and onto a detection device. The electron beam is emitted from an electron source at the top of the microscope, either a so-called field emission gun (FEG) or a thermionic gun. A FEG is typically more advantageous in its use as the emitted electrons have a higher spatial and temporal coherence, and thus higher resolution

imaging can be achieved in comparison to other electron sources. The accelerating voltage of a TEM microscope typically ranges from 80 to 300 kV; the faster the electrons, the smaller the electron wavelength, and therefore the higher will be the highest achievable resolution.
A TEM consists of a series of lenses that focus the electron beam on the. The electron beam passes through the sample and gets magnified onto a detection device with another lens system. As the electrons pass through the specimen, they interact with the atoms comprising it, leading to different scattering events. Back-scattered electrons (BSE) are reflected by the sample after an elastic scattering event and do not pass through the sample. These electrons are used for sample detection in SEM but are ignored in standard TEM.
The remaining electrons are scattered either elastically or inelastically. Elastically scattered electrons pass through the sample without any interactions and lose no energy. Inelastically scattered ones, however, suffer energy loss through interactions with the sample. These interactions can break bonds and produce secondary electrons and free radicals. This is especially problematic for studying biological specimens as it damages and ultimately destroys the sample in the imaging area. Higher voltage and hence a smaller electron wavelength reduces beam-sample interactions and beam-induced sample damage. The entire EM column is kept at high vacuum to avoid air-electron interaction and, thereby, undesired scattering of electrons.
Different types of detection devices exist, such as fluorescent screens, photographic films, charge-coupled devices (CCDs), and direct electron detection devices (DDDs)(Jin et al., 2008). DDDs are nowadays used especially for high-resolution data acquisition as they can directly detect electrons and have the best signal-to-noise ratio (SNR). Some DDDs can even count single electrons hitting the detector, thus further significantly increasing the obtainable resolution. New detectors allow recording several consecutive micrographs called frames during a single exposure which can be aligned post-acquisition to reduce stage or beam-induced sample motions, further improving data quality.
Modern EMs also have energy filters to increase data quality further. Energy filters remove inelastically scattered electrons, improving the contrast of the final image.
There are two types of energy filters: In-column energy filters that are located before the projection lens system and post-column energy filters that are positioned just before the detector. The microscope used in this thesis is equipped with a post-column filter.
TEM relies on the electrons that pass through the sample; therefore, sample thickness is critical for this method. The thicker the sample, the fewer electrons can pass through without being scattered multiple times, and the weaker the signal on the detector will be. Ideally, TEM samples should not be thicker than 200-300 nm, although samples of up to 500 nm can be imaged on a 300 kV microscope.

1.2.2. Scanning Electron Microscopy (SEM)

In contrast to TEM, SEM uses back-scattered and secondary electrons for image generation rather than the elastically and inelastically scattered ones that pass through the sample. As a result, instead of providing information about the structures within the sample, SEM provides high-resolution information on the sample's surface.
Back-scattered electrons (BSE) originate from elastic interactions between the electron beam and sample and have no or nearly no energy loss. BSEs are reflected

back from deeper regions of the sample and provide information on sample topology and atomic composition. The higher the atomic number, the brighter the material will appear in the resulting image.
In contrast, secondary electrons (SE) originate from the surface or near the sample's surface and have lower energy than BSE. They result from inelastic interactions between the electron beam and the sample and provide higher-resolution topographic information than BSE.
An SEM column is built very similarly to a TEM column. However, the accelerating voltage of an SEM microscope is typically much lower, with only up to 30kV, and in accordance, the achievable resolution is also lower. As in the TEM, the electrons are emitted from an electron source at the top of the column, often an FEG in high-end systems. The electron beam is then directed toward the sample through apertures and a series of condenser lenses. SEMs have pairs of scanning coils situated within the condenser lens system. These scanning coils deflect the beam in the x and y axes and are responsible for the raster-like scanning of the electron beam over a rectangular sample area. When the electron beam hits the sample, the electrons interact with the sample elastically or inelastically and are reflected back.
One component that differs drastically between SEM and TEM is the sample stage: in an SEM, the sample stage is much larger and allows the mounting of much larger and thicker samples, although it is also compatible with standard TEM substrates, such as EM grids and EM sapphire discs. Due to this, whole organisms, such as small spiders, isopods, or other insects, or dissected tissues, such as rat tail tendons, can be mounted in an SEM and imaged.
Another significant difference to TEM is the detectors used for SEM, as different types of electrons need to be detected. Both SE and BSE are collected by the Everhart-Thornley electron detector (ETD), which is mounted above and to the side of the stage, with the specimen typically tilted toward it. A low positive voltage is applied to it in order to attract low-energy SE, while high-energy electrons are not affected. While an ETD can detect both BSE and SE, it is primarily used to detect SEs.
The detectors used for BSEs are typically solid-state detectors located between the sample and the condenser lenses, often directly integrated into the SEM column. The electron beam passes through a hole in the center of the detector, and the BSE are collected as they are reflected back from the specimen during the scanning process.
These different detector types can be used simultaneously to acquire an image set with complementary information on the specimen.

In order to enable cryo-EM with vitrified samples, dedicated SEM and TEM microscopes are available that can be cooled down to around -180°C – 190°C by using LN_2. Specifically, all parts of the instrument in contact with the vitrified specimen are kept at temperatures below -150°C to avoid devitrification.

1.2.3. Cryo-Electron Tomography (cryo-ET)

Studying the (ultra)structure of macromolecules in their native context remains one of the biggest challenges in cryo-EM. The method of choice for this task is **cryo-electron tomography (cryo-ET)**, which allows the imaging of macromolecules *in situ* in 3D at sufficient resolution.
In contrast to conventional 2D EM, where single micrographs are obtained, cryo-ET relies on acquiring a series of 2D micrographs in a defined tilt range. This way, images of a region of interest are acquired from different tilt angles under identical imaging

conditions. These are then computationally aligned and reconstructed into a 3D volume called a tomogram (see Figure 7 for a schematic depiction of tomography).
In an ideal scenario, a tilt series would cover a tilt range of 180° in infinitely small angular steps to obtain the complete isotropic information of the 3D volume. Mechanical and practical limitations, however, usually lower the tilt range to ~120° in 1-3° increment steps instead and result in incomplete information sampling of the object of interest, a phenomenon called the missing wedge problem.

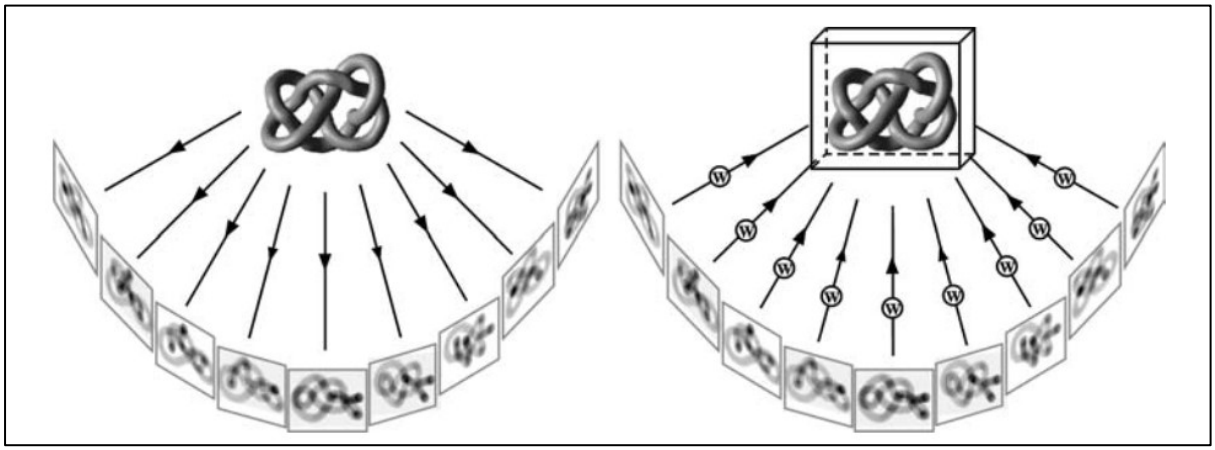

Figure 7: A schematic depiction of the principle of tomography.
Projections of an object are recorded in a tilt series from different angular views (*left*). Tomogram reconstruction via weighted back-projection results in a 3D volume (*right*). This figure was obtained from Lučić et al., 2005 (Lučić et al., 2005), with permission from Annual Reviews.

There are several ways to compensate for this problem to at least some degree. For example, dual tilt-axis tomography converts the missing wedge into a missing pyramid. Another option is subtomogram averaging, which averages subvolumes of tomograms containing identical objects in different orientations and fills in the missing regions.
Biological specimens have inherently very low contrast in EM images as they consist mainly of elements with low atomic numbers and thus low electron scattering power, such as carbon and oxygen. Conventional sample EM sample preparation workflows employ contrasting methods to compensate for this, while cryo-EM has to rely on the native properties of the specimens. Additionally, the total dose of electrons that can be used for imaging has to be carefully set to limit beam-induced sample damage and depends on the acceleration voltage of the electrons used, as well as the exact composition of the sample. Already 10 to 20 electrons per $Å^2$ can destroy high-resolution details (Grant and Grigorieff, 2015; Karuppasamy et al., 2011). Especially in tomography, where the total dose has to be divided over the single micrographs composing the tilt-series, this can result in a very low signal-to-noise ratio (SNR) and can negatively impact subsequent image processing steps such as tomogram reconstruction (Lučić et al., 2005).
With the invention of DDDs, which detect even single electron events, and energy filters, the low contrast can be compensated to some degree. Additionally, the quickly increasing number of algorithms improves the speed and efficiency of tomogram reconstructions and data analysis.
In numerous studies, cryo-ET has been successfully applied to biological specimens to investigate the native architecture of cellular structures *in situ*(Asano et al., 2016; Dunstone and de Marco, 2017; Lučić et al., 2005; Small et al., 2008). Many structures of proteins and protein complexes at near-atomic resolution have been solved by cryo-

ET in the last decade(Nogales, 2016; Wagner et al., 2017). This method is still rapidly developing and is a fundamental pillar of structural biology, especially in combination with other powerful tools and new technologies.

1.2.4. The contribution of new technologies to cryo-ET

New technologies, such as DDDs and new algorithms for data processing, are continuously advancing the power of cryo-ET in investigating cellular structures and helping to overcome its limitations.
One main restriction of cryo-ET is sample thickness. While cryo-ET can be used to image specimens of up to roughly 500nm, tomography works best on samples that do not exceed ideally 250nm. Additional sample preparation steps are necessary for structures exceeding ~250nm (Ben-Harush et al., 2010).
Until about 15 years ago, there was only one method to overcome this limitation: Cryo-electron microscopy of vitreous sections (CEMOVIS)(Al-Amoudi et al., 2004). CEMOVIS combines HPF and cryo-sectioning with an ultramicrotome to produce thin, vitreous sections of a specimen that are thin enough for TEM. CEMOVIS enables high-resolution imaging of native biological specimens but is technically very demanding and introduces artifacts, such as distortions, blade marks, and compression fractures (Richter, 1994).
In 2006, focused ion beam (FIB) for sample thinning was introduced as an alternative to CEMOVIS (Al-Amoudi et al., 2004; Schertel et al., 2013). A dual-beam focused ion beam scanning electron microscope (FIBSEM) can be used at cryogenic temperatures to remove material from a biological sample in a very controlled manner. This process is described in detail in section 1.2.6.

Correlative light and electron microscopy (CLEM) combines the advantages of both fluorescence microscopy (FM) and EM. FM provides positional information on specific proteins and helps to locate them in EM, which in turn provides information on the (ultra)structure of the protein and its microenvironment. CLEM will be discussed in more detail in section 1.2.5.

1.2.5. New technology: cryo-CLEM

A notorious challenge in cryo-ET is the poor intrinsic contrast of biological samples and the necessity of keeping the total electron dose low enough to avoid beam damage to the sample. Consequently, it is often difficult to detect and identify the structures of interest before data acquisition and after tomogram reconstruction, especially when they are rare and their exact location within a cell is unknown. A tomogram typically covers only ~1/100th of a cell, and the chance to hit regions of interest (ROIs) by chance when selecting random data acquisition points is slim.
CLEM has been of immense help to circumvent this problem by employing LM, specifically FM, to help identify and locate specific ROIs and then transfer the knowledge about their location to the EM to guide data acquisition. Moreover, the chance to record data on the sought macromolecules is significantly increased, and the identity of observed structures can be potentially confirmed.
A CLEM workflow typically employs a two-step imaging approach (Schellenberger et al., 2014). In the first step, the specimen is imaged by LM, and ROIs of interest and distinct landmarks are identified. The sample can then be contrasted and coated before EM imaging, if required, and is transferred to an EM, where an overview is

taken. By using landmarks visible on both LM and EM images, the two images can be correlated, and ROIs can be located for high-resolution data acquisition. This can help to identify macromolecules or structures of interest and increase the interpretability of data.
One of the main caveats of CLEM is that, ideally, it needs to be performed on the same specimen in the same state to maximize the accuracy of correlation (Schorb et al., 2017). If FM is performed before vitrification, vital landmarks used for correlation can potentially change due to the time delay between imaging and vitrification or damage to the specimen during the vitrification process.
Hence, the challenge of performing FM at temperatures well below -150°C without the devitrification of the specimen arises. Additionally, the potential contamination of the sample by atmospheric humidity during imaging and transfer has to be minimized (Schellenberger et al., 2014).
Currently, several commercial systems are available for cryo-FM, such as the CMS196 Cryo-CLEM stage from Linkam Scientific and the Cryo-CLEM system from Leica Microsystems. However, all cryo-CLEM instruments encounter the same limitations and function similarly. The specimen is kept on a cryo-stage cooled with cold LN_2 gas to ≤150°C to prevent devitrification. The optical performance of all cryo-CLEM systems is limited by the types of objectives that can be used (Schorb et al., 2017; Schorb and Briggs, 2014). Due to the low working temperature and the need to keep the specimen cooled, immersion-free objective lenses with a high working distance (WD) and correspondingly low numerical aperture (NA) are preferentially employed. Currently, the Leica Cryo-CLEM system has the best available thermally insolated objective lens integrated into its system, with a WD of 0.28 mm and NA of 0.9 (as per product specifications).
The accuracy of CLEM can be significantly increased with the use of fiducials visible in both LM and EM (Kukulski et al., 2012, 2011). For example, in combination with the Leica Cryo-CLEM system, fluorescent, electron-dense beads (e.g., TetraSpeck, Thermo Fisher Scientific) with a size of 50-100 nm have been used to reach a correlation precision of ~30-40 nm in x and y (Schorb et al., 2017).
However, LM usually has a much lower resolution in z than in x/y and, in consequence, also correlation accuracy is much lower in z, only in the range of hundreds of nm. Additionally, depending on the specimen, the fiducials might only stay on the surface area and not allow for high precision regardless of the LM imaging system used.
There is no straightforward solution to this problem, but various companies and research groups are trying to advance 3D CLEM to improve accuracy in all three dimensions (Arnold et al., 2016; Prabhakar et al., 2021; Sandvold Beckwith et al., 2015). Better accuracy of cryo-CLEM in z would be particularly beneficial during the sample thinning process to make specimens amendable to cryo-ET and increase the data throughput for rare events.
A promising approach is the installation of LM systems into SEMs, such as the METEOR system by delmic (“METEOR: an integrated top down cryo-CLEM imaging system.,” 2022). METEOR can be integrated into (cryo)-FIBSEMs as an additional module without hampering the functionality of the dual-beam instrument. This reduces the necessary transfer steps and potential contamination and can guide the sample thinning in all three dimensions with higher accuracy than other workflows throughout the whole process. However, to ensure high reproducibility and the use of only high-quality samples, it might be preferential to screen samples prior to this step, in which case other systems might be preferable.

Cryo-CLEM opens up new possibilities for the analysis of cellular and extracellular ultrastructures by cryo-ET, especially in combination with EM-sample preparation methods such as FIB-milling.

1.2.6. New technology: cryo-FIBSEM

A dual beam FIBSEM microscope combines a FIB column with a standard SEM set-up in a single corpus to create precise cross sections or lamellae for subsequent imaging via SEM, STEM, or TEM. While SEM can be used to monitor progress, the FIB is employed to remove material from the sample step by step. This allows for precise targeting and observation throughout the processing of the sample.
Overall, a FIB system operates similarly to an SEM, except that instead of electrons, it uses a finely focused ion beam with a dual function. It can be used for high-resolution imaging at low beam currents. At high beam currents, it can remove material in a targeted manner. As the ion beam hits the surface of the specimen, it sputters away small amounts of material in the form of secondary ions, neutral atoms, or electrons. This process is called FIB milling. The signal of these ions and electrons is collected and used to form an image. Modern FIB instruments can achieve a resolution in the 1-2nm range (Orloff, 2001, 1996).
Dual-beam FIBSEM systems are relatively young instruments: while the first FIB instruments were used in the 1970s, the first dual-beam microscope was assembled in the late 1980s (Young and Moore, 2005). It took until the early 1990s for the first dual-beam FIBSEMs to be commercially available (Young and Moore, 2005).
Initially, FIB microscopes have been used as single-column instruments (Krohn and Ringo, 1975), but this has the disadvantage that assessment of the progress of each preparation step requires a tilting of the sample. This reduces the achievable precision and is more time-consuming. Hence, using a dual beam instrument is preferable (Young and Moore, 2005), where the instrument is typically set up with a vertical electron column and a tilted ion column, as it is easier to achieve optimum performance at a tilted angle with an ion column than with an electron column. In order to allow simultaneous observation and processing of the sample, the two beams have a coincident point on the sample.
FIBSEMs are produced by only a few companies: Thermo Fisher Scientific, Zeiss, Tescan, Jeol, and Hitachi. Among these, Thermo Fisher Scientific is the only one that offers dedicated cryo-FIBSEM instruments. The principles of all the dual beam systems are identical, and the general set-up is very similar.
The SEM is operated like any standard SEM and uses a FEG as the electron source. The ion column typically uses a liquid-metal-ion source which works as a point source based on field emission to produce ions.
Gallium is the most commonly used source of ions, both in material science and biological sciences. Its advantages include a relatively long lifetime, high robustness, a low melting point of 29.8°C, low volatility, and good emission characteristics. Furthermore, gallium ions are sufficiently heavy to remove material from various materials efficiently, and the theoretical implantation zone is relatively narrow, with only ~10 nm (Marko et al., 2007; Wolff, 2020). Beyond Gallium, other ion sources are available, where plasma can be generated from gases, such as Xenon, Argon, Oxygen, and Nitrogen. Some potential advantages to each of these elements could be helpful in sample preparation: Xenon and argon are both noble gases and are unlikely to interact with the specimen to form a chemical bond of any sort, reducing the risk of ion implantation into the sample. Xenon ions are also heavier than gallium

ions and have a higher sputtering rate (Zhong et al., 2021). Plasma FIBs (pFIBs) can generally be operated at higher currents than Gallium, resulting in higher sputtering rates (Dumoux et al., 2022). This is especially useful for large-area milling at faster rates.
FIBSEMs were initially invented for material science, particularly in the analysis and processing of semiconductors. The first use for the analysis of biological samples at room temperature was only recorded in 2001 (Ballerini et al., 2001) and 2004 (Drobne et al., 2005), but already back then, the high potential of this method for biological sciences was recognized.

The first attempt using a FIBSEM at cryogenic temperatures was published in 2006 (Marko et al., 2006). At that time, only vitreous water was milled, but the study worked as a proof-of-principle and could successfully show that no devitrification occurred upon milling. Within the next few years, research groups started to employ cryo-FIBSEM to prepare lamellae from vitrified biological samples for subsequent cryo-TEM (see Figure 8)(Marko et al., 2007; Rigort et al., 2010). Importantly, in contrast to microsectioning approaches, FIB milling produces no mechanical artifacts or large-scale structural distortions. While subtle FIB-induced alterations, such as beam damage, cannot be ruled out completely, they would be expected to be limited to a narrow ion implantation zone (Marko et al., 2007), depending on the ion source used. Based on this significantly lower chance of introducing critical artifacts, cryo-FIB milling is thought superior to cryo-ultramicrotomy, even though CEMOVIS can produce thinner sections (Al-Amoudi et al., 2004) that would, in theory, allow for higher resolution imaging.

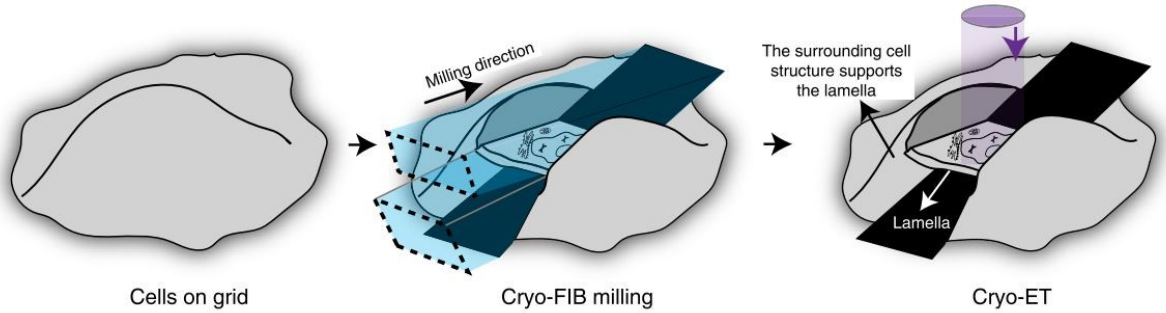

Figure 8: The preparation of thin lamellae from biological samples via cryo-FIB milling for cryo-ET.
A schematic drawing shows the use of a FIB (blue boxes) to remove bulk material from a specimen to create a thin lamella compatible with cryo-ET (TEM beam represented by purple cylinder). The surrounding cell structure supports the created lamella. The figure was obtained and adapted from (Wagner et al., 2020) with permission from Springer Nature.

For cryo-applications, microscopes are fitted with a cryo-stage, with a cryo-shield that is usually operated at colder temperatures than the stage itself to trap water contamination and prevent it from reaching the sample. Ideally, the stage is operated at ~-193°C. The stage and the cryo-shield are cooled through N_2 gas run through tubes that carry the gas from an external heat exchanger submerged in liquid nitrogen (LN_2)(Hayles and de Winter, 2021; Schaffer et al., 2017). The stage is mobile and can be rotated up to 180° and tilted up to 45° depending on the z-height of the stage.
The running time at cryo-temperatures of the instruments depends on the LN_2 dewar size and the speed of the gas flow in the tube, as the faster flow will lead to more rapid use of the coolant. The dedicated TFS dual-beam cryo-FIBSEM Aquilos I has a

running time of ≥10 h, according to the specification sheet. The next generation instrument, the Aquilos II, has an extended running time that enables overnight runs, according to their specification sheets. In my personal experience, the Aquilos I could be operated for around 11-12 hours, while the Aquilos II can be operated for up to 18 hours.
The samples are loaded into a shuttle in a loading station under cryo-conditions. It is important to note that the samples sit at a 45° angle in their positions in the shuttle (see Figure 9)(Wagner et al., 2020). Once the samples are loaded, it is transferred to the cryo-FIBSEM via a transfer rod under vacuum conditions.
Modern dual beam instruments such as the TFS Aquilos II also have an integrated sputter coater and a gas injection system (GIS) which can coat the sample with platinum. A sputter coater is used to cover a sample with a few nm of platinum to counteract the charging of biological samples, which often makes SEM imaging difficult. The GIS is used to coat the sample surface with a protective layer of organometallic platinum of around 1.5-2µm for the milling process. This protective layer is vital to reduce the charging of the sample during milling and imaging, gives extra support to the final lamella, and protects the sample during milling. In contrast to the very heterogenic composition of a cell, the platinum layer offers a very uniform and dense layer of material, which avoids curtaining effects that arise from differences in the material that lead to different milling rates (Wagner et al., 2020). It also aids in the prevention of unwanted ion beam erosion of the sample (Hayles et al., 2007).
The cellular samples for cryo-FIB milling can be either grown directly on the grids or deposited just before plunge-freezing. After the GIS platinum coating, the regions of interest (ROIs) are selected based on SEM imaging or CLEM, and the sample is brought to the coincidence point of both SEM and FIB for the milling process. Typically, these ROIs should be located within a ~600 nm radius of the center of the grid to allow optimal access for the FIB milling and subsequent TEM imaging (Wagner et al., 2020).
Next, the milling angle has to be chosen; for this, the position of the SEM and FIB columns relative to each other and the sample must be considered. The default sample pre-tilt is 45°, while the tilt-angle between FIB and SEM is 52°. This results in a -7° angle of the FIB beam relative to the sample in the default position and would mean that the FIB can only reach the backside of the sample rather than the position of interest. Thus, the sample tilt has to be lowered to ideally 15-20°, which results in a milling angle of 8-13°. This milling angle is the pre-tilt the generated lamella will have in subsequent SEM and TEM imaging (see Figure 9). Hence, it is vital to keep the milling angle as low as possible as it has to be accounted for in cryo-ET in subsequent steps and lower pre-tilts are easier to compensate for to achieve a usable ~120° tilt scheme still. However, if the stage is tilted too low, the FIB would hit the rim of the AutoGrid™ rather than the sample or could be distorted by proximity to it. It is, therefore, vital to choose the milling angle with care (Wagner et al., 2020).

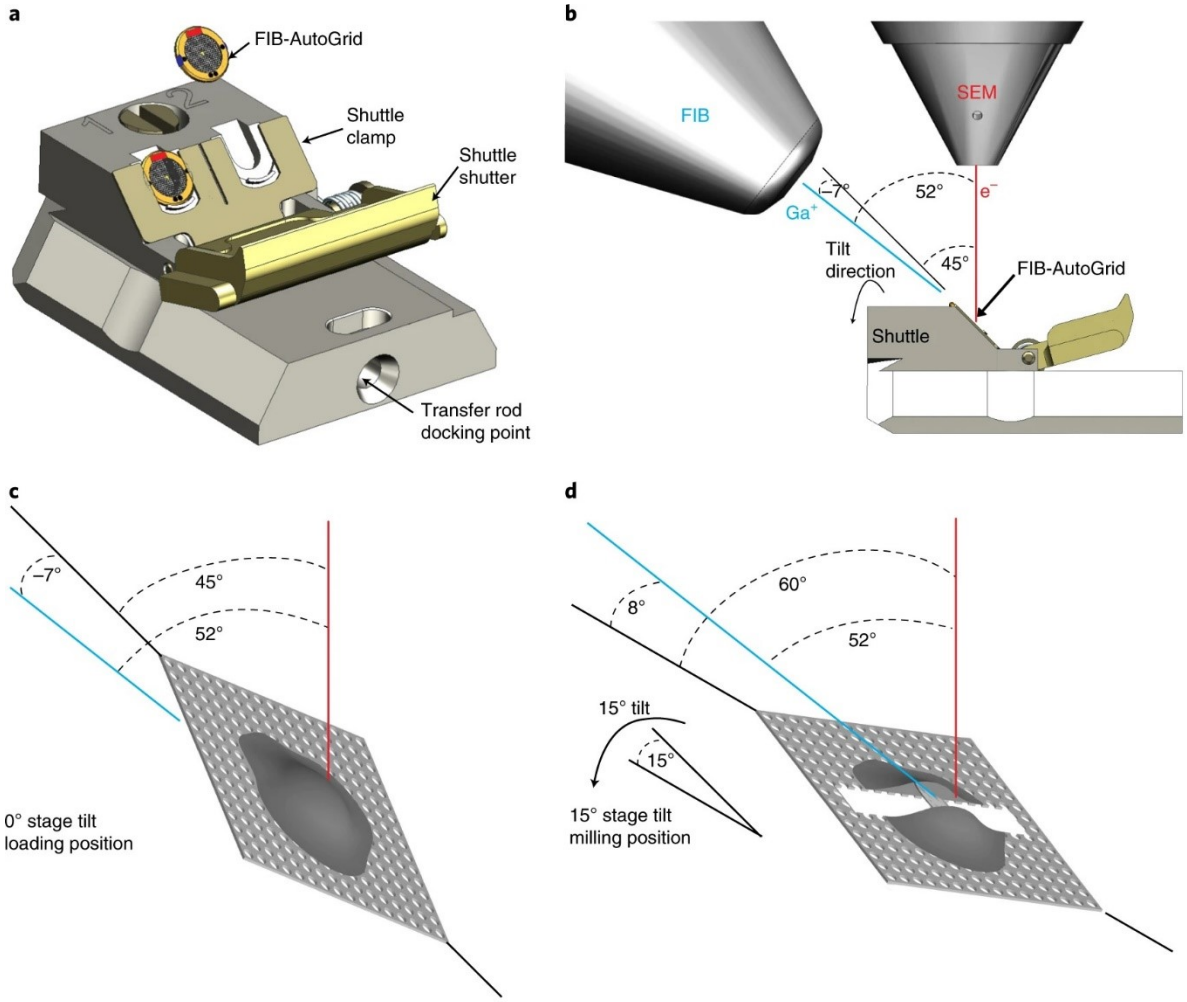

Figure 9: An overview of the milling geometry of a dual-beam FIBSEM.
As an example portrayed with the TFS Aquilos set-up. a) FIB-AutoGrids™ can be placed into a dedicated shuttle and locked in place with the Shuttle clamp. A Shuttle shutter protects the samples during transfer in and out of the FIBSEM with a transfer rod. b) The SEM and FIB columns are placed at 52° from each other. The sample has a pre-tilt of 45° in regard to the SEM beam and -7° to the FIB. c and d) A schematic drawing of a specimen at 0° stage tilt and 15° stage tilt show the relative tilt of the sample to the FIB (blue) and electron beam (red). A 0° stage tilt results in a -7° tilt to the FIB, rendering milling impossible. A 15° stage tilt leads to an 8° milling angle. This figure was obtained from (Wagner et al., 2020) with permission from Springer Nature.

Once the right milling angle is chosen, the ROI is milled down in several steps into an electron-transparent slice thinner than 300nm. The initial milling steps can be done with higher milling currents (i.e., ≤1nA). The closer the FIB comes to the desired lamella thickness, the lower the milling current used. One distinguishes between rough milling and fine milling, where the fine milling takes place below 1µm of lamella thickness and uses only low milling currents (i.e., ≤50pA). Wolff et al. showed that using micro-expansion joints in the form of narrow, long trenches on each side of the lamella could significantly increase the success rate of cryo-FIB milling by keeping the lamella from bending and breaking (Wolff et al., 2019). An alternative stress-relief system has recently been introduced by milling a notch into one side of the lamella, seemingly performing equally well (Kelley et al., 2022).
The preparation of thin cryo-lamellae is only possible because the FIB can be directed with high precision through the placement of so-called milling patterns. The beam will only be active in these exact patterns. Typically they are rectangular, but specific

patterns can also be defined. An example of a milling protocol will be given in section 3.3.2.
Several lamellae can be created on each grid by employing a multi-step milling scheme to multiple ROIs. The overall number is only limited by the time the microscope can stay at cryo-temperatures and the contamination rate of the microscope (explained in more detail below). The larger in x and y the lamella is, the longer the single milling steps will take. After the final milling step of one lamella, one moves on to the next ROI – in the time it takes to finish this lamella, the first will contaminate at a specific rate. Even though FIBSEM instruments are operated under a vacuum, their chambers are typically larger than those of cryo-TEMs, and the vacuum that can be reached is poorer. The residual moisture can deposit on the lamella in the form of amorphous ice.
The Aquilos I instrument, for instance, has a maximum contamination rate of 50 nm per hour, according to the manufacturer's specifications. However, it is typically at around 15 nm per hour after an upgrade to the Aquilos II, per manufacturer specification. In order to keep the contamination of each lamella to a minimum, it is common practice to first do the rough milling steps for each selected target and then finish the fine milling for all of them in the shortest time possible (Tacke et al., 2021).
Several new developments now help to increase the number of lamellae that can be produced and decrease the contamination rate. Only recently, the so-called CERES Ice Shield was developed by Delmic and collaborators at the Max Planck Institute for Molecular Physiology in Dortmund (Tacke et al., 2021), where a cryo-shutter is positioned between the SEM column and the sample during milling. It not only further locally improves the vacuum close to the sample but also acts as a cold finger to trap contamination from the comparatively warmer SEM column. Overall, this would reduce the potential accumulation of amorphous water enough to produce a much higher number of lamellae without drawbacks. A glove box and a high vacuum transfer system can be additionally employed as an additional measure against contamination during the transfer of the sample into and out of the microscope (Tacke et al., 2021). These implementations have been suggested to help reduce contamination outside the FIBSEM.
The process of sample thinning by FIB milling is highly manual and time-intensive. A milling session requires constant attention as the milling must be monitored every few minutes, especially during exemplary milling steps. To counteract this disadvantage, several methods for automating this milling process were developed over the last few years for Thermo Fisher Scientific and ZEISS systems, called AutoTEM (Kuba et al., 2021) and SmartFIB (Zachs et al., 2020), respectively. They follow the same basic principle: The overview SEM image is used to identify ROIs and track the lamella position, and the single milling steps with their milling and imaging currents are defined. In this way, multiple lamellae can be prepared without constant supervision once the optimal parameters have been scouted. This can significantly increase the throughput of lamella preparation, especially when the contamination rate is neglectable.
Thermo Fisher Scientific offers an additional alternative with API ThermoFisher Autoscript. In contrast to AutoTEM, it does not have a user interface but can be used by employing Python scripts and is thus very versatile and adaptable (Buckley et al., 2020).
Klumpe et al. recently published an open-source package called SerialFIB for automated milling through an interface or scripting. Milling protocols for a range of

cellular sample types are additionally provided for the community (Klumpe et al., 2021).
Recent publications additionally suggest that a thin 5-10 nm layer of sputter-coated platinum on the final lamella could counteract charging, which often has problematic effects on the stability of the lamella during subsequent cryo-TEM (Khavnekar et al., 2022). While this can reduce contrast and image quality to some degree, it might be an acceptable trade-off in some cases.
One limitation of cryo-FIB milling is the increasing milling time with increasing sample bulk size. This method is of immense usefulness in studying samples thinner than 10 µm that can be plunge-frozen, such as single mammalian cells or cell clusters of bacteria or other microorganisms, where multiple lamellas can be prepared within a single day. Once samples exceed this thickness, HPF has to be employed to achieve proper vitrification. An HPF specimen brings several challenges: typically, these samples are 50 µm or higher, and standard milling workflows face physical constraints and require a significantly higher time investment. Furthermore, identifying ROIs requires cryo-CLEM unless one can be sure that the sample is uniformly distributed over the whole area. Lastly, HPF samples commonly remain in their carriers which are too thick to cut by cryo-FIB milling and prevent the use of transmitted light imaging for CLEM. Before the introduction of cryo-FIB milling, such samples were processed with CEMOVIS, which has been discussed above.
With the advent of cryo-FIBSEM for biological samples, one workaround is using the cryo-slice-and-view (cryo-ASV) method. For this method, an ROI in a bulk specimen is located and thinned down until a site of interest is identified via SEM imaging. Subsequently, thin slices of several tens of nanometers are milled away, and the surface is sequentially imaged at high resolution by SEM. Depending on the size of the chosen location and the section thickness, several µm of the sample can be imaged in an automated fashion. While this provides insight over a larger sample volume, the overall resolution is in the tens of nanometers in (x,y,z) and far below the resolution achievable by TEM (Kuba et al., 2021).
The first attempt at mitigating the problem of bulk samples and the drastic increase in milling time was published by Harapin et al. in 2015. In their study, they vitrified *C. elegans* embryos and worms by HPF directly on grids using 2-methylpentane as a cryo-protectant and filler for the carriers. 2-methylpentane is liquid at -150°C and solid at -190°C. The *C. elegans* specimen were frozen directly on grids sandwiched by carriers, and the grids with the specimen on them could easily be recovered by warming them to -150°C. Moreover, after just a few minutes at -150°C at a high vacuum, the remaining 2-methylpentane can be sublimated, and only the specimens themselves are left behind on the grid. This is a vast advantage over using other cryoprotectants or fillers, which will remain as a frozen bulk surrounding the sample.
The disassembly of the carriers with other materials at LN_2 temperatures can lead to the fracturing of the specimens or their dislodging from the EM grids. This protocol made it easy to find ROIs and significantly reduced the bulk milling time. It still took three hours per embryo and 30 hours per adult worm to create a single lamella, and as such, the time requirement is still immense for bigger bulk samples (Harapin et al., 2015). It also must be noted that both C. elegans eggs and worms have a protective chitin layer that might prevent potential damage from interaction with 2-methylpentane. There is no conclusive evidence yet on how vertebrate tissue samples might be affected by direct contact with 2-methylpentane.
Hsieh et al. published another option for thinning bulk material for cryo-TEM. After HPF, they trim the sample with a cryo-ultramicrotome and only then employ cryo-FIB

milling to generate thin lamellae for cryo-TEM (Hsieh et al., 2014). While this method works well for homogenous samples that do not require targeting, specific structures cannot be targeted in this way. Another concern is the requirement for additional instruments and transfer steps, significantly increasing the risk of sample damage and contamination.

The introduction of the cryo-lift-out method in 2015 opened up new possibilities for the preparation of biological bulk samples for cryo-TEM. Once again, this technique has long since been employed in material science and transferred to biological science. A micro-manipulator in the form of a thin, cooled needle is added to the FIBSEM instrument and can be freely moved in (x,y,z) directions. The lift-out process works in two distinct steps: In the first step, an ROI is isolated from the specimen by high current milling until a thick slice of the sample of around 20x20x8µm is attached to the bulk sample only by a small hinge. In a subsequent step, the micromanipulator is attached to the isolated slice via platinum deposition, and the slice is then cut free of the bulk sample and lifted out. The slice is then transferred to a second grid with pre-prepared slots into which the lift-out can be placed and fixed with another round of platinum coating. The needle can then be cut via FIB milling and retracted, and the slice can be milled into a thin lamella as is in the standard procedure. This lift-out technique drastically reduces the time needed to produce lamellae from thick tissue samples and can be targeted with CLEM to specific ROIs (Mahamid et al., 2015).
The lift-out technique has opened up new possibilities for high-resolution imaging of near-native biological samples. It can be used with any vitrified bulk sample, tissue, organism, or cell suspension. The time requirement is higher than for single-cell samples, but the method is compatible with samples of even 100-200 µm thickness (Klumpe et al., 2021).
Since its first introduction in 2015 by Mahamid et al. in cooperation with Thermo Fisher Scientific, several other research groups have published adaptations and improvements of the cryo-lift-out technique by employing different micro-manipulators, such as a gripper instead of a needle or different grids for lift-out attachments (Wagner et al., 2017).
Mahamid et al. showed a lift-out lamella from a *C. elegans* worm containing mitochondria, lipid granules, and a nucleus as a proof-of-principle for the feasibility of the lift-out workflow. However, the lamella depicted is affected by strong curtaining effects, and no high-resolution data could be collected (Mahamid et al., 2015). In 2019, a follow-up paper with the same type of sample and an improved lift-out workflow was published. In this publication, high-resolution tomograms of cellular structures, such as the endoplasmic reticulum (ER), mitochondria, ribosomes, and even microtubules, are shown. Importantly, this marks the first time that a glimpse into a multicellular organism under native, hydrated conditions could be obtained at such high resolution (Schaffer et al., 2019). Only recently, a lift-out lamella from HPF *D. melanogaster* egg chambers was depicted in the publication of Klumpe et al. with a closer look at ribosomes and a Golgi apparatus (Tacke et al., 2021).
The first cryo-lift-out lamella from a bulk tissue sample of a vertebrate was published in 2021, where a lamella was obtained from HPF mouse brain. At this point, however, only SEM and no TEM images were obtained, making it difficult to judge the quality of the lamella for high-resolution imaging (Kuba et al., 2021).
The first commercially available cryo-FIBSEM capable of performing lift-outs is the Aquilos II from Thermo Fisher Scientific, employing a micromanipulator in the form of a needle. For this thesis, I started working on vitrified bulk samples with the Aquilos in

2019. In late 2020, it was upgraded to the Aquilos II, allowing me to use this cutting-edge technology to optimize the workflow I describe in this thesis. Detailed descriptions of bulk milling by standard milling as well as by lift-out will be described and discussed in detail in section 3.3.2.
Cryo-FIB milling, especially the cryo-lift-out technique, is still a very young method with a steep learning curve and requires considerable user expertise and experience. This makes it an immensely powerful but also challenging method that is still in a phase of rapid development. It is vital, that robust and versatile workflows are established for the community, allowing us to study complex tissue samples in a nearly artifact-free way. Moreover, established workflows will also lay the groundwork for the automation of even cryo-lift-out procedures and high-throughput lift-out lamella generation in the near future.

2. AIMS AND OBJECTIVES

The ECM has been initially considered a mostly passive mechanical support in the past. It has long since become clear that it dynamically regulates many critical cellular processes in health and disease. Furthering our understanding of the ECM and its components will enable us to understand these processes better.
A wide array of methods has been employed in the study of ECMs, ranging from different model systems to different experimental techniques. Especially the last couple of decades, with their fast technological advancement, have led to many vital discoveries that aided our understanding of the ultrastructure of ECM. Still, current EM methods used to investigate the ECM and its components have significant disadvantages: Conventional TEM approaches rely either on the isolation of single ECM components and/or include sample preparation steps that involve dehydration, drying, sectioning, and contrasting. These processes can introduce artifacts and distortions and might destroy delicate structural features. Currently, no straightforward approach is available to visualize ultrastructural features of 3D ECM at the near-native condition at high resolution *in situ*.

The main aim of this thesis is the design of a novel workflow of specimen preparation and imaging protocols for cryo-ET to study the ultrastructure of the ECM and the structure of its components under native conditions.

Specifically, I intend to develop an experimental set-up that allows the generation of cell-derived matrices directly on EM specimen carriers compatible with cryo-FIBSEM and cryo-ET to visualize the ECM in its native state at unprecedented detail.

In order to achieve the above-described aim, I will have to address the following objectives and their respective tasks:

Objective 1: CDM specimen generation compatible with cryo-FIBSEM and cryo-ET
CDMs offer unique possibilities for investigating the ECM ultrastructure and its underlying processes. They are already widely used in the investigation of cell migration and cell adhesion, but also in cancer research and medical research for regenerative medicine. Several cell lines have already been established for the generation of CDMs, and there are existing protocols that I plan to adapt to growth on EM substrates. Moreover, this system is highly versatile and adaptable through genetic modification of the producing cells or alteration of the culturing conditions.
I aim to establish an optimized protocol that allows the reproducible production of 3D CDMs by different cell lines on EM substrates compatible with the subsequent steps in the workflow.

In order to overcome the limitations of traditional EM sample preparation methods, I plan to employ cryo-fixation to retain the hydrated and native state of the extracellular proteins of the CDM. To this end, different vitrification methods will be tested and optimized. Ideally, the samples will be vitrified without prior chemical fixation and treatments.
Objective 1 will be addressed in sections 3.1.2. and 3.2.

Objective 2: Cryo-FIBSEM and Cryo-ET of CDMs
One of the main limitations of TEM, and specifically ET, is sample thickness. In order to thin the vitrified CDM samples down sufficiently for cryo-ET, I will employ cryo-FIBSEM. The current state-of-the-art technique of cryo-lift-out will be established and optimized for this sample preparation workflow.
Data acquisition via cryo-ET will then be optimized on the created cryo-lamellae to obtain high-resolution information on CDMs and the cells embedded within them.
Objective 2 will be addressed in sections 3.3. and 3.4.

Objective 3: Ultrastructural characterization of natively preserved CDMs
The generated data will be used to investigate the relationship between different ECM molecules and between ECM molecules and cellular structures in a fully hydrated state. The sample preparation workflow guarantees the best possible preservation of native, unaltered ECM ultrastructure at an unprecedented resolution. Cryo-ET allows for reconstructions at a low-nanometer resolution over a volume of 250-300nm and provides us with 3D information of the reciprocal interactions between cells and ECM. This information lays the basis for the study of still poorly understood processes in ECM initiation and maintenance, such as the secretion of ECM components (i.e., collagen), remodeling processes, or the impact of changes in the matrisome composition on ECM ultrastructure.
Objective 3 will be addressed in sections 3.5. and 3.6.

Establishing such a workflow will lay the groundwork for further structural studies of the ECM *in situ,* and the versatility and adaptability of the system will allow the community to address a wide array of biological questions.

Below, an overview of the workflow I plan to design and optimize is given.
CDM specimens will be generated and vitrified. Targeted cryo-FIB milling will allow for data acquisition by cryo-ET on cryo-lamellae and subsequent characterization of the CDM ultrastructure.

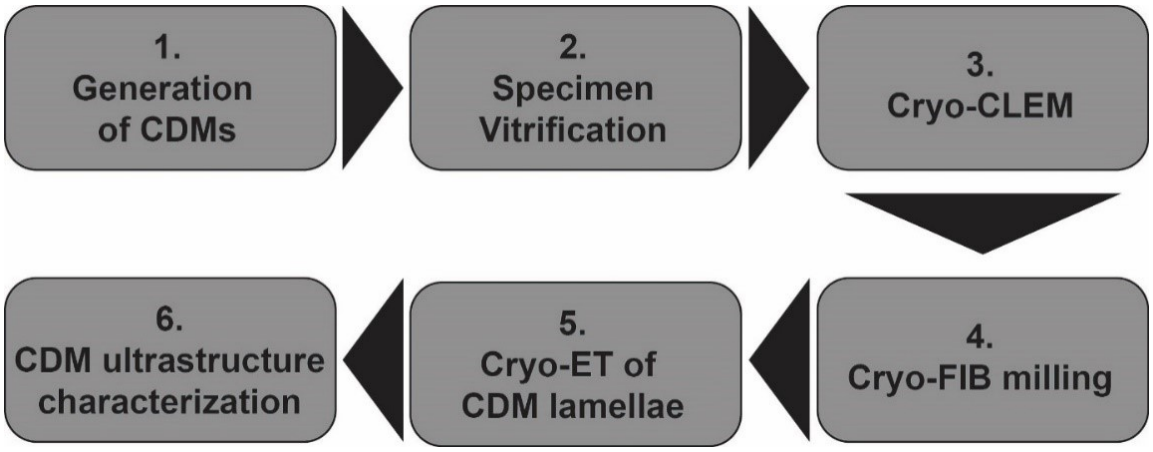

3. RESULTS AND DISCUSSION

3.1. The preparation and initial characterization of CDM specimens

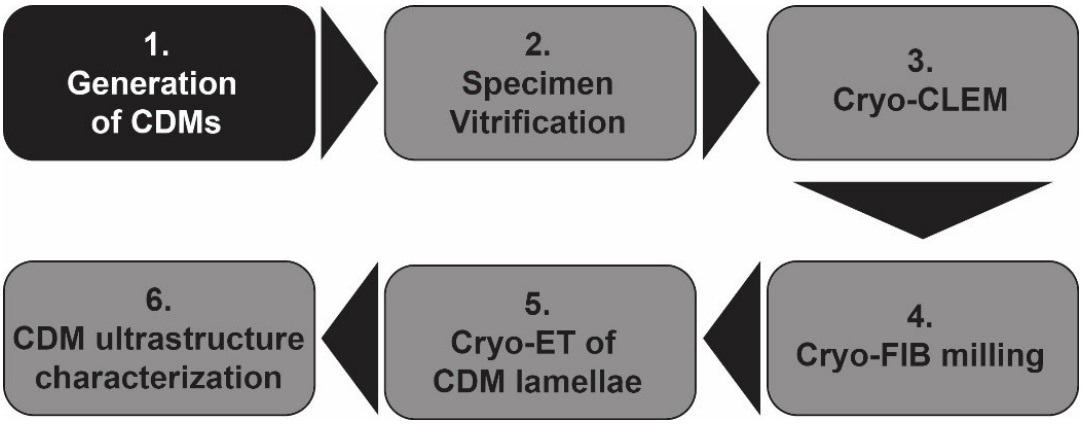

CDMs are a versatile and highly adaptable tool in the study of the ECM and its components and are widely used in the investigation of cell migration and cell adhesion. The reproducible generation of a CDM specimen compatible with cryo-FIBSEM and cryo-ET is the foundation for the design of this novel workflow.
Existing protocols, such as the one from (Kaukonen et al., 2017), typically employ glass cover slips for the generation of CDMs. I used this protocol as a basis and adapted it for EM substrates. Three different wildtype fibroblast cell lines were initially tested for this process:

- Telomerase Immortalized Foreskin Fibroblasts (TIFF), *Homo sapiens*
- NIH 3T3 mouse embryo fibroblasts (NIH 3T3, RRID: CVCL_059), *Mus musculus*
- Rat embryo fibroblasts (REF, RRID: CVCL_051), *Rattus norvegicus*

CDM generation of these cell lines on different EM substrates was optimized, and the CDMs were then characterized as outlined below in section 3.1.2.

During the optimization process for CDM generation on EM substrates, 3D printed grid holders were developed together with Florian Fäßler to facilitate specimen preparation. This work was published in 2020 in the Journal of Structural Biology and is described in more detail below, in section 3.1.1.

3.1.1. 3D printed grid holders for improved specimen preparation

The work described in this section has been published in
"*Fäßler, F.*; **Zens, B.***, Hauschild, R., Schur, FKM. (2020). 3D printed cell culture grid holders for improved cellular specimen preparation in cryo-electron microscopy. Journal of Structural Biology. 212(3). doi:10.1016/J.JSB.2020.107633*"
**Equal contribution*
For more information, see the "Publications and Permissions" section.

Efficient and reproducible specimen preparation is fundamental in the design of any experimental workflow and becomes more challenging with each step involved. It was

of particular importance to me to optimize the process of CDM production in cell culture. I wanted a reproducible, high-throughput specimen preparation protocol with minimal sample loss as a basis for the whole workflow I aimed to create.
Among the forefront of challenges in the preparation of cellular specimens for cryo-EM in cell culture are the sensitivity of many cellular specimens to culturing conditions and the fragility of EM-grids and their coating.
EM grids are notoriously sensitive to mechanical manipulation, and repeated handling of cell culture dishes or relocation of grids may result in bending and distortion of the grid or its substrate and even the potential loss of the specimen. Typically, single EM grids are placed in sufficiently large cell culture dishes, such as 6-well or 12-well plates, to enable proper accessibility for sample handling. If 6-well plates are used, this means that a 7.3 mm^2 EM grid sits in a 9.6 cm^2 well and requires excessive amounts of resources, such as media, reagents, and cells. Sample retrieval remains difficult even in large well plates, especially for untrained users, and often results in mechanical damage to grids. Moreover, during long-term cell culture over several weeks, the necessary medium changes can lead to repeated translocation of the grid. This may disrupt sensitive samples such as growing CDMs.
An additional layer of Parafilm® may be used at the bottom of the wells to reduce movement of the grids during well-plate handling and to facilitate the retrieval. However, this impedes observation of cells by light microscopy throughout culturing.
To address these challenges, Florian Fäßler, a postdoc in the Schur lab, and I developed reusable 3D printed grid holders compatible with cell culture specimen preparation. These holders can be freely adapted to the workflow requirements and the EM substrates used, whether they are standard EM grids, sapphire discs, or other EM substrates.
Grid holders are compatible with most experimental steps required for the preparation of adherent cells for EM, such as glow discharging, coating the grid surface, cell seeding, light microscopy, and even micropatterning (Toro-Nahuelpan et al., 2020). Once the grid is placed in the holder, it does not have to be directly manipulated again until retrieval for subsequent applications, drastically reducing the risk of mechanical damage to the grid and sample loss. As accessibility for retrieval is no longer a concern, smaller well plates, such as 24-well or even 96-well plates, can be chosen, reducing the amount of resources required (see Figure 10).

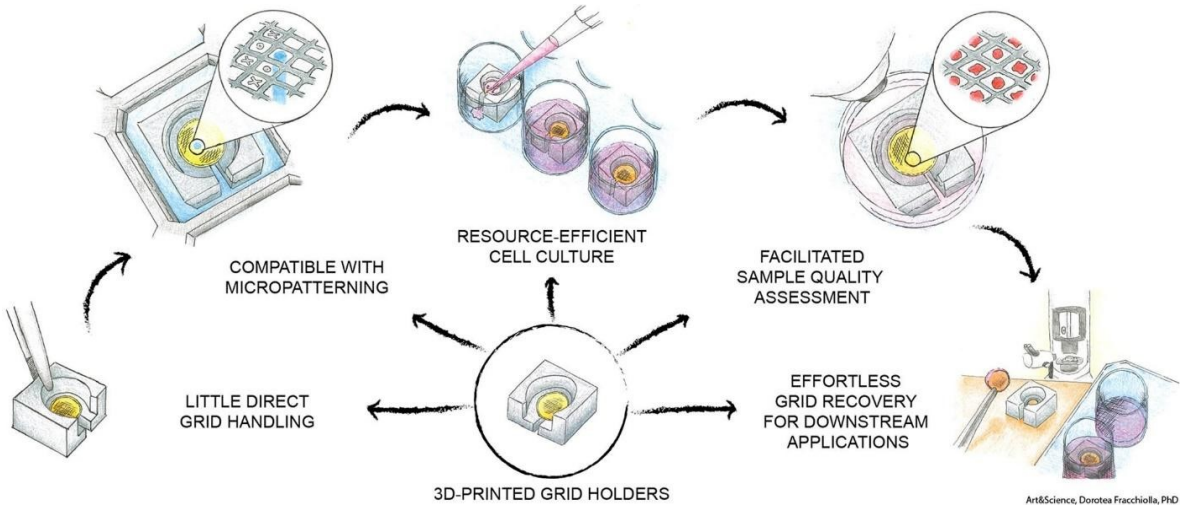

Figure 10: A schematic overview of the advantages of 3D printed grid holders.
3D printed grid holders improve the efficiency and reproducibility of cell culture specimen preparation. They reduce direct grid handling, enable resource-efficient cell culture, allow for quality assessment during culturing and allow for an effortless grid recovery for downstream applications. This figure was obtained from (Fäßler, F.*, Zens, B.*, et al., 2020) under the Creative Commons CC-BY license. It was created by Dorotea Fracciolla (Art&Science).

We developed several shapes and sizes for grid holders to adapt them for their specific cellular samples and EM substrates used. The design for grid holders optimized for CDM growth has a square base that fits into a 24-well plate. The grid is sitting in a recess in its center, and the relatively high walls on three sides of the grid holder protect the growing CDM from disruption during medium exchange (see Figure 11). This design has been used for this thesis, and the use of grid holders has significantly increased the efficiency of CDM sample preparation in cell culture.

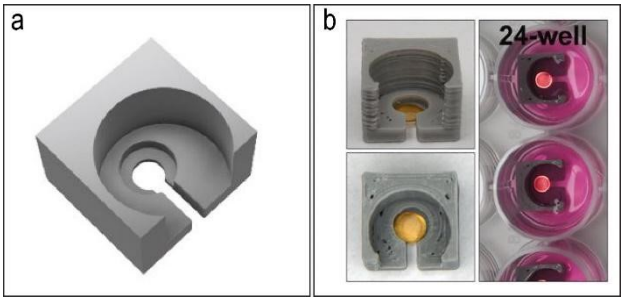

Figure 11: Design of 3D printed grid holders for CDM growth.
a) Schematic representation of the grid holder design, showing the recess in which the grid is placed and the opening for visualization by light microscopy. b) Photographs of square-base grid holders with loaded grids in a standard 24-well cell culture plate. The figure was adapted from (Fäßler et al., 2020) under the terms of the Creative Commons CC-BY license.

While grid holders were intended primarily for use with EM grids, I have also used this design for sapphire discs and ACLAR® discs and employed them during CDM generation on these EM substrates. As all the substrates I used have nearly the same dimensions, no adaptations were necessary.
For detailed information on grid holder design, compatibility with standard techniques for cryo-ET samples preparation, and viability tests for different materials used for grid holder production, see our main publication describing their development and characterization (Fäßler et al., 2020). The grid holder designs introduced in this

3.1.2. CDM generation on EM substrates

3.1.2.1. Optimization of CDM generation

The standard protocols for CDM generation are tailored to larger glass or plastic surfaces, such as glass coverslips (≥1 cm diameter) or cell culture dishes (≥3 cm diameter). In contrast, standard EM substrates are much smaller (≤3.05 mm diameter) and made from different materials with various coating options.
Initially, different EM substrates were tested for their compatibility with CDM growth and downstream cryo-EM sample preparation: EM grids, sapphire discs, and ACLAR™ discs. To adapt and optimize a protocol for CDM generation on these substrates, different materials, coating options, seeding densities, and growth conditions were tested.
EM grids are a standard substrate for downstream sample preparation steps such as plunge-freezing and cryo-FIBSEM milling and are available from different materials (as mentioned in section 1.2) and with different coatings. To test their compatibility with long-term cell-culture needed for CDM growth Gold (Au) and Titanium (Ti) had to be chosen. Grids were chosen with 150 and 200 mesh to avoid having too many grid bars that could potentially obstruct downstream sample preparation steps such as cryo-FIB milling. Different standard coatings were tested with these grids: Holey Carbon (HC), holey SiO_2, and a thermoplastic resin called formvar, either as the sole substrate or with added continuous carbon coating.
In addition, sapphire discs (3 mm diameter, 50 µm thickness) and ACLAR® discs punched from ACLAR® film (3 mm diameter, 51 µm thickness) were tested as they more closely resemble the standard materials used for CDM growth.
Acid-washed glass coverslips were used to test the reproducibility of the protocol as a standard for CDM growth for comparison to the tested EM substrates.
An overview of all tested EM substrates is given in Table 2.

Table 2: A summary of the different EM substrates tested for CDM growth.
EM grids coated with HC 2-2 and SiO_2 2-2 were procured from Quantifoil Micro Tools. All other EM substrates were procured from the manufacturers stated above and coated in-house, as detailed in section 4. Materials and Methods. Sapphire discs were standard 3 mm diameter discs. ACLAR® discs had 3 mm diameter. Glass coverslips were 1 cm diameter.

EM substrate	Material	Coating	Manufacturer
EM grid	Au, 200 mesh	HC, R2-2	Quantifoil Micro Tools
	Au, 150 mesh	HC, R2-2	Quantifoil Micro Tools
	Ti, 200 mesh	SiO_2, R2-2	Quantifoil Micro Tools
	Au, 200 mesh	Continuous formvar (0.75%)	Gilder
	Ti, 150 mesh	Continuous formvar (0.75%)	Graticules Optics
	Au, 200 mesh	Continuous formvar (0.75%) + Continuous carbon (10 nm)	Gilder
	Ti, 150 mesh	Continuous formvar (0.75%) + Continuous carbon (10 nm)	Graticules Optics
Sapphire disc	Sapphire	Continuous carbon (10 nm)	Engineering Office M. Wohlwend GmbH
ACLAR® disc	ACLAR® film	Continuous carbon (10 nm)	Science Services
Glass coverslip	Glass	Continuous carbon (10 nm)	BARTELT GmbH

The preparation of all substrates uses the same protocol, adapted from (Kaukonen et al., 2017) as foundation. Briefly, in this publication, sterile glass coverslips were coated with 0.2% (w/v) gelatin for 1 h and washed with PBS. The gelatin was then cross-linked with glutaraldehyde for 30 min, washed with PBS, and any remaining glutaraldehyde was then quenched with 1 M glycine for 20 min. After another wash with PBS, the coverslips were incubated for 1 h with cell culture medium prior to fibroblast seeding. Once the cells had grown confluent, they were treated with ascorbic acid-supplemented cell culture medium every or every second day for 7-21 days.
This protocol was optimized over several rounds, and the cells and developing CDMs were assessed for their density and morphology during cell culturing and CDM growth using a standard phase-contrast cell culture microscope. The result of these optimizations is the cell seeding protocol outlined below.
All stated volumes and cell numbers are calculated for EM grids, sapphire discs, and ACLAR® discs. Acid-washed glass coverslips were placed directly in 24-well plates without glow discharging and volumes and cell numbers were adjusted according to the difference in the volume needed (20 µl for standard EM substrates, ≥250 µl for glass coverslips). The final protocol is given below. Additional information on the optimization process of the single protocol steps is given where relevant and marked in *italics*.

Optimization of cell seeding

1. EM substrates are glow discharged to change the surface charge of the substrate and allow for even spreading of liquids and cells added in subsequent steps.
   Sapphire discs, ACLAR® discs, and EM grids with HC or SiO_2 coating are glow discharged for 2 min. All EM grids with formvar coating are glow discharged for 30 s to avoid damage to the coating.

   Different times for glow discharging were tested to ensure that enough surface charge was imparted for sufficient hydrophilicity while the EM substrate was not damaged. Higher times than stated here did not have an additional beneficial effect and led to damage to the coating in some cases.

2. EM substrates are transferred with forceps to a sterile dish with Parafilm®. Sterile, acid-washed glass coverslips are placed directly into single wells in 24-well plates without any Parafilm®. All work is performed under sterile conditions from here on out.

   Parafilm® is cut to size for the lid of a 10 cm diameter cell culture dish. It is attached to the inside of the lid by using the back of a forceps and gently stretching the Parafilm® while applying pressure. This fixes the Parafilm® in place and enables easier recovery of EM substrates than from smooth cell culture plastic or glass. Additionally, using the lid of a cell culture dish and not the bottom allows for a flatter access angle, further facilitating substrate recovery without damaging it.
   Dishes with Parafilm® in them are sterilized by exposure to UV light in a laminar flow for 20 min prior to use.

3. EM substrates are washed 1x with PBS and then coated with 20 µL of 50 µg/ml fibronectin in PBS and incubated for 1 h at RT.

   (Kaukonen et al., 2017) used gelatin in their CDM growth protocol instead of fibronectin. However, I decided that a more clearly defined base layer was advantageous for the subsequent characterization and analysis of CDMs. Hence, I chose fibronectin as a base layer, as it is a standard ECM protein that should be present in all CDMs. Different concentrations were tested (25 µg/ml, 50 µg/ml, 100 µg/ml), and the lowest concentration that led to quick cell attachment on all EM substrates was chosen.

4. EM substrates are washed with 2x with PBS, and the fibronectin is cross-linked with 20 µl of 1% (vol/vol) glutaraldehyde for 30 min at RT.

5. After 3x washes with PBS, any remaining glutaraldehyde is quenched with 20 µl of 1 M glycine in PBS for 20 min at RT.

6. After 1x wash with PBS and 2x washes with cell culture medium, EM substrates are incubated with cell culture medium for at least 15 min prior to cell seeding.

7. The fibroblasts of choice are seeded onto the substrates by adding 20 µl of cell suspension with a defined concentration. The difference in concentration for the different cell lines accounts for their growth rate.
   NIH 3T3: $2.5*10^5$ cells/mL (20 µL results in ~5000 cells)
   REF: $1.75*10^5$ cells/mL (20 µL results in ~3500 cells)
   TIFF: $3.5*10^5$ cells/mL (20 µL results in ~7000 cells)

   A range of seeding densities was tested for all three different cell lines, and the one that resulted in a confluent monolayer after 2-3 days was chosen for the protocol. Higher or lower seeding densities can be chosen to speed up this process or slow it down if required for the experimental timing. To define optimal seeding densities for each cell line that would result in a confluent monolayer within 2-3 days of seeding, a range of seeding densities was tested for each to account for their difference in proliferation rate. Based on my observations, REF have a significantly lower doubling time than TIFF, ~24 h compared to ~48 h respectively, and NIH 3T3 cells are in between these two.

8. The EM substrates with the seeded cells are incubated for 1-2 h in the cell culture incubator.

   Fibroblasts attach quickly to fibronectin-coated surfaces and the substrates can be transferred to grid holders already 1 h after seeding without disrupting the cells. Incubation times longer than 2 h could result in too much evaporation of the 20 µL droplet and potentially cause stress to the cells and should therefore be avoided.

9. During this incubation time, 3D printed grid holders are prepared for the subsequent steps by washing them 1x with PBS and 2x with cell culture medium. The 3D printed grid holders are explained in more detail in **3.1.1.1.**

   It is advantageous to prepare the grid holders ahead of time to avoid a temperature difference for the cells when the EM substrates are placed into the holders. Moreover, the transfer of EM grids to grid holders works significantly better when the grid holders are pre-wetted as it avoids bending of EM grids during placement in the grid holder, as well as their floating up.

10. Each grid holder is placed into a well in a 24-well plate and incubated in the cell culture incubator for at least 30 minutes before the next step.

11. Transfer the EM substrates to the prepared 3D printed grid holders. The glass coverslips remain in their 24-well plate and do not require a transfer. The EM substrates remain in the grid holders throughout the CDM growth.

The use of fibroblasts with low passage number is recommended to ensure the production of a reproducible and strong CDM (Kaukonen et al., 2017). Cells were passaged at least two times after thawing before they were used for CDM growth.
EM substrates may be placed into the grid holders already before the glow discharging process in order to reduce the amount of direct sample handling steps. However, it has to be taken into account that this significantly increases the volume of reagents required for this step.
Similarly, EM substrates may already be placed into the grid holders after the surface coating but before the cell seeding. This requires some expertise in cell seeding, and the technique described in the protocol above typically results in a more even spread of the cells over the EM substrate, as well as higher reproducibility.

Optimization of CDM growth

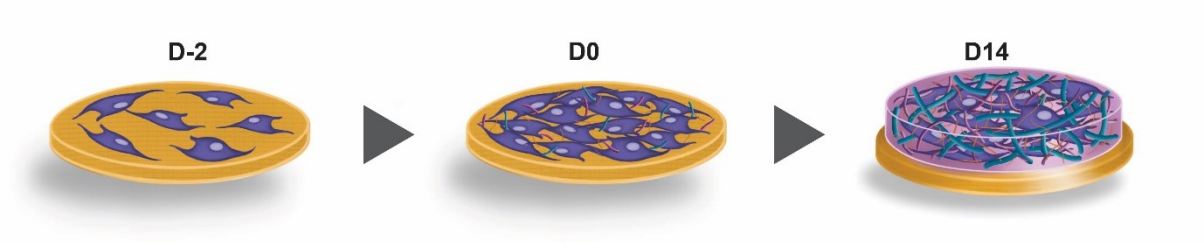

Figure 12: A schematic representation of CDM growth over time.
Fibroblasts are seeded onto EM substrates (represented by a golden disc; D-2) and then allowed to grow confluent. Once confluency is reached (D0), the ascorbic acid treatment is started to facilitate collagen crosslinking and, thereby, the generation of a resilient CDM. Already at D0, ECM proteins are synthesized and secreted but do not yet form a matrix. Within 14 days (D14), the fibroblasts produce a 3D CDM in which they become embedded. This CDM contains fibronectin, collagen, and other ECM proteins. This image is courtesy of Verena Baumann, Ph.D., who created it specifically for this thesis.

Fibroblasts synthesize and secrete ECM components already within a few hours of their seeding (see Figure 13 and Figure 14, timeline staining). The cell confluence and state should be assessed by phase-contrast microscopy after seeding and throughout CDM generation. Once a confluent cell monolayer is formed, ascorbic acid can be added during CDM growth. Ascorbic acid treatment is essential for the hydroxylation

of proline and lysine residues within the collagen and is thus required for the cross-linking of collagen (Grinnell et al., 1989). According to (Kaukonen et al., 2017), ascorbic acid treatment must only be started after confluency has been reached, or the CDM may form improperly.

Optimization of ascorbic acid treatment

1. The ascorbic acid treatment is started once a confluent cell monolayer is formed.

2. Cell culture medium is supplemented with 50 µg/mL ascorbic acid and 10 mM HEPES (final concentration) for ascorbic acid treatment.

3. The medium in each well is carefully aspirated to not disturb or move the EM substrate through direct contact. As the substrate is sitting in a grid holder, it is protected from mechanical stress during this process.
   For glass coverslips, this process has to be done very carefully and slowly by pipetting along the rim of the well. This step is critical as the forming CDM can easily be disrupted and damaged during this process.

   The grid holders used for EM substrates throughout the growth time were adjusted to have high walls to protect the specimens during this medium exchange. Initially, the grid holder used had lower walls and EM grids sometimes floated to the surface of the medium during this process. Higher walls protected EM grids from this effect. Additionally, they reduced the chance of potential damage due to high flow rates during medium exchange.

4. 800-900 µL of ascorbic acid treatment medium is added by pipetting it next to the grid holder and not directly onto the EM substrate. This ensures that the growing CDM is not disturbed during this process. For glass coverslips, the medium is pipetted slowly over the rim of the well.

5. The ascorbic acid treatment is repeated every other day for 7-21 days.

   In initial CDM growth experiments, ascorbic acid treatment every day was compared to treatment every other day. No negative effect on CDM resilience during transfer and antibody staining could be detected between these two growth conditions. Additionally, antibody stainings against collagen I and fibronectin I showed no differences in fiber formation (data not shown). Hence, I decided to treat the growing CDMs every other day to reduce the chance of disturbing them by growth medium exchanges.

In the course of my work, 14-16 days of matrix growth were found sufficient for all three tested cell lines to produce a dense and stable CDM. Shorter growth times resulted in less dense and more fragile CDM (see Figure 13 and Figure 14 for a time-course study of CDM generation).
During CDM growth, the addition of growth factors may increase the rate of synthesis and deposition of ECM components and result in a denser matrix. However, this was not tested for in this thesis (Ahlfors and Billiar, 2007; Soucy et al., 2011).

The compatibility of the tested EM substrate for CDM growth was assessed based on four criteria: 1) cell behavior and proliferation after seeding, 2) resilience of the resulting CDM after 14 days during specimen transfer, 3) substrate handling, and 4) the compatibility of EM substrates in downstream sample handling steps. All criteria were graded with either Very Good, Good, Acceptable, or Low based on personal experience during specimen preparation. An EM substrate compatibility was graded as **Very Good** if it performed better than glass coverslips and **Good** if it performed equally well. The grading **Acceptable** was given to EM substrates that performed less well than glass coverslips without impeding specimen preparation drastically. EM substrates were graded as having **Low** compatibility if they performed less well than all other substrates and reduced the success rate of CDM sample preparation for cryo-ET. I deemed all EM substrates that were graded with **Low** in any criteria as incompatible with the workflow I aimed to design.
The results for the overall grading are summarized in Table 3.

Table 3: An overview of the general assessment of the EM substrates for CDM growth.
Substrates and their different coatings were judged based on four criteria. Cell proliferation and formation of a monolayer after seeding; CDM resilience during specimen recovery from cell culture and sample processing; resilience of the substrate and resistance to distortions during handling; compatibility of the substrate with downstream processing steps such as traditional EM techniques, and also vitrification and cryo-FIB milling. *Only for traditional EM sample preparation techniques such as resin embedding.

EM substrate	Material	Coating	Cell proliferation	CDM resilience	Substrate handling	Downstream compatibility
EM grid	Au 200	HC 2-2	Good	Very Good	Acceptable	Good
	Au 150	HC 2-2	Good	Very Good	Acceptable	Good
	Ti 200	SiO_2 2-2	Good	Very Good	Very Good	Good
	Au 200	formvar	Acceptable	Good	Acceptable	Good
	Ti 150	formvar	Acceptable	Good	Very Good	Good
	Au 200	formvar + carbon	Acceptable	Good	Acceptable	Good
	Ti 150	formvar + carbon	Acceptable	Good	Very Good	Good
Sapphire disc	Sapphire	carbon	Good	Low	Good	Low
ACLAR® disc	ACLAR® film	carbon	Good	Low	Good	Low
Glass coverslip	Glass	carbon (10nm)	Good	Good	Good	Good*

The adapted protocol led to the production of CDMs with all three cell lines on all tested EM substrates. However, cells attached and proliferated more readily on some substrates compared to others, and some EM substrates fared better during different handling steps compared to others.
On EM grids with an HC coating, the seeded cells attached more quickly and proliferated at a similar or higher speed to cells seeded on glass coverslips to form cell monolayers. On grids coated with formvar, cell attachment and proliferation rate were reduced. Even with an additional continuous carbon coating, this effect could not be fully compensated for. However, gold grids are fragile and get easily distorted during any direct handling steps, making it challenging to work with them.
Ti grids coated with SiO_2 performed better than Au grids throughout the whole sample preparation process as they have much higher durability and are rarely damaged during handling. However, as the supply of these grids could not be guaranteed by the

manufacturer Quantifoil Micro Tools, these grids had to be excluded from further testing.
Initially, sapphire discs and ACLAR® discs with continuous carbon coating were also tested for this workflow, and both showed higher resilience to distortions and damage than EM grids. The cells grew into monolayers and deposited matrix at comparable rates to EM grids. However, both substrates are considerably thicker (~50 µm) than EM grids (~20 µm) and were more difficult to handle during subsequent sample preparation steps. Both the Leica cryo-CLEM system and the TFS FIBSEM used for this workflow are designed to be compatible with AutoGrids™, which cannot be used in combination with sapphire discs or ACLAR® discs without significant modifications. Additionally, both these EM substrates are transparent, and it is difficult to determine which side is the top side once the specimen has accidentally flipped during any subsequent handling step.
Moreover, the CDMs appeared to be more firmly attached to EM grids with carbon coatings when subjected to antibody stainings and downstream sample processing as judged by light microscopy during and after sample processing. It could regularly be observed that removal from the 3D printed holders for subsequent steps resulted in a partial or full loss of CDM from sapphire discs and ACLAR® discs but not from EM grids.
In contrast, CDM production on acid-washed glass coverslips had a high rate of success. Cells readily attached and grew into a monolayer at comparable speeds to EM grids. However, medium exchange was more challenging without the use of grid holders, and the removal of glass coverslips from the well plates for imaging or other sample processing steps regularly resulted in partial damage to or loss of the CDM.
An overview is given in Table 3.

Overall, among all tested substrates, EM grids showed the highest success rate for the generation of resilient and intact CDMs throughout initial characterization, particularly those with HC coating, while being compatible with all downstream sample processing steps. While Ti SiO_2 grids showed the highest overall compatibility, they had to be excluded due to supply insecurities. Instead, Au grids with HC coating were chosen for this workflow as their high compatibility for CDM growth, sample handling, and downstream processing steps compensate for their relative fragility.
Their use led to a reproducibly high quality of CDMs derived from all three cell lines with little to no sample loss up until vitrification.

3.1.2.2. Initial CDM characterization

The assessment of CDMs by phase-contrast microscopy is difficult and only allows inferring whether the matrix is at all present. A more thorough initial characterization of CDMs derived from all three different cell lines with additional methods, as described below, helped to define their main structural components and architecture.

3.1.2.2.1. Characterization by light microscopy

To characterize the CDMs derived from NIH 3T3, REF, and TIFF cells, they were chemically fixed at different time points throughout CDM growth: a few hours after cell seeding (Day (D) -2), on the day the cells reached confluency and ascorbic acid treatment started (D0), and after 7, 14, and 18 days of ascorbic treatment (D7, D14, and D18 respectively). Following fixation, they were stained with primary antibodies

against fibronectin I and collagen I and imaged with confocal microscopy, as shown in Figure 13 and Figure 14.

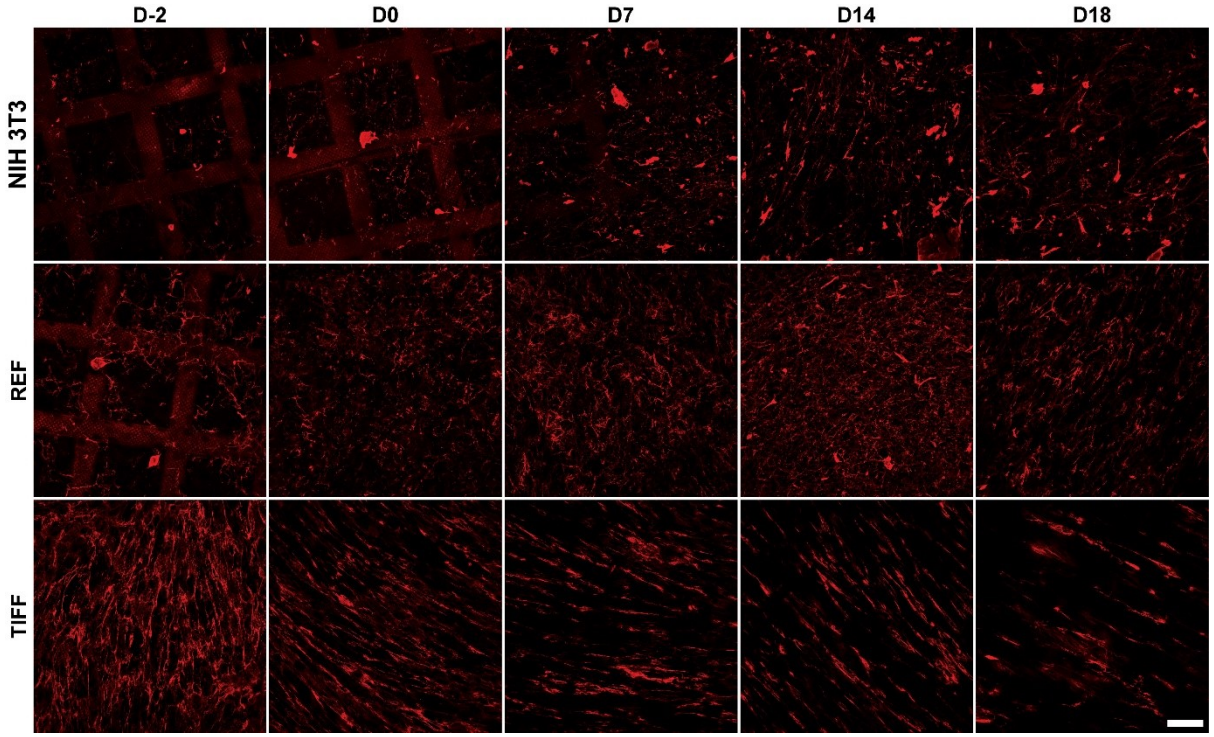

Figure 13: Fibronectin I fiber formation in CDMs over the course of up to 18 days.
CDMs generated on EM grids by the three different fibroblast cell lines NIH 3T3, REF, and TIFF were fixed at different time points, and fibronectin was visualized using immune fluorescence staining employing a fibronectin I antibody. The chosen time points were the day of seeding (D-2), the day ascorbic acid treatment was started (D0), 7 days of matrix growth (D7), 14 days of matrix growth (D14), and 18 days of matrix growth (D18). All three cell lines show the formation of a fibronectin fiber networks over time. These fibronectin I fibers differed in both the rate of formation and their morphology. Scale bar = 20 µm.

The antibody staining revealed that both REF and TIFF synthesized fibronectin I already hours after seeding (D-2, Figure 13), while NIH 3T3 cells did not.
By the time the cell lines had grown confluent, REF and TIFF had formed discernable fibronectin I fibers. In TIFF CDMs, these fibers were already aligned, while in REF CDMs, their arrangement looked random, and they were both thinner and shorter. NIH 3T3 cells showed only a weak signal for fibronectin I at D0.
For all three cell lines, the fibronectin I signal grew stronger by D7, and a more intricate fiber network could be observed. REF CDMs showed thinner, randomly oriented fibers that formed a fine mesh, while TIFF CDMs had thicker, more aligned fibers. NIH 3T3 CDMs had a comparatively low signal for fibronectin I that showed a predominantly loose network of randomly oriented fibers. However, the fibronectin I fibers looked longer and thicker than in REF CDMs.
By D14, the fibronectin I network had grown more pronounced and intricate in all three cell lines. No additive effect could be observed from D14 to D18.
The collagen I antibody staining resulted in very weak staining in CDMs of all three cell lines on D-2 and D0. Signal was predominantly detected in the cell bodies, which could indicate collagen I expression already before a confluent cell monolayer was formed (D-2, Figure 14). At these time points, the cell culture medium was not supplied

with ascorbic acid, which could be a reason for the lack of early fiber formation of collagen I.

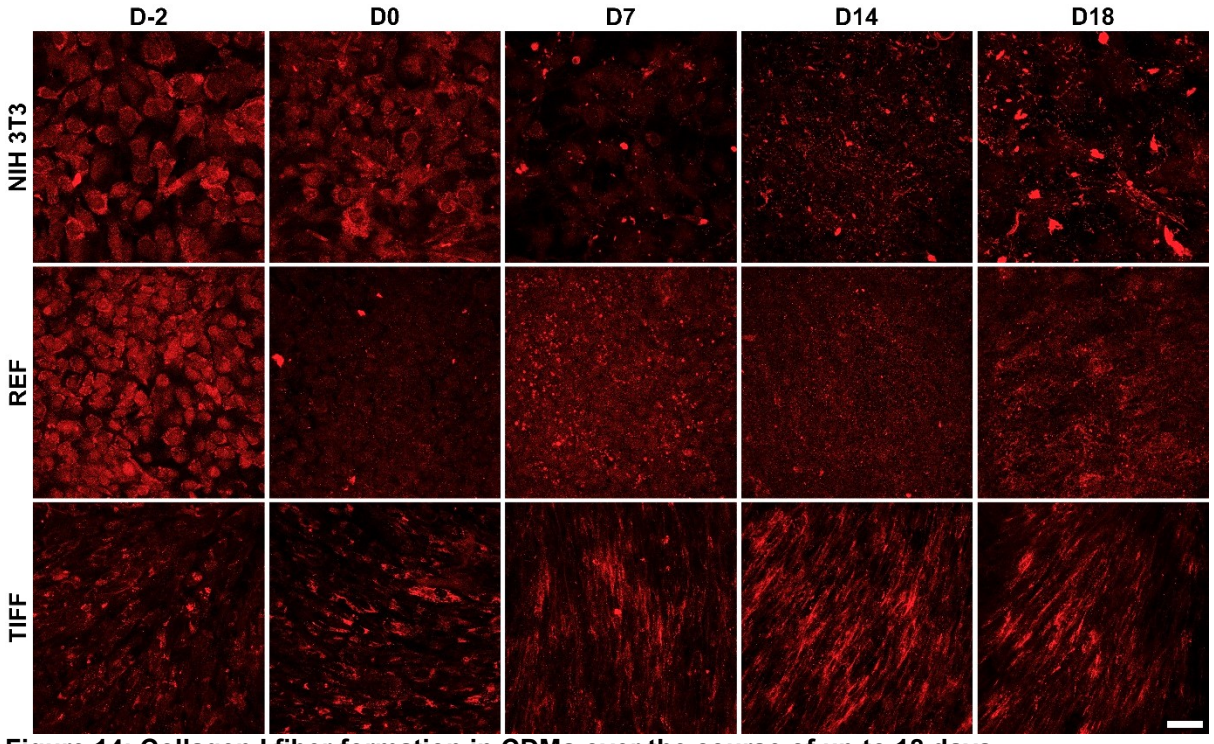

Figure 14: Collagen I fiber formation in CDMs over the course of up to 18 days.
CDMs generated on EM grids by the three different fibroblast cell lines were fixed at different time points, and collagen I was visualized using immune fluorescence staining employing a collagen I antibody. The chosen time points were the day of seeding (D-2), the day ascorbic acid treatment was started (D0), 7 days of matrix growth (D7), 14 days of matrix growth (D14), and 18 days of matrix growth (D18). TIFF are the only cells that show the formation of a distinct collagen I fiber network. REF show no collagen I fiber formation even at D18. By D14, NIH 3T3 cells produce a fine, intricate collagen I network with a significantly weaker signal than that in TIFF CDMs. Scale bar = 20 µm.

By D7 of CDM growth with ascorbic acid treatment every other day, REF and NIH 3T3 CDMs showed no collagen I fiber formation. In contrast, collagen I staining of TIFF matrices at D7 revealed thin fibers that were aligned parallel to each other.
D14 stainings showed more pronounced, thicker collagen I fibers with a stronger signal that were aligned to each other in TIFF CDMs. At the same time point, REF CDMs still did not show any specific collagen I signal, while NIH 3T3 CDMs had developed an intricate network of fine, short collagen I fibers. Staining of D18 CDMs did not show an increase in fiber formation compared to D14: REF CDMs still showed no signal for collagen I fibers, and the fiber network of both TIFF and NIH 3T3 CDMs did not grow more pronounced (see Figure 14). The anti-collagen I antibody chosen should react with all three species the different cell lines derived from. However, it cannot be excluded that it has a higher reactivity with human collagen I than with mouse or rat collagen I. This could explain the drastic difference in the collagen I fiber formation between the three different types of CDMs seen in Figure 14. Another possibility is that both NIH 3T3 cells and REF synthesize collagen I at a lower rate than TIFF.
To test whether increased CDM growth time could increase the total amount of collagen I and fibronectin I detected in NIH 3T3 and REF matrices or lead to fiber alignment, D21 matrices of all three cell lines were also stained for both proteins. However, the density of fibers of fibronectin I and collagen I did not increase for any

of the CDM types (data not shown). Based on these observations, I determined that 14 days of matrix growth are sufficient to generate structured and resilient CDMs appropriate for subsequent sample preparation steps.
It is possible that significantly increased growth time could result in a denser fiber network or thicker fibers. However, it would also significantly increase the sample preparation time and was thus not explored for this workflow.

To elucidate the relation between fiber alignment and cell morphology, D14 CDMs were additionally stained with DAPI to mark the nucleus and fluorescently labeled phalloidin to visualize the actin-cytoskeleton (see Figure 15 and Figure 16).

NIH 3T3 cells grew less dense in a monolayer than REF and TIFF and showed no clear alignment to each other as judged by actin staining. Accordingly, also their fibronectin I and their collagen I fibers showed random orientations (see Figure 15 and Figure 16).

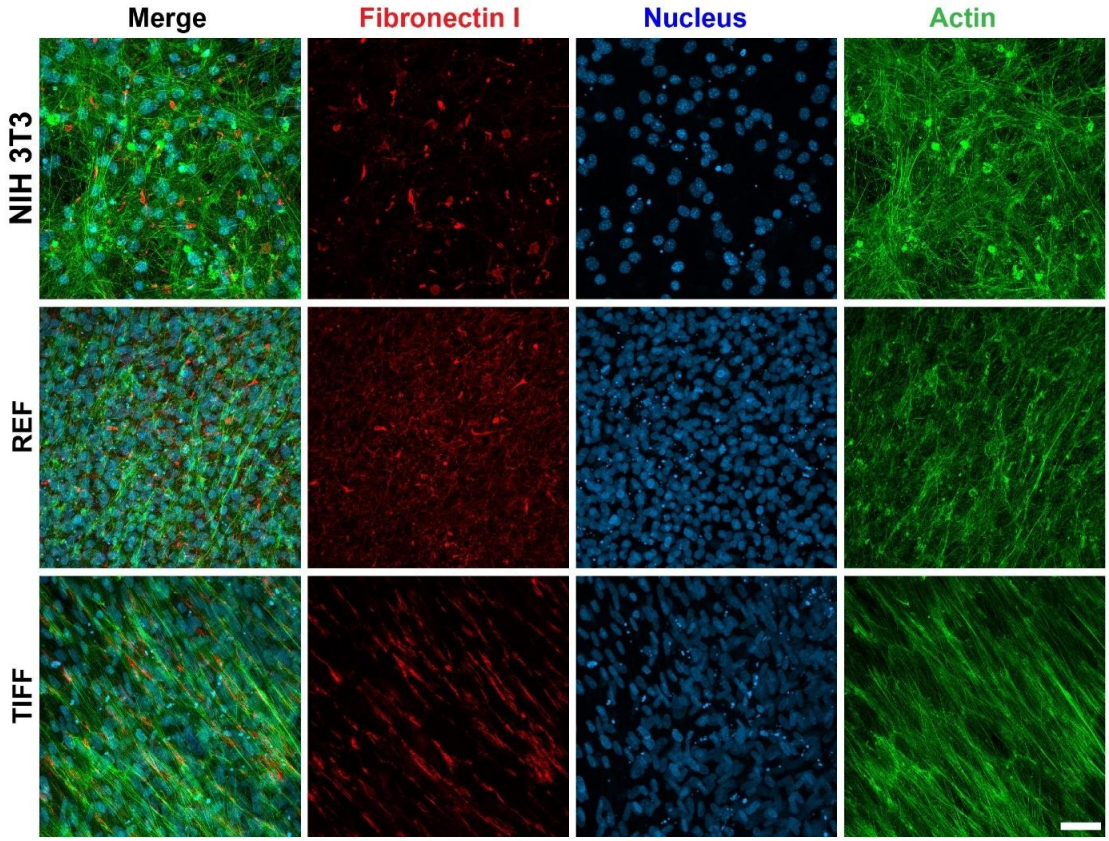

Figure 15: D14 CDMs stained for fibronectin I, the actin cytoskeleton, and the nucleus reveal fibronectin I alignment to cells in TIFF CDMs.
Fibronectin I was visualized by immunofluorescence antibody staining, DAPI was used to visualize the nucleus, and phalloidin coupled to a fluorophore to visualize the actin cytoskeleton. All three CDMs show different architectures of cells and fibronectin I matrix alignment. The images used for TIFF CDMs are the same that were used in part for Figure 13. Scale bar = 50 µm. CDMs were generated on EM grids.

The actin staining in REF indicated a low level of directionality in their orientation, while the fibronectin I matrix looked more stochastic. In contrast, TIFF demonstrated a clear alignment along their longitudinal axis for both their cell body and nucleus. Moreover, both fibronectin I and collagen I fibers of the ECM were running parallel to cells and

seemed to be aligned with them. This alignment of fibers in the ECM is achieved through contractile forces exerted on them by neighboring cells, as shown by (Abhilash et al., 2014). By arranging fibers into thick bundles of aligned fibers, force transmission over distances of several cell lengths is possible and plays a role in cell migration, proliferation, and differentiation (Abhilash et al., 2014).
Hence, among the three tested cell lines, TIFF showed the closest resemblance to physiological ECM, where collagen fibrils are organized into aligned fibers by fibroblasts (Frantz et al., 2010; Theocharis et al., 2016).
All images shown in Figure 15, Figure 16, and Figure 18 were acquired with confocal microscopy and allowed to estimate the height of the fibronectin I/collagen matrix. To this end, the fibronectin I or collagen I signal was measured from its starting point at the EM grid surface to the top of the CDM. At D14, NIH 3T3 matrices were on average ~16.4 µm high (n = 14, SD = ±2.5 µm), REF matrices ~18.5 µm (n = 6, SD = ±2 µm) and TIFF matrices ~14.4 µm (n = 14, SD = ±2.5 µm).
TIFF CDMs had the best signal for both fibronectin I and collagen and thus could be measured more accurately. NIH 3T3 CDMs had a weaker signal for both, and accordingly, measurements were more difficult, which might result in lower accuracy. Due to the lack of collagen I staining in REF CDMs, fewer data points were available for this type of matrices.

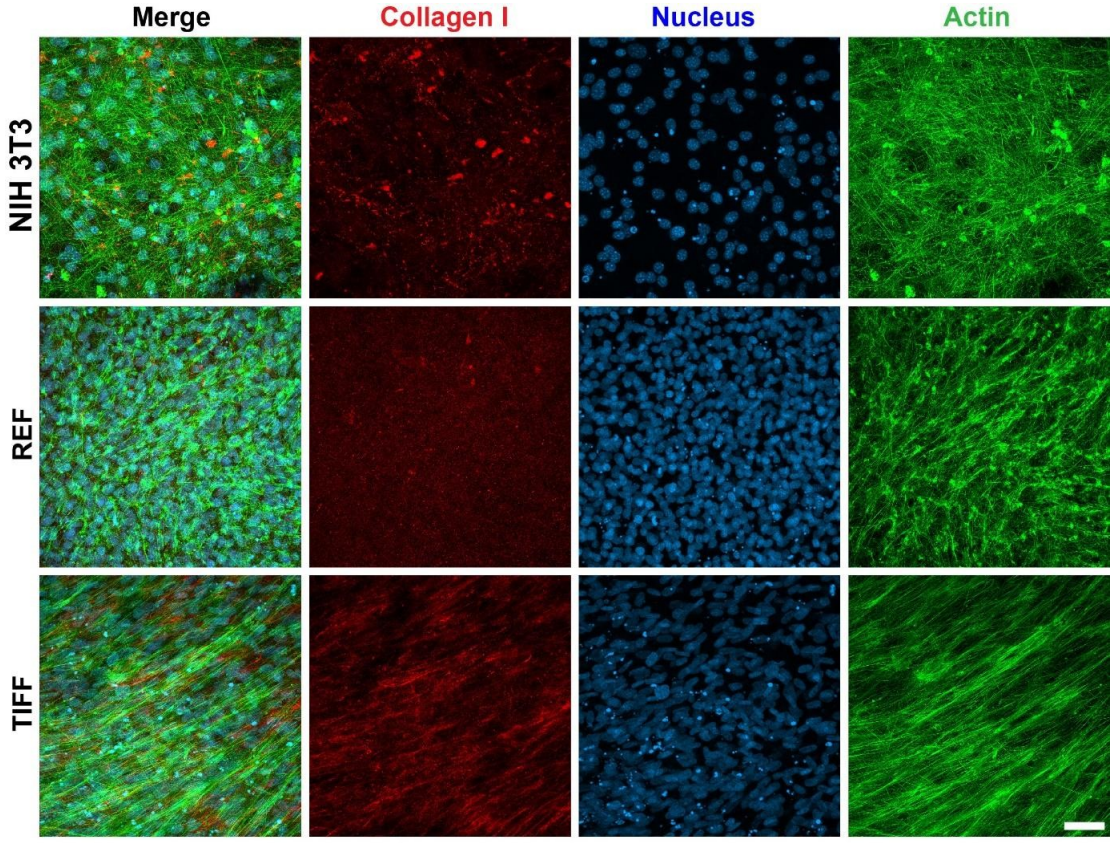

Figure 16: D14 CDMs stained for collagen I, the actin-cytoskeleton, and the nucleus reveal collagen I alignment in TIFF CDMs.
Collagen I was stained via antibody staining, the nucleus with DAPI, and the actin cytoskeleton with phalloidin coupled to a fluorophore. All three CDM types are very diverse in their collagen I architecture. Both NIH 3T3 and REF show a high background for collagen I antibody staining and no clear fiber formation. TIFF CDM shows collagen I fibers that are aligned with the longitudinal axis of the producing cells. Scale bar = 50 µm. All CDMs shown here were generated on EM grids.

Importantly, the D14 CDMs stained for actin and DNA revealed that the overall CDM height exceeds the height of the fibronectin I/collagen matrix. The fibroblasts can extend beyond the fibronectin I/collagen matrix and add to the overall height by ~4-5 µm (n = 10).
In an attempt to better characterize the generated CDM, matrices were also stained for fibrillin, an ECM protein associated with elastic fibers and collagen VI. Additionally, an alternative collagen I antibody was tested to exclude the possibility that the lack of visible collagen fibers in REF and the low collagen I signal in NIH 3T3 CDMs was caused by the chosen antibody. Again, Fibronectin I staining was performed in parallel as quality control for the sample preparation workflow (see Figure 17).

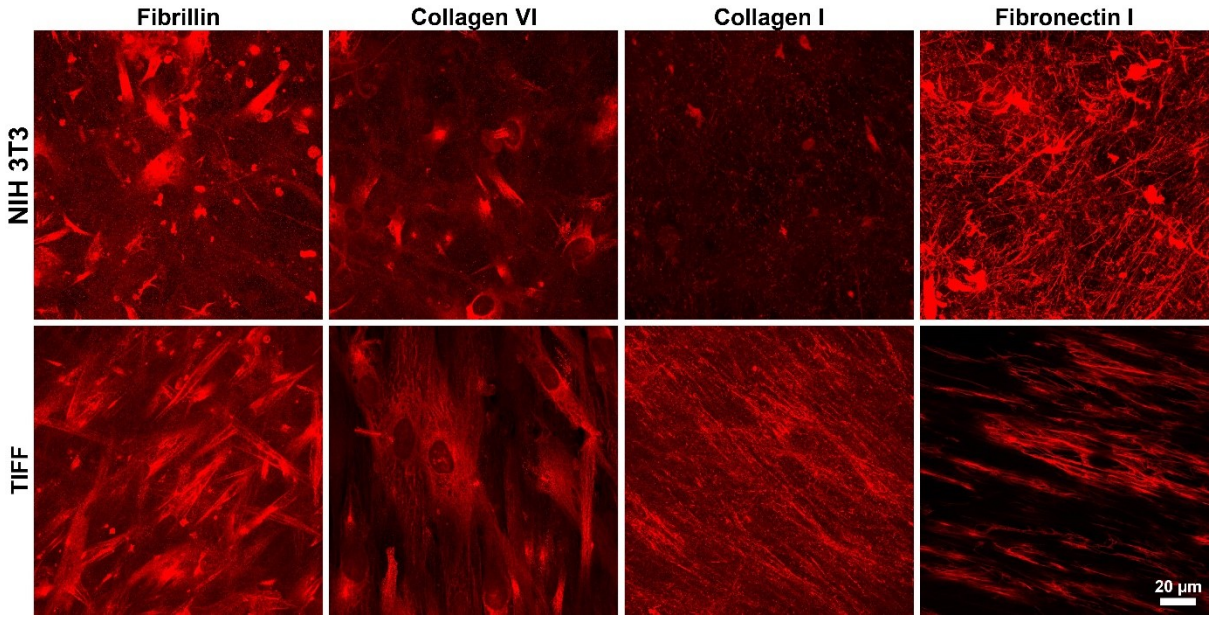

Figure 17: Testing the applicability of different antibodies on CDMs.
Antibodies against Fibrillin, collagen VI, and an alternative collagen I antibody were used on NIH 3T3 and TIFF CDMs. Neither the fibrillin nor the collagen VI antibody showed any ECM fibers and predominantly resulted in stainings of the cell body. The alternative collagen I antibody showed higher background than the one initially used for the characterization. The already established fibronectin I antibody showed clear fibers for both types of CDMs. All CDMs shown here were generated on EM grids.

Neither the fibrillin nor the collagen VI antibody showed specific staining and instead only seemingly cytoplasmic staining. The collagen I antibody resulted in a lower signal than the initially used one and did not allow any further insights into the collagen I fiber organization of these matrices. Compared to the distinct fibronectin I staining, neither of these three antibodies resulted in sufficient staining quality to be used for further characterization of the CDMs.
During sample handling (i.e., retrieval from cell culture, antibody staining), I noticed that TIFF matrices were consistently more resilient than REF or NIH 3T3 matrices. This could be explained by their aligned fiber matrix and higher content of collagen I and fibronectin I according to the brightness and density of the antibody stainings.

Based on all these observations, I concluded that TIFF cells produce a CDM that most closely resembles physiological ECM in comparison to NIH3T3 or REF cells. Both NIH 3T3 and REF are derived from embryonic tissue and can, therefore, not be associated with a defined tissue architecture. This might be linked to the results shown here. In

contrast, TIFF are originally obtained from human foreskin and are expected to reflect the requirement for mechanical resilience in this tissue to at least some degree.

3.1.2.2.2. Characterization by collagen live-staining

To further optimize the workflow, I opted for a live staining method that would render chemical fixation and the dozens of washing steps needed for antibody staining unnecessary. Initial staining trials with a universal stain for proteins, 5-Carboxytetramethylrhodamine, also called TAMRA, resulted in labeling with a high background. No clearly discernable features in D14 matrices were visible using this stain (data not shown).

Upon recommendation by Prof. Johanna Ivaska (Univ. Turku, personal communication), I then decided to use a collagen-binding peptide called CNA35. This peptide consists of two soluble domains of a native collagen-binding protein from *Staphylococcus aureus* bacteria, which recognize the collagen triple helix (Aper et al., 2014). It has the most efficient binding with collagen I but also binds type II, III and IV to a lesser extent while showing barely any labeling of collagen V and VI (Krahn et al., 2006). Importantly, it does not label other ECM proteins such as fibronectin, elastin, and laminin.
CNA35-EGFP is well suited for live stainings and long-term studies because it binds collagen reversibly and is unlikely to interfere with ECM formation (Aper et al., 2014). It is also considerably smaller than an antibody, with only ~64 kDa.
I used CNA35-EGFP as a live stain to visualize a time course of collagen matrix formation during CDM generation (see Figure 18). The time course chosen was the same as described in section 3.1.2.2.1.
The specimens were imaged live at a confocal microscope to assess the relative amount of collagen and the rough architecture of the forming collagen matrix over the course of CDM growth. On the day of seeding, both NIH 3T3 cells and REF show only faint amounts of collagen, while higher amounts of collagen can be seen in TIFF specimens. After confluency is reached on the EM grid after 2-3 days of culturing, all NIH 3T3 and REF cells show increased amounts of anisotropic collagen signal. In contrast, collagen synthesized by TIFF cells starts forming fibrils already at this point. The three cell types show very distinct collagen architecture after 7 and 14 days. The collagen matrix in NIH 3T3 cells forms an anisotropic network of thick fibers which stands in stark contrast to the collagen antibody stainings shown in Figure 14. This may imply that the collagen detected with CNA35-EGFP in these samples is neither collagen I nor collagen VI. However, it cannot be excluded that the antibodies used for the characterization of NIH 3T3 matrix do not bind to mouse collagen as well as to human collagen, while CNA35 does. The level of intricacy of the fiber networks in all CDMs seems to increase from D7 to D14, as a denser architecture with a greater variety in the thickness of the single fibers could reproducibly be observed (see Figure 18, D7 and D14 of the NIH 3T3 panel).
REF cells, on the other hand, seem to synthesize lower amounts of detectable collagen and show no defined fiber formation, even at D14. This reflects what has been observed with antibody staining for collagen I.
In contrast, TIFF cells display very aligned collagen fibers of different sizes, as already shown by the antibody staining for both fibronectin and collagen. The staining with CNA35-EGFP closely resembles the collagen I antibody staining but has a brighter

signal and, therefore, a better SNR, allowing for clearer images (see Figure 18 in comparison to Figure 14).

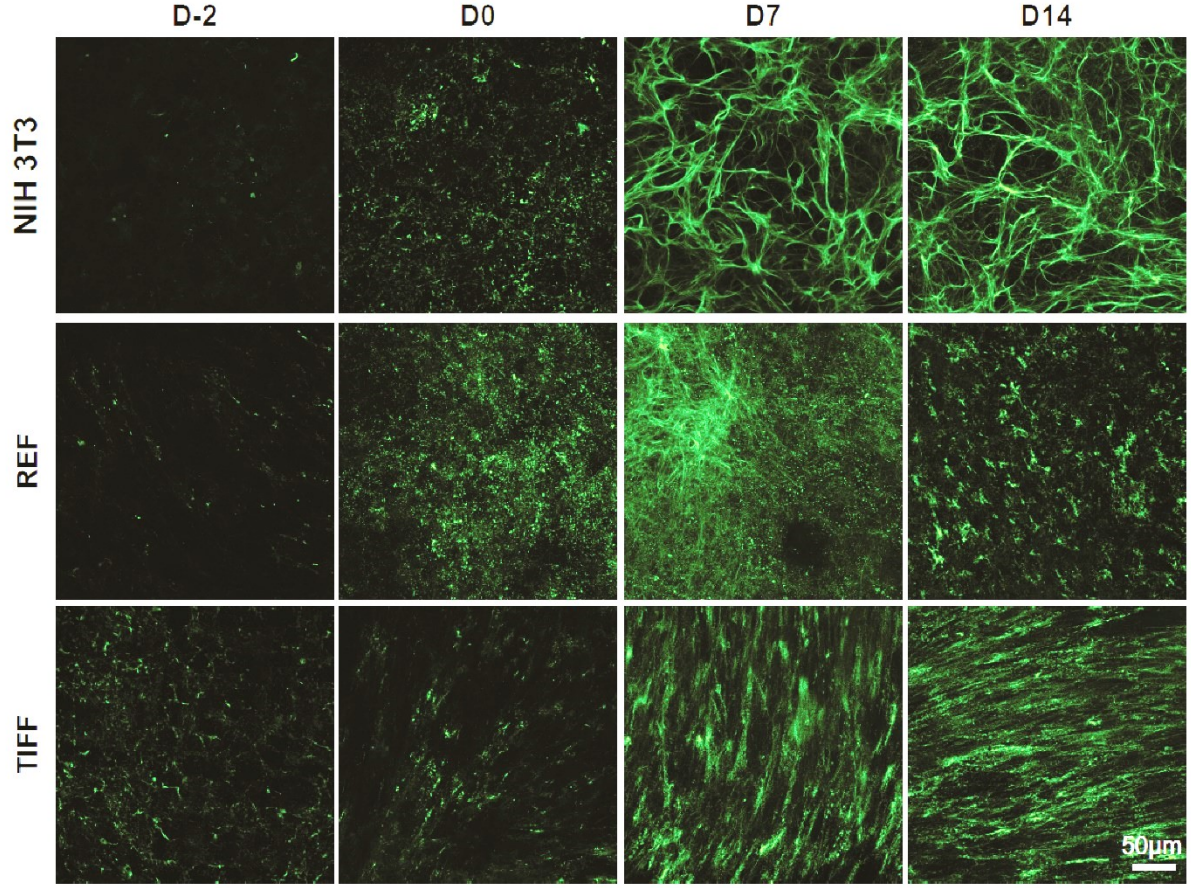

Figure 18: Collagen live-staining with CNA35-EGFP over the course of CDM growth.
CDMs generated on EM grids by the three different fibroblast cell lines were stained at different time points for their collagen. Scale bar = 50 µm.

Based on these observations, it can be concluded that the live staining with CNA35-EGFP works very well for these samples and can be used to circumvent antibody staining for cryo-CLEM characterization after vitrification. This allows for removing the chemical fixation step from sample preparation and for retaining the fully native character of CDMs prior to vitrification if desired.

The characterization by antibody staining and live staining has shown that TIFF CDMs resemble skin ECM in terms of fiber alignment of both fibronectin and collagen. I have therefore concluded that they represent the best recapitulation of the physiological ECM of a given tissue. Moreover, it was consistently more resilient to sample handling steps than other matrices, and specimen loss only rarely took place prior to vitrification. For these reasons, the TIFF matrices were used for further CDM characterization and the design of this workflow.

3.1.2.2.3. Characterization of TIFF CDMs by Mass Spectrometry

In order to gain an overview of the matrisome of TIFF CDMs and the relative amounts of the single components, mass spectrometry was employed.
To this end, TIFF CDM generation was expanded to 10 cm² cell culture dishes to produce sufficient material for this method. In this particular case, no fibronectin

surface coating was used on the cell culture dishes in order to avoid false positive fibronectin results. After CDM growth for 14 days, the matrix was decellularized following the standard protocol described by (Kaukonen et al., 2017) to remove cellular components as well as DNA. Briefly, CDMs were washed 3x with detergent and ammonium hydroxide diluted in PBS for a total of 10 minutes to remove cellular membranes. The CDMs were then washed thoroughly with PBS, and DNase I was added for 1 h to remove leftover DNA. Therefore, it has to be taken into consideration that throughout the decellularization process, some components, especially PGs, might be removed. Cellular proteins, such as integrins, still bound to ECM components and remaining DNA contamination could not be fully removed in this process as detected in the proteomics data (data not shown).
For Mass Spectrometry sample processing, two different protocols were followed as described in detail in 5. Materials and Methods. One sample processing protocol was adapted from (Lansky et al., 2019), and the other one was recommended by the lab support facility (LSF, ISTA). After Mass Spectrometry sample processing, both samples were analyzed separately, and the resulting data was filtered for ECM proteins and sorted by relative interpreted expression values. Table 4 shows the 25 proteins with the highest expression (out of 110 identified ECM proteins) based on the sample processing protocol adapted from (Lansky et al., 2019). The results based on the other sample processing protocol are very similar, with only small changes in the order of proteins, and hence are not shown here.

Table 4: The most abundant ECM proteins in TIFF CDMs as determined by Mass Spectrometry. TIFF CDMs were grown for 14 days with ascorbic acid treatment every other day and decellularized. Subsequently, they were subjected to mass spectrometry, and resulting data was filtered for core matrisome components. Here the proteins with the highest abundance are listed according to their expression value. The expression value given here is the Log10 of the estimated protein expression values calculated from unnormalized individual unique peptide intensities. It was normalized using the Levenberg-Marquardt procedure to minimize sample-to-sample variation.
Shown here are the results based on the sample preparation protocol based on (Lansky et al., 2019).

Leading protein IDs	Common Names	Genes	Express. value
P02751-1	Fibronectin, Isoform 1	FN1	9,9618
P24821	Tenascin	TNC	9,7028
P12111	Collagen alpha-3(VI) chain	COL6A3	9,6882
P12109	Collagen alpha-1(VI) chain	COL6A1	9,6753
P02452	Collagen alpha-1(I) chain	COL1A1	9,6404
P08123	Collagen alpha-2(I) chain	COL1A2	9,6010
P09382	Galectin-1	LGALS1	9,5746
P12110	Collagen alpha-2(VI) chain	COL6A2	9,5491
Q15582	Transforming GF-beta-induced protein ig-h3	TGFBI	9,4492
P35555	Fibrillin-1	FBN1	9,2462
P02458	Collagen alpha-1(II) chain	COL2A1	9,2386
P17931	Galectin-3	LGALS3	9,2203
P50454	Serpin H1	SERPINH1	9,2026
P14618	Pyruvate kinase PKM	PKLR;PKM	9,1534
P05997	Collagen alpha-2(V) chain	COL5A2	9,1376
P07585	Decorin	DCN	9,1299
P07996	Thrombospondin-1	THBS1	9,1077

Leading protein IDs	Common Names	Genes	Express. value
Q99715	Collagen alpha-1(XII) chain	COL12A1	9,0896
Q9Y6C2	EMILIN-1	EMILIN1	9,0528
P02751-11	Fibronectin, Isoform 11	FN1	8,9851
P98095-2	Fibulin-2, Isoform 2	FBLN2	8,9825
CON__A0A4W2C0I9	Fibulin-1	FBLN1	8,9396
P98160	Basement membrane-specific heparan sulfate proteoglycan core protein	HSPG2	8,9378
P02461	Collagen alpha-1(III) chain	COL3A1	8,9193
P24821-4	Tenascin, Isoform 4	TNC	8,9181
P20908	Collagen alpha-1(V) chain	COL5A1	8,9122

Based on this data, several fibrillar proteins are present in high abundance in TIFF CDMs. Fibronectin I, as well as collagen VI and collagen I, show the highest relative expression along with Tenascin. Tenascin-X has been shown to be expressed in skin and has the ability to cross-link collagen I, III, and V (Lethias et al., 2006), all of which also show up among the top hits of the analysis.
Among the remaining proteins are sugar-binding proteins such as galectins, which are known to be involved in cell-matrix adhesion (Ochieng et al., 1998), and fibril-binding proteins such as fibrillin and fibulin. Fibrillin is essential for the formation of elastic fibers (Kielty et al., 2002), while fibulin interacts not only with elastic fibers but also with fibronectin, laminin, and other ECM components (Timpl et al., 2003).
Overall, these results further underscore the complexity of the formed ECM. This confirms TIFF CDM to be a physiological model for skin ECM and its suitability for the study of ECM architecture.

3.1.2.2.4. Characterization by RT-TEM/SEM

Conventional TEM and SEM methods have been routinely applied in the past to characterize the ultrastructure of the ECM, despite their shortcomings in the preservation of hydrated environments.
In order to have a baseline comparison to results obtained by cryo-ET and to already established models, I also performed TEM and SEM to acquire ultrastructural insights on the overall fiber architecture in CDMs.

Initially, conventional RT SEM was employed to visualize CDMs, in particular, their surface topology. To this end, NIH 3T3 CDMs were grown on EM grids and then prepared for SEM via dehydration and critical point drying before being coated with 7 nm platinum.
As this data was acquired very early on during the work for my thesis, only NIH 3T3 cells were available for CDM growth at that time. Based on the results shown in Figure 19, demonstrating the significant alteration of the CDM ultrastructure during sample preparation, I reasoned that no further insights could be gained with this method. Due to this, these experiments were not repeated with CDMs from other fibroblast lines.
Figure 18 shows an NIH 3T3 CDM at increasing magnification. The overview image in Panel A clearly shows the drastic effect of dehydration on a hydrogel, such as a CDM. The CDM that originally spanned the whole grid has shrunk considerably in size and

has been deformed in the process. This is important to keep in mind, as this effect is no longer apparent at higher magnification and may change the interpretation of these images.
Conventional SEM shows the surface of single cells at the top of the matrix (Panel B) and a fine meshwork of dense fibers (Panels C and D). The fibers visible in these images are of different thicknesses and are randomly oriented. It has to be taken into consideration that the platinum coating might obscure other cells and fibers sitting at the very surface. Moreover, the fiber network likely collapsed during dehydration and critical point drying. It is likely much less dense, and what can be seen here as single fibers might in originally have been several thinner fibers.

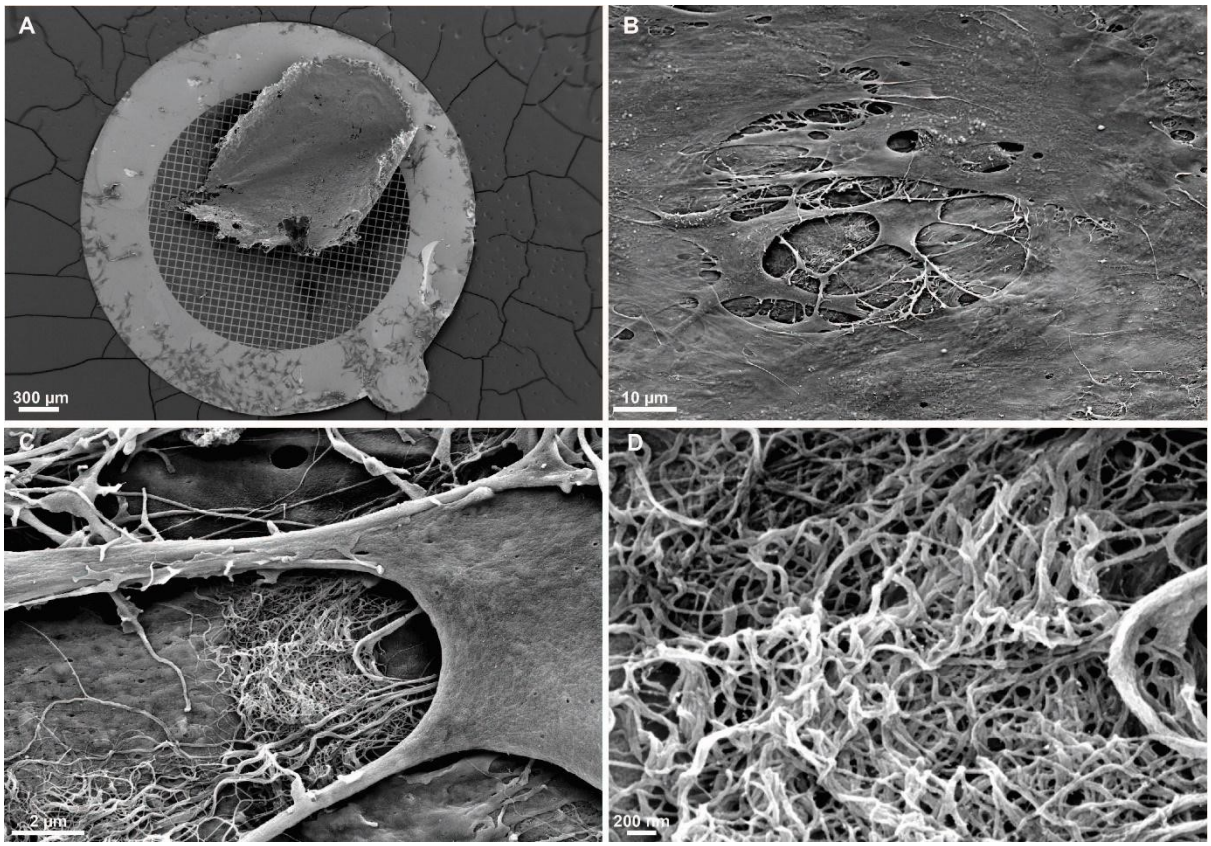

Figure 19: Conventional SEM of NIH 3T3 CDMs.
A) An overview image of a NIH 3T3 CDM grown on an EM grid shows the significant shrinkage of the matrix upon dehydration and drying. B-D) A fibroblast positioned at the matrix surface and the fibers lying beneath it are shown at increasing magnification.

Figure 19 demonstrates one of the main disadvantages of the use of standard RT SEM techniques on CDM samples. The dehydration and drying processes drastically alter the ultrastructure and arrangement of single components of the ECM.

Instead, I shifted my focus to standard TEM methods. To this end, TIFF CDM was grown on glass coverslips as described previously and prepared for thin-section TEM by resin embedding and ultramicrotomy. Single 70nm sections were imaged at different magnifications, as shown in Figure 20. In Panels C-F, ECM fibers can be observed with increasing magnification. As expected, the sections show a high number of collagen fibers that can be identified via their characteristic banding pattern. They have a width of ~40-50 nm and are, for the most part, aligned relatively parallel to each other with fewer fibers showing a more stochastic arrangement. Based on the

banding pattern and overall abundance, they are most likely collagen I. A comparatively lower number of thinner fibers of only around ~10 nm are visible in between single collagen, again similarly aligned with respect to the cell axis. Their identity is unclear at this point, as both fibronectin I and collagen VI should be present in these specimens in high abundance. The TEM micrographs of plastic-sections exemplify the power but also limitations of conventional TEM. Fine details, such as single ECM components, are potentially lost during the sample preparation process. Additionally, the staining and sectioning of the specimens can introduce artifacts that are difficult to identify.

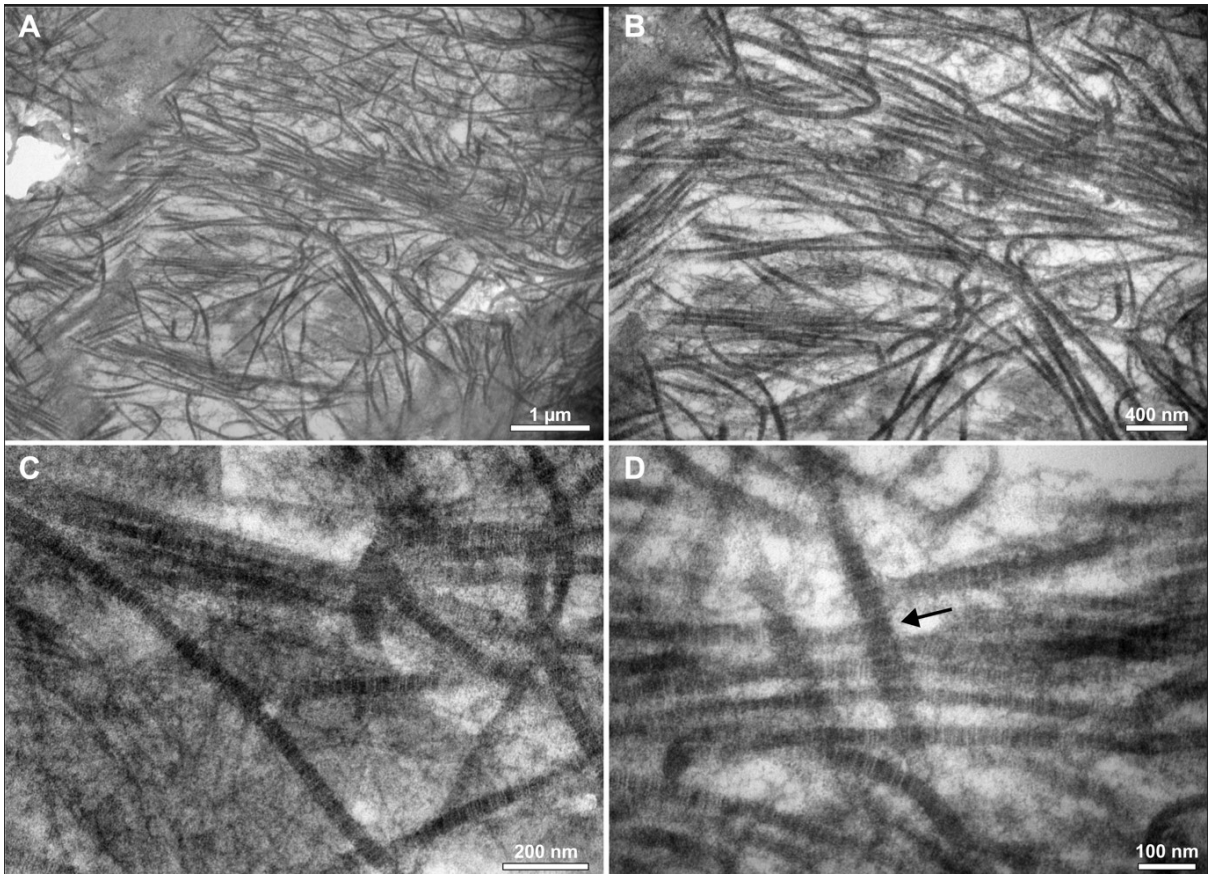

Figure 20: Characterization of TIFF CDM by thin section RT-TEM.
A-D show a representative section of TIFF CDM grown on a glass coverslip in increasing magnifications. Thicker fibers with a width of ~40-50 nm occur in high abundance, while smaller fibers of ~10 nm are interspersed in between in lower numbers. The majority of fibers are aligned with the longitudinal axis of the cells, but some interspersed fibers show random orientation. At higher magnifications, the typical collagen banding pattern is recognizable, indicated here by an arrow.

In order to assert the identity of the thin fibers and to confirm whether the thicker collagen fibers are indeed collagen I, immuno-gold labeling of the CDM prior to sample preparation via resin embedding and thin sectioning was attempted (Figure 21).
For the immunogold-labeling, two standard protocols were followed, using the same fibronectin I and collagen I primary antibodies already used for fluorescence microscopy. The specificity of these antibodies was confirmed in Figure 13 and Figure 14. Using the first protocol (referred to as Protocol 1 in section 5, Materials and Methods), no secondary antibody coupled to 10 nm nanogold could be detected in any of the imaged sections (data not shown). In the second protocol (referred to as Protocol 2 in section 5, Materials and Methods), the TIFF CDM was permeabilized by

freeze-thaw treatment, and the incubation time for the secondary antibody was increased to 3 days. Additionally, in parallel with a secondary antibody coupled to 10 nm fiducial gold, one with 5 nm nanogold was tested to exclude the possibility that the size of the secondary antibody prevented it from penetrating into the CDM. However, as can be seen in Figure 21, also this approach did not result in the successful labeling of any fibers.

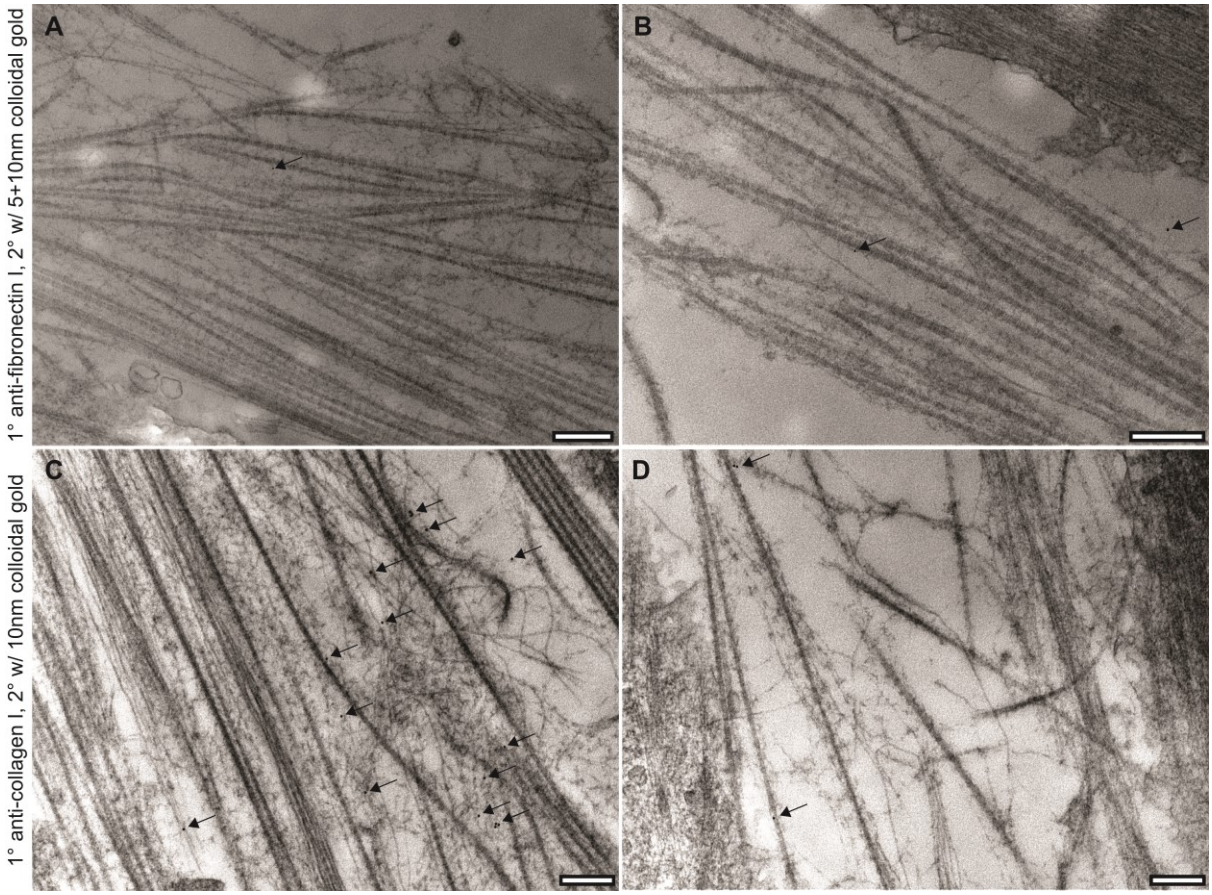

Figure 21: Immuno-gold labeling trial of collagen I and fibronectin I in thin-section TEM of TIFF CDM.
Secondary antibodies coupled to 10 and 5 nm fiducial gold were used in combination with a primary antibody against fibronectin I (A and B). A secondary antibody coupled to 10 nm fiducial gold was used in combination with a primary antibody against collagen I (C and D). In both cases, fiducial gold could be seen only very rarely, not showing specific localization patterns. Scale bars = 300 nm. The TIFF CDM was grown on a glass coverslip.

In all screened sections, immuno-gold could only be observed rarely, and even in regions that showed a higher abundance (Figure 21, Panel C), it did not stain fibers of a specific type.
Biological replicas of these samples were simultaneously prepared following the same protocol but stained with secondary immunofluorescence antibodies instead of the nanogold-coupled ones. These specimens showed a signal for both the fibronectin I and collagen I fibers (Data not shown), proving that the primary antibody successfully penetrated and stained the ECM fibers. Based on this, I concluded that the immuno-gold labeling had not worked even with increased incubation times and permeabilization due to an issue with the secondary antibodies in combination with these samples or staining protocols. Hence, I decided to abandon this attempt for the

identification of fibers, as optimization would have required a considerable time investment without any guarantee for its success.

The combination of light microscopy, mass spectrometry, and RT EM could show the presence of fibrous CDM in the generated samples. Moreover, it became clear that TIFF CDMs were the best candidate for downstream sample processing steps and that fibronectin I, collagen I, and collagen VI should account for a high portion of these matrices.

3.2. Vitrification for cryo-EM sample preparation

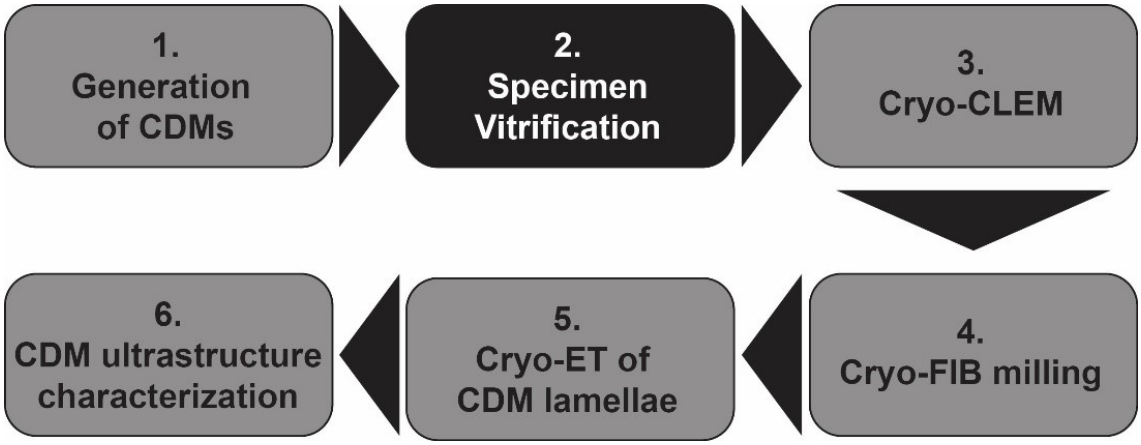

There are two options for the vitrification of specimens for cryo-EM sample preparation: Plunge-freezing and HPF. Typically, only samples thinner than 10 µm can be successfully vitrified by plunge-freezing, but this can be even less, depending on specimen composition. Even small clusters of 2-3 mammalian cells already have too much overall volume to vitrify entirely with this method.
TIFF CDMs are bulk specimens with a dense monolayer of cells and the surrounding matrix, summing up to a height significantly beyond 10 µm over the whole grid. Hence, HPF was the more promising of these two options for vitrifying such samples.
However, HPF adds to the overall sample bulk as it requires a filler medium to be added to the specimen to avoid the entrapment of air that would impede vitrification. This is described in more detail in section 1.2. HPF is also technically more challenging than plunge-freezing. For these reasons, plunge-freezing was still explored in initial trials in an attempt to keep the vitrification process as simple as possible.

3.2.1. Vitrification by Plunge-Freezing

I reasoned it to be nearly impossible to achieve vitrification of a TIFF CDM by plunge-freezing due to its volume and high water content. The bulk of the fibroblast monolayer and the CDM surrounding it made it extremely unlikely to achieve a sufficiently fast vitrification rate.
For this reason, CDMs were decellularized, as described in section 5. Materials and Methods. After decellularization, only the CDM and a low amount of cellular debris, such as clumps of DNA, remained, as assessed by confocal microscopy (see Figure 22). Collagen I and fibronectin I fibers did not appear to be distorted upon decellularization as judged by confocal microscopy (see Figure 22, collagen I data not shown).
TIFF CDMs showed a high resilience to mechanical damage during the decellularization process, and only a few specimens were lost, as confirmed by confocal microscopy.
In comparison, initial tests with NIH 3T3 CDMs showed higher sensitivity. Damage to the matrix and sample loss during decellularization and antibody staining occurred more often compared to TIFF CDMs. This is possibly an effect of their stochastic and less dense fiber alignment.

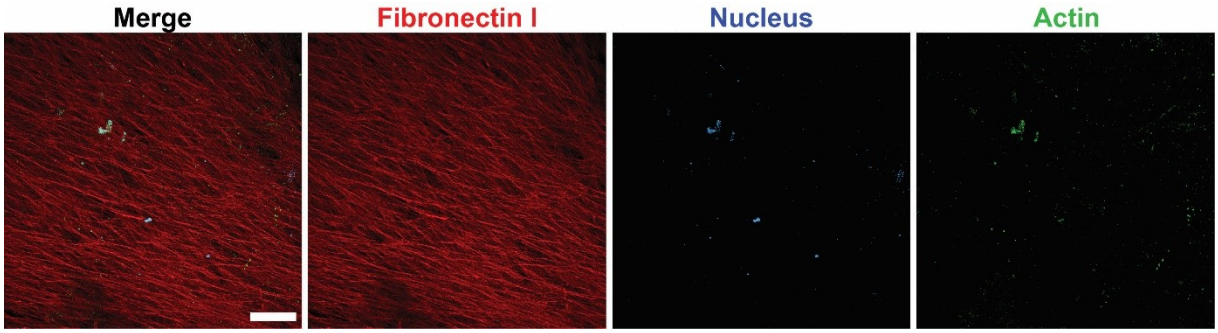

Figure 22: Confocal imaging of extracted TIFF CDM.
D14 TIFF CDMs grown on EM grids were decellularized and treated with DNase to remove the remaining DNA. After fixation, the CDMs were stained for fibronectin I, DNA (Nucleus), and actin. The fibronectin fibers did not appear to be altered, and only low amounts of cellular debris remained. Scale bar = 20 µm.

After imaging by confocal microscopy for quality control, only specimens without grid distortions or CDM damage were used for plunge-freezing. Even after decellularization, the CDMs were not reduced in height as judged by confocal microscopy.
The specimens were sitting in a drop of liquid at all times to avoid sample damage due to drying. This resulted in a comparatively high amount of liquid entrapped on and within the specimen compared to standard samples for plunge-freezing, which does not readily vitrify by plunge-freezing. Due to this, the matrices were blotted with filter paper for up to 8 s before plunge-freezing to remove as much liquid as possible.
For these attempts, the GP2 was used employing backside blotting, as I suspected that front-side blotting might damage and, in some cases, remove the CDMs. After plunge-freezing, the EM grids were clipped into AutoGrids™. Cryo-FM was then used to assess the state of the EM grids and the CDMs.
The final read-out for the success of these plunge-freezing attempts could only be done by cryo-TEM after sample thinning by cryo-FIB milling, which resulted in a long feedback loop.
As expected, the results clearly showed a lack of proper vitrification. Hexagonal ice was evident throughout the lamellae (see section 3.3.2.1 for a detailed description). Therefore, I concluded that decellularized CDM could not be vitrified by plunge-freezing.

3.2.2. Vitrification by High-Pressure Freezing (HPF)

After confirming that vitrification of CDM could not be achieved by plunge-freezing, I shifted all vitrification attempts to HPF. Typically, HPF is used on tissues, cell suspensions, or small multicellular organisms, such as *C. elegans* or *D. melanogaster* embryos. These specimens are then subjected to freeze-substitution or freeze-fracturing and subsequent ultramicrotomy.

HPF of specimens on EM grids is not routinely performed and only recently has been proposed in two different protocols, both not applicable to my workflow (Kelley et al., 2022; Kolovou et al., 2017). Hence, I needed to develop a protocol for the vitrification of CDMs on EM grids with reproducible vitrification success and sample quality for the novel workflow I wanted to establish. There are several significant challenges for performing HPF of CDMs on EM grids:

- Gold EM grids are easily distorted by mechanical forces. This aggravates the retrieval of EM grids from HPF carriers without losing the CDM or bending grids.
- The final height of the vitrified bulk sample depends on the chosen carriers. As the specimen is never precisely the height of available carriers, filler medium needs to be added to avoid having residual air within the carriers, which would impede vitrification. Commercially available carriers typically have a minimum recess depth of 50 µm, significantly exceeding the average TIFF CDM height. Using a carrier with a considerable excess depth would lead to an empty top layer consisting of only filler medium of ≥30 µm. Hence, custom carriers with reduced recess heights are required. The samples must be kept at ≤ 150°C following HPF while avoiding contamination from atmospheric humidity.
- CDMs have not been vitrified in any previous publication, so no protocol exists. The optimal filler liquid for the HPF carriers and a strategy for carrier assembly must be determined first.

The standard assembly of an HPF sandwich consists of two metal carriers, one on each side of the sample to be vitrified (see Figure 23). One or both of these carriers have a recess to accommodate the size of the specimen to be vitrified. Ideally, the total recess depth should closely match the specimen height, as a lower overall volume has a higher chance of successful vitrification. The total sandwich height should be 1 mm. Even slight derivations of only ±0.05mm can negatively impede the vitrification process, as I have experienced during the work for this thesis.
Such 3 mm aluminum carriers were tailored to exact specifications at the ISTA Machine Shop. Carrier A was designed to have a height of 0.5mm, and a circular recess of 2 mm diameter and 20 µm depth (± 5 µm machining inaccuracy). The recess depth was adjusted to CDM height to ensure that the matrix would not be squeezed during sandwich assembly while also not adding an excessive empty bulk layer on top. It was essential to keep the added bulk to a minimum to keep the cryo-FIB milling time as low as possible. Carrier B was designed as a flat disc with 0.5mm in height. To ensure optimal vitrification conditions, every carrier used to assemble HPF sandwiches was carefully measured before use.
The exact carrier sandwich assembly is shown in Figure 23: Prior to sandwich assembly, both carriers are coated in 1-hexadecane to increase the chances of specimen recovery without sample damage. Initial tests showed that carriers coated in 1-hexadecane were easier to disassemble, and sample loss was significantly reduced compared to non-coated carriers.
Carrier B functions as a flat “lid” to the sandwich, which is placed at the backside of the EM grid carrying the CDM. A drop of filler medium is placed on top of the specimen to avoid trapping any air bubbles. Then carrier A is placed on top of the specimen with the recess side facing down. It is crucial to place carrier A straight on top of carrier B in a single step to avoid having to adjust carrier position and thereby damage the CDM through excessive movement of the single sandwich components.

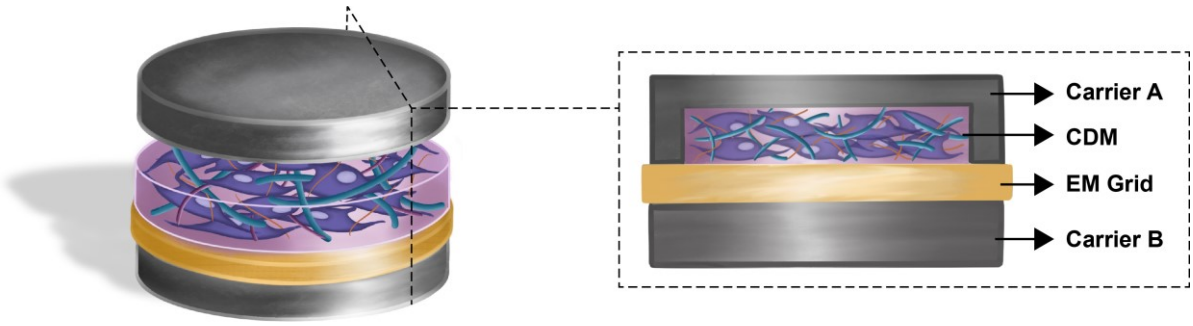

Figure 23: A schematic representation of the HPF sandwich assembly for CDM vitrification. Carriers A and B are made from aluminum and have a 3 mm diameter and height of 0.5 mm. The 2 mm diameter recess of carrier A is ~20 µm deep to fit the height of the CDM. Both carriers are coated in 1-hexadecane to facilitate sample recovery. This image is courtesy of Verena Baumann, Ph.D., who created it specifically for this thesis.

The total sandwich height is the sum of both carriers (0.5 mm each) and the gold EM grid (0.02 µm), leading to a total height of 1.02 mm.
HPF sandwiches with a total height below 0.9 mm resulted in total sample loss in more than 30 single specimens frozen in several separate batches as determined by cryo-FM. In all these specimens, both the CDM and the coating of the EM grids had been lost during HPF (data not shown). This was caused due to the delivery of falsely machined A carriers, which had a height of ≤0.4 mm instead of 0.5 mm. This error was only discovered when each carrier from this very delivery was manually measured for diameter and height.
Similarly, carriers that had a diameter of ≥3.05 mm did not fit into the specimen holder needed for HPF and could not be used. Based on these observations, I suspected that HPF sandwich height and diameter were crucial for the success of HPF. To this end, every single carrier was measured and discarded when height or diameter deviated more than ± 0.02 mm from the specified values.
For this thesis, a BAL-TEC HPM010 was employed for HPF. After recovery from the HPF machine, the sandwich was kept in LN_2 until disassembly with forceps and recovery of the specimen. Specimens that showed no apparent distortions or EM grid damage were clipped into AutoGrids™ for cryo-FIB milling, so-called FIBSEM AutoGrids™. These FIBSEM AutoGrids™ were marked with permanent markers prior to clipping to facilitate sample orientation in the cryo-CLEM, cryo-FIBSEM, and cryo-TEM instruments, as shown in Figure 24. A brightly colored marker is used to mark the milling window so it is more discernable in liquid nitrogen. A different color is used to mark the upper surface and the edge of the AutoGrid™ at 90° to the milling window on either side, as indicated in Figure 24.
The colored milling window is used to orient the sample in the same direction in the cryo-CLEM and the cryo-FIBSEM. This greatly facilitates correlation, as only slight differences in the relative sample rotation have to be accounted for. The markings on the sides are used to orient the AutoGrid™ in the TEM so that the tilt-axis is perpendicular to the milling direction (as described in more detail in section 3.2.2).

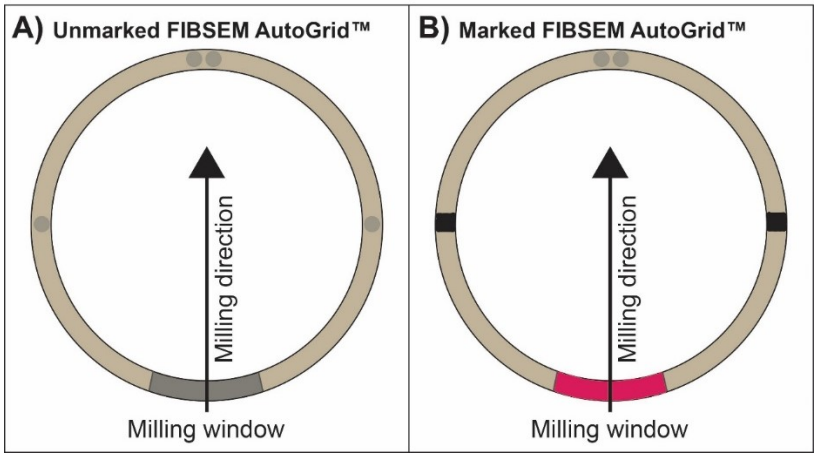

Figure 24: Schematic of FIBSEM AutoGrid markings.
A) Shows an unmarked FIBSEM AutoGrid™. Markings are etched into the surface of the AutoGrid™ at 90° relative to the milling direction on either side of the milling window (one dot) and directly opposite the milling window (two dots). These dots and the milling window are difficult to distinguish when the AutoGrid™ is submerged in LN_2 and are not visible in side view. B) The milling window is marked with a bright permanent marker. The sides are marked on the surface and also on the edge, indicated here in black. These markings are more visible when the AutoGrid™ is submerged in LN_2, and by drawing them over the side, they are also visible in side view. These markings facilitate AutoGrid™ orientation during sample loading of the cryo-CLEM, cryo-FIBSEM, and cryo-TEM instruments.

The samples that have been clipped into FIBSEM AutoGrids™ are then screened for sample quality by cryo-FM as detailed in section 3.3.1.
Interestingly, the type of EM grids used also made a difference in the success rate of the recovery of intact specimens. EM grids coated with HC proved to dislodge much easier from the carriers, while those coated with formvar were often frozen to the carrier and got severely bent during removal. During sample recovery, titanium grids with formvar coating proved more resilient to bending and distortions. However, they often showed damage or loss of the CDM with cryo-FM imaging (example data shown in section 3.3.1).
This further confirmed that gold grids with HC coating were the best choice for this workflow in the absence of titanium grids with HC or SiO_2 coating.
One concern during sample recovery was contamination through atmospheric humidity, as sandwich disassembly takes at least 60 min from the first to the last specimen. HPF sandwiches were stored in cryo-vials directly after vitrification in groups of 4-5 specimens to reduce contamination. The carriers were then transferred to a freshly cooled-down clipping station, disassembled, and directly clipped. Contamination was then assessed by cryo-LM as described in section 3.3.1
Throughout this thesis, matrices that had been fixed and antibody-stained, as well as unfixed matrices with CNA35-EGFP live staining, were used with this workflow. No differences in sample quality could be observed, as determined by cryo-FM. Similarly, their vitrification status was similar, which was determined by cryo-TEM.

Testing cryoprotectants for vitrification optimization

Initially, I tested cryoprotectants commonly used in HPF, followed by freeze-substitution (McDonald et al., 2007). In such experiments, samples are fixed by vitrification but then still gently warmed up to RT while being dehydrated and infiltrated with resin prior to TEM. The dehydration in this process occurs at low temperatures, which preserves structures better than conventional RT resin embedding. If incomplete vitrification occurs, crystalline ice is visible in freeze-substituted samples,

although the presence of small ice crystals is potentially obscured by this method. However, crystalline ice is generally less problematic for data acquisition and interpretation in freeze-substituted samples compared to cryo-TEM samples.
Using cryo-TEM as a final readout in my workflow allowed me to assess the different cryoprotectants I tested for their ability to fully vitrify CDMs as judged by the presence of ice crystals. Introducing high molecular weight cryoprotectants to the specimens leads to additional electron scattering upon TEM imaging, which reduces the SNR and can impede the acquisition of high-quality data. Hence, I also evaluated the background of each tested cryoprotectant.
However, the usefulness of a cryoprotectant could only be judged after cryo-FIB and cryo-TEM, which resulted in a long feedback loop. This reduced the achievable throughput and did not allow for statistical analysis of the results (e.g., by repeating all experiments with either three biological or three technical replicates). The different cryoprotectants tested and assessed for the optimization of the vitrification process are outlined in Table 5.

Vitrification was graded as *Incomplete* if reflections of hexagonal ice were still visible in cryo-TEM. This was observed for most cryoprotectants to different degrees, with some resulting in larger areas with crystalline ice and others resulting in much smaller areas that still allowed for tomogram acquisition. Vitrification was graded as *Complete* if no crystalline ice could be observed in cryo-TEM.
The background was graded according to the negative effect the filler medium had on the contrast and overall visibility of cellular and extracellular structures. It was deemed as *None* if no background was added. It was graded as *Acceptable* if the contrast was reduced, but the visibility of cellular and extracellular structures still allowed for the acquisition of high-quality data. The background was graded as *High* if the filler medium rendered the structural features in the specimens hard to discern and tomogram acquisition not desirable.

The vitrification success of CDMs by HPF was first tested using cell culture medium and PBS instead of cryoprotectants as filler medium. At this point, I hypothesized that the comparatively low height of CDMs and the high sugar content of the ECM would facilitate vitrification via HPF. However, different types of cryoprotectants were tested once it became evident that CDMs frozen without cryoprotectants did not vitrify properly.

Table 5: An overview of the cryoprotectants tested as filler medium for HPF of CDMs.
The cryoprotectants and buffer of the filler medium are listed in the left column. Filler media degassed with a vacuum pump before use are marked with +. The classification of vitrification status as determined by cryo-TEM, termed incomplete or complete, is explained in the main text. The background describes the negative effect the filler medium had on the contrast and overall visibility of structures. *True for fixed and unfixed CDMs for ~50% of the frozen CDMs. **While vitrification was incomplete, tomogram acquisition and reconstruction were still possible.

Filler medium	Degassed	Vitrification	Background
Native	-	Incomplete	None
PBS	-	Incomplete	None
15% PVP in PBS	-	Incomplete	Acceptable
15% PVP in 0.1 M PB	-	Incomplete	Acceptable
15% BSA in 0.1M PB	-	Incomplete	High

Filler medium	Degassed	Vitrification	Background
20% Dextran/5% Sucrose in PBS	-	Incomplete	High
20% Dextran/5% Sucrose in PBS	+	Complete	High
20% Dextran in PBS	+	Incomplete	Acceptable
10% Dextran in PBS	+	Incomplete	Acceptable
10% Dextran in PB	**+**	**Complete***	**Acceptable**
5% Dextran in PB	+	Incomplete	Acceptable
Native	+	Incomplete**	None
10% BSA in 0.1M PB	+	Incomplete	Acceptable
20% BSA in medium	+	Complete	High

All cryoprotectants were left to incubate with the samples for 15-30 min prior to vitrification. Based on my observations, shorter incubation times of 5 min resulted in a reduced success of vitrification and more hexagonal ice reflections in cryo-TEM.
All cryoprotectants dissolved in PBS resulted in incomplete vitrification. In worse cases, reflections caused by hexagonal ice prevented tomogram acquisition as they caused errors during tilt series data acquisition. In less severe cases, tomograms could still be acquired, but single tilts had to be excluded due to reflections.
Some filler media, such as those with 20% dextran/5% sucrose or 20% BSA, introduced high background levels, obscuring ultrastructural features in the acquired tomograms. Even though both of these cryoprotectants resulted in complete vitrification, they were discarded as options for this workflow due to the high background they introduced.
As none of the standard HPF filler media led to vitrification levels that allowed for high-quality data acquisition, I decided to include a degassing step before use for HPF. I hypothesized that air bubbles introduced during filler media preparation might reduce the local pressure in the specimens during HPF. The high pressure applied to the specimen can compress gas to a higher degree than liquid. This can cause reduced pressure in the area directly surrounding gas bubbles and negatively impact vitrification. Indeed, degassing filler media improved vitrification success and was introduced as an essential step to this workflow.
Additionally, reducing ions in the filler medium by switching from PBS to PB appeared to facilitate vitrification further. The exact reason for this phenomenon is unclear, but reducing the ions in the solution might reduce the number of potential nucleation sites for hexagonal ice formation.
An image overview of the results of these tested cryoprotectants is shown in Figure 25. Overall, 10% Dextran in 0.1M PB (degassed) turned out to be the best choice for the vitrification of CDMs by HPF. It was the only cryoprotectant that resulted in complete vitrification. However, this was only the case for some specimens high pressure frozen under these conditions. Other specimens that were biological and technical replicates showed reflections stemming from hexagonal ice, although to a much lesser extent than those frozen with other cryoprotectants. Tilt series acquisition was still possible, though, and tomogram reconstruction was also successful for these specimens with partially incomplete vitrification.

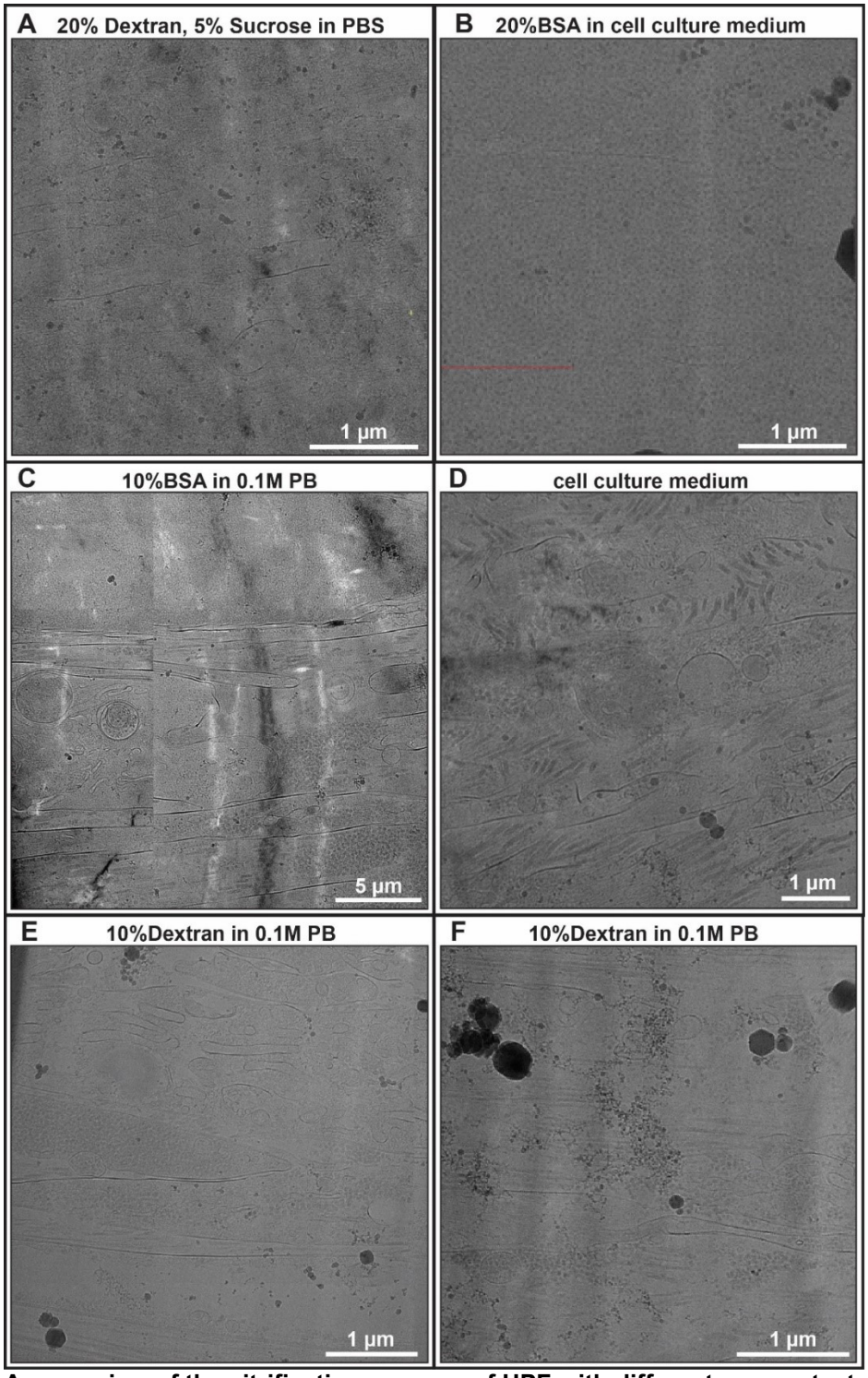

Figure 25: An overview of the vitrification success of HPF with different cryoprotectants.
A, B) Examples of cryoprotectants that resulted in a too high background to be considered useful for HPF of CDMs. Cellular and extracellular structures are not or only barely distinguishable. A) 20% Dextran/5% Sucrose in PBS resulted in incomplete vitrification. Over small areas, reflections stemming from hexagonal ice crystals were visible. Moreover, the background introduced to the sample by the cryoprotectant obscured biological structures. B) 20% BSA in cell culture medium (degassed) resulted in complete vitrification. No reflections were caused by hexagonal ice. However, the background introduced to the sample is too high to discern any biological structures. C, D) Examples of cryoprotectants that resulted in incomplete vitrification. Cellular and extracellular structures are still visible, but reflections caused by hexagonal ice hamper data acquisition. **Figure legend continued on next page**.

C) 10%BSA in 0.1M PB (degassed) resulted in incomplete vitrification with severe reflections over large areas of the lamellae. Biological structures were still discernable but the reflections hampered data collection and tomogram reconstruction. D) The use of cell culture medium (degassed) without added cryoprotectants resulted in incomplete vitrification. Mild reflections caused by hexagonal ice covered several small areas of the lamellae. Data acquisition and tomogram reconstruction were still possible. The contrast was very high as no background was introduced to the sample by a cryoprotectant. E, F) Examples of a cryoprotectant that resulted in complete vitrification. 10% Dextran in 0.1M PB (degassed) was the only tested cryoprotectant that achieved complete vitrification in at least a portion of frozen specimens. In those specimens that were incompletely vitrified, only mild reflections were seen, and data acquisition was still possible.

Interestingly, a high portion of CDMs that had been fixed prior to HPF was entirely vitrified when frozen with 10% Dextran in 0.1M PB (degassed). In contrast, only a smaller portion of CDMs that were frozen completely natively were entirely vitrified (less than one-third). Notably, 10% Dextran in 0.1M PB did not introduce a high background and thus was deemed the best of the tested cryoprotectant for CDMs.

3.3. Cryo-Correlative Focused Ion Beam milling

3.3.1. Quality control and target identification by cryo-CLEM

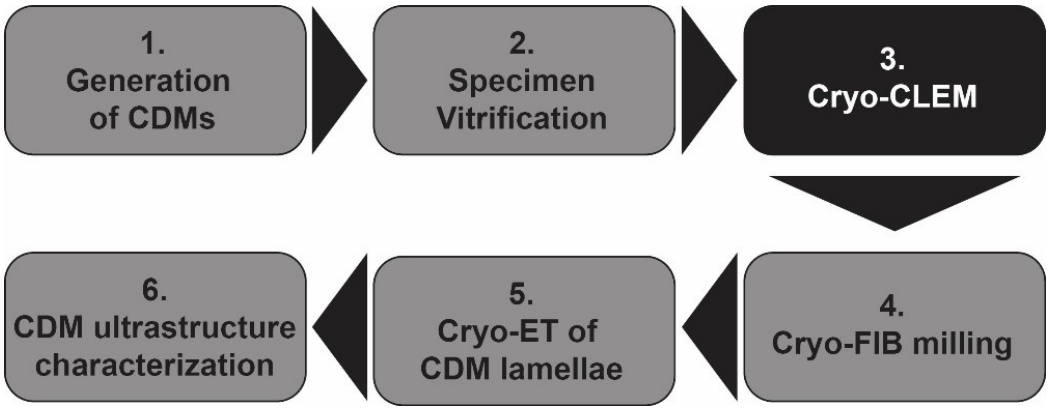

Cryo-light microscopy was integrated into the workflow designed for this thesis for two purposes:

1) To assess the quality of CDMs after vitrification and ensure that only high-quality specimens are used in subsequent steps.

   Imperfectly assembled HPF carrier sandwiches can result in damage to or loss of the CDMs. It is vital that only high-quality specimens without significant damage to the CDM are used in cryo-FIB milling. Cryo-FIB milling is a time-intensive sample preparation step, and the choice of specimens is essential for the success of this process.

2) To identify regions of interest (ROIs) and landmarks in high-quality specimens for targeted sample thinning via cryo-FIB milling by cryo-CLEM.

   HPF samples are bulk samples with few or even no discerning landmarks. The use of cryo-FM allows the identification of ROIs in the sample that contain the structures of interest, such as fiber-rich and undamaged regions of CDMs.

To fulfill these goals, a Leica cryo-CLEM system was employed. The system was installed at ISTA in November 2018. As the sole user of this instrument after its installation, I was mainly responsible for its establishment for biological samples. The EMF provided technical support during this process. This process included repeated optimization of the microscope operation and data acquisition. I also provided feedback to the manufacturer to fix bugs and inconsistencies in the system.

During my Ph.D. thesis work, I established a workflow for whole-grid tile scans and data export for subsequent cryo-CLEM:

1) For more straightforward correlation in subsequent steps, all specimens are loaded into the Leica cryo-CLEM specimen shuttle with the FIB-milling window of the AutoGrid™ facing up. This way, it can be ensured that the general orientation for correlation is identical for all specimens.

2) The fluorescence channels for imaging are chosen accordingly. All CDMs have been stained using either a fibronectin I antibody or CNA35-EGFP live staining prior to HPF.
   Additionally, reflected light and transmitted light are chosen for imaging.

3) Two options in the Leica software LasX allow the acquisition of a tile scan of the whole grid: The Matrix Screener and the LasX Navigator. The LasX Navigator is recommended for this workflow.

   Both options were tested thoroughly for the acquisition and export of whole grid tile scans. The LasX Navigator was consistently stable, while the MatrixScreener regularly crashed the LasX software and made frequent restarts of the software and, in some cases, even of the computer necessary. This often necessitated the repeated acquisition of the same specimen.
   Moreover, the LasX Navigator was much more adaptable when choosing a focusing strategy and exporting data, allowing for the most common file formats, such as JPG and TIFF, with or without data compression. In contrast, the MatrixScreener followed a strict workflow and allowed export only in specific formats such as MAPS and LeicaXML. It necessitated using screenshots to save the acquired data in JPG or PNG format for easy visualization for documentation, which is incompatible with a proper scientific workflow.

4) The stage is moved to the center of the grid, indicated by a center mark. From here, a spiral scan is done to image the entirety of the grid

   Once this has been done, the center position for the EM grid can be marked as a fixed position on the control panel of the microscope. The positions of the grid within the cryo-CLEM shuttle and the shuttle within the microscope are fixed. Thus, once the center position is marked, it can be used for all subsequent specimens to facilitate the identification of the grid center.
   Similarly, all grids have the same diameter. Once the outer margins of the grid are known, they can also be used for subsequently imaged specimens for faster tile scan acquisition.

5) A circular pattern is placed over the specimen to cover its surface, including the surface of the AutoGrid™. Typically, the Leica cryo-CLEM requires a circular pattern consisting of at least 109 tiles.

6) A focus map is then defined prior to imaging. Focus points are set over the whole area of the specimen every second to third tile. Ideally, they are set at a higher density at every or every other tile at positions of high importance. One of these positions is the recess for cryo-FIB milling of the AutoGrid™ to aid correlation. The other is the center of the grid, ranging out to ~1.5 mm, which is typically a better target for cryo-FIB milling than outer regions.

7) There are two options to acquire the focus position for each set focus point: The autofocus function or manually setting up focus points. For HPF samples, I recommend setting the focus points up manually.

The autofocus function allows setting a z-range over which a focus will be searched in one defined channel (e.g., a range of 100 µm in the GFP channel). The CDM and upper rim of the AutoGrid™ have a distance in z of ≥150 µm. Thus, a high z-range would be required to cover both surfaces, increasing the time required for the auto-focus operation.
Different channels are required to find the ideal focus for CDM and AutoGrid®, which is impossible with this function. Moreover, the autofocus function often does not work on the CDM regions, and focus points have to be manually redone. This results in a second acquisition of a whole-grid tile scan for higher quality data, thereby doubling the time needed for a single sample.
Setting each focus point manually requires more time before image acquisition, but any channel and a wider z-range can be employed. Typically, manual focusing has higher accuracy, and a single tile scan acquisition is sufficient. Thus, manual focusing requires more user input but reduced acquisition time and increased data quality.
Based on this, manual focusing for HPF specimens is highly recommended.

8) After placing focus points along the rim of the AutoGrid™ and the CDM, the automatic tile scan acquisition is started. The acquisition takes around 15 minutes for a tile scan of ~109 tiles in 2 channels if the focus points have been set manually. A tile scan of the same size with the autofocus function and a range of ~100 µm requires around 30 minutes.

   Typically, 8-16 specimens can be screened in a single day, depending on the user experience.

9) The single tiles are then merged into one overview image. The single channels and the merge of all channels are exported in TIFF format with 60% size compression and JPG format without size compression.

   Different file formats were tested. Size compression of 60% for TIFF format files results in smaller, more manageable files that still have a high resolution and separate color channels (~60 MB compared to 1 GB). In most cases, even for correlation, uncompressed JPG format files are preferable due to their smaller size while maintaining sufficient detail (~1.2 MB).

The general state and quality of each CDM were determined by fluorescence microscopy to visualize the fiber network. This also allowed the assessment of any damage the specimens might have suffered during HPF. Specimens with damaged CDMs were removed from the sample pool (see Figure 26). Initial attempts using CDMs grown on sapphire discs showed a high rate of partial or complete sample loss, further demonstrating the low compatibility of sapphire discs for this workflow.

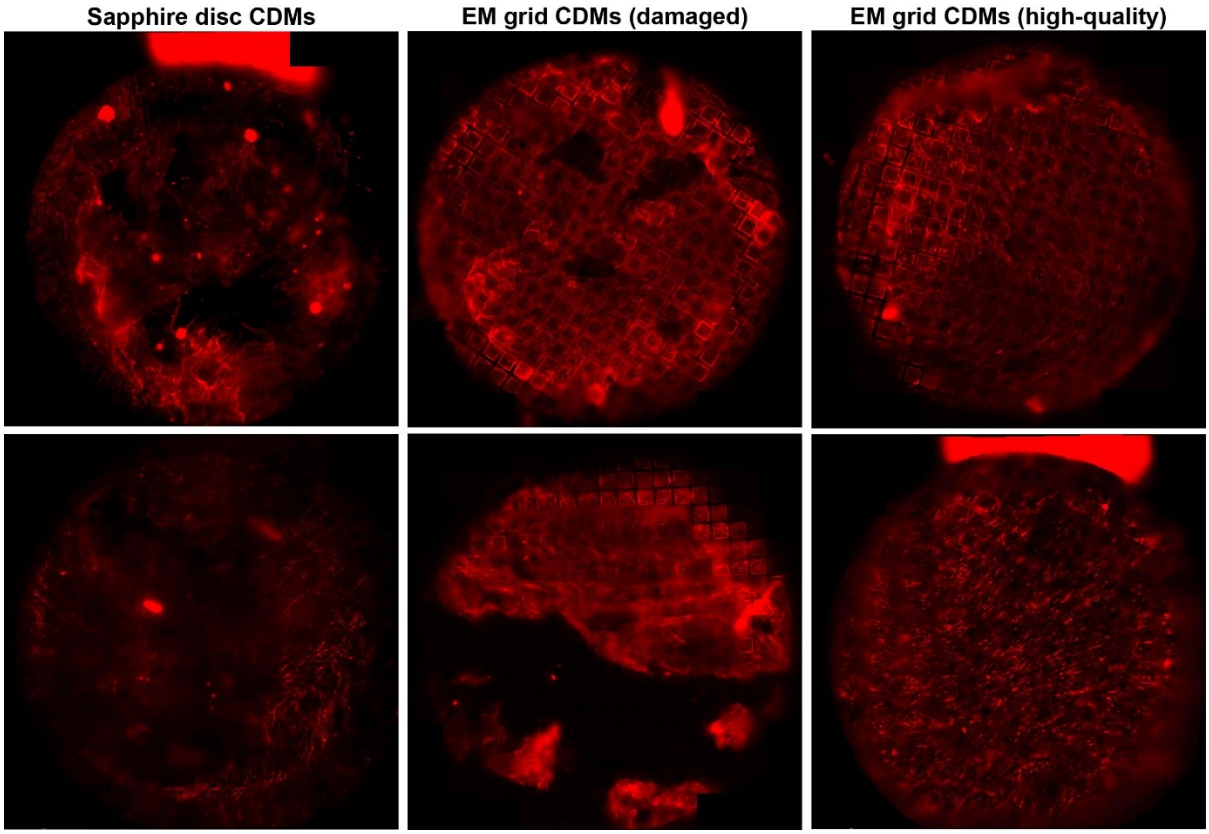

Figure 26: Quality assessment of d14 TIFF CDMs after HPF by cryo-FM.
All CDMs shown here have been stained for fibronectin I via antibody staining. The quality of each specimen was determined by assessing the overall damage to the CDM. CDMs that showed an even signal of discernable ECM fibers throughout the EM grid surface were deemed intact. Those that showed a lack of fluorescence signal in several small regions or one big region were deemed damaged. Moreover, if CDMs did not display discernable ECM fiber staining, they were also deemed as damaged. CDMs grown on sapphire discs (left column) showed a higher rate of severe damage and sample loss after HPF. Damaged CDMs grown on grids (middle column) were removed from the specimen pool. High-quality CDMs grown on grids (right column) showed little to no damage to the CDM and a fiber network resembling confocal images obtained prior to vitrification.

Reflected light allowed the visualization of the AutoGrid™ surface, grid bars, and even very fine surface contamination. In contrast, transmitted light could only visualize grid bars and contamination but could not be used to image the AutoGrid™ surface (Figure 27). Due to this, reflected light was used in combination with fluorescence microscopy to assess sample quality and remove any specimens with high amounts of contamination that could interfere with cryo-FIB milling, as explained in section 3.3.2

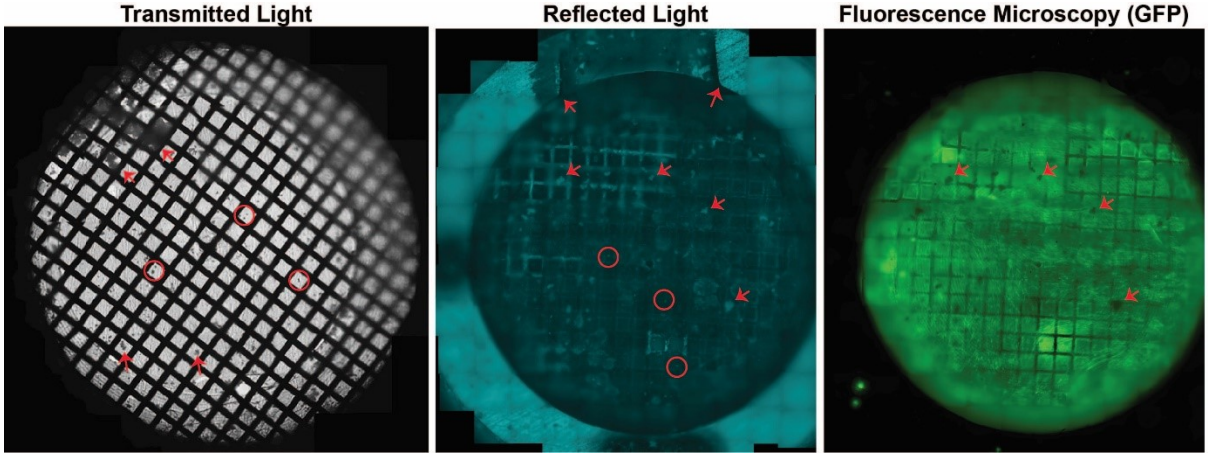

Figure 27: A comparison of transmitted light microscopy, reflected light microscopy, and fluorescence microscopy on high pressure frozen CDMs.
D14 TIFF matrices were high pressure frozen and imaged with a Leica cryo-CLEM system. Transmitted light microscopy (left panel) and reflected light microscopy (middle panel) reveal ice contamination on the specimen surface. Big ice crystals (examples indicated by red arrows) are visible in transmitted light, reflected light, and fluorescence microscopy. Smaller ice crystals (examples indicated by red circles) are only visible in transmitted and reflected light microscopy. Only reflected light microscopy reveals the rim and recess of the AutoGrid™ (indicated by the top two red arrows).
The transmitted light image (left panel) was not taken from the same specimen as the reflected light and fluorescence image (middle and right panel, respectively). The specimens displayed here show only low amounts of contamination.

The use of reflected light also helped identify landmarks for cryo-CLEM. HPF of CDMs results in a bulk sample with no discernable landmarks if the specimen is not damaged during the HPF carrier assembly, which is the ideal case scenario. Instead, the topology of the AutoGrids™ dedicated to FIB-milling was used for landmarks: The window-recess of these AutoGrids™ has precise edges visible in both reflected light microscopy and SEM and can be used for coarse correlation (see Figure 28).
All high-quality CDM specimens were imaged by reflected light microscopy and fluorescence microscopy to identify at least two landmarks and appropriate ROIs for ion beam milling (see Figure 28). Typically, these high-quality samples were not limited to small ROIs, as for good samples, the whole inner diameter of the specimen showed CDM fibers and no sample damage. In these cases, only exemplary ROIs were identified for easier targeting and to avoid grid bars where necessary.
The potential introduction of additional contamination was the main downside of sample screening by cryo-FM prior to cryo-FIB milling. This risk was mitigated as much as possible by using standard protective measures such as employing a face shield and working in a humidity-controlled room. Overall, the screening speed at the cryo-CLEM system was much faster than at a cryo-FIBSEM, and the gathered data allowed for a better sample quality assessment. Using only high-quality CDMs for downstream processing was essential for acquiring high-quality data.

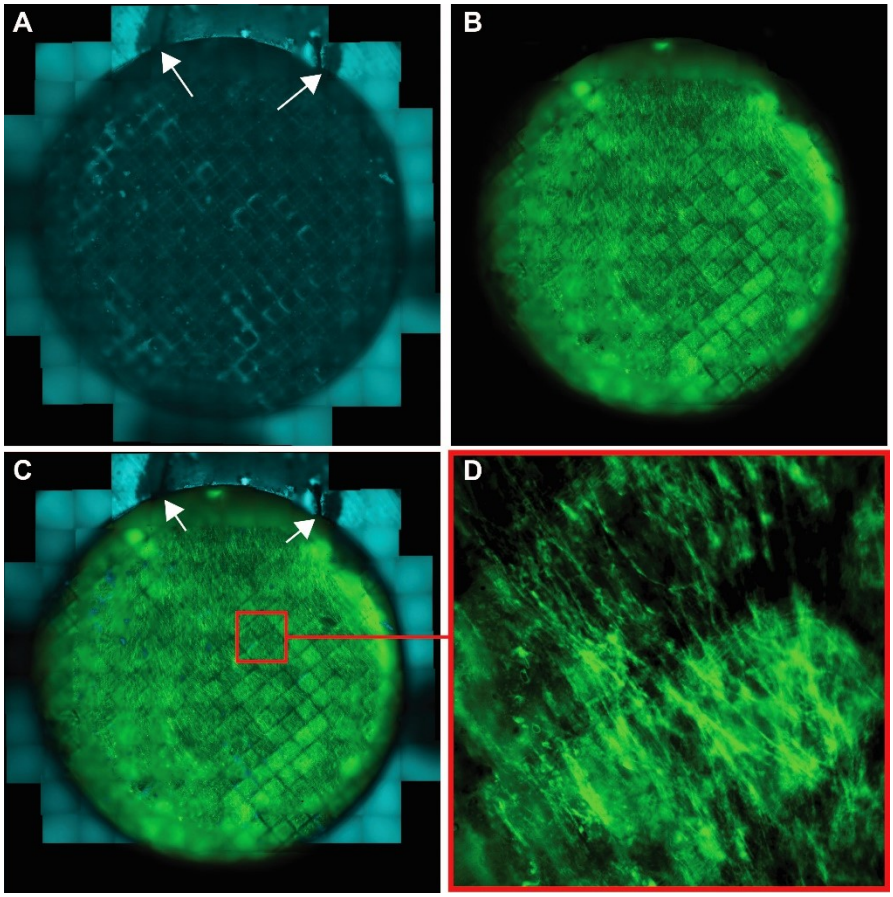

Figure 28: A high-quality D14 TIFF CDM after HPF imaged by cryo-FM.
A) Reflected light microscopy allowed the identification of landmarks, where the edges of the FIB milling window in the AutoGrid®, indicated by white arrows. Only low amounts of contamination were detected on this specimen. B) Fluorescence microscopy revealed a high-quality CDM with no damage and clearly visible collagen fibers stained with CNA35-EGFP. C) The merged image of A and B. An ROI is marked in red, although the whole inner diameter of the sample can be considered as ROI here. D) A maximum projection of a z-stack taken in the ROI marked in red in C). Single collagen fibers are clearly visible, similar to their appearance in confocal microscopy.

The correlation precision achievable by using the recess window edges as landmarks was sufficient to target regions of interest, i.e., regions of undamaged CDM with visible fibronectin I or collagen fibers. For this workflow, there is no need for high-precision correlation. Hence, no further optimization for this took place.
With the application of the workflow established in this thesis to other specimens, such as tissues or organoids, the correlation step will be of even greater importance to target cryo-FIB milling to rare structures and events. To this end, additional markings can be manually etched into the AutoGrid™ rim to increase the number of landmarks for rough correlation, further facilitating this process. Additionally, the recently introduced FinderTOP carriers can be used (De Beer* et al., 2022). These FinderTOP carriers have a matrix with letters and numbers engraved on their flat surface, which is imprinted on the specimen surface during HPF. These imprints are visible in both reflected light and in the SEM and can be used to increase correlation precision further.

3.3.2. Sample thinning by targeted cryo-FIB milling

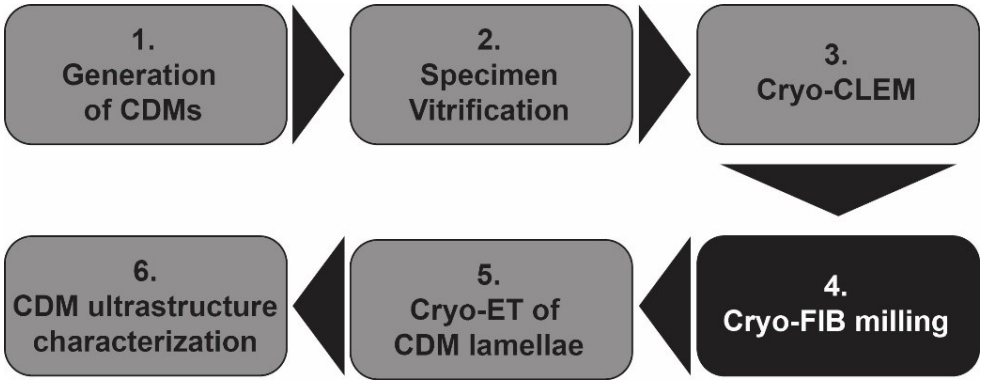

The process of sample thinning to render vitrified CDMs amenable to high-resolution cryo-ET was a crucial part of the design of the workflow introduced in this thesis. Currently, there are only two options to achieve this goal under cryogenic conditions: CEMOVIS and FIB milling.
CEMOVIS has the advantage that it allows the screening of multiple consecutive sections of the same sample, thereby covering a large area and volume. However, it is known to introduce artifacts, such as distortions and compressions of up to 20-45% in the cutting direction, depending on the sample composition and sectioning technique (Al-Amoudi et al., 2005, 2004, 2003).
In contrast, cryo-FIB milling produces small lamellae of around 15 x 10 µm (150 µm²) and a thickness of ~200 nm, and the final size strongly depends on the sample morphology. Importantly, cryo-FIB milling has been shown to introduce virtually no artifacts during sample thinning (Marko et al., 2007, 2006; Wagner et al., 2020). Cryo-FIB milling is still a relatively young and not yet fully explored technique but is increasingly applied to biological samples in combination with subsequent cryo-ET (Schaffer et al., 2019, 2017; Wolff et al., 2019).
I decided to employ cryo-FIB milling for sample thinning in my designed workflow in order to retain the native *in situ* structures without the introduction of artifacts.

My main aim for this step in the workflow was to create high-quality cryo-lamellae compatible with cryo-ET. This necessitated these lamellae to have several properties:

1) The lamellae had to be thin enough for unrestricted cryo-ET, so I aimed for a final thickness of around 200-250 nm. Thinner lamellae are better suited for high-resolution tilt series acquisition and have better contrast but cover much less cellular. For the ultrastructural characterization of ECM, thinner lamellae would provide less cellular context and would therefore be unfavorable.
2) The lamellae had to be resilient enough to stay intact during the transfer from the cryo-FIBSEM to the cryo-TEM. Ideally, they should stay intact without cracks or breaks occurring before or during transfer.
3) The lamellae had to be of sufficient quality and size. This meant they needed to be wide and long enough to allow the acquisition of at least six tilt series per lamellae, i.e., around 10x10 µm at least. Additionally, they should not show beam damage, severe curtaining effects, or gallium embedding. I initially aimed to create 2-3 lamellae per session or, if this should prove impossible, one large lamella.
4) The lamellae had to contain relevant extracellular structures of the ECM.

To this end, a TFS Aquilos system was employed, which was installed at ISTA in December 2018 and later upgraded to its second generation (Aquilos II) in December 2020. The xT user interface software (TFS) was used to operate the microscope. As the sole user of this microscope for the first year, I was responsible for its establishment in combination with biological samples under cryo-conditions. In addition to developing and optimizing FIB milling workflows for different types of samples, I also provided feedback to the manufacturer and the EMF to fix issues that arose with the system. The EMF provided technical support throughout this process.
The upgrade to the Aquilos II opened the possibility of cryo-lift out FIB milling. Here, I was again the sole user for the lift-out technique on biological specimens and was responsible for establishing a routine lift-out workflow and communicating with the manufacturer with the technical support of the EMF.

Hence, given the upgrade process of our dual-beam system, two approaches for the generation of thin lamellae compatible with cryo-ET were employed:

1) Initially, cryo-FIB milling of bulk samples by adapting the standard FIB milling workflow to high pressure frozen CDM specimens.
2) Later, the cryo-lift-out technique with subsequent sample thinning on a separate grid.

3.3.2.1. Cryo-FIB milling of bulk samples

As described in previous sections of this thesis (3.2.1, 3.2.2, and 3.3.1.), TIFF CDMs for bulk milling approaches were decellularized, plunge-frozen, and subsequently screened by cryo-FM to select high-quality specimens for sample thinning.
To this end, I adapted standard protocols for cryo-FIB milling single mammalian cells to CDM specimens. These standard protocols had been demonstrated to me during the Aquilos I application training given by TFS and by Alicia Borgeaud (research group of Wanda Kukulski, LMB Cambridge/University of Bern).

Overall, the process of FIB milling of bulk samples can be divided into three stages:

1) **Preparatory steps for FIB milling**
2) **Preparation of the lamella site**
3) **Lamella generation from bulk samples**

1. <u>Preparatory steps</u>

1.1. Cooling down and specimen loading: The Aquilos I (TFS) is cooled down 40-60 min before use. Temperature sensors at the cryo-stage and the cryo-shield report the current temperature at any given time. Once both temperatures are below -190°C, the samples can be loaded. Then, SEM overview images are taken prior to any coating steps.

The xT user interface software used to operate the instrument requires the input of the distance between the sample and the SEM column, the free working distance (FWD). This is done by linking the Z-height of the stage to the FWD by pressing the designated "Link Z to FWD" button in the software. After linking, the distance between the SEM column and the sample is reflected in the Z

coordinate given for the stage. Without this FWD input, the stage can only be moved with restrictions to protect the SEM column from damage by stage touch. *When the stage is in its standard rotation (loading rotation), the scanning rotation of SEM and FIB view is set to 180°in the software. The scanning rotation denotes the image rotation on the screen and can be adjusted for a more intuitive and natural view for the user. This scanning rotation of 180° is used throughout the FIB milling process described here.*

1.2. **Correlation and ROI identification:** SEM overview images are then correlated to the previously acquired cryo-FM images, employing MAPS software, version 3.14 (TFS) (see Figure 29). ROIs are identified based on cryo-CLEM and marked as potential lamella sites. These ROIs are regions with undamaged CDM as determined by fibronectin I or collagen I staining. Moreover, they are located centrally on the grid and grid squares. Large ice crystals below the platinum coating can dislodge during milling and damage the protective coating. Moreover, they can result in strong curtaining effects on the final lamellae and are thus avoided whenever possible when choosing ROIs.
Per specimen, ~3-4 potential lamella sites were chosen.

A rough correlation is possible using 2-3 visible landmarks in both SEM and cryo-FM. Typically, these landmarks can be broken grid squares where available. Ideally, the chosen landmarks should be far apart to allow for better correlation results.
Platinum coating can obscure smaller landmarks such as flat, topological features of the sample or contamination crystals. The correlation efficiency can be increased using the SEM overview image taken prior to GIS coating for CLEM.
This selection of potential lamella sites based on cryo-CLEM ensures that lamellae contain relevant CDM structures. Choosing lamella sites located centrally on the grid allows the use of flat milling angles of ~17-20° stage tilt, resulting in a lamella pre-tilt of ~10-13°. Importantly, by choosing lamella sites located centrally on grid squares, grid bars that would hamper the milling process significantly can be avoided during the milling process. Large ice crystals below the platinum coating can dislodge during milling and damage the protective coating. Moreover, they can result in strong curtaining effects on the final lamellae and should be avoided whenever possible.

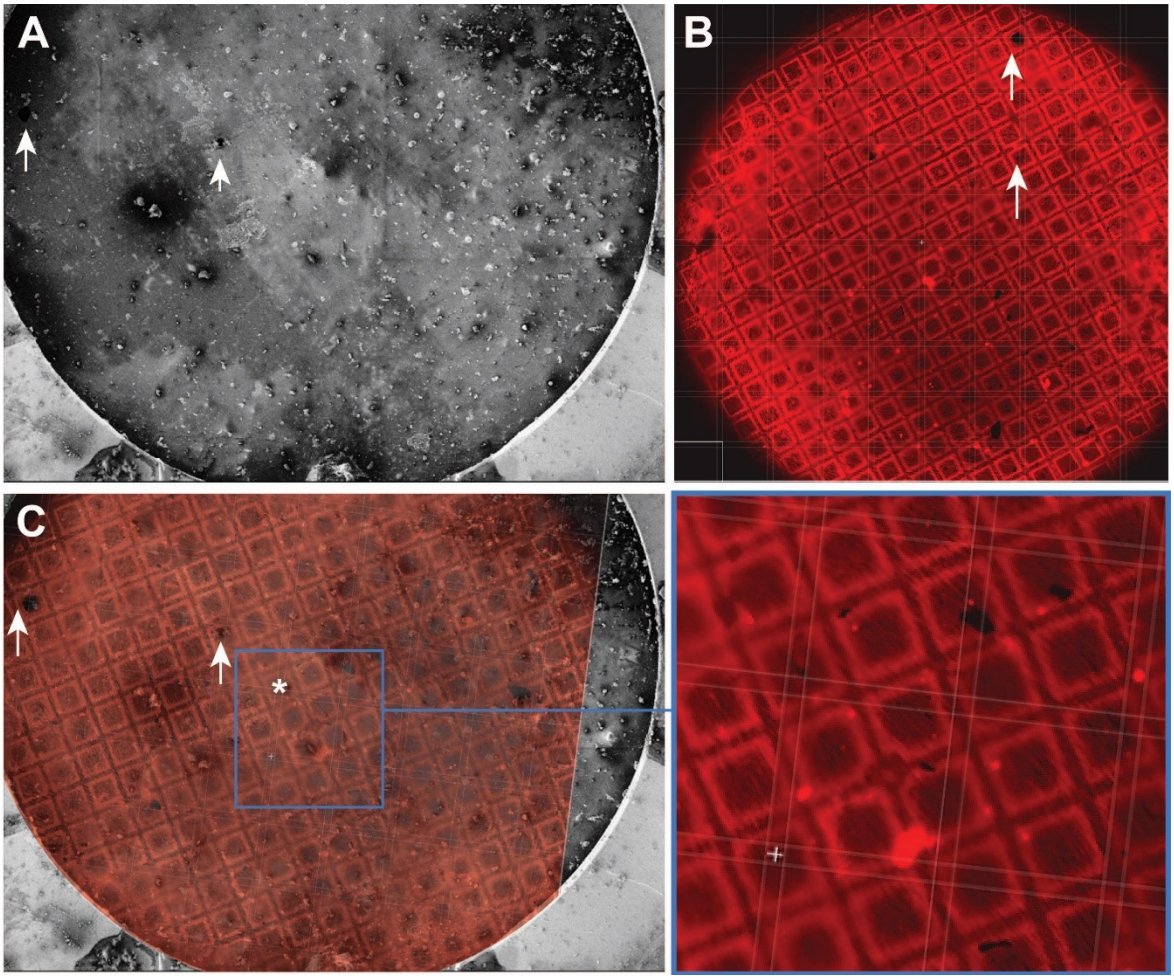

Figure 29: Cryo-CLEM on a TIFF CDM bulk specimen.
A) SEM overview image before GIS coating. Two broken grid squares were used as recognizable landmarks and are indicated with white arrows. Grid bars are not visible, necessitating CLEM to identify potential lamella sites. B) The same specimen as in (A), imaged by cryo-LM. This specimen shows no grid distortions or damage to the CDM, and fibronectin I fibers are visible throughout the grid. The landmarks used for correlation are indicated in (A) with white arrows. C) Correlated SEM and FM images, using the TFS MAPS software employing the annotated landmarks. A white asterisk annotates the targeted area for ion-beam milling. D) Magnified view of the ROI surrounding the defined lamella side (blue box in Panel C), showing the fibronectin I fibers visualized by cryo-FM.

1.3. **Coating**: Specimens are coated with a ~1-1.5 µm layer of organometallic platinum using the GIS system, with the EM grids in the standard deposition position. Another SEM overview image of the specimen is taken after GIS coating

The coating time needed to get a coating of 1-1.5 µm platinum was tested over several rounds on different samples and was found optimal at 20 seconds.
The positioning of the GIS system with respect to the stage was set at the specified standard distance by TFS in our Aquilos I instrument. Upon the upgrade to the Aquilos II, the distance of the GIS system relative to the sample changed, which caused changes in the coating times, as described in section 3.3.2.2. The exact GIS coating time required to create an optimal platinum coating depends on the distance of the GIS to the sample. It, therefore, has to be defined for every individual system and upon any change of this distance.
The application of a sputter coating prior to GIS coating was tested in initial

trials, as recommended by TFS. However, no difference between sputter-coated and non-sputter-coated samples in overall sample charging or lamella behavior during milling could be observed. Thus, this step was removed from this milling protocol.

1.4. **Eucentric height determination:** Eucentric height and the milling angle are determined for each potential lamella site using the MAPS software. Eucentric height should be at a z-height (FWD) of around 7 mm for each site, but this varies slightly depending on the exact position on the grid. The milling angle is chosen to be as flat as possible without incurring interference to the FIB by the rim of the AutoGrid™. Where possible, a milling angle of 17° is chosen.
The exact desired lamella position is then defined at eucentric height. As stated, both SEM and FIB imaging should be centered on the same feature to allow for proper monitoring of the milling progress.

Eucentric height in dual beam FIBSEM instruments is also the coincidence point for SEM beam and FIB. Hence, points of interest can be identified in SEM, and once the sample is at eucentric height, they should also be centered in FIB imaging.
However, depending on the position of the lamella site on the grid and the accuracy of the set eucentric height, the ROI might initially not be fully centered in both SEM and FIB view. This, together with the different imaging angles of SEM and FIB, makes it necessary to manually adjust the center of the FIB beam by beam shift. Using small landmarks such as contamination points as landmarks facilitates this process.
This process can be facilitated by starting at higher stage tilt angles of ~30°, as higher tilts typically allow for easier recognition of small landmarks for orientation. By gradually lowering the stage tilt to the final milling angle, the defined site can be tracked and marked by placing a non-milling pattern on it.

Typically, 4-6 lamellae can be milled per grid in a single session when working with isolated adherent cells. CDM specimens have more bulk and exceed the size of single cells in all dimensions. This results in more material that has to be removed to create thin lamellae. Moreover, I expected the lamellae to be longer, resulting in longer milling times. Based on this, I assumed that I would only be able to produce 2-3 CDM lamellae in a single session.

2. <u>Preparation of the lamella site</u>

Throughout the process of FIB milling, its progress is observed by live FIB imaging to judge whether all bulk material within a milling pattern has been removed. SEM imaging is simultaneously used to judge the state of the lamella and its protective coating. Upon the complete removal of the protective coating at even a single site of the lamella or damage to the lamella, the milling process was stopped.
All FIB milling patterns used in this protocol are rectangle-shaped milling patterns with their milling direction set toward the sample.

2.1. **Trench milling at 35° stage tilt:** In the first step, two trenches are milled at a high tilt angle of 35°. Rectangle-shaped milling patterns with a width of 25

µm are placed above and below the lamella position with a spacing of ~25 µm between them at a stage tilt of 35° (see Figure 30). These patterns are FIB milled with a current of 3 nA until all bulk material is removed, as assessed by FIB imaging.
At the same time, micro-expansion joints are milled on either side of the lamellae with a distance of ~10 µm to counteract any stress that might lead to lamella bending or breakage, as reported previously (Wolff et al., 2019).

Initial attempts to proceed with sample milling without creating trenches at higher tilt angles did not work out. Even prolonged milling times did not fully remove the bulk material due to the length of the lamella. Moreover, it was difficult to judge whether all bulk material had been removed below the created lamella. The lamella is shortened to a reasonable length by cutting trenches, making it easier to judge its state (see Figure 30 for lamella geometry explanation).
In hindsight, I believe that higher milling currents of up to 7 nA could have been tested for this step to lower the milling time. Moreover, trench milling at an orthogonal angle between the sample and the FIB, as employed in the lift-out technique, could have further reduced the milling time and led to better results.

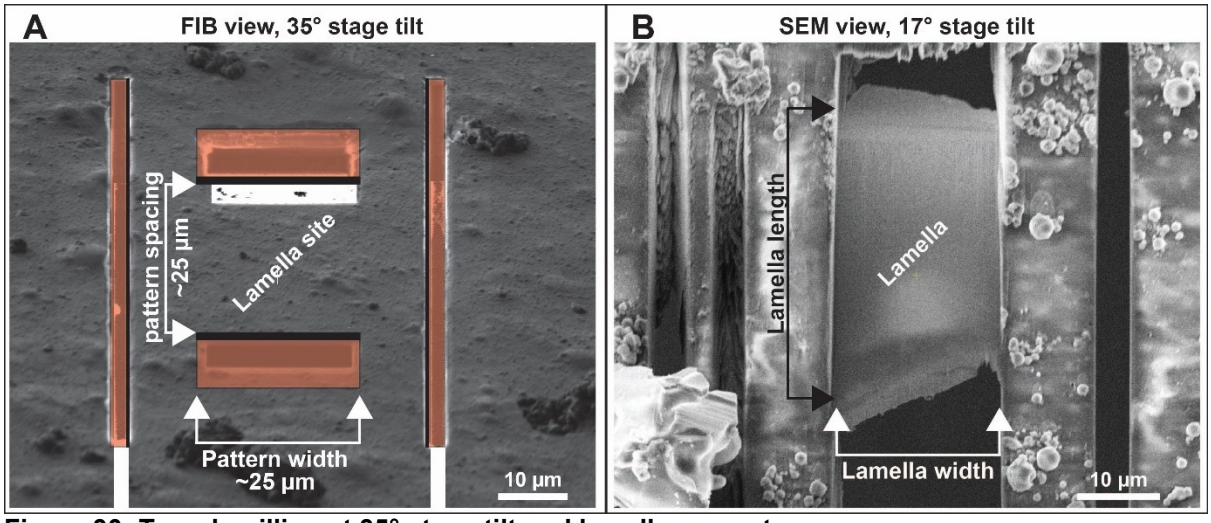

Figure 30: Trench milling at 35° stage tilt and lamella geometry.
A) FIB view. At a 35° stage tilt, rectangle patterns are placed with a pattern spacing of ~25 µm and a pattern width of ~ 25 µm above and below the lamella site. This shortens the final lamella length and facilitates bulk milling. Patterns for micro-expansion joints are placed on either side of the lamella site at a distance of 10 µm. The milling direction of all patterns is set toward the lamella site (indicated by a strong black line). B) SEM view. At 17° stage tilt, the rough milled lamella was imaged to assess its integrity. Lamella width is determined by the pattern width chosen. Lamella length is determined by the pattern spacing during trench milling.

2.2. **Trench milling at 25° stage tilt:** After lowering the stage tilt to 25°, the milling patterns are set to be 12 µm apart, and more bulk material is removed with 3 nA.

As in the previous step, milling at a higher angle allows faster removal of bulk material and further helps to shorten the lamella.

2.3. **Trench milling at 17-20° stage tilt:** The stage tilt is lowered to the final milling angle between 17-20° stage tilt, and the milling pattern distance is reduced to 5 µm. Bulk material is removed with a milling current of 1 nA.

It is crucial to ensure that all bulk material has been removed below the lamella. This can only be confirmed by FIB imaging due to the angles of the two imaging beams relative to the sample. Here it helps to tilt the sample to higher and lower degrees and use FIB imaging to facilitate the visual assessment. The next milling steps were performed only once no bulk material was present above or below the lamella.

3. Lamella generation from bulk samples

Once the lamella site has been prepared by the trench milling described above, it should be more accessible for further sample thinning. The lamella length has been limited by the trench placement, facilitating subsequent milling steps. The final lamella width is determined by the pattern width chosen during the subsequent FIB milling steps.

3.1. Rough milling:

The pattern width is reduced to ~20-17 µm, and the spacing between the patterns to 3 µm, see Figure 31. Bulk material is removed with a milling current of 1 nA.
Then the pattern width is reduced by 1 µm, and the pattern distance is lowered to 2 µm. Bulk material is removed with a milling current of 0.5 nA.
In consecutive steps, the pattern width, distance, and milling current are reduced sequentially, as shown in Figure 31.

The reduction in lamella width for each milling step resulted in a step-like anchor of the final lamella to the remaining bulk sample.

In initial FIB milling trials with single cells, this step-like anchor seemed to decrease the likelihood of lamella breakage and loss during sample transfer from the FIBSEM to the TEM. As only a few lamellae were milled without the step-wise lowering of the lamella width, no statistics can be given. However, based on my early observations and the standard milling protocols I was introduced to, I decided to include this step-like anchor in the protocol.

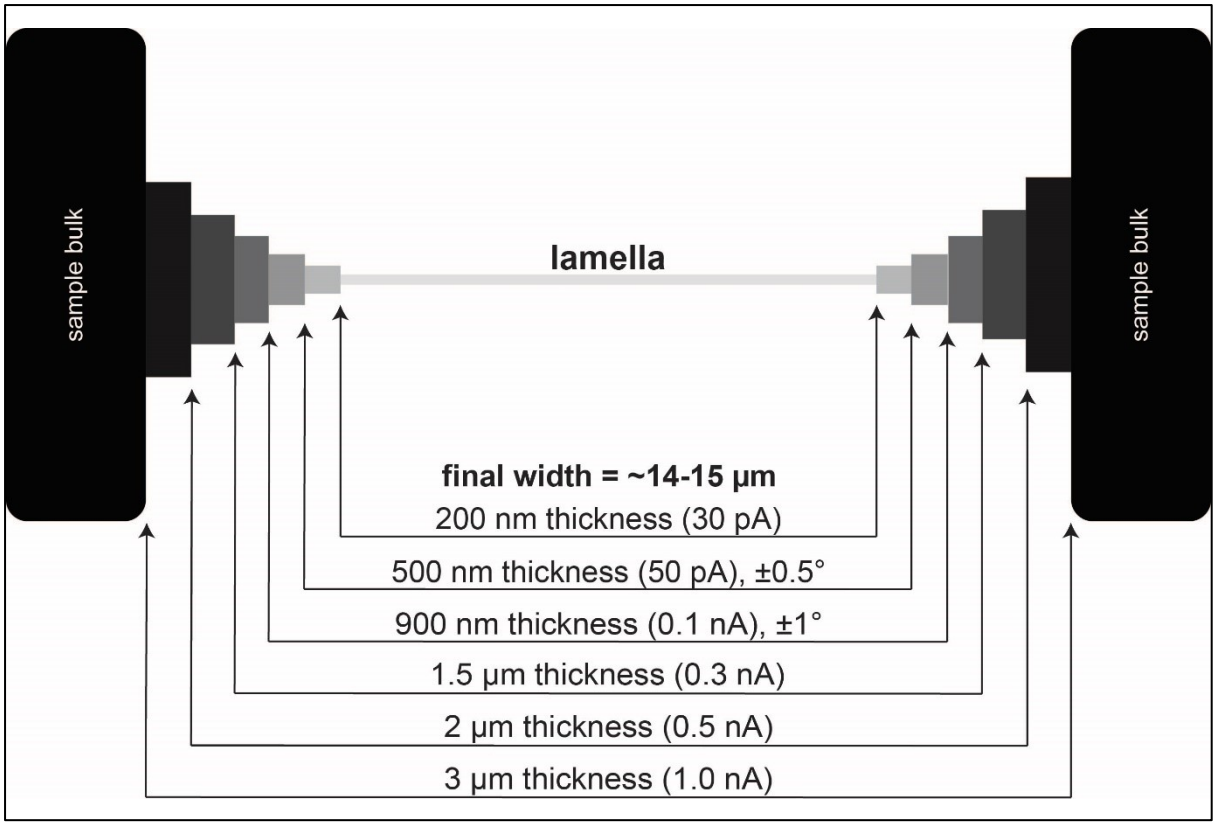

Figure 31: FIB milling scheme for lamellae.
This scheme shows the milling scheme employed after trench milling on bulk CDM specimens. The lamella width was reduced step by step to create a stable anchor for the final lamella. Both milling current and pattern distance were reduced for each milling step, as depicted above. At the end of rough milling, when lamella thickness reaches 900 nm, the stage is tilted by ±1° to remove excess thickness at the far end of the lamella. This step is repeated after the first fine milling step at 500 nm thickness by tilting the lamella by ±0.5°.

3.2. **Removal of excess thickness**: Once a lamella thickness of 900 nm is reached, the stage is tilted to ±1° to reveal and remove the excess thickness at the back end of the lamella. This assures a relatively even thickness of the lamella throughout its whole length.

This excess thickness typically occurs in all lamellae. It is neglectable for very short lamellae but should be evened out in longer lamellae to ensure that the whole lamella length can be used for cryo-ET. This effect is caused by the inherent Gaussian profile of the ion beam (Schaffer et al., 2017).
This excess thickness can be visualized in FIB imaging by over- and under-tilting the stage relative to the chosen milling angle and adjusting brightness and contrast.

Typically, these **rough milling** steps are done for all potential lamella sites before proceeding with the so-called **fine milling**. This significantly reduces the time water vapor condenses on final lamellae, leading to contamination and adding to their thickness. This contamination rate is measured for each instrument individually and depends on the vacuum achieved in the main chamber. Technological improvements in hardware resulted in an improved vacuum and a reduction of contamination in

available instruments over the last few years. According to our EMF, the contamination rate in the TFS Aquilos II at ISTA has been measured to be ≤5 nm/h.
When bulk milling CDM specimens, setting up ROIs and rough milling takes ≥10 h if successful at all; thus, typically, no second lamella site is prepared due to time constraints. Instead, the rough milling was immediately followed up with fine milling. During fine milling, the lamella and its protective platinum coating were continuously checked by SEM to survey the lamella state.

3.3. Fine milling:

The stage is set to the original tilt angle, and the pattern width is reduced to ≤14 µm with a pattern spacing of 500nm. Bulk material is removed with a milling current of 50 pA. Subsequently, the stage is tilted ±0.5° to remove the excess thickness at the far end of the lamella.
The stage is returned to its original tilt angle, and the pattern width is reduced to ~10-12 µm. The pattern spacing is set to 200 nm, and a milling current of 30 pA is used. The single steps are shown in Figure 31.

Milling is stopped once the protective platinum layer gets too thin or the lamella took damage (see Figure 32 for examples). Subsequently, the specimen is removed from the instrument and stored before subsequent cryo-TEM imaging.

Results of bulk milling of D14 TIFF CDMS

Initially, plunge-frozen D14 TIFF CDMs were used for these bulk milling attempts. The specimen proved very challenging for this approach as the time needed to complete each milling step was higher than anticipated. Even after ≥14 h, rough milling could not be completed. In all cases, the protective platinum coating and the lamella were damaged before the completion of rough milling. Moreover, in most cases, the bulk material below the lamella could not be removed within a single session (see Figure 32, Panel A).
Based on the expertise I gained throughout this project, I now believe that steeper tilt angles for the initial trenches and higher milling currents could have significantly reduced the time required for rough milling. Moreover, later results confirmed that the decellularized D14 TIFF CDM specimens used in the bulk milling experiments were not vitrified, which increased the time required for sample thinning. The reason for this increased milling time of unvitrified samples compared to fully vitrified samples remains unclear but could potentially be due to a difference in their crystallographic orientation of atoms. It has been previously shown in Material Science that this influences the FIB sputtering rate (Wendt and Nolze, 2007).
Overall, these specimens did not result in high-quality lamellae.

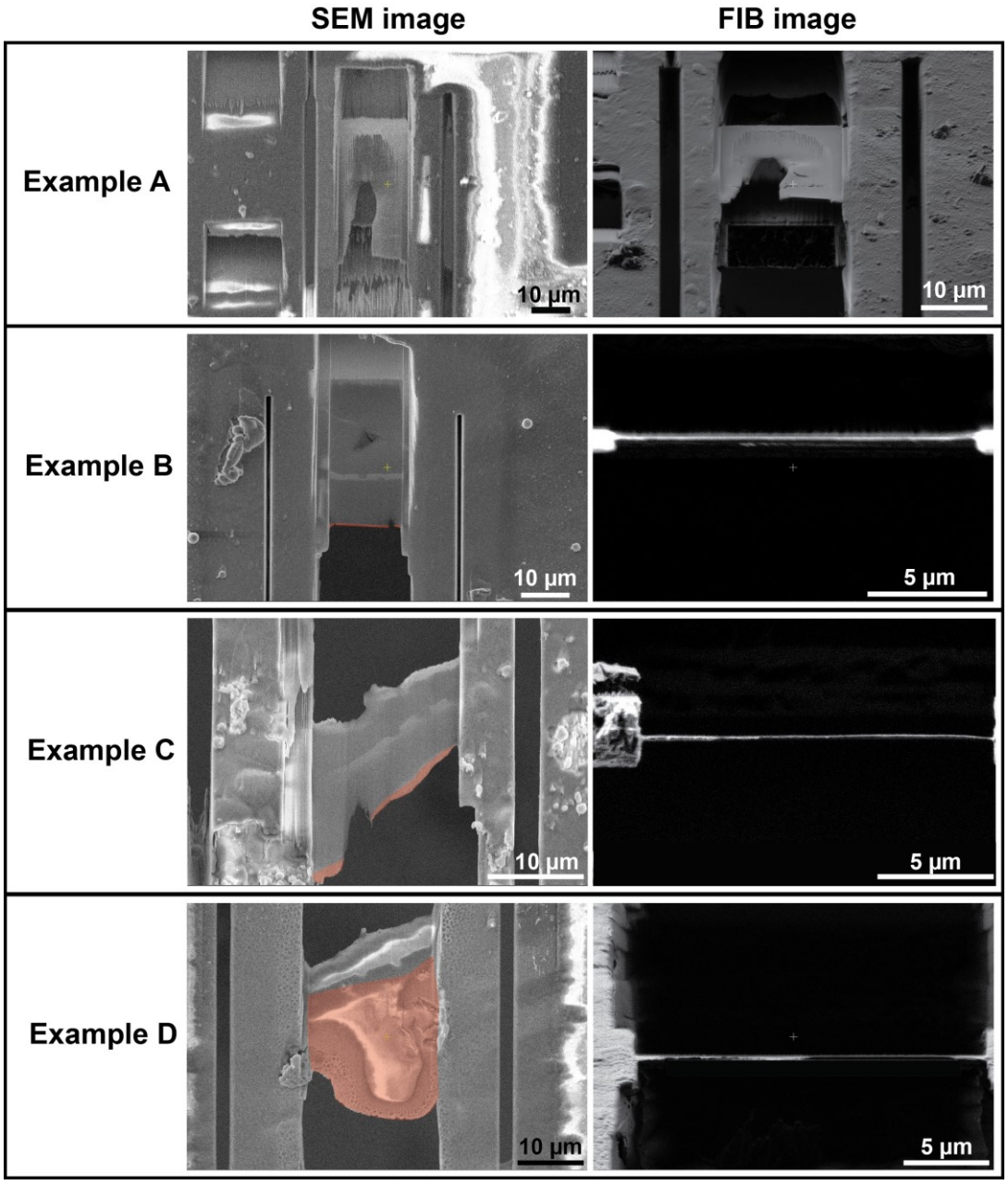

Figure 32: Different examples of lamellae created by bulk-milling of plunge-frozen CDMs. The left panel shows the SEM top-down view of the lamella, while the right panel shows the lamella by FIB imaging at the milling angle. A) A D14 TIFF CDM was not amenable to cryo-FIB milling. The combination of sample bulk and hexagonal ice instead of vitrified ice prevented the generation of a thin lamella. B-D) D3 TIFF CDM specimens were thinned down. B and C show lamellae that had lost their protective platinum partially before the desired thickness of ~200 nm could be reached. Panel D shows a lamella that consists primarily of platinum and only a smaller portion of biological material. The remaining platinum front is indicated in red in B-D.

Adaptation of CDM specimens for bulk milling

After several failed attempts to produce lamellae from decellularized D14 TIFF CDMs, I decided to adapt the specimen preparation to grow CDMs with reduced height and density by reducing the growth time from 14 days to only 3 days. D3 TIFF CDMs were decellularized, plunge-frozen, screened by cryo-LM, and milled as outlined above. Examples of a D3 TIFF CDM are shown in Figure 32 and Figure 33.

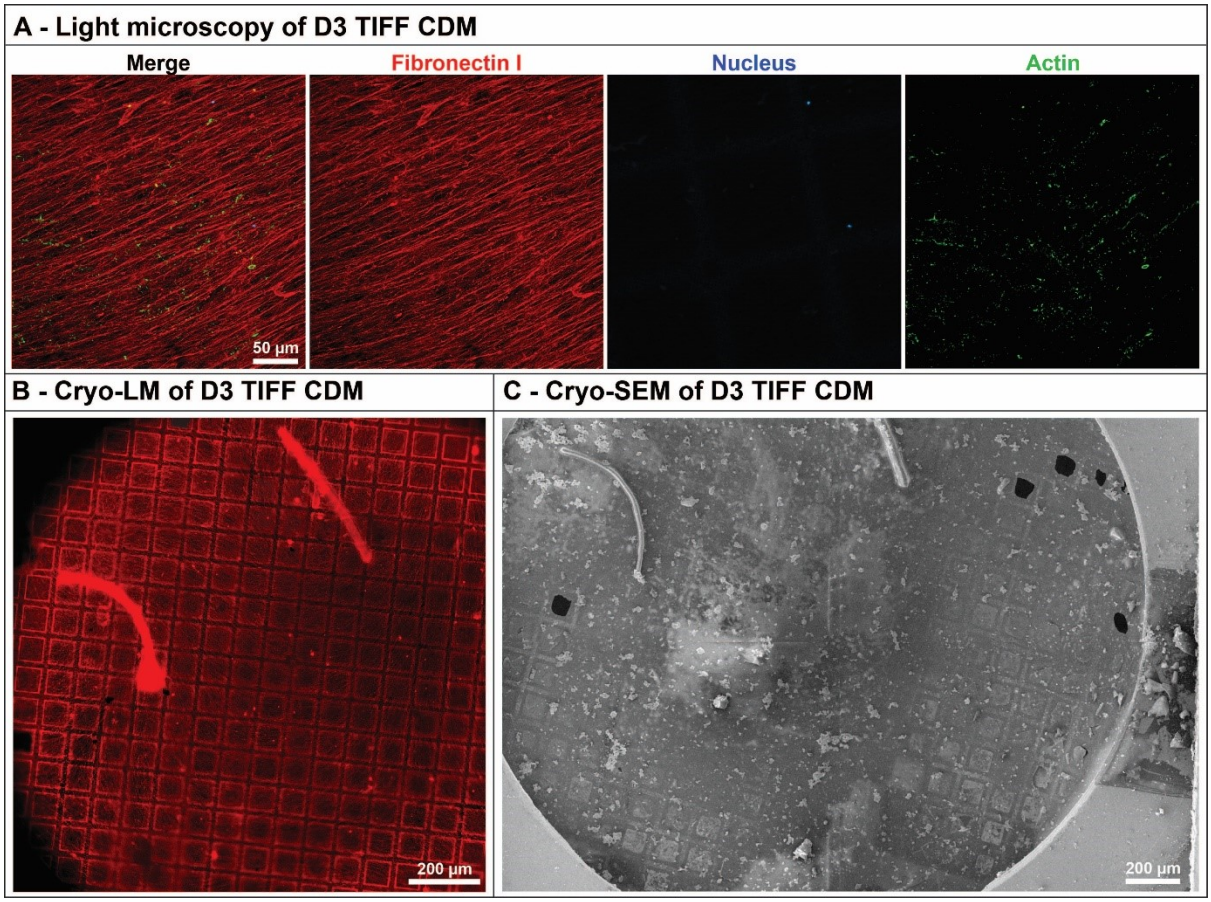

Figure 33: A decellularized D3 TIFF CDM specimen used for bulk FIB milling.
A) D3 TIFF CDMs were fixed after decellularization and stained for fibronectin I, the nucleus, and actin. In this specimen, fibronectin I fibers were densely aligned, and no or barely any signal for the nucleus (DNA) and actin (cytoskeleton) could be detected, indicating a successful decellularization process. Only samples with intact fibronectin I matrix throughout the whole grid were then plunge-frozen. B) Specimens were screened by cryo-LM. Here the visualization of the fibronectin I staining is shown. This specimen had two pieces of contamination positioned on its surface which aided correlation. Fibronectin I fibers were visible throughout the whole grid area, albeit fainter than in D14 matrices. C) The specimen shown in Panel B was used for cryo-FIB milling. An SEM tile scan overview image revealed different thicknesses of CDM in different areas of the specimen. In some regions, grid bars and squares are visible without any obstructions, indicating a lack of bulk material despite the fibronectin I signal detected in these areas by cryo-FM. This signal is likely caused by the fibronectin coating of the EM grids prior to cell seeding.

The reduction in bulk material allowed for better correlation as the grid bars were visible at several positions in SEM imaging. Moreover, less milling time was required for rough milling with these samples. In several sessions of 14-16 h, single lamellae with a final thickness of 250-400 nm could be generated (see Figure 33 and Figure 32) for assessment by cryo-TEM. However, I encountered different issues also with these adapted specimens.

Specifically, the protective platinum coating was either partially or entirely removed in most cases before the final milling step, as shown in Figure 32 in Panels B and C. This resulted in lamellae with a thickness of ≥350 nm that still allowed for cryo-TEM but is potentially too thick for cryo-ET.
This too-early loss of protective platinum coating is detrimental to the success of bulk milling of CDMs and would have to be prevented if this milling strategy is further pursued. I thought of different options to overcome the loss of coating.

For example, increasing the initial thickness of the platinum coating could counteract the early ablation of the protective platinum layer but would increase milling time. Another solution could be introducing a second platinum coating step after the initial rough milling steps. This would add to the protective layer after most bulk material has already been removed. However, the sample geometry and the lamellae position within the sample bulk could potentially reduce the efficiency of a second GIS platinum coating step due to steric hindrance. Moreover, the platinum should be added to the front of the lamella rather than just on top, which would require optimizing the deposition position.
Due to time constraints and the cryo-lift-out technique becoming available as an alternative, these options to overcome the loss of protective platinum coating were not yet explored.

A second issue that occurred several times was that some lamellae seemed to consist mainly of platinum coating rather than biological material (see Figure 32, Panel D). This was likely due to the reduced overall bulk and a lack of 3D information on the CDMs at the chosen lamella sites. D3 TIFF CDMs were thinner in some areas and thicker in others, as determined by SEM, even though cryo-FM wide field imaging indicated the presence of fibronectin in both types of areas (see Figure 33, Panel B and C). Targeting the thinner areas allowed for a faster generation of thin lamellae, but often these lamellae contained mainly platinum, as judged by SEM imaging.

Despite these issues, 3 of the generated lamellae were compatible with cryo-TEM and revealed that all specimens were not vitrified, as shown in Figure 34. Severe hexagonal ice crystal reflections were visible in every single lamella. In several cases, the lamellae were already damaged to some degree. Only rarely some biological structures were visible despite the low contrast and strong ice crystal reflections (see Figure 34, Example Set B). Overall, these results confirmed that D3 TIFF CDMs were not compatible with plunge-freezing, even when decellularized and heavily blotted. Therefore, I decided to abandon the exploration of plunge-freezing for vitrification.

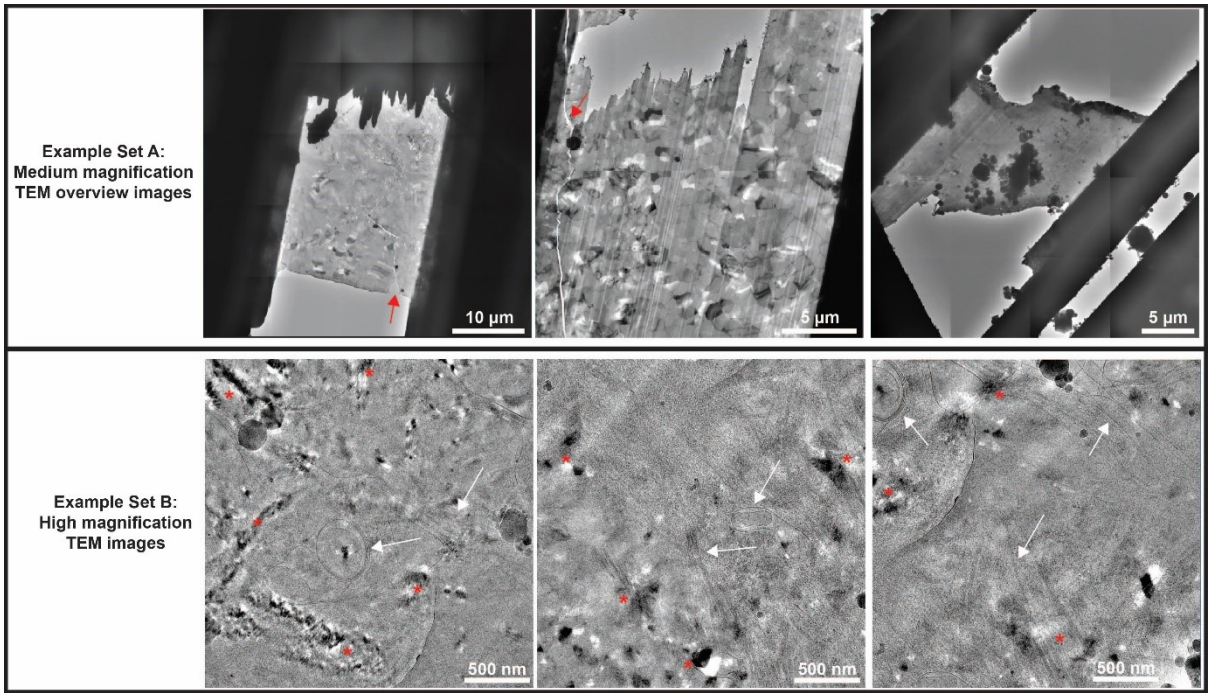

Figure 34: Vitrification assessment of bulk-milled D3 TIFF CDMs lamellae.
Example Set A shows medium magnification TEM overview images of three different lamellae. In each of them, severe reflections of hexagonal ice are visible throughout the whole area. Lamellae showed cracks (indicated by red arrows) and strong curtaining effects. Only in one case were biological structures visible despite the reflections (left panel). Examples of these are given in Example Set B, where high-magnification TEM images of these biological structures are shown (indicated by white arrows). Vesicles and fibers of some kind could be discerned in a few areas of one lamella. However, the hexagonal ice reflections (red asterisk) were so severe that they often obscured any structures. Data acquisition was not possible on these lamellae.

Milling of high pressure frozen specimens

Instead, D14 TIFF CDMs were high pressure frozen without decellularization or heavy blotting, as described in section 3.2.2. While technically more challenging, this allowed me to fully preserve the native ECM ultrastructure in context with the cell embedded within it. Another advantage was the much higher chance of (almost) complete vitrification.

However, HPF of CDMs on grids added more bulk to the sample: The cryoprotectants used to fill the sandwich added to the overall mass of the specimens and increased the height of the CDM part of the specimens to ~20-25 µm instead of only ~15-20 µm. Moreover, the space between the grid bars below the HC film was also filled with cryoprotectant, adding another ~20 µm of bulk height. This summed up to an overall bulk height of ~40-45 µm from the top of the CDM to the bottom of the grid bars and drastically increased the required milling time.

Several attempts at milling high pressure frozen D14 TIFF CDMs with the above-described protocol failed. In only one case, a lamella thickness of ~500 nm was reached, albeit bulk material could not be removed entirely from below the lamella (data not shown).

Overall, the issues I encountered with bulk milling, as described in this section, and the very low throughput I thought achievable with this method convinced me to explore alternative options. I decided to instead focus on the cryo-lift-out technique once this option became available with the upgrade to the Aquilos II.

3.3.2.2. Cryo-Lift-out: A novel technique for sample thinning of bulk specimens

Cryo-lift-out still is a relatively new technique. There are only a few research groups worldwide that have both the required instruments and expertise for the successful application of this technique. While it promises to be very powerful for a wide variety of samples, existing literature on its application is still scarce.
For my project, this meant that after the initial application training provided by TFS, I myself needed to establish a cryo-lift-out protocol for generating high-quality lamellae for cryo-ET. To this end, I had to explore this technique and the different factors affecting its success or failure.
Cryo-lift-out FIB milling is technically more challenging than bulk milling due to changed milling geometry, additionally required FIB milling steps and the use of a micromanipulator. However, it can significantly reduce the milling time required to produce a single lamella compared to bulk milling of thick samples. Moreover, bulk milling has been reported to work on samples of ≤50 µm but only with a considerable time investment of ~30 h. The overall success of bulk sample milling is strongly sample-dependent and will likely differ between Plasma and Gallium FIB instruments (Harapin et al., 2015; Kelley et al., 2022),
In contrast, cryo-lift-out is, in theory, only limited by the vitrification success of HPF on thick samples.
The lift-out technique usually targets the top layers of a bulk sample unless additional trimming steps are involved.

Overall, the process of cryo-lift-out FIB milling can be divided into five stages:

1) **Preparatory steps**
2) **Cryo-lift-out: Preparation of the lift-out block**
3) **Cryo-lift-out: Micromanipulator attachment and lift-out**
4) **Cryo-lift-out: Attachment of the lift-out to the half-moon grid**
5) **Lamella generation from the lift-out by cryo-FIB milling**

1. <u>Preparatory steps</u>

1.1. **Preparation of the half-moon grid:** A so-called half-moon grid is clipped into a marked FIBSEM AutoGrid™ precisely as depicted in Figure 35.

These half-moon grids must be accurately placed into a marked FIBSEM AutoGrid™. The front edges of the fingers must be in line with the center of the milling window to allow for milling at low tilt angles. The relatively small surface of the half-moon grid compared to standard EM grids necessitates special care when clipping it with a C-ring. The opening of the C-ring must never overlap with the surface of the half-moon grid. If this is neglected, the half-moon grid can detach from the AutoGrid™ at any given time, resulting in sample loss.

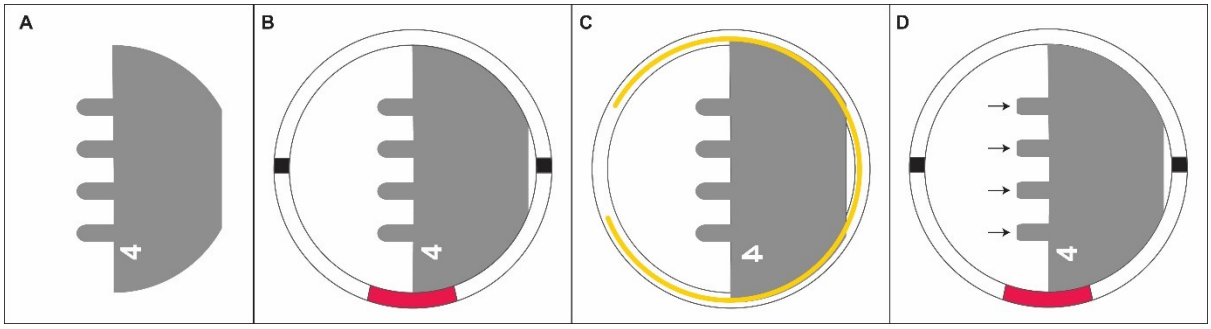

Figure 35: The use of a half-moon grid for cryo-lift-out FIB milling.
A) Shows the form of a half-moon grid. The number 4 etched onto the grid indicates the top surface of the grid, allowing for the correct placement of the grid. Half-moon grids used for this study have four protrusions called "fingers," to which lift-outs are attached. B) The half-moon grid is clipped into a FIBSEM AutoGrid™ in the orientation depicted. The front of the fingers has to be in line with the milling window, and the top surface (4 is visible) should be facing up. The fingers are not only rounded at the front but also at the bottom. Any surface curvature affects the attachment of the cryo-lift-outs negatively and has to be avoided. C) This shows how the half-moon grid is clipped into the FIBSEM AutoGrid™ from the back, also showing the position of the C-clip, depicted in gold. D) The fingers are FIB milled to have a straight front instead of a rounded one before cryo-lift-out attachment, further improving cryo-lift-out attachment conditions.

1.2. **Sample loading**: The instrument is cooled down at least 30 min before sample loading and set to the imaging mode called “Standard”. Once the cryo-shield and cryo-stage reach a temperature of ≤-190°C, the loading station is cooled down, the sample loaded in one position, and the prepared half-moon grid into the other position. After transfer into the instrument, an SEM overview tile scan of the half-moon grid and the CDM specimen, including the surface of the FIBSEM AutoGrid™, is acquired. The free working distance is set by linking Z to FWD.

The Aquilos II has an improved cooling system and cools down faster than the Aquilos I. The nitrogen gas flow rate used to cool down the instrument can be manually adjusted to ensure the desired temperatures are reached. An increased flow rate typically leads to better cooling.
The “Standard” imaging mode allows for optimized SEM imaging in all stage positions, regardless of z-height. This mode can be used in any stage position and is the default mode. It typically has a lower SEM imaging quality than other modes. There are two other modes, “OptiTilt” and “OptiPlan”. “OptiTilt” is optimized for SEM imaging at eucentric height, with the stage positioned for lamella milling. “OptiPlan” is optimized for SEM imaging at eucentric height with the stage positioned for volume imaging, such as for Auto Slice&View.
An overview of the whole lift-out technique is given in Figure 36.

1.3. **Cryo-CLEM and lift-out targeting**: Cryo-CLEM is performed using the MAPS software, as described in section 3.3.2.1. High pressure frozen specimens rarely have any landmarks recognizable in both SEM and LM. To overcome this problem, the edges of the milling window on the AutoGrid™ are used as landmarks for correlation (see Figure 28 and Figure 36).
2-3 potential sites for cryo-lift-out are selected and marked on the overview image in MAPS based on the FM image used for correlation. The eucentric height of these sites is then determined using the MAPS software.

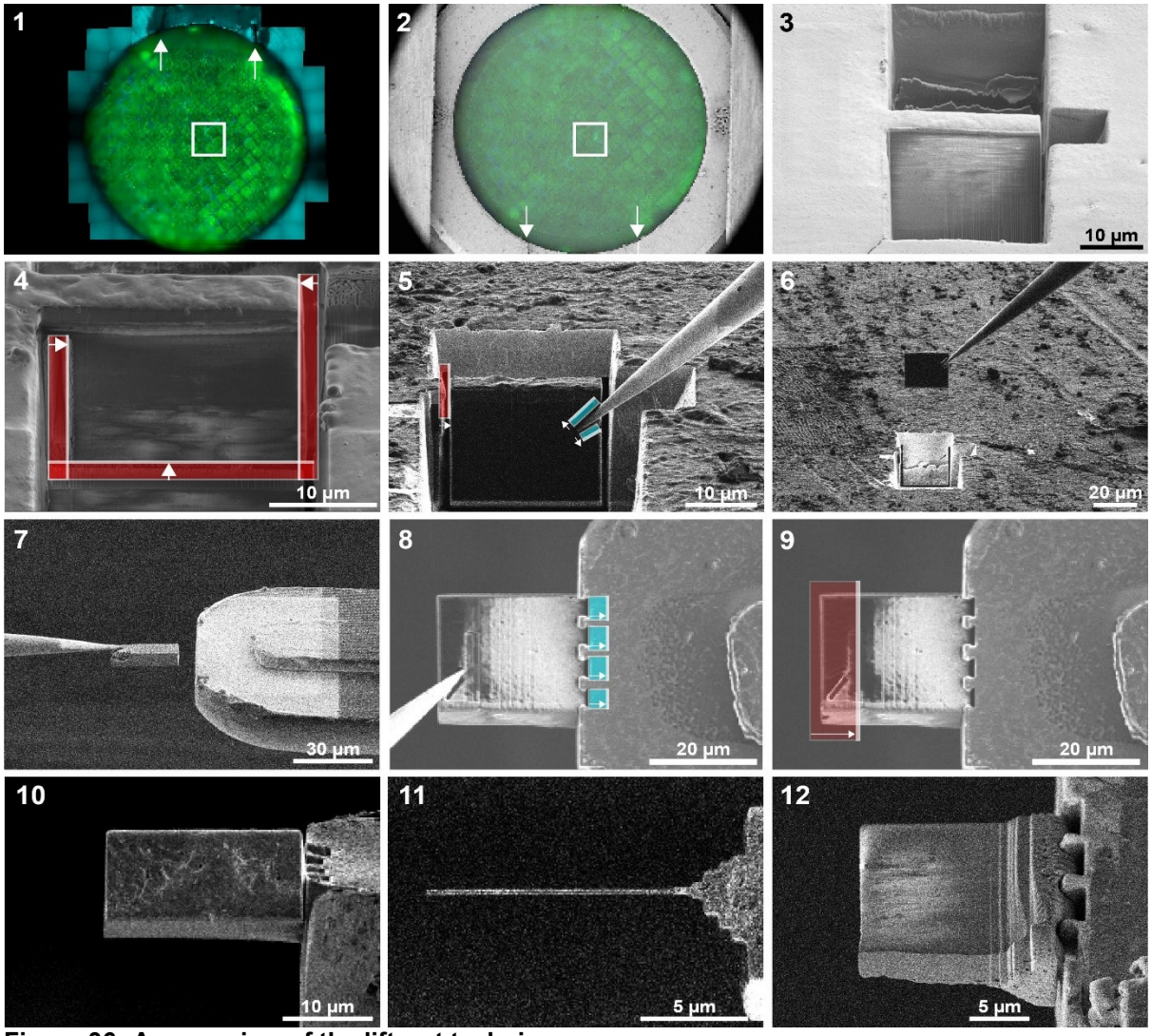

Figure 36: An overview of the lift-out technique.
Cryo-CLEM (1 and 2) is accomplished using the milling window edge for correlation. The ROI is indicated with a white square. A lift-out block is isolated from the bulk sample by milling trenches (3) and performing an undercut (4, red pattern, milling direction indicated by arrows). Next, the micromanipulator needle is positioned against the lift-out block as shown (5) without exerting any force on the lift-out block. Two re-deposition milling patterns (5, blue patterns, milling direction indicated by arrows) are placed above and below the needle as shown and the lift-out block is attached to the needle by redeposition milling. Finally, the remaining anchor of the lift-out block to the bulk sample is removed by FIB milling (5, red pattern, milling direction indicated by the arrow). The lift-out block is then lifted out (6) and transferred to the finger of a half-moon grid (7). Here, it is attached by re-deposition milling (8, blue patterns), and the needle is removed by moving it to the side and off the lift-out. The part of the lift-out where the needle was attached is removed (9). The lift-out is then thinned down to 200 nm (10 to 11/12). 11 shows the FIB view of the created lamella, and 12 shows the SEM overview over the whole lamella.

1.4. **Sample cleaning**: The specimen is cleaned from contamination. At eucentric height and a stage tilt of ~20°, the EM grid is imaged with the FIB with a current of 1 nA. This dislodges surface contamination and cleans the sample. Single larger ice crystal contaminations can be removed by focusing the ion beam on

them at higher magnifications for several seconds. Typically, this results in a barely contaminated surface.

This cleaning step was introduced as a crucial step in this protocol as after HPF, subsequent clipping into AutoGrids™, and cryo-FM screening, most samples had accumulated ice contamination. This cleaning can significantly improve the quality of the protective platinum coating. Larger pieces of contamination below the platinum coating can break off during FIB milling and consequently dislodge pieces of the surface coating. When this occurs, the sample is no longer protected and takes damage. A second application of platinum coating by GIS should be avoided as it increases the thickness of platinum on the whole sample and increases milling time. Moreover, additional platinum coating reduces the reusability of the sample.
Initial attempts at cryo-lift-outs without this cleaning step were often hampered by the loss of the protective platinum layer, particularly on more contaminated samples.

1.5. **Platinum sputter coating**: The specimen is sputter coated with a conductive platinum layer for 30 s at 30 mA and 10 PA with the in-built sputter coater, followed by another tile scan overview SEM image.

This step is optional but advantageous for two reasons: Covering the sample with a thin layer of conductive platinum, a tile scan overview image can be taken with even contrast and brightness. This results in images better suited for data recording and use in publications. It was also my impression that sputter coating further reduced the chance of loss of the protective platinum layer. However, the number of trials without sputter coating is too low for statistics. I hypothesize that making the sample evenly conductive prior to GIS coating might facilitate the even deposition of organometallic platinum and result in a better attachment of the protective coating to the sample.

1.6. **Protective platinum coating**: Using the GIS, the specimen is coated with a layer of ~1.5-2 µm metalorganic platinum. Deposition is performed for 55 s at the deposition position set by the EMF (ISTA). Another tile scan overview image of the whole specimen is then taken. The addition of a protective platinum layer changes the topology and obscures small landmarks. Thus, an updated overview image is required for better visual orientation and correlation.

It should be noted that the Aquilos II employed for this work has been adapted for both cryo-FIB milling on biological samples and FIB milling of samples studied in material science. Consequently, the GIS position was changed from the standard position, and the deposition position of the shuttle was adjusted accordingly. The deposition time strongly depends on the distance between the sample and the GIS and therefore had to be determined anew after this change of the GIS position.

2. Cryo-lift-out: Preparation of the lift-out block

A block of the sample must first be isolated from the main sample bulk by milling a series of trenches, as outlined below. The aim is to separate the lift-out block from the bulk sample on all sides except for one anchor point and to create enough room to access the lift-out block with the micromanipulator. Unless stated otherwise, 10 pA milling current was used for FIB imaging. The currents used for FIB milling are stated for each step.
Importantly, the scanning rotation used throughout the SEM imaging and FIB milling process depends on the stage rotation. When the stage is in its standard rotation, the scanning rotation for both SEM and FIB is set to 180°. When the stage is rotated by 180° relative to the standard rotation, the scanning rotation is set to 0°. This allows a more natural image rotation for the user. All pattern placements described in this protocol depend on the scanning rotation for correct placement. If a different scanning rotation is chosen, the pattern positioning has to be adjusted accordingly.

2.1. **Initial positioning of the stage**: The stage is moved to the lift-out site at eucentric height, rotated by 180° relative to the standard rotation, and tilted to 7°. The scanning rotation is changed to 0°. The FIB is orthogonal to the sample surface in this position, facilitating trench milling.
The exact lift-out position is defined and centered in both SEM and FIB view by visual correlation of the live FIB imaging and the position marked on the overview SEM image.

Due to the conducted stage rotation and stage tilt, the selected position is typically not centered in either SEM or FIB imaging, even at eucentric height. Small remaining contaminations were used for more accurate visual orientation and correlation. The stage was moved to center the lift-out position in SEM. The position was then centered in the FIB view by beam shift. As the FIB beam shift has more range than the SEM beam shift, this proved to be the best method. If the necessary beam shift in FIB was too far, the z-height of the stage was adapted until the coincidence point between both beams was achieved. Typically, this movement was only in the range of 0.1-0.5 mm.

2.2. **Trench-milling for cryo-lift-out – Trench 1**: The block of material targeted for lift-out is marked in the FIB view by placing a non-milling pattern of 25 x 8-10 µm (x/y).
The first trench milling pattern is placed below the marked lift-out site (pattern 1, Bottom pattern, see Figure 37). A Cross-Section (CS) milling pattern with a defined size of 25 x 50 x 5.5 µm (x/y/z) is placed with a set milling direction from bottom to top. It is milled with a current of 3 nA and usually requires ~45 min milling time.

The CS milling pattern differs from the rectangle milling pattern in that it mills with a gradient. A rectangle milling pattern mills every point in the pattern to the same extent. A CS milling pattern mills in a step-wise gradient in the milling direction, thereby removing material in the form of a wedge. This significantly reduces the milling time while removing enough bulk material for consecutive steps. The sizes recommended here work for precisely this protocol and would need to be adjusted for deeper or flatter lift-outs. The y and z chosen for this

pattern define at which position on the lift-out block the undercut can be placed later.
The success of this milling step is visually confirmed by SEM and FIB imaging. The lift-out block should have no remaining material on its front side.

2.3. **Trench-milling for cryo-lift-out – Trench 2:** The second trench-milling pattern is placed above the marked lift-out site (pattern 2, Top pattern, see Figure 37). A CS milling pattern with a defined size of 25 x 15 x 7 µm (x/y/z) with a set milling direction from top to bottom is set and milled with a current of 3 nA. Pattern milling is typically completed after ~20 min.

Trench 1 needs to be long enough to allow access to the FIB to separate the lift-out block from the bulk sample with an undercut in a later step. However, this is not necessary for Trench 2 as it only serves to separate the lift-out block from the bulk sample. This allowed me to reduce the y of Trench 2 to 15 µm compared to Trench 1 to cut down on milling time. A higher z-depth ensured that the lift-out block got milled over sufficient depth at its backside, even without visual confirmation.

2.4. **Trench-milling for cryo-lift-out – Trench 3:** The third trench pattern is placed on the right side, i.e., the side where the micromanipulator accesses the sample (pattern 3, Side pattern, see Figure 37), overlapping with patterns 1 and 2. A CS milling pattern with a defined size of 12 x 20 x 5 µm (x/y/z) with a set milling direction from right to left is set and milled with a current of 3 nA. Pattern milling is typically completed after ~10 min.
To ensure that the depth of the top trench allows for a clean undercut later on, the top pattern milling is repeated with a Cross Section Cleaning (CSC) pattern and a changed pattern size of 25 x 2 x 35 µm (x/y/z).

The CSC pattern resembles the CS pattern but mills in a linear gradient, creating a smooth and even surface toward the milling direction.

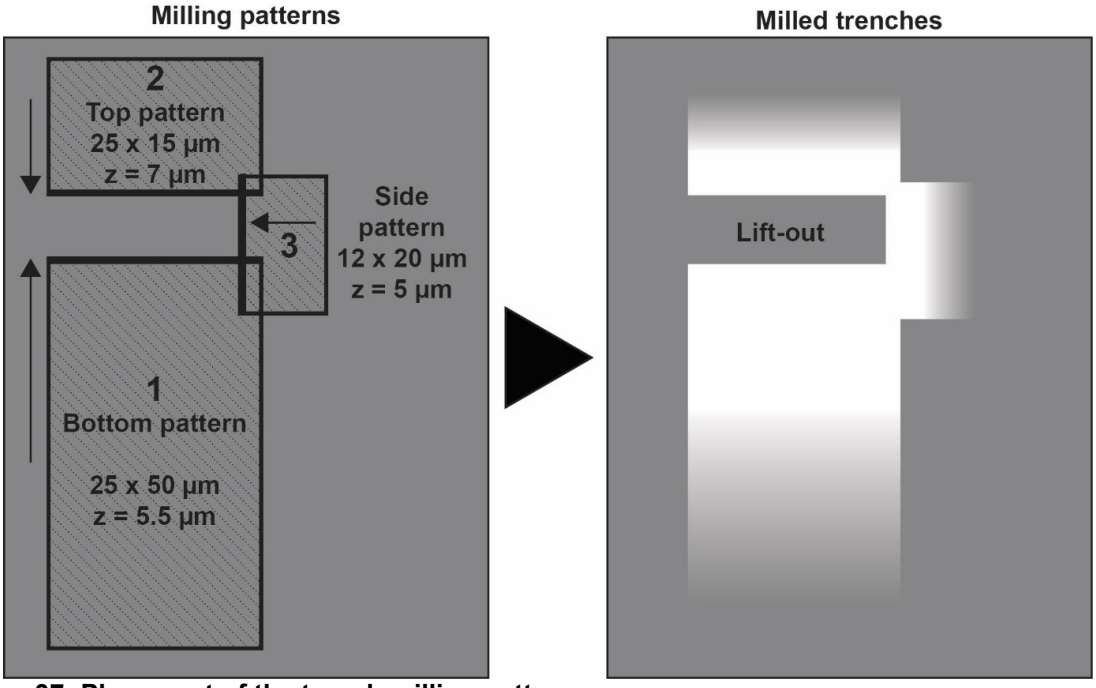

Figure 37: Placement of the trench milling patterns.
Trench 1, the bottom pattern, isolates the lift-out from the bulk samples and is designed to allow access of the FIB to the lift-out block during later steps. Trench 2, the top pattern, mainly isolates the lift-out block further from the bulk sample. Trench 3, the side pattern, further isolates the lift-out block while also allowing access to the micromanipulator for the lift-out procedure. The milling direction of each pattern is indicated with an arrow.

2.5. **Undercut of the cryo-lift-out block:** The stage is returned to its standard rotation and tilted to 28°. This allows imaging of the front side of the lift-out block. The scanning rotation is changed to 180°. In this position, the undercut patterns are placed as depicted in Figure 38. One pattern is placed at the very bottom, and one pattern is placed on either side of the lift-out block. Rectangle milling patterns with a set milling direction toward the lift-out block and a z-depth of 10 µm are placed and milled with a current of 1 nA.
Milling progress is closely monitored by FIB live imaging within the milling patterns, which is only possible when using rectangle milling patterns. By adjusting brightness and contrast, the remaining material can be visualized. Milling is only stopped when no more material is visible. Milling times depend on the dimensions of the lift-out block.
This is a crucial step, as any remaining connection to the bulk sample will result in the potential loss of the lift-out block.

Different pattern placement options have been explored; the lower down the bottom pattern is placed, the longer the lift-out block and the lamella created from it will be. With the defined trench pattern sizes given above in this protocol, this length is typically ~15-20 µm if the bottom pattern is placed as low as possible. The undercut pattern placements that worked best are shown in Figure 38. At this point, the remaining connection of the lift-out block to the bulk sample is removed except for a small anchor point. This anchor point can either be in the upper part, including the platinum layer (Option 1), or slightly below the platinum layer (Option 2). Option 2 had a higher rate of successful lift-outs in those specimens that showed charging issues. I speculate that this could be due to the difference in the anchor position. For Option 1, the anchor contains

the platinum coating, which is conductive. Thus, removing the anchor could result in a stronger discharge or charging event than in Option 2. This, in turn, could lead to a shift of the lift-out on the needle, thereby breaking the attachment.
A strong enough charging effect could even lead to the lift-out being repulsed by the needle, which would explain why the lift-out virtually completely jumped off the needle in many cases. Based on this observation, I recommend the use of Option 2.
The milling progress of the bottom pattern was the most difficult to judge, even with adjusted brightness and contrast. Visual confirmation of the removal of all bulk material below the lift-out block is impossible due to the sample geometry and the chosen trench pattern sizes.
It has proven helpful to monitor the backside of the top trench by SEM. Once the FIB has milled through the lift-out block, it will reach the bulk material behind it next, which is visible in SEM. However, the lift-out block obscures any feedback on the milling state of the bottom undercut pattern and only allows assessment of the side patterns of the undercut. In my experience, the milling of the bottom undercut pattern should be continued for ~10 min after milling in the side undercut patterns has been completed. Typically, this almost always guarantees a successful undercut milling.

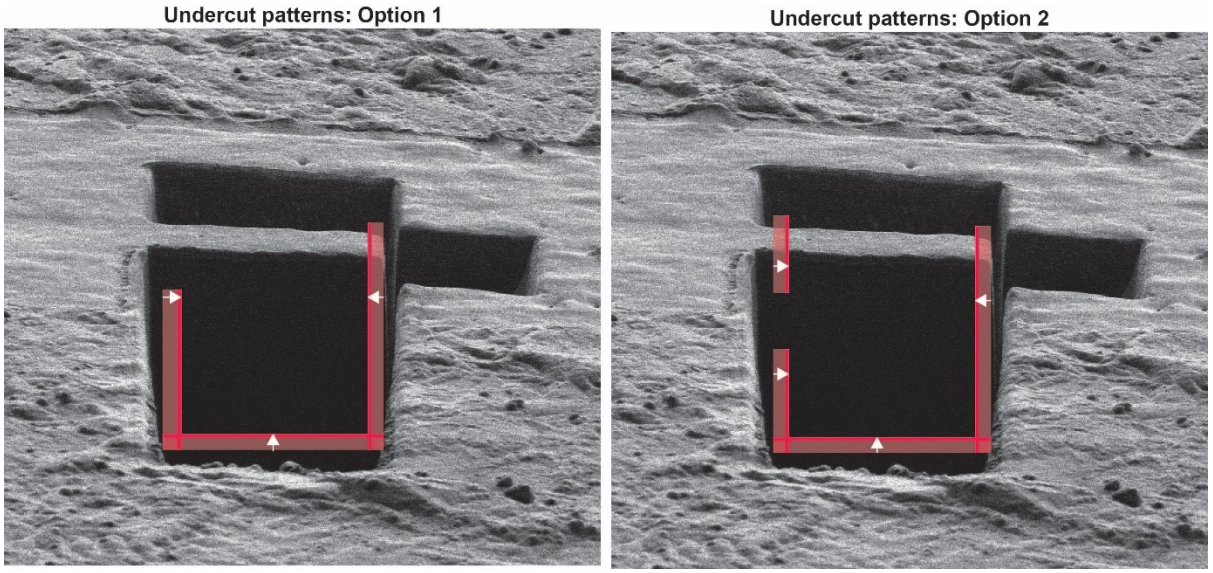

Figure 38: Placement of the undercut milling patterns.
I suggest two options for the placement of the undercut patterns that only differ in the side pattern of the undercut that creates the anchor point of the cryo-lift-out block. In Option 1, a single side pattern is placed on the anchor side, which results in the remaining anchor covering both biological material and the protective platinum coating. In Option 2, two side patterns are placed along the anchor side instead, so the remaining anchor covers only biological material. White arrows indicate the milling direction.

2.6. **Surface polishing of the cryo-lift-out**: The attachment of the micromanipulator works best on smooth surfaces. Due to this, the front surface of the lift-out block is polished by FIB milling.
To this end, the stage is again rotated by 180° and tilted to 7° to return to the trench milling position. The scanning rotation is set to 0°. A Cross-Section-Cleaning (CSC) pattern with a set milling direction from bottom to top and a z-depth of 35 µm is placed in the bottom pattern position shown in Figure 37. The CSC pattern should overlap with the lift-out block by ~0.5-1 µm. The X

dimension of the pattern is adjusted to the sample to ensure it covers the whole width of the cryo-lift out. The Y dimension is also adjusted to the sample to ensure all remaining material on the front side of the lift-out block is removed, typically to ~3 µm. The pattern is milled with a current of 1 nA, and milling typically takes ~15-20 min.

This polishing step was initially done before the undercut. However, this resulted in contamination through the sputtering of material during the undercut milling and often necessitated a second polishing. Hence, I decided first to do the undercut and only then the polishing.

This whole process typically took around 3 h to complete per lift-out site. In some cases, the bottom and top trench pattern width was adjusted to 50 instead of 25 µm, which allowed two lift-outs directly next to each other and safe time. However, at least one lift-out per session was always taken from a different sample region, as HPF specimens are often vitrified to different degrees in different areas.

3. Cryo-lift-out: Micromanipulator attachment and lift-out

After trench and undercut milling, I could observe both image drift and stage drift in several FIB milling sessions. This happened more often when more lift-outs had already been performed on the sample in either the same milling session or previous ones, and the conductive platinum layer was no longer present in some surrounding areas. The sputter coating step was repeated when this was observed, usually solving this problem.

3.1. **Positioning of the micromanipulator needle**: The stage is moved to the standard rotation, tilted to 28°, and the scanning rotation is set to 180°. The micromanipulator, a tungsten needle with a tip diameter of 1 µm in the case of the Aquilos II, is moved close to the lift-out.
The needle is moved to the front side of the lift-out and positioned with an approximately 4 µm overlap to the lift-out block and just below the platinum coating (see Figure 40). It is then moved to sit right against the lift-out without pushing against it or putting any strain on it.

At this point, a high-resolution SEM image of the front surface of the lift-out block can be taken to visualize its content to some degree. When in doubt, this can confirm the presence of biological material before the lift-out process is continued (see Figure 39 *for an example).*
In cases where it is unclear whether the undercut worked, the needle can be used to confirm this. In these cases, the needle is placed on top of the lift-out on the side opposite the anchor and lowered slowly. If the lift-out is visibly pushed down, the undercut was successful. If it did not move, the undercut was unsuccessful, and the lift-out block was still connected to the bulk sample on its underside.
Notably, the needle placement is crucial to the success of the lift-out. It has to touch the lift-out slightly but without exerting any force on it. If it is too far from the lift-out, the attachment will not work. If it is pushing on the lift-out, the connection between the needle and lift-out can break once the anchor to the remaining bulk material is removed.

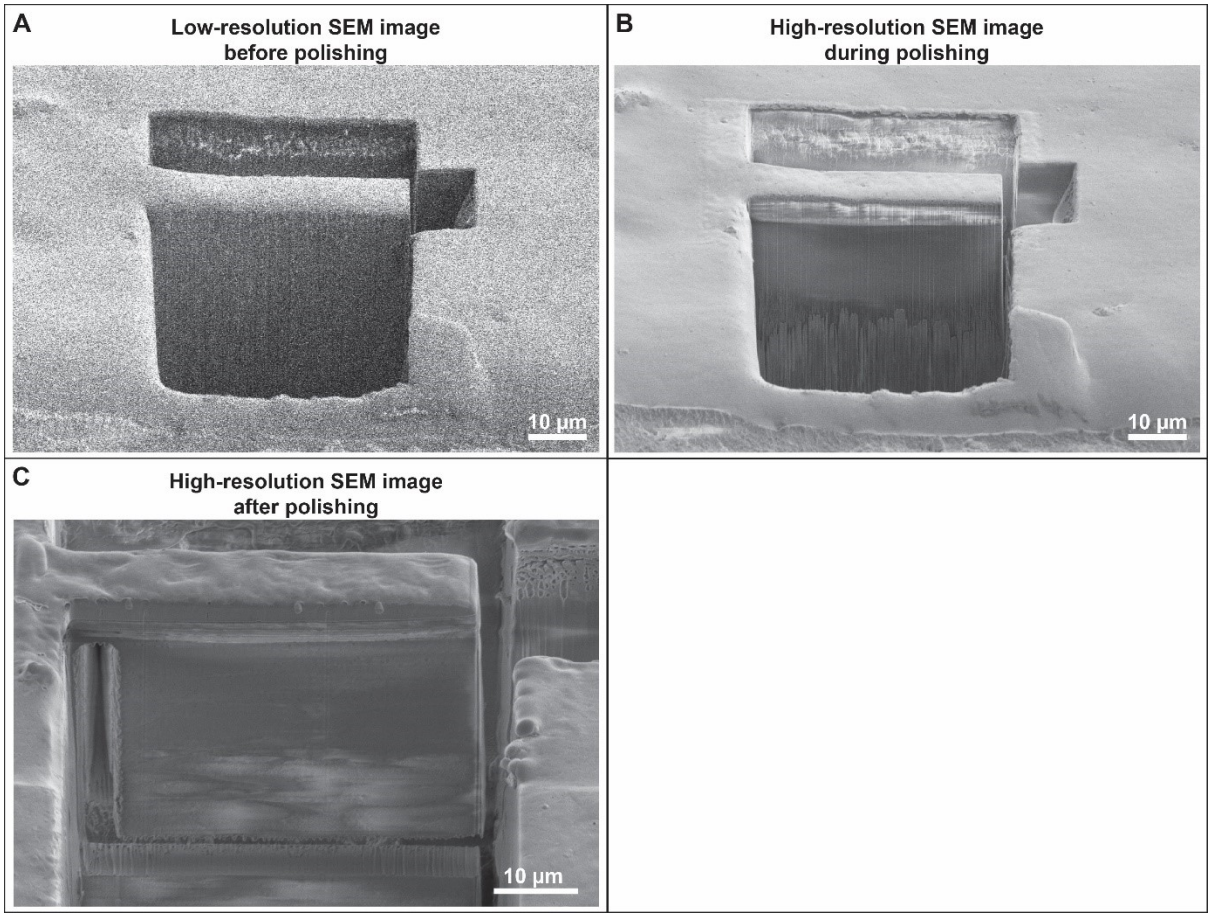

Figure 39: Assessing the presence of biological material by high-resolution SEM imaging.
A) A low-resolution SEM image taken after the three trenches have been milled. Without polishing and high-resolution image settings, the content of the cryo-lift-out block cannot be assessed. B) High-resolution imaging after a first, unsuccessful round of polishing. The surface is not entirely smooth yet, and the z-depth of the CSC pattern was not deep enough, resulting in a half-polished surface. Charging effects right below the platinum coating indicate the presence of biological material. C) High-resolution SEM imaging was repeated after a second successful round of polishing. Differences in contrast indicate differences in charging effects and thereby suggest the presence of biological material throughout the whole lift-out block.

3.2. **Micromanipulator needle attachment**: A cross-section milling pattern of 4 x 1.2 x 0.5 µm (x/y/z) is placed above the needle and adjusted to run along its upper edge without overlap. The milling direction is set from bottom to top, away from the needle. The milling strategy is changed from the default 4-pass to single-pass. The pattern is milled with a current of 0.5 nA, which takes ~4 s. This is then repeated below the needle with an adjusted pattern width and milling direction.
Single-pass milling with a CS pattern results in the re-deposition of biological material from the sample onto the needle, thereby attaching it to the lift-out. The success of the attachment is judged by SEM imaging, see Figure 40.

Changing the milling strategy from the default 4-pass to single-pass is crucial for sample redeposition. In the default 4-pass setting, the FIB passes over every single point in the pattern four times, resulting in a lower dwelling time for each individual pass. This reduces damage and sample sputtering and is typically favorable. However, the milling strategy is changed to single-pass to achieve a

higher sample sputtering rate. With single-pass, the FIB passes over every point in the pattern only once and thus has a higher dwell time and material redeposition rate.
This is the most crucial step for the lift-out. The exact position of the milling pattern should be confirmed at the milling current before FIB milling is started to ensure the best possible re-deposition and avoid damage to the needle. If the re-deposition fails or the attachment is too weak, the lift-out block cannot be lifted out of the bulk sample or can be lost in subsequent steps. If SEM imaging reveals that the attachment was unsuccessful, the needle can be moved to a different position, and the process can be repeated.
The attachment success at the lower side cannot be visually assessed; therefore, it remains unclear whether it contributes to the overall attachment strength. However, milling this pattern only takes ≤4 s and potentially reinforces the attachment, which is why I included it in my protocol.

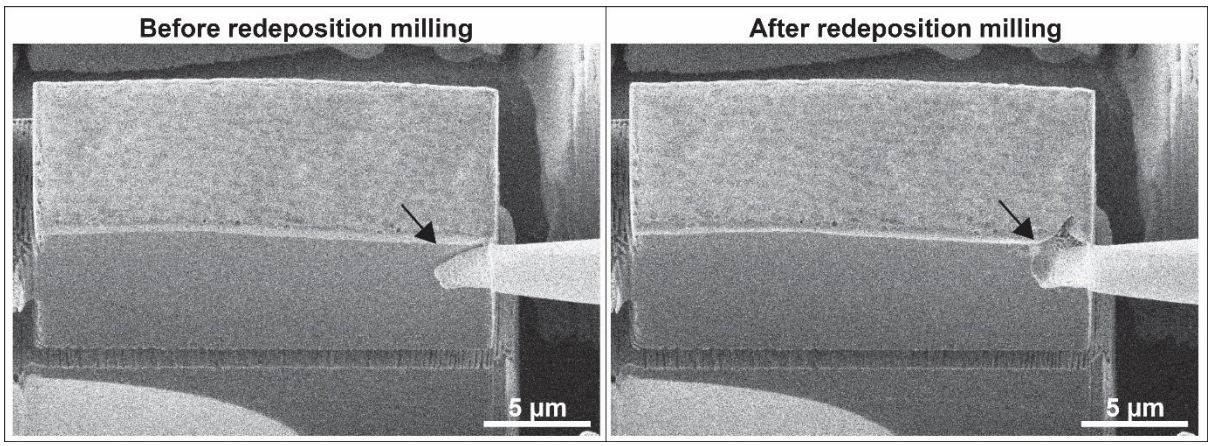

Figure 40: Assessment of redeposition milling for the attachment of the micromanipulator needle to the cryo-lift-out by SEM.
A comparison between a picture taken before redeposition milling (left) and after (right) shows what a successful needle attachment looks like. After redeposition milling, biological material has been removed just above the needle. Some of this material has been redeposited onto the needle, which looks now fused with the cryo-lift-out. A black arrow indicates the site.

3.3. **Removal of the lift-out anchor**: A rectangle milling pattern is placed over the remaining anchor between the lift-out and bulk sample, with the milling direction set toward the sample.
The pattern is placed over the anchor material along the line of the side pattern of the undercut on this side to create an even surface, which is essential for the attachment to the finger on the half-moon grid. The pattern is milled with a current of 0.5 nA and closely monitored in SEM and FIB live view. Milling is stopped as soon as the remaining material has been removed.
From this point on, until the lift-out is attached to the half-moon grid, it is only ever imaged with FIB currents of 30 pA or lower. Exposing the lift-out on the needle to higher FIB currents resulted in the loss of the lift-out in several cases, likely when the attachment was imperfect.

If the attachment to the needle is strong enough, the lift-out should stay completely fixed in its position on the needle. However, in around 1/4 of the lift-outs, the lift-out block moves on the needle upon milling through the anchor. This changes the attachment angle and the position of the lift-out block on the

needle. In a few cases, cutting the anchor resulted in a complete loss of the lift-out as it virtually jumped off the needle and could no longer be found. I hypothesize this is the case when there is untypically strong charging of the sample or the needle itself. It occurred even when the attachment to the needle had been judged as good by SEM imaging.
Interestingly, loss of the lift-out occurred in 100% of the lift-outs when the needle had been previously used for milling specimens from material science. This could be due to the redeposition of other materials onto the tungsten needle, which have different properties that change the strength of the attachment. They could also potentially affect the charging between the needle and the biological sample. While the reason is still unclear, I strongly recommend using either a new needle or a needle that has been previously only used for biological samples.
The effect of sample loss upon FIB imaging with a current higher than ~30 pA is probably due to charging rather than direct damage to the attachment. Initially, I tried to mill the far edge on those lift-outs that had shifted their position on the needle upon anchor removal into an even line with a milling current of 0.5 nA. They no longer presented an even front for their attachment to the half-moon grid, which is detrimental to the attachment success. However, in most cases, a single FIB image taken with a higher current led to a complete loss of the lift-out. This is likely due to a combination of charging of the lift-out and an already weak attachment. Based on these observations, I strongly recommend using only low FIB imaging currents from this point onwards.

3.4. **Lift-out of the isolated sample block**: The needle with the attached lift-out is lifted up and out of the bulk sample and finally retracted. Not a single lift-out that could be removed from the bulk sample was lost during the retraction of the needle, even those that had shifted in their position on the needle.

4. Cryo-lift-out: Attachment of the lift-out to the half-moon grid

Following successful lift-out, the sample block immediately needs to be attached to one of the fingers on the half-moon grid. The half-moon grids used here had four fingers. Typically, I used the two centrally located fingers first and the finger on the far side of the milling window as a third option. This allowed for low milling angles.

4.1. **Preparation of the finger for lift-out sample attachment**: The stage is lowered to 7° tilt and rotated by 180° for an orthogonal milling angle. The scanning rotation is set to 0°.
The target finger is then centered in both SEM and FIB view at eucentric height. A CS milling pattern is placed over the rounded front of the finger with the milling direction set toward the finger and a z of 13 µm (see Figure 41). The x and y dimensions are adjusted as needed. The rounded front of the finger is then milled at a current of 5 nA, which typically takes ~10 min.
Then, a CS pattern with a defined size of 2 x 3 x 8 µm and a milling direction from bottom to top is placed on the finger toward the side closer to the milling window (see Figure 41). With this, a notch is milled into the finger with 5 nA milling current.

This created a straight and even front of the finger for the attachment of the lift-out. Ideally, both should have straight fronts so they can be placed directly adjacent to each other without gaps.
This step is optional but recommended. Initially, the navigation of the needle with the lift-out in x/y/z was very challenging, and it was difficult to place the lift-out at the same z-height as the upper rim of the finger. This, however, is important to ensure a strong attachment. By creating this notch, it became much easier to judge the z-height of the lift-out in relation to the finger; subsequent steps were more successful and could be completed more quickly.

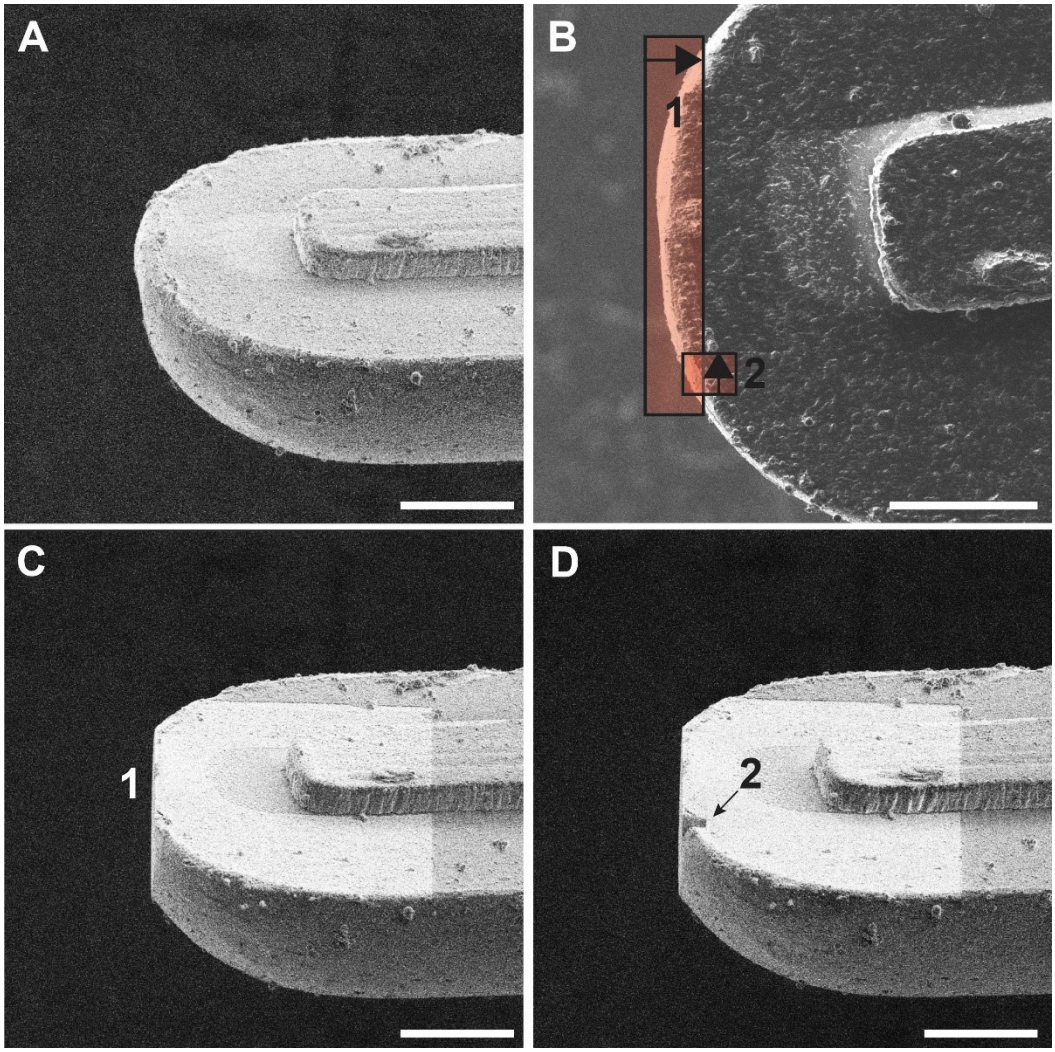

Figure 41: Preparation of the finger for lift-out sample attachment.
A) SEM view of the finger before preparation for the attachment. B) View of the finger at an orthogonal angle. A CS milling pattern (1) is placed along the front of the finger to mill an even edge for attachment of the lift-out. In the second step, a small CS pattern is placed to mill a notch that aids orientation during lift-out placement. The milling direction is indicated with an arrow. C) SEM view of the finger after pattern (1) was milled. The front edge is now even. D) SEM view of the finger after pattern (2) was milled. A small notch is now clearly visible.

4.2. **Lift-out sample alignment**: The stage is tilted to 16° for the attachment of the lift-out to the finger while keeping the 180° relative rotation. The needle and attached lift-out are inserted and moved next to the finger. The lift-out should be placed directly next to the milled front of the finger, aligned with the top of

the finger in z-height. The edge of the lift-out and finger should touch slightly without any pressure.

The attachment can also be performed at higher or lower tilts. However, this changes the angle at which the lift-out is placed on the finger. By attaching it to the finger in this position at 16°, it is at a perfect angle for FIB milling. Altering the attachment angle changes the angle of the final lamella, which can result in a shorter final lamella.
This alignment step is easier when the lift-out has a straight edge relative to the finger. This is typically the case when the lift-out worked without any shift in the position of the lift-out block on the needle. However, the lift-out can sit at an angle to the finger. Using FIB milling to straighten the edge of the lift-out is not recommended, as stated above. Instead, a skilled user can maneuver the lift-out against the finger by moving the needle accordingly. However, this takes skill and expertise and is not always successful.

4.3. **Lift-out sample attachment**: Four CS patterns with a defined size of 2 x 2 x 5 µm (x/y/z) are placed on the finger next to the lift-out (see Figure 36). The milling direction is set from left to right, away from the lift-out, and the milling strategy is switched to single-pass to increase the deposition rate for attachment.
The milling patterns are placed under the guidance of low-current FIB imaging. The milling current is set to 0.5 nA, and an imaging window is placed over the finger to double-check the pattern placement without exposing the lift-out to high FIB currents. The patterns should only slightly overlap with the lift-out. After milling, re-deposition of the material from the finger to the lift-out should have resulted in a firm attachment that can be assessed by SEM, provided the lift-out and finger had been well aligned in z.

Updating the whole FIB view at a current of 0.5 nA led to the loss of lift-outs in several cases, especially when the needle-lift-out attachment was not very strong from the beginning and the lift-out had previously shifted position during the lift-out.

4.4. **Removal of the micromanipulator**: The needle is removed by simply moving it either to the side or up and away from the lift-out. Typically, the connection between the lift-out and needle is much weaker than between the lift-out and finger. Throughout this project, no lift-outs were lost when using this technique.

In the application training and the few published protocols for the cryo-lift-out technique (Kuba et al., 2021; Mahamid et al., 2015)*, removing the needle through FIB milling is suggested. The different and novel removal technique described above has several advantages over the standard ones, as discussed in more detail later.*

4.5. **Removal of the needle attachment site**: After the needle is removed, the part of the lift-out where it had been attached is then removed by FIB milling. To this end, a rectangle pattern is placed over the length of the lamella with a width to cover the needle attachment site. The milling direction is set toward

the lift-out, and the pattern is milled with 0.5 nA until all material has been removed.

The needle attachment site typically showed gallium embedding around the milling sites. Hence, I decided to entirely remove that area as it could not be used for tomogram acquisition.

All cryo-lift-outs were performed one after the other in the above-described manner. Typically, an experienced user can complete one lift-out in 3-4 hours, depending on the dimensions of the lift-out block and whether any complications arise during one of the steps. After each lift-out is attached to a finger, they are thinned down into lamellae compatible with cryo-ET. The geometry of the cryo-lift-out during the lift-out process and the lamella generation is shown in Figure 42.

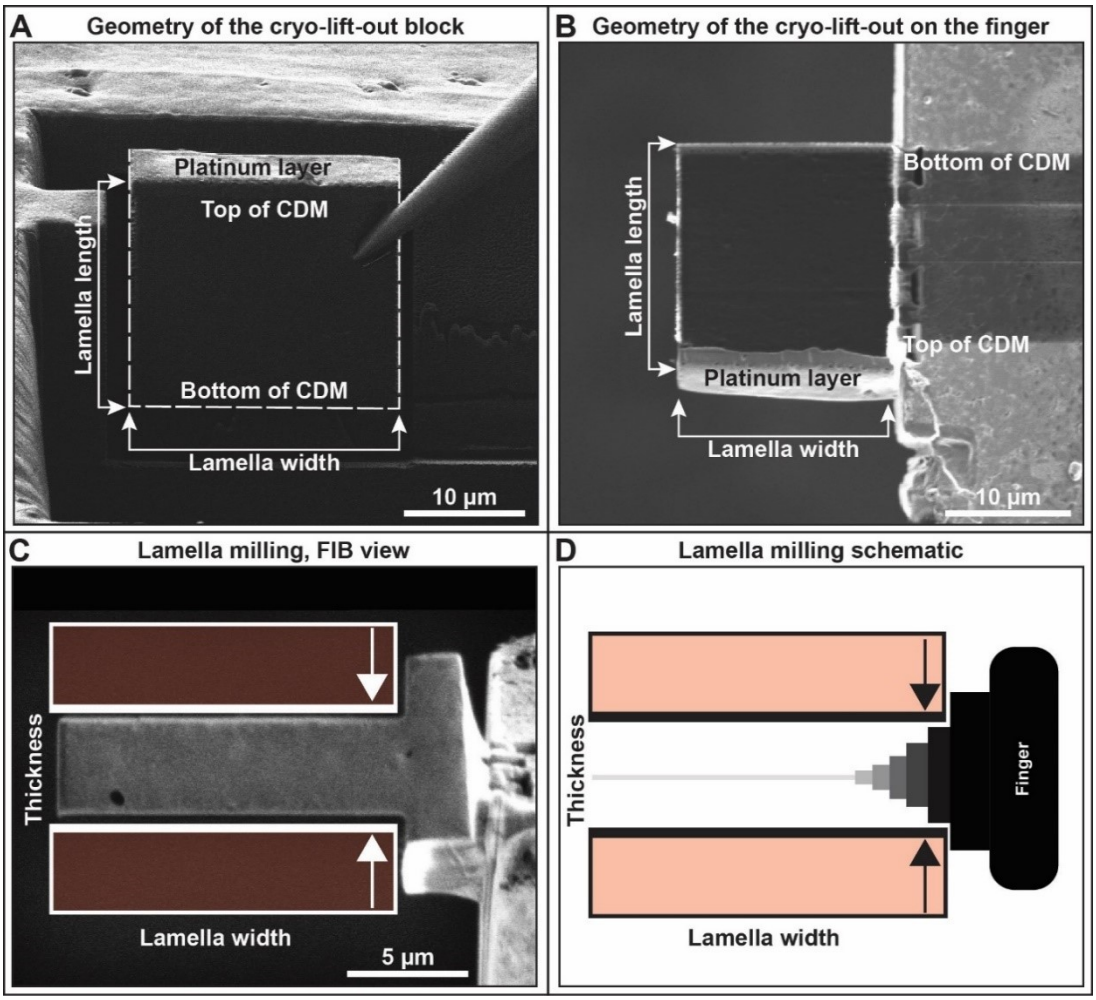

Figure 42: The geometry of the cryo-lift-out during lift-out and lamella generation.
A) The cryo-lift-out during the lift-out process is shown. The lamella length is determined by the trench patterns' set depth (z) and by how low the undercut patterns are placed on the lift-out block. Lamella width (x) depends on the pattern size chosen. The thickness of the lift-out is determined by how far the trenches are placed apart in the initial trench milling. B) The cryo-lift-out after attachment to the finger is shown. The platinum layer serves as an orientation point that indicates where the top and the bottom of the CDM are located. C) FIB view of the lamella during the thinning process. Patterns (indicated by rectangles) are placed above and below the cryo-lift-out block. Arrows indicate the milling direction. In consecutive steps, the lamella thickness is reduced. D) A schematic of the consecutive FIB milling steps is shown.

5. Lamella generation from the lift-out by cryo-FIB milling

5.1. **Setting up lamella FIB milling**: The stage is returned to the standard rotation, the scanning rotation is set to 180°, and an SEM overview image of the half-moon grid was acquired. The imaging mode of the instrument is changed from the "Standard" mode to the "OptiTilt" mode. The lamella positions are marked in the MAPS software, and their eucentric height and milling angle are determined. Using the FIBSEM AutoGrid™ and the outlined lift-out attachment protocol, milling angles of 15-17° are possible for all positions. Typically, a milling angle of 16° is chosen, resulting in a lamella pre-tilt of 9°.
Before rough milling is started, the lamella is centered in both SEM and FIB views.

The "OptiTilt" imaging mode of the Aquilos II is a mode optimized for high-resolution imaging at eucentric height with a low stage tilt angle for FIB milling. It allows for higher quality SEM images.

5.2. **Rough milling of lamellae**: The lift-out typically has a thickness of 5-8 µm. For sample thinning, two rectangle patterns are placed above and below the lift-out with at least a 2 µm distance to the edge of the finger (see Figure 43). This leaves a thick anchor for the lamella at the attachment site and ensures that the attachment is not damaged during FIB milling. Ideally, the lamella width is around 16 µm or less for the first milling step.
The rectangles are placed with a spacing of 3 µm between them, and the milling direction is set toward the sample. FIB milling is then performed with a current of 1 nA and monitored using the FIB live view and regular SEM imaging.
As described for bulk milling, the sample is thinned down to 900 nm thickness by reducing the spacing between the milling patterns and the pattern width to form a step-like anchor. The single steps are outlined in Figure 43.
Lastly, the stage is tilted to ±1° to remove access thickness at the far end of the lamella, as previously described. I recommend continuing directly with fine milling for every single lamella instead of first rough milling all the lamellae. This helps to prevent lamella bending, as discussed in detail below.

5.3. **Fine milling of lamellae**: Fine milling is performed by further reducing milling pattern spacing and width, as outlined in Figure 43. Stable lamellae can be thinned down to ~180-200 nm, as judged by FIB imaging. The final lamella width should be around 10 µm but not exceed ~11 µm.
During fine milling, assessment of milling progress is mainly done by FIB imaging. This requires user expertise for sound interpretation but allows a drastically reduced SEM imaging frequency. Thus, the pre-TEM electron dose the lamella is exposed to can be minimized. Moreover, this reduction of SEM imaging significantly reduces lamella bending, as discussed in detail below.
Towards the end of each fine milling step, a maximum of three SEM images with low dwell time and resolution are taken to ensure that the lamellae and their protective platinum coating are intact.

5.4. **Sample storage**: After fine milling all lamellae, they are stored in AutoGrid™ Boxes in LN_2.

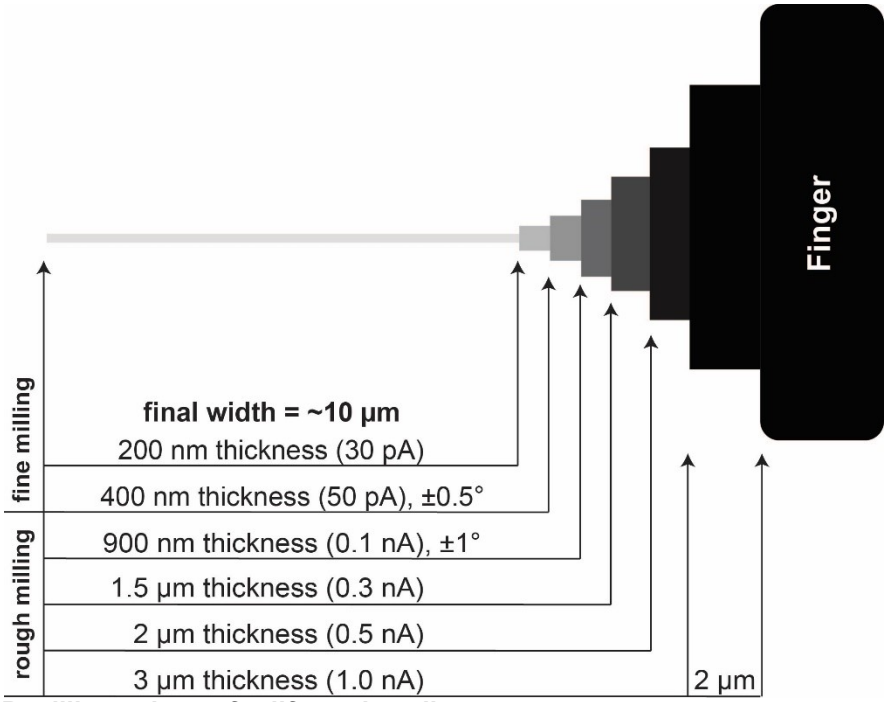

Figure 43: FIB milling scheme for lift-out lamellae.
An anchor of at least 2 µm is left to preserve the attachment of the lift-out to the finger. Rectangle milling patterns are placed above and below the lamella, with an initial width of ≤16 µm, a spacing of 3 µm, and the milling direction set toward the lamella. In consecutive steps, the lamella is thinned down by lowering lamella width and spacing as well as milling current, as outlined in the figure. Rough milling finishes at 900 nm lamella thickness, where the stage is tilted to ±1° to remove excess lamella thickness on its far end by FIB milling. In the first fine milling step, when lamella thickness reaches 400 nm, excess lamella thickness is again removed at ±0.5° stage tilt. Then the lamella is thinned down to ~200nm with a final length of ≤11 µm.

By employing this optimized protocol, three high-quality lift-out lamellae could routinely be prepared in a 12-14 h session.

Main factors for the success of lamella generation

Creating thin lamellae from lift-outs is technically more challenging than bulk milling. The lamella is only attached to the half-moon grid on one side, which makes it less stable than a lamella that is attached on both sides.
When I initially set out to optimize this protocol, the biggest challenge was the behavior of the lamellae during fine milling. Lamellae often started bending downwards on their far end opposite the lamella anchor during or even before fine milling. Thinner lamellae bent more strongly, resulting in uneven milling. In many cases, I had to completely abandon sample thinning as no patterns could be placed without destroying the lamella. While lamellae typically bent downward, they would also bend upward or distort fully over their whole length in a few cases.
Lamella bending could not be reversed once it occurred and typically worsened with time, regardless of whether FIB milling was continued.
To counteract this lamella bending problem, I began exploring different factors that I thought might factor into this issue. Due to the low throughput of the lift-out technique, only a low number of lamellae per condition could be produced and compared. Moreover, the observed bending effects were of different severity. In some cases, lamellae bent only slightly. In others, they were completely distorted. Hence, there are no statistics for these observations.

Main factors for the success of lamella generation: Rough and fine milling

The first factor potentially influencing lamellae bending I explored was the transition between rough and fine milling. In the first lift-out and lamellae milling attempts, I could observe that when all lamellae were first rough milled and only then fine milled, the initially rough milled lamellae had started to bend by the time I returned for fine milling. The thinner lamellae were, the more likely they would bend with time. While lift-out blocks with a thickness of 3 µm never bent, rough milled lamellae with 900 nm thickness often did, which was detrimental to further sample thinning. The bending could initially be compensated for to some degree, but it worsened throughout the fine milling until I had to abandon the lamella in many cases.

Typically, it is suggested first to do the rough milling for all lamellae and then commence with the fine milling for all of them to minimize the accumulation of contamination on finished lamellae. However, for lift-out lamellae, I strongly recommend continuing with fine milling after rough milling for each lamella individually. It significantly reduces the chance of lamella bending until a 200 nm thickness is reached. Moreover, the current contamination rate of our instrument is less than 5 nm/h, according to the measurements of the EMF. As lamella milling is typically completed within 2 h for all lift-out lamellae, this should result in a maximum contamination thickness of ~10 nm, which I deemed acceptable.

Main factors for the success of lamella generation: SEM monitoring

SEM imaging was initially employed to assess FIB milling progress and the state of the lamella, especially during fine milling. This is the easiest way to judge the state of the platinum coating and whether the lamella is still intact. However, it became apparent early during the optimization process that the lamellae were sensitive to SEM imaging, particularly towards the final thinning steps. No effect could be observed on lamellae thicker than 500 nm. However, thinner lamellae visibly bent after only a single SEM image with a dwell time of 500 ns was acquired at low resolution (see Figure 44, Example Set A).

This could be observed repeatedly with different severity, but it hampered further sample thinning considerably in all cases. In some severe cases, the lamellae bend and distorted to the point of being unusable for cryo-TEM.

Once I stopped acquiring SEM images below 500 nm lamella thickness, I could observe fewer cases of bending and thus strongly recommend reducing the number of SEM images acquired as much as possible.

I have no clear explanation for this phenomenon. However, I hypothesize that SEM imaging imparts some charge on the lamella that leads to its bending, which worsens with each consecutive SEM image.

Main factors for the success of lamella generation: Lamella width

To counteract the lamella bending problem during fine milling, I started to explore the effect of the lamella geometry on its stability. To this end, I compared the bending of lamellae with different widths and lengths and discovered that lamellae with higher widths proved to be less stable and bent more often once a thickness below 400-500 nm was reached. Initially, I aimed for lamellae with an area of ~20 x 20 µm to allow for many tomogram positions. However, these lamellae all bent, and fine milling was not possible.

I started to reduce the lamella width and, over several iterations, could determine that the chances of bending lowered with decreasing width, although they could never be eliminated. I could determine that lamellae with a final width below 11 µm typically did

not bend as long as all other factors outlined in this section were also considered. While there are some rare outliers, the final lamella width is crucial for creating a thin lamella (see Figure 44, Example Set B).
The lamella length was less crucial for obtaining high-quality, thin lamella. Different lamellae lengths were tested, starting with 15-20 µm. However, I could not observe a strong impact on lamella bending. Here, it also has to be considered that depending on the sample, a certain lamella length might be required to ensure the targeted structures are in the lamella. Overall, lamellae with a length of up to ~20-22 µm could be successfully thinned down and used for cryo-ET, provided their width did not exceed 11 µm.

Main factors for the success of lamella generation: Incomplete vitrification
Lamella bending occurred with different severity for different specimens. Typically, all lift-outs from the same sample would behave very similarly to each other regarding lamella stability when the same conditions were used during lamella milling.
When the optimized protocol given here was employed, most specimens resulted in high-quality lamellae of ~200 nm thickness with no or only minimal bending. In some cases, lamella bending was still an issue, and lamellae could only be thinned down to ~250 nm in some areas of the lamella. In other cases, the lamellae were so stable throughout the milling process that they could be thinned down to ~180 nm before lamella bending was observed.
Once these different lamellae were imaged by cryo-TEM, I could conclude that the sample's vitrification status played a role in lamella stability. Perfectly vitrified specimens resulted in highly stable lamellae that did not or only barely bent. Specimens that showed incomplete vitrification to a small degree typically behaved similarly and showed only minimal bending, which still allowed sample thinning. Specimens that were incompletely vitrified to a more severe degree often produced lamellae that bent more and were more challenging during fine milling. Images of these different degrees of vitrification are shown in Figure 25.
Based on these observations, I could conclude that the vitrification status of the specimen factors into the stability of the lamellae during FIB milling. The reason for this remains unclear, but it has been stated previously by Schaffer et al. that incomplete vitrification can impede lamella generation, albeit no direct statement on lamella stability was given (Schaffer et al., 2017).

Main factors for the success of lamella generation: Anchor Symmetry
The lamella anchor recommended in this cryo-lift-out lamella milling protocol is symmetrical. I wanted to explore whether the symmetry of the anchor affected lamella bending and therefore created lift-out lamellae with asymmetric anchors, which were flat on one side and had a step-like form on the other. Asymmetric anchors with a step-like form on the top side resulted in non-bent lamellae in some cases. However, in most cases, they led to upward lamella bending instead of downward bending (see Figure 44, Example Set D). This effect was stronger in some lamellae than in others, and I do not have a clear explanation for it at this point. I hypothesize that the shape of the anchor could influence the stress placed on the lamella during sample thinning or affect the charge distribution. It would be interesting to explore further whether the even placement of the single steps has any influence. To this end, a higher number of lamellae with different step patterns could be milled and compared to each other to see whether a slightly asymmetric anchor shape could further stabilize lamellae. Ideally, the single lamellae for one condition should originate from different samples,

while lamellae that are directly compared to each other should originate from the same sample. This could grant a better insight into the effect of the anchor shape on lamella stability.
In Example Set D (shown in Figure 44), the lamella with the less accurately milled asymmetric step-like anchor shows more severe upward bending (right panel) compared to the one with a more accurately milled anchor (middle panel, left panel). However, the overall number of lamellae tested with this anchor shape is too low to draw any conclusions (n = 5).
Interestingly, this upward bending effect could be counteracted to some degree by employing repeated SEM imaging, which typically leads to the downward bending of the lamella.
I also explored using asymmetric anchors with the step-like form at the bottom (data not shown) and could observe downward bending for these lamellae. However, only two lamellae like this were produced so that no conclusions could be drawn.

Main factors for the success of lamella generation: stage temperature
Typically, the cryo-stage was kept at temperatures of ≤-192°C at all times during FIB milling. When our instrument's cooling system did not work properly and required repair, it only reached temperatures of ~185°C even with increased nitrogen flow rates. During this time, I could consistently observe downward lamella bending (data not shown). All other steps of the lift-out did not appear to be influenced by the higher temperatures. However, the lamellae bent downward once the lamella thickness reached ~400-500 nm. With decreasing thickness, the bending worsened and sample thinning down to 200 nm became impossible in most cases.
It remains unclear why this slight change in temperature resulted in decreased lamella stability. It is possible that the reason for lamella bending lies with the stage itself rather than the increase in temperature. As the cooling system was not properly operational during this time, it is possible that obstructions in the nitrogen lines could have resulted in vibrations of the stage that were not visible during SEM or FIB imaging. Such vibrations could have worsened with the increased flow rate necessary to keep the stage cooled throughout the milling process. These undetectable vibrations rather than the slightly higher temperature itself could have potentially destabilized the lamella, particularly after it had been thinned down to below 500 nm.
Based on these observations, I strongly recommend ensuring a stable temperature of ≤-192°C is kept throughout the milling process.

Main factors for the success of lamella generation: Optimized lamellae
Considering all the above-discussed factors that play into lamella stability, I optimized the protocol for creating lamellae from lift-outs. Entirely or nearly completely vitrified high pressure frozen TIFF CDMs could reproducibly be used to produce high-quality lamellae for cryo-ET (see Figure 44, Example Set E). The final lamellae had a width of ~10 µm and a length of up to ~ 20 µm. By using symmetrical step-like anchors and avoiding exposure to SEM during the fine milling, the lamella stability was increased sufficiently to reach a final thickness of ~200 nm routinely.
I attempted to reduce lamella thickness further, but even with stable lamellae bending occurred in most trials once a thickness of ~180 nm was reached. Due to this, I recommend stopping sample thinning once a thickness of ~190-200 nm is reached.
In some rare cases, lamella bending still occurred even with this fully optimized fine milling strategy (see Figure 44, Example Set E, right panel), but usually only to a small degree that still allowed sample thinning.

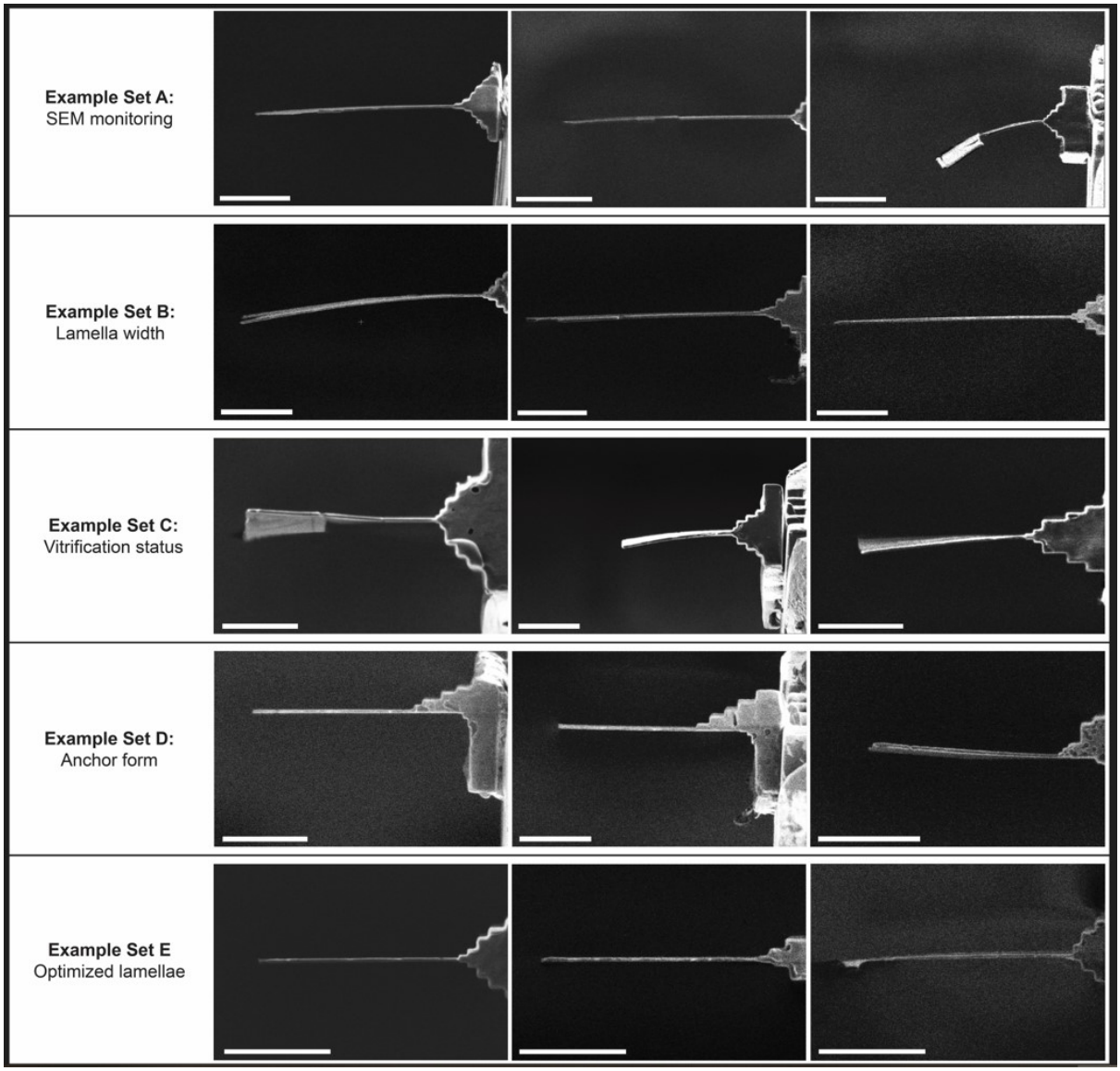

Figure 44: An overview of different factors that influence lamella stability.
Example Set A) SEM imaging for monitoring purposes during fine milling resulted in lamella bending. Continued SEM imaging worsens this effect, as seen in the right panel. Example Set B) The lamella width impacted lamella bending. The longer the width, the earlier the bending typically occurred and the more severe it became. Lamellae, which are ≤ 11 µm wide, are more resistant to bending. In some rare cases, even lamellae with a width of ≥ 12 µm remained mostly unbent and could be thinned down, as seen in the right panel. Example Set C) The vitrification status strongly impacted lamella stability during fine milling. Specimens that were only incompletely vitrified produced lamellae that bent and distorted during fine milling and often could not be thinned down sufficiently for cryo-ET. Example Set D) The typical anchor form is step-like and symmetrical, as seen in other example sets. Changing the anchor form to an asymmetrical anchor with a step-wise form only on the top side resulted in upward bending in most cases. Example Set E) Using the optimized protocol outlined in this thesis, most lamellae behave more stable and can be thinned down sufficiently for cryo-ET. Scale bar = 5 µm.

A specimen that resulted in high-quality lamellae with little or no bending could be used to create cryo-lift-out lamellae with the Aquilos II up to 8 times. By using re-deposition milling for the attachment of the needle to the lift-out block, no additional platinum coating is placed on the sample. Samples reused several times for cryo-lift-out showed image drift effects more often than freshly coated ones. This is likely again

due to charging effects at the sites of previous lift-outs, as the issue could be fixed through sputter coating a thin layer of ~40 nm platinum onto the sample.
The samples could be reused until too much surface contamination accumulated due to multiple sample transfers and storage. Contamination acquired after GIS coating cannot be cleaned off by FIB imaging with high currents. I suspect this is due to a difference in the charging of biological samples and platinum.

The lamellae survival rate from the FIBSEM to the TEM was at ≥80% after the protocol had been optimized and the lamellae were more stable. Complete loss of a lamella was rare; however, in some cases, parts of lamellae broke off and reduced the area available for image acquisition.

Innovations introduced in this cryo-lift-out protocol
So far, no detailed protocol for cryo-lift-out and subsequent cryo-FIB milling of thin lamellae for cryo-ET has been published. To my knowledge, the protocol presented here is the first of its kind, where several crucial factors relevant to the generation of thin lamellae have been explored.
The only comparable protocol was published in 2019 by Schaffer et al., where they describe an alternative cryo-lift-out protocol employing a slightly different custom-made instrument setup (Schaffer et al., 2019). Instead of using a material redeposition milling to attach the lift-out-block to a micromanipulator, they use a mechanical cryo-gripper. The instrument setup described in the publication Schaffer et al. is not commercially available at this point. In their publication, they show a proof-of-principle protocol for the cryo-lift-out technique that enabled the ultrastructural study of native tissue of an adult *C. elegans* worm. They state the success rate of lamella generation to be at ~20%. Additionally, the engineered TEM grids holding the lift-out lamellae were clipped into AutoGrids™ after FIB milling, dramatically increasing the chance to damage the lift-out lamellae before cryo-TEM imaging.
Since the publication of this protocol in 2019, it has likely been improved to increase the lamella generation success rate and improve the preservation of the thinned down lamellae.
In contrast, the protocol I describe here is based on the commercially available Aquilos II (TFS) system. Detailed descriptions of each single step in the generation of cryo-lift-out lamellae are provided, together with schematics for all pattern placements. Additionally, I elaborate on the factors influencing the success rate of lamella generation in detail and have optimized the lift-out protocol over several iterations, resulting in a lamella generation success rate of ≥80%.
Moreover, I introduce a novel strategy for removing the micromanipulator from the lift-out block after its attachment to the half-moon grid finger. TFS and other users recommend cutting the needle at the attachment point or, alternatively, the sample block next to the attachment via milling.
When the needle itself is milled to remove it from the lift-out, it gets consecutively shortened, resulting in a larger needle diameter. This can necessitate FIB milling to shape the tip of the needle to a smaller surface for a better attachment. However, once the needle has been cut several times, the resulting surface curvature of the needle can render it unusable for another lift-out. Once the surface curvature is not optimal, the re-deposition milling attachment will no longer work.
When the cryo-lift-out is cut next to the attachment site, a small block of biological material is still attached to the needle. The needle must then be manually cleaned by brushing it against a hard surface. This is challenging, especially for inexperienced

users, and can lead to needle damage and distortion. Both would potentially render it unusable for the next lift-out process or require at least a shape-correcting FIB milling step. Due to the imaging angles, it is also impossible to determine whether all material has been successfully removed from the backside of the needle.
Removal of the needle from the sample block, as suggested in my protocol, by simply pulling it off, eliminates these risks. Moreover, the needle is not shortened and remains clean. It can be immediately used for the next lift-out without any cleaning or FIB-milling, which saves time and preserves the needle. Using this strategy, I have not lost a single lift-out and can reuse the needle for at least up to 6 sessions without any detrimental effect. I believe that this can be very useful for the community.

3.4. Cryo-electron tomography of cryo-lift-out lamellae

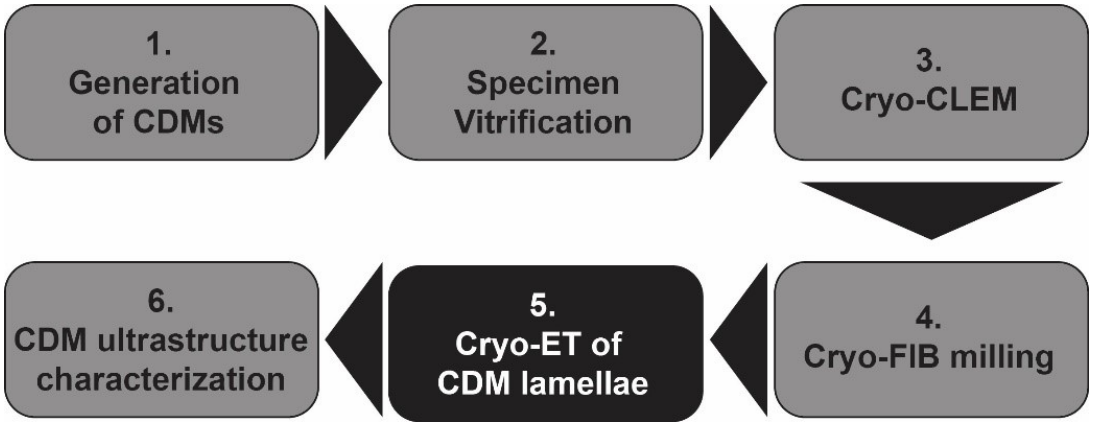

Cryo-lift-out lamellae were imaged on a TFS Titan Krios G3i. Samples were loaded, ensuring optimal lamella orientation in relation to the tilt axis, using the markings placed on the FIBSEM AutoGrids™ (shown in Figure 24) as guidance. The grid has to be oriented so that the tilt-axis is perpendicular to the milling direction. This ensures that the bulk of the half-moon grid finger and thicker parts of the lamella are not obstructing the view during tilt series acquisition (see Figure 45). Consequently, a larger area of the lamella can be used to acquire tilt series. To this end, the FIBSEM AutoGrids™ were loaded with the black side-markings facing up and down in the loading cassette.

All data acquisition was performed using the Serial EM software package (Mastronarde, 2005). Data acquisition was aided by Victor-Valentin Hodirnau (ISTA, EMF), who prepared the instrument for image acquisition, implemented and helped to test newly published scripts for tilt series acquisition, and provided technical support.

Medium magnification overview tile scans at a nominal magnification of 6,500x with a pixel size of 13.74 Å were acquired of all lamellae to assess their overall condition and vitrification state. This allowed the comparison of the different cryoprotectants used for HPF, see Figure 25 and Figure 47.

The survival rate of cryo-lift-out lamella transfer from the FIBSEM instrument to the TEM was assessed to be ≥80% (n = 30). Of these surviving lamellae, 20% were partially broken, and only small areas could still be used for data acquisition. Another ~20% suffered a crack that partially interfered with data acquisition in its immediate surrounding due to increased lamellae instability (see Figure 46). The remaining 60% were fully intact and suffered no or barely any restrictions for data collection.

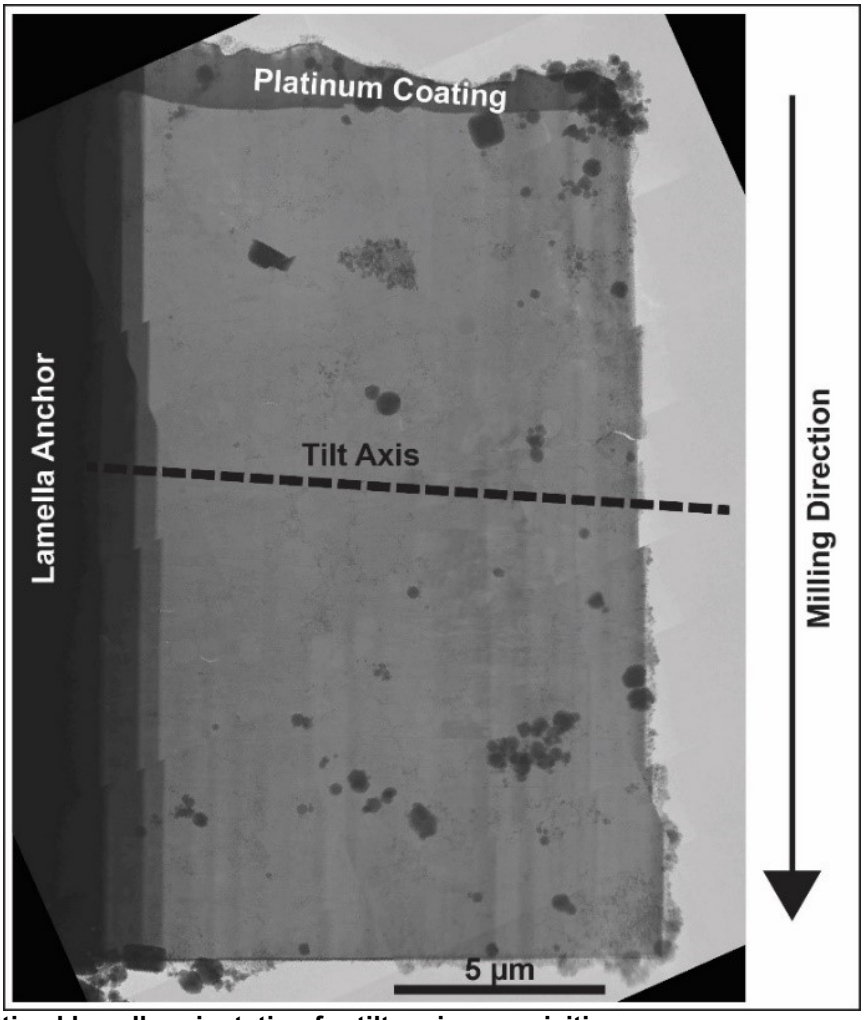

Figure 45: Optimal lamella orientation for tilt series acquisition.
The FIBSEM AutoGrid™ is inserted using the markings placed on it as guidance, resulting in a perpendicular orientation of the tilt axis to the milling direction. This ensures that the bulk of the half-moon grid finger and the lamella anchor are not obstructing the view during tilt series acquisition.

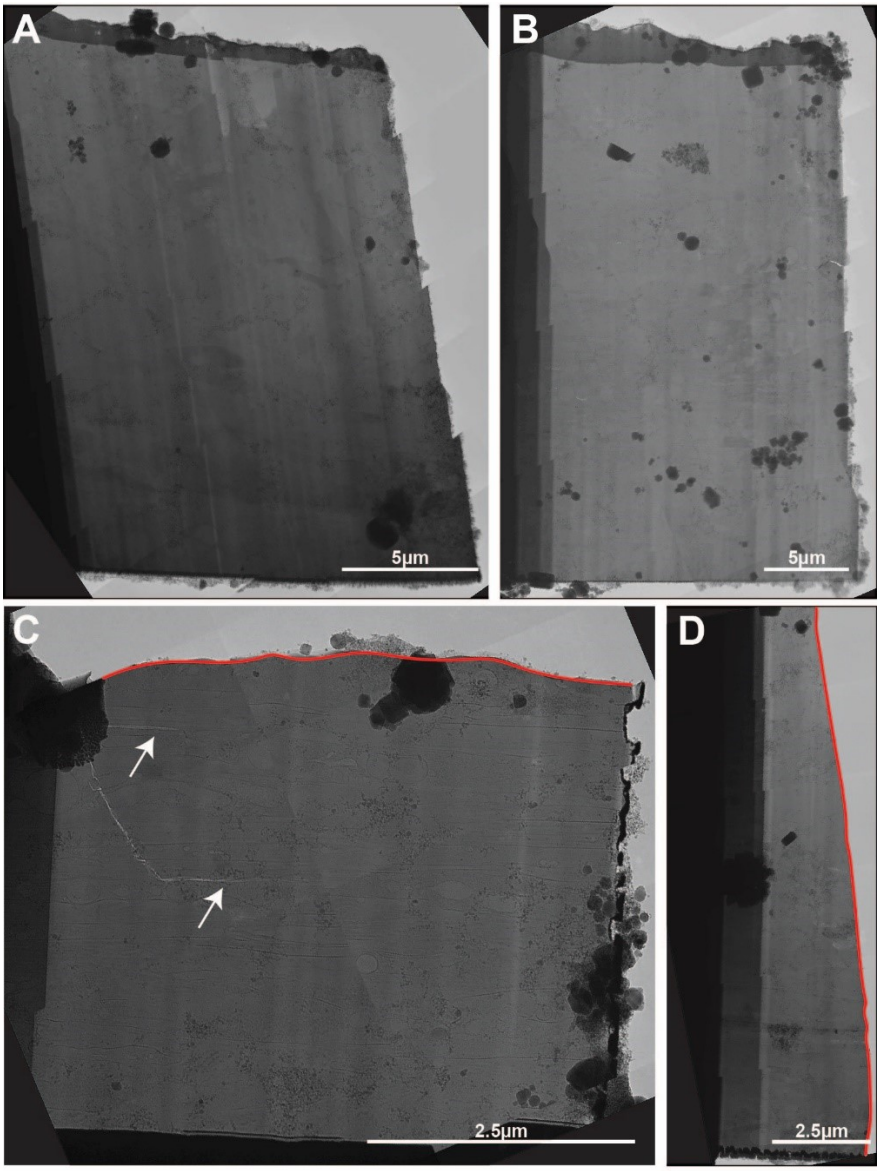

Figure 46: Examples of lamellae that survived sample transfer to the TFS Titan Krios 3Gi. 80% of lamellae survived sample transfer. A, B) Of these surviving lamellae, 60% were still fully intact and typically had an intact protective platinum layer. C) Around 20% of the surviving lamellae were partially broken. The fracture line is indicated with a red line. These lamellae could still be used for data collection, provided they were stable enough. In cases where fractures within the lamella occurred, as indicated here by white arrows, data acquisition was hampered in its direct surroundings. D) Some of the partially broken lamellae fractured along the milling direction and often broke close to the anchor site. This rarely allowed the collection of more than 1 to 2 tilt series.

3.4.1. Assessment of vitrification state of the cryo-lift-out lamellae

The vitrification state of the lamellae was determined by assessing the severity of hexagonal ice-induced reflections and the area size they covered. All high pressure frozen CDMs were vitrified to at least some degree and did not show the extensive damage caused by ice crystals that plunge-frozen CDMs displayed (see Figure 34 for comparison). Lamellae showed incomplete vitrification to different degrees. Severe cases of incomplete vitrification resulted in reflections spread throughout large areas of the lamellae that introduced strong differences in contrast and hampered data acquisition, see Figure 47, Panel A.

The tilt series that could be acquired on these lamellae did not result in high-quality tomograms. In mild cases of incomplete vitrification, only small areas of the lamella were affected and contrast differences were less drastic, as shown in Figure 47, Panel B. In these cases, data acquisition was still possible. However, the severity of the reflections changed with the used tilt angle, even in mild cases. In more severe cases, as shown in Figure 47, Panel A, tilt series acquisition often failed as the ice crystal reflections hampered area tracking and focusing, leading to an abortion of data acquisition already at low tilts.
Moreover, even in successfully acquired tilt series, a number of single tilts of the series had to be excluded during tomogram reconstruction due to the complete obscuring of all structures resulting from ice reflections over the whole micrograph. In severe cases, more than half of the tilt angles had to be excluded during tomogram reconstruction. Typically, lower tilt angles showed less severe reflections than tilt angles above ~±20°. Nevertheless, a number of tomograms reconstructed from tilt series acquired on lamellae with only mild reflections were comparable to those from completely vitrified lamellae.
Completely vitrified lamellae did not show any ice crystal reflections, both in the medium magnification overview tile scan and during the tilt series. An example is shown in Figure 47, Panel C. Tilt series acquired on stable regions of these lamellae regularly resulted in high-quality tomograms.

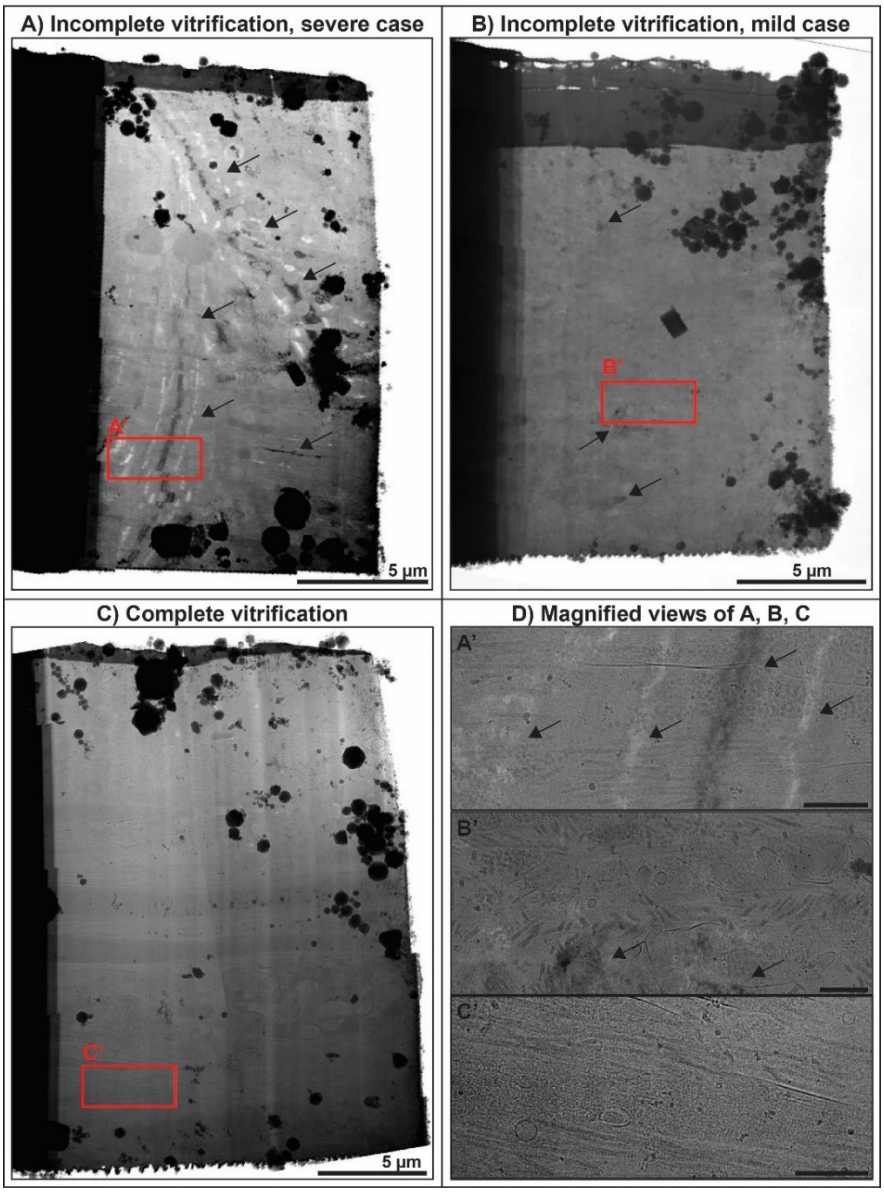

Figure 47: Assessment of the vitrification state of high pressure frozen lamellae.
Figure legend continued on next page.
Lamellae showed different degrees of vitrification depending on the cryoprotectant used. A) Some lamellae were incompletely vitrified and showed severe reflections of hexagonal ice over large areas, as indicated here by arrows. Typically, data acquisition on these lamellae was hampered by reflections. A magnified view of the area indicated by a red rectangle is shown in Panel D. The sample from which this lamella originates was frozen with 10%BSA in 0.1M PB (degassed). B) Some incompletely vitrified lamellae showed only mild reflections over small areas, as indicated by arrows. These reflections rarely prevented data acquisition of tilt series. A magnified view of an affected area, indicated by a red rectangle, is shown in Panel D. The CDM this lamella was prepared from was frozen in cell culture medium without the addition of cryoprotectants (no degassing. C) Completely vitrified lamellae showed no sign of reflections throughout the whole lamella in the overview tile scan and during tilt series acquisition. A magnified view of the area indicated with the red rectangle is shown in Panel D. The CDM this lamella was created from was frozen with 10% Dextran in 0.1M PB (degassed). D) Magnified views of the lamellae shown in Panel A, B, and C are shown here, as indicated in the left upper corners of the single images. Reflections stemming from hexagonal ice are indicated with arrows. Scale bar = 1 µm.

3.4.2. Challenges during data collection on cryo-lift-out lamellae

Lamella stability

I could observe that cryo-lift-out lamellae were less stable than bulk-milled lamellae. Cryo-lift-out lamellae were most stable close to their anchor and the protective platinum layer but were less stable with increasing distance to these two points. The instability could be seen in the form of lamella movement during image acquisition. For some lamellae, this resulted in low-quality images of the overview tile scan and improper stitching of the single images into a merged overview image (see Figure 48, Panels A and B, positions marked with an asterisk).

Different lamellae showed a different extent of this instability, which seemed to correlate with the lamella bending observed during cryo-FIB milling. Those lamellae that had already been unstable during FIB milling typically behaved similarly during TEM image acquisition. Some lamellae were bending and distorting during TEM imaging to such an extent that they could not be used for tilt series acquisition. Other lamellae were stable only in regions close to the anchor. These areas could be used to acquire data.

High-quality lamellae created with the optimized workflow typically only showed movement on the outer edge of the lamella; the majority of the lamella area could be used for data collection.

Factors that played into lamella stability were, as already during FIB milling, the vitrification state of the sample and their width. Additionally, also the intactness of the lamellae played a vital role. On several occasions, lamellae broke at positions where the platinum coating had been damaged and the lamella was consequently particularly thin or along a plasma membrane, as shown in Figure 48, Panel C and D. This often led to increased lamella instability and prevented data acquisition in the regions directly adjacent to the fracture. In some rare cases, very unstable lamellae broke away partially or fully during the acquisition of an overview tile scan.

Interestingly, on several occasions, the lamellae also fractured along intracellular membranes (see Figure 48, Panel E). These small fractures typically did not affect lamella stability unless they occurred on the outer edge of the lamella. Data acquisition directly on these sites was avoided.

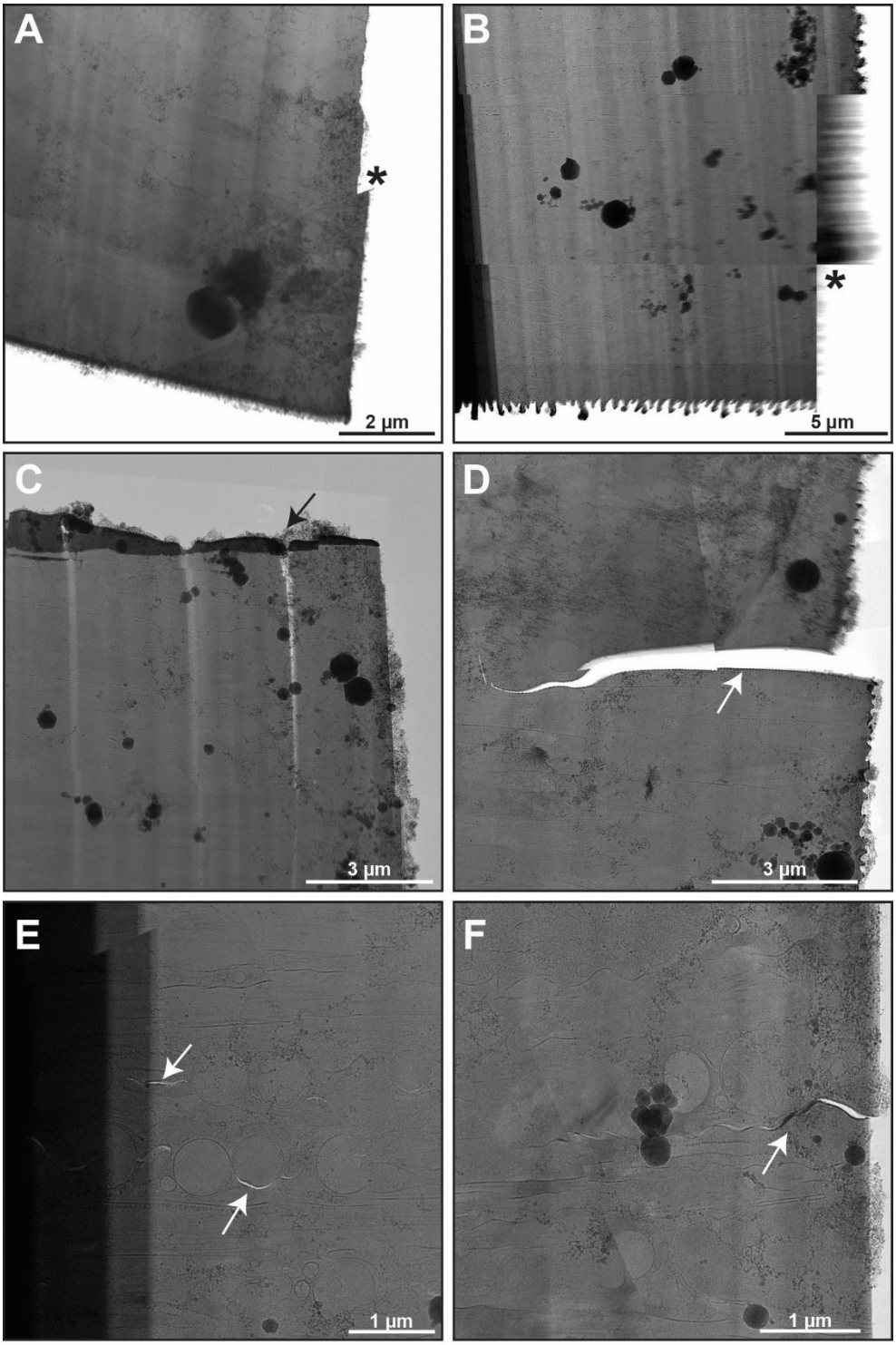

Figure 48: Examples of lamella instabilities.
A, B) Panel A shows a magnification of a region of the lamella shown in Figure 46. The regions of the lamellae furthest from the platinum coating and the protective anchor are typically the most unstable ones. Lamella movement during image acquisition regularly results in blurry, low-quality images of the tile scan overview that hamper tile alignment. An asterisk marks the site of failed tile stitching. C) Lamellae are more likely to break at sites of damaged platinum coating, where they have been thinned down more than in neighboring areas. An arrow indicates the site of breakage. D) In some instances, lamellae fractures along plasma membranes. The plasma membrane is indicated with a white arrow. E, F) In rare cases, lamellae fracture along intracellular membranes, as indicated by arrows. In E), fractures occurred along the membrane of vesicles. In F), a fracture occurred along an inner cellular membrane, the exact identity of which is unclear.

Charging effects on non-conductive lamellae could be at least partially responsible for lamella movement during image acquisition. Cryo-lift-out lamellae are more isolated than bulk-milled lamellae, leading to reduced charge-dissipation and hence accumulation during imaging. A new theory states that a thin layer of sputter-coated platinum could counter these detrimental charging effects (Sven Klumpe, personal communication, (Khavnekar et al., 2022)).

Lamella contamination

Cryo-lift-out lamellae act as a cold finger as they protrude out of the sample and attract residual water molecules during sample transfer and storage. Big ice crystals obscured target areas in several instances, and, in some cases, heavy contamination prevented data collection completely (see Figure 49).

An initial observation by Victor-Valentin Hodirnau, allowed the investigation of a potential countermeasure to reduce contamination: Cryo-lift-out lamellae that had been loaded several days prior to TEM imaging seemed to carry fewer ice crystals than usual. This led to the hypothesis that the application of high vacuum over a prolonged period of time in combination with the vibrations caused by the Turbo pump of the Autoloader of the TFS Titan Krios might remove contamination.

To test this hypothesis, samples were loaded ≥36 h prior to data acquisition and left in the AutoLoader of the TFS Titan Krios G3i TEM with the Turbo pump on. The sampling size was once again small, with only 25 lamellae. Of these 25 lamellae, 52% barely had any contamination, 40% had a low level of contamination that still allowed for data collection in at least some areas of the lamellae, and 8% were so strongly contaminated that data collection was not possible (see Figure 49 for a comparison).

In comparison, of 9 lamellae loaded directly before data acquisition, 6 had a low level of contamination that still allowed data collection in some areas (~67%), and 3 were too contaminated to allow any data acquisition (~33%). None of them were free of contamination.

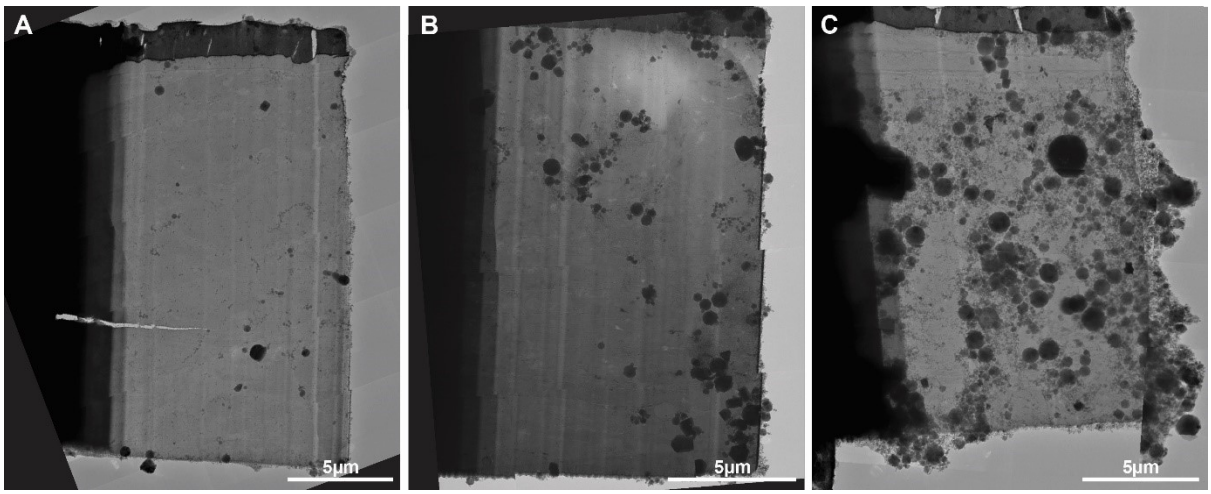

Figure 49: Lamella contamination comparison.
A) Shows a lamella with barely any contamination, allowing data acquisition with almost no restrictions. B) Shows a lamella with a low level of contamination that still allows data collection in some areas. C) Shows a heavily contaminated lamella that could not be used for data collection.

A more thorough investigation on the efficiency of contamination reduction by high vacuum application to the lamellae prior to imaging would be interesting but was not conducted due to time restraints. However, based on these numbers, I recommend using the above-described cleaning procedure on lamellae whenever possible

(although noting that access time to a Titan Krios will be limiting for regularly using this approach).

3.4.3. Tilt series acquisition

Tilt series were acquired at a nominal magnification of 42,000x, resulting in a pixel size of 2.137 Å, with a dose-symmetric dual-walkup tilt scheme (Hagen-scheme)(Hagen et al., 2017). For all tilt series, the pre-tilt of the lamellae was taken into consideration and compensated for to start at 0° lamella tilt. Typically, this pre-tilt was at ±9°, based on a stage tilt of 16° during lamella generation. Starting from the lamella 0° tilt, a tilt range from -60° to +60° in 2° or 3° increment steps was chosen.
All acquisition parameter settings used for data collection are listed in Table 6.

Table 6: An overview of the acquisition parameter settings used for data collection on cryo-lift-out lamellae.

Acquisition Parameter	Acquisition Setting
Microscope	TFS Titan Krios G3i
Acquisition software	Serial EM, version 4
Voltage (kV)	300
Detector	K3 Direct Electron Detector
Energy-filter	Gatan BioQuantum energy-filter
Energy-filter slit width (V)	20
Pixel size (Å/pixel)	2.137
Spot size	7
Defocus (microns)	-8
Acquisition scheme	Hagen-scheme
Sample pre-tilt	Yes
Tilt range	-60° to +60°
Tilt increment	2° or 3°
Objective aperture	70
C2 aperture	70
Total electron dose	180
Nominal magnification	x42,000
Frames/tilt	8

Initially, tilt series acquisition on cryo-lift-out lamellae was performed using both the SerialEM tilt series controller and a SerialEM script from Wim Hagen (EMBL Heidelberg) (Hagen et al., 2017).
One problem of tilt series acquisition on lamellae is the loss of acquisition area due to the need for focusing/tracking areas. Each tomogram requires a focusing/tracking area along its tilt axis during data acquisition. This area must be stable and have sufficient features to allow tracking. However, this means that 50% of a lamella's potential acquisition area cannot be used for data collection as it is exposed to a high dose of electrons during tracking and focusing. This percentage can be lowered by reusing tilt series sites as tracking area for the next tomogram. Even so, the loss of these tracking areas for data acquisition further reduces the number of tilt series that can be acquired on a cryo-lift-out lamella and, thereby, the overall possible throughput.
Eisenstein et al. recently introduced a new method for parallel cryo electron tomography (PACE-tomo) (Eisenstein et al., 2022). In this method, optical image shifts are used to record tilt series in parallel with only a single tracking area. This opens up

areas that would otherwise have to be sacrificed for tracking and decreases the time investment per tilt series. This maximizes the amount of data that can be collected per lamella and increases the throughput. This method was implemented for cryo-lift-out lamellae with the help of Victor-Valentin Hodirnau. Based on my experience, I highly recommend using PACE-tomo for tilt series acquisition on lamellae.

3.5. Visualization of native CDMs by cryo-ET

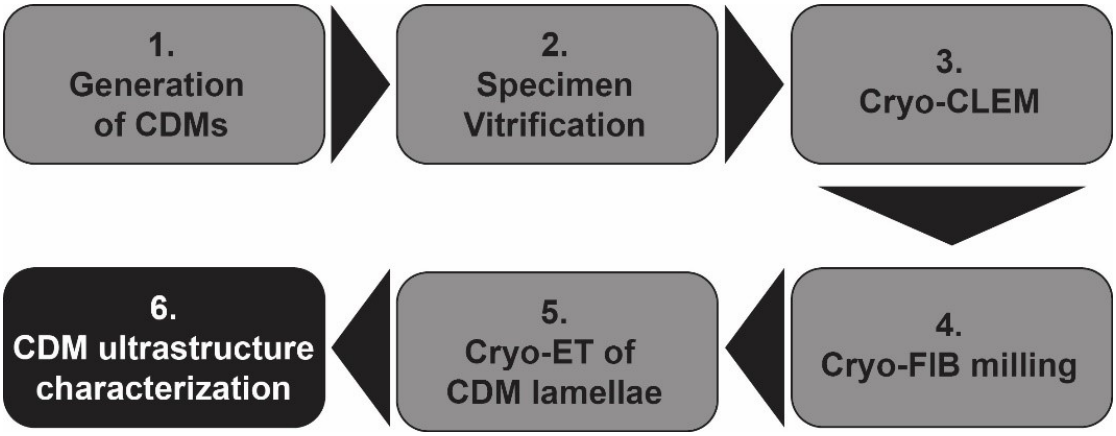

Figure 50 shows an example overview image of a representative lamella region of D14 TIFF CDMs. This figure illustrates the general orientation of the lamella overview image in relation to the cryo-lift-out block. Figure 50, Panel A shows a cryo-SEM image of the lift-out block used for lamella generation. The platinum coating is on top of the specimen, and the top of the CDM layer is directly below it. A region of this lift-out block after successful lamella generation is shown in Figure 50, Panel B as a medium magnification cryo-TEM image. Here, the top of the CDM layer is at the top of the image, and the bottom part of the CDM layer, closer to the EM grid, is at the bottom. All subsequent lamella overview images and tomograms have the same orientation. All images shown in sections 3.5 and 3.6 originate from fully vitrified lamellae of specimens that were high pressure frozen without chemical fixation unless stated otherwise.

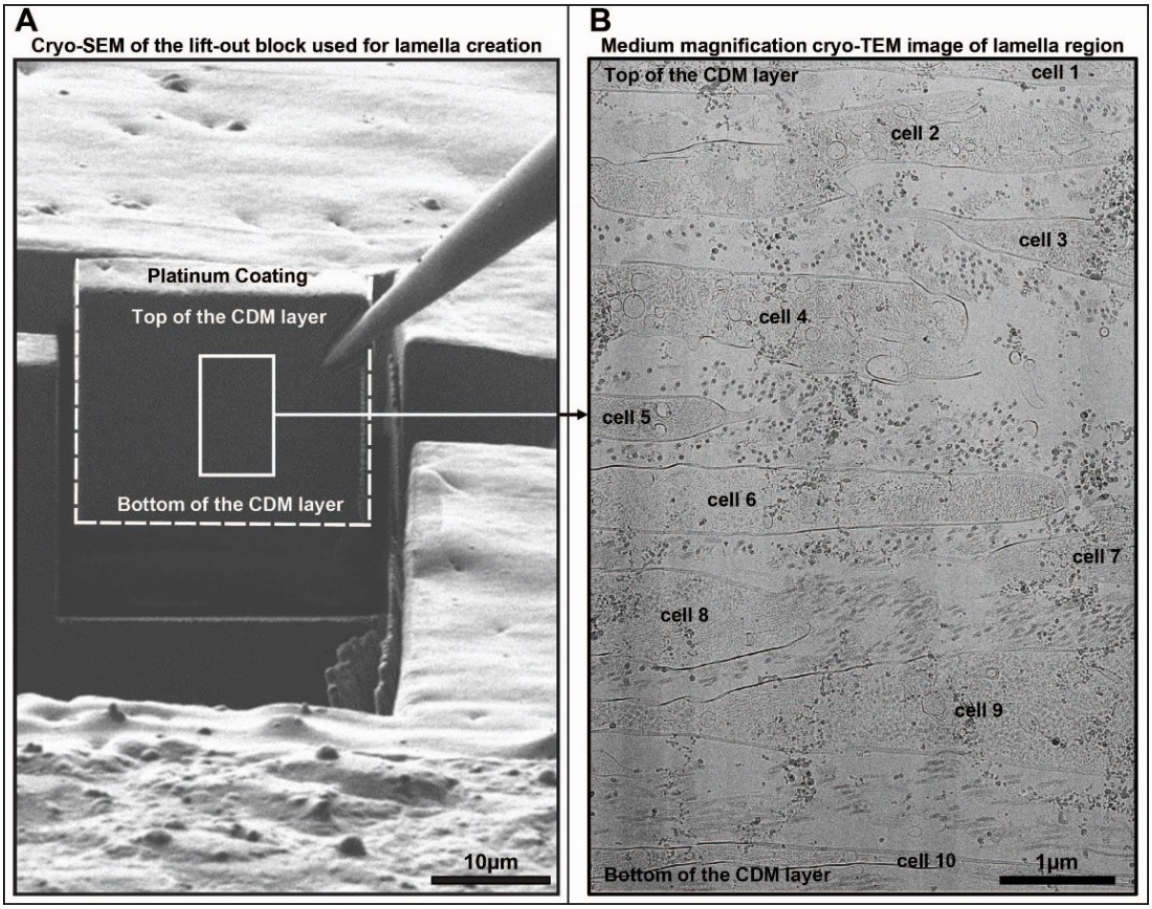

Figure 50: The orientation of lamella overview images in relation to the cryo-lift-out.
A) A cryo-SEM overview image of the lift-out block on the micromanipulator needle during the lift-out process shows its general orientation. The top of the CDM layer is covered with the protective platinum layer. B) The medium magnification cryo-TEM image shown here has been selected for a lamella region where several tomograms have been acquired. This overview image reveals what are presumed to be several individual cells stacked in layers on top of each other (see annotations), surrounded by extracellular matrix structures.

The medium magnification overview image of a cryo-lift-out lamella shown in Figure 50, Panel B reveals the CDM ultrastructure. Single details are shown at higher magnification in Figure 51.
Several TIFF cells are stacked above each other (annotated in Figure 50, Panel B), with thinner cell protrusions reaching into the extracellular space between two thicker cell bodies. TIFF cells typically have a very elongated but slim morphology, allowing them to stretch to a length of more than 25 µm while remaining not more than 2.5 µm high even at their nucleus (see Figure 51, Panel F). This morphology makes it difficult to understand from which cell a protrusion originates from. They may belong to one of the cells within the field of view of the lamella or a cell outside of the lamella volume.
For example, cell 5 annotated in Figure 50, Panel B, could be the protrusion of a cell outside of the lamella volume, but it could also originate from cell 4 or 6. This aggravates the understanding of whether the observed cell parts belong to one cell or have to be viewed as separate cellular entities.
In between cells, the extracellular space is predominantly filled with filaments, some of them parallel to the electron beam and some perpendicular to it. Interestingly, their direction changes over the depth of the lamella. In the regions closer to the top of the CDM, they are consistently oriented parallel or close to parallel to the electron beam, resulting in a cross-section view of them (see Figure 50, upper part of Panel B and

Figure 51, Panel E and G). In contrast, closer to the bottom of the CDM these fibers are orientated more perpendicular to the electron beam (see Figure 50, lower part of panel B, and Figure 51, Panel H-J). These fibers that were oriented parallel to the tilt axis (and orthogonal to the electron beam) were often observed to have a distinct banding pattern, which led me to believe that they are a type of collagen. This will be discussed in more detail further down.

In these medium magnification overview images, I could also consistently observe an increasing density of ECM from the bottom close to the EM substrate to the top in 16 different lamellae. The lamella overview images showed that empty spaces exist within the ECM and can be found throughout the whole depth of the CDM. However, these empty spaces are often larger in the upper layers than in the lower layers (compare Figure 51, Panel C-G to Panel H-J). In lower layers, there are fewer and smaller empty spaces, and ECM fibers are more densely packed (see Figure 51, Panel D-J). These observations are subjective, as no measurements and statistics were performed at this point.

This likely reflects how the ECM is synthesized: The bottom layer of the cells initiates ECM production hours after seeding (as shown in section 3.1.2.2.1). As time progresses, the bottom part of the CDM already grows denser close to the substrate and is slowly built up from there. The top part of the CDMs does not yet have a fully formed ECM (see Figure 51, comparison of Panels A-D to Panel H-J).

The carriers are designed to have a recess that has slightly more depth than the CDMs, although a potential machining inaccuracy of ~5 µm must be taken into consideration. Indeed, different specimens show differences in the top layer of the lamella directly beneath the platinum coating.

In some of them, a relatively empty zone of ~2-4 µm is located directly below the platinum coating, which still contains some vesicles and cellular protrusions. At times, a high density of membrane protrusions and vesicles can be seen in areas close to the surface of the CDM (as shown in Figure 51, Panel A). These could be indicative of the secretion of high amounts of ECM proteins. In lamellae derived from other specimens, the cells sit directly below the platinum layers and typically contain a high number of vesicles of different sizes (Data not shown).

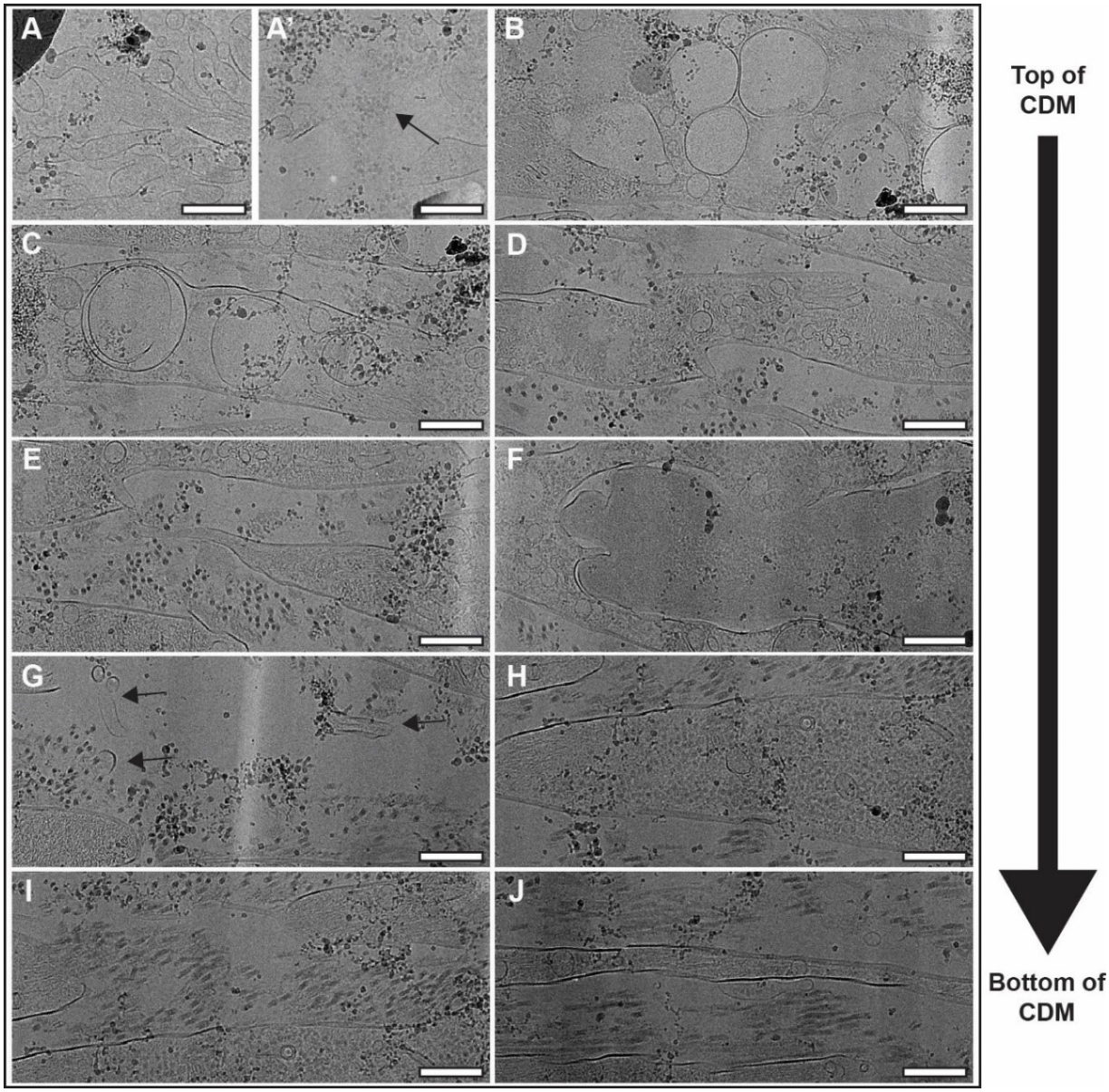

Figure 51: An overview of different features of interest throughout the CDM.
Single images originate from the lamella shown in Figure 50, Panel B, and are shown at a higher magnification here. Scale bars = 500 nm. They are ordered from their position within the CDM from top to bottom, as indicated by the arrow on the right. A) In some cases, membrane protrusions could be seen at the very top of the cryo-lift-out lamellae. A') Granules of unknown identity were also observed in the top layer on several occasions, indicated by an arrow. They were not present in lower layers. B-C) Cells closer to the top of the CDM often contain large vesicles with a size of 500-1500 nm. Vesicles in this image have a size of up to 800 nm. D) Vesicle size and density in cells decreased the closer to the CDM bottom they were. Vesicles in this image only have a size of 100-200 nm. E) ECM fibers closer to the top of the CDM typically were parallel to the electron beam, resulting in a cross-section image of them. F) The nucleus of a TIFF cell is relatively narrow, with a width of only 2-2.5 µm. Here, also small vesicles can be seen between the nucleus and the plasma membrane. G) Within the ECM, empty spaces could be seen. These were typically bigger and more frequent closer to the top of the matrix. Vesicles of different sizes and shapes were also present in these layers (indicated here by arrows). H) Fibroblasts closer to the bottom of the CDM contain fewer vesicles and are often packed with granules. I, J) In the layer close to the EM substrate, the collagen fibers typically run perpendicular to the electron beam, offering a view over their length. There appear to be fewer and smaller empty spaces in the ECM.

Interestingly, in the upper layers of the CDM, granules of some kind could also often be seen intra- and extracellularly (shown in Figure 51, Panel A'). The identity of these granules remains unclear, but they could be unassembled ECM components.
This further supports the idea that the CDM is at different stages of assembly at different depths, and the fibroblasts are more active closer to the top of the CDM than at its bottom.
In the uppermost layer of the 16 assessed lamellae, cells often contain several big vesicles with a diameter of ≥500 nm (see Figure 51, Panel B-C). These vesicles are typically rather electron-transparent, and no cargo can be seen at this magnification and acquisition settings. However, they could potentially play a role in ECM synthesis and excretion. Lower down in the CDM, the cells typically only have smaller vesicles of only ~100-200 nm (see Figure 51, Panel D-F). Toward the bottom of the CDM, the cells contain fewer vesicles and, instead, more often granular densities (see Figure 51, Panel H). This could indicate that these fibroblasts are less active in the synthesis and excretion of ECM proteins and, thus, that the ECM production is slowed down in the lower layers that already have a denser matrix than in the upper layers.
Vesicles can also be found in the extracellular space in some instances, as shown in Figure 51, Panel E. Their identity is unclear, and they vary in size and shape. Some seem to contain some sort of density, but further investigation requires additional data. At this point, these observations are subjective as no systematic measurements and statistics on these vesicles have been performed yet.

ECM fiber orientation throughout the CDM

After observing the change in ECM fiber orientation over the depth of the CDM, I wanted to get a better overview of both ECM fiber and cell orientation. Moreover, it remained unclear whether the cell bodies and protrusions throughout the CDM depth were likely to originate from a few cells with several protrusions or rather from several different cells stacked on top of each other. The limited field of view of the cryo-lamellae (~15 x 20 µm) made this difficult to interpret. Often, only a small volume of each cell in the lamellae was visible, and cell alignment and connectivity could not be judged.
To address these questions, D14 TIFF CDMs were grown on coverslips and prepared for array tomography. Array tomography is a volumetric microscopy method based on physical serial sectioning. For this thesis, samples were prepared as described in section 5, Materials and Methods. Briefly, samples were fixed, contrasted, and resin embedded before sectioning into 70 nm thick slices that were serially imaged by SEM and then semi-automatically aligned using IMOD.
An area of ~120 x 120 µm was scanned over ~15 µm depth, allowing visualization of cell and ECM fiber arrangement throughout the CDM (see Figure 52, single images are ~2.8 µm apart).
The array tomography showed a change in the direction of fibroblasts and ECM fibers over the height of the CDM, confirming that the ECM fibers stayed aligned with the cells throughout TIFF CDMs. This observation is in line with my findings in the medium magnification TEM images of lamellae, where ECM fibers changed direction depending on their positin in the CDM.

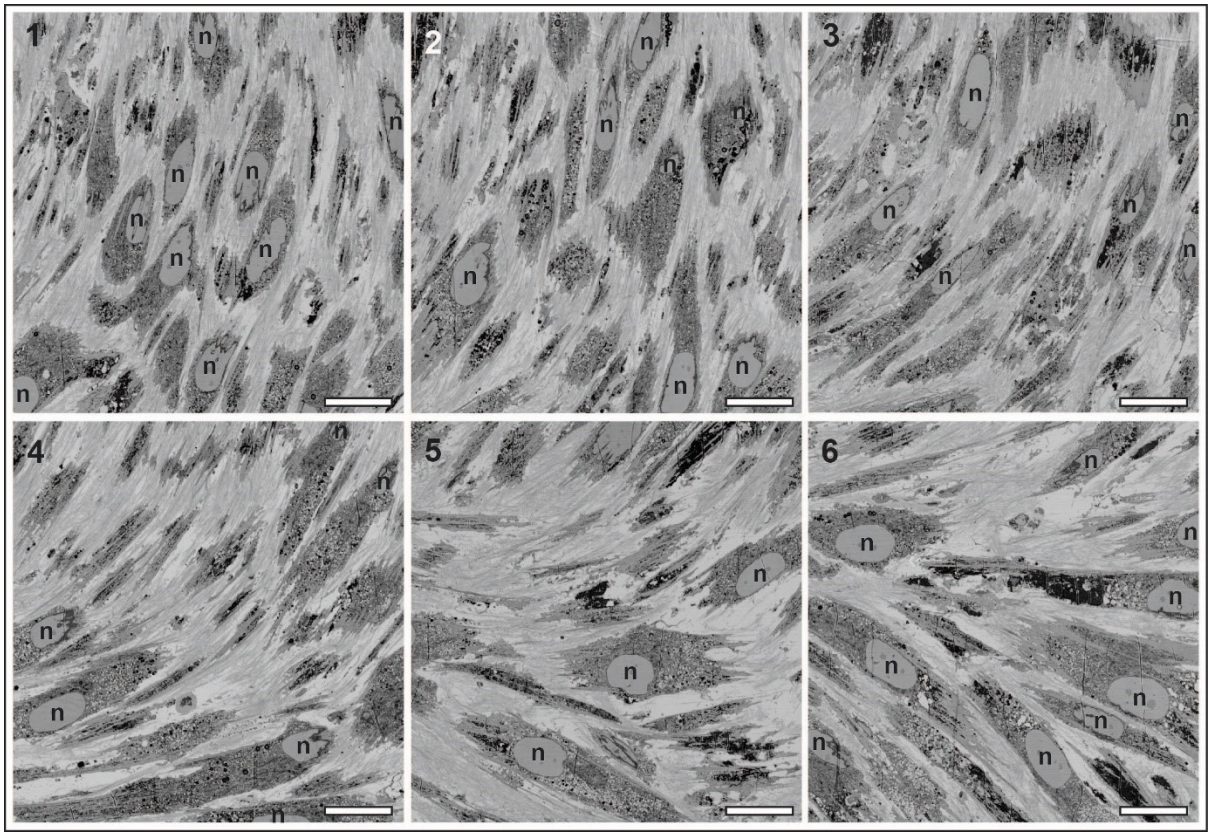

Figure 52: Array tomography of D14 TIFF CDMs shows that ECM fibers stay aligned to fibroblasts.

CDMs were prepared for array tomography and sectioned into 70 nm slices. An area of ~120 x 120 µm was scanned over ~15 µm depth to determine cell and ECM fiber orientation over the depth of the CDM. The single images of the array tomography shown here are ~2.8 µm apart, starting at the bottom (1) and running to the top (6) of the CDM. A change in the direction of fibroblast alignment is evident, and the ECM fibers stay aligned with the cells throughout the depth of the CDM.
The nuclei of each cell are marked with n; the darker areas surrounding them are the cell bodies, and the light grey areas in between consist of ECM fibers.
Scale bar = 20 µm.

In lamella overview images, I could observe that the CDM grew less dense toward the top (see Figure 50, Panel B for an example), with fewer cells and collagen I fibers. The array tomography did not reflect this result.
This effect of decreasing CDM density from bottom to top is likely more evident in the cryo-lift-out lamellae because they reach a depth of ~20 µm from the top of the CDM. In contrast, the array tomography spans a depth of ~15 µm, starting from closer to the bottom of the CDM. Hence, it does not cover the top layers of the CDM that show the lowest density of cells and fibers, which makes a direct comparison between these two techniques impossible.
However, the array tomography did show that the TIFF cells do not form extensive protrusions. This makes it more likely that the cell bodies and protrusions seen at some distance from each other in the lamella overview pictures belong to different cells rather than the same cell.

Tomograms of fully vitrified cryo-lift-out lamellae

Tomograms shown here were acquired on fully vitrified lamellae and reconstructed from acquired tilt-series using either IMOD (Kremer et al., 1996) or AreTomo (Zheng et al., 2022). All lamellae originate from two different TIFF CDMs that were prepared

as detailed in the previous sections of this thesis. Weighted back-projection (WBP) and patch tracking were used for the final tomogram reconstruction, with a binning of 8 to keep the individual file size low and ease visual assessment of the observed structures. During reconstruction, single tilts of low quality that showed significant image shifts, strong reflections caused by hexagonal ice, or blurring were excluded. Tomograms were removed from the data pool if more than half of the tilts had to be discarded. After reconstruction, every tomogram was visually assessed in IMOD for correct alignment and content.
For the future investigation of structures of interest, tomograms will also be reconstructed with a lower binning of 4 and 2 to potentially reveal further details and allow for more accurate measurements.
Of 59 tilt series collected on vitrified lamellae, 25 (~42%) could not be successfully reconstructed because either too many single tilts had to be removed or the alignment during tomogram reconstruction did not work out. 23 (~39%) tomograms were high-quality; they contained extracellular structures, had been successfully aligned, and had high contrast that allowed me to identify cellular and extracellular structures. The remaining 11 (~19%) tomograms were of acceptable quality but had lower contrast, making structures more difficult to discern. The reason for this relatively high proportion of unsuccessfully reconstructed tomograms will be discussed in more detail later in section 3.6. The success rates are also summarized in a figure there (see Figure 62).
Examples of high-quality tomograms are shown in Figure 53. Within the cells several structures are discernable: vesicles (v), microtubules (mt), actin filaments (a), intermediate filaments (if), and plasma membranes (pm). The vesicles within the cells are typically round and of different sizes, as described earlier. The extracellular matrix predominantly contains thicker fibers that show a distinct banding pattern when running parallel to the tilt axis, leading me to assume they are collagen (col). Smaller fibers are also visible in some tomograms (f), interspersed between collagen fibers, but they are more difficult to discern.

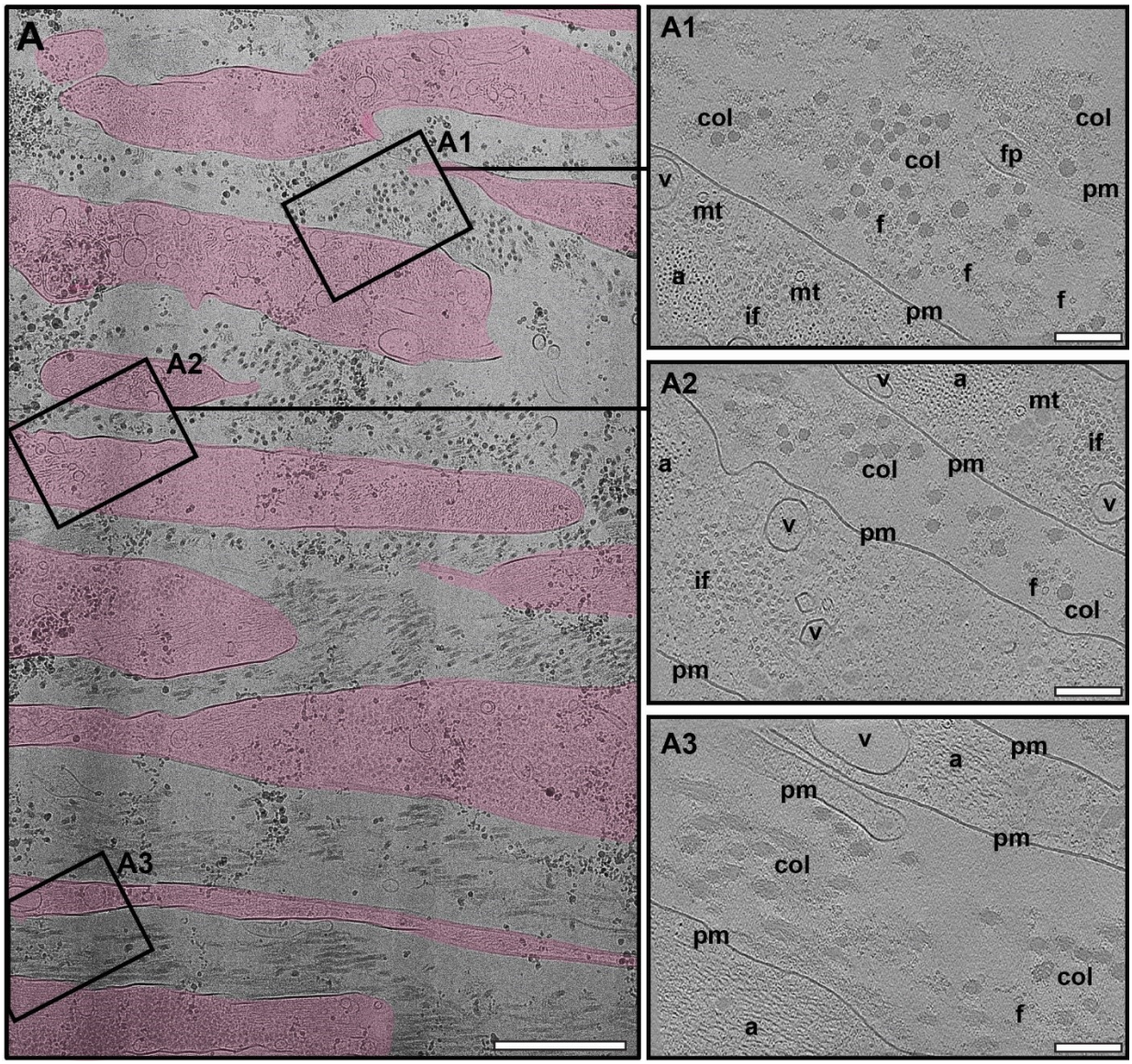

Figure 53: High-quality tomograms acquired from vitrified lamellae reveal intra- and extracellular structures.

A) A medium magnification cryo-TEM image of a lamella region on which several tilt series were acquired. Cells (marked in pink) are embedded within the ECM in several layers. The ECM shows a high content of fibers running in different directions. At medium magnification, collagen fibers are the main feature visible in the ECM. Tilt series were acquired in areas containing collagen and other extracellular structures, as indicated by black rectangles. A1, A2, A3 show a sum of 10 computational slices (= 17 nm) through a tomogram of the specified area. Different intra- and extracellular features are annotated: actin filaments (a), intermediate filaments (if), plasma membranes (pm), vesicles (v), filopodia (fp), microtubules (mt), collagen (col), and unidentified extracellular fibers (f). **Figure continued on next page.**

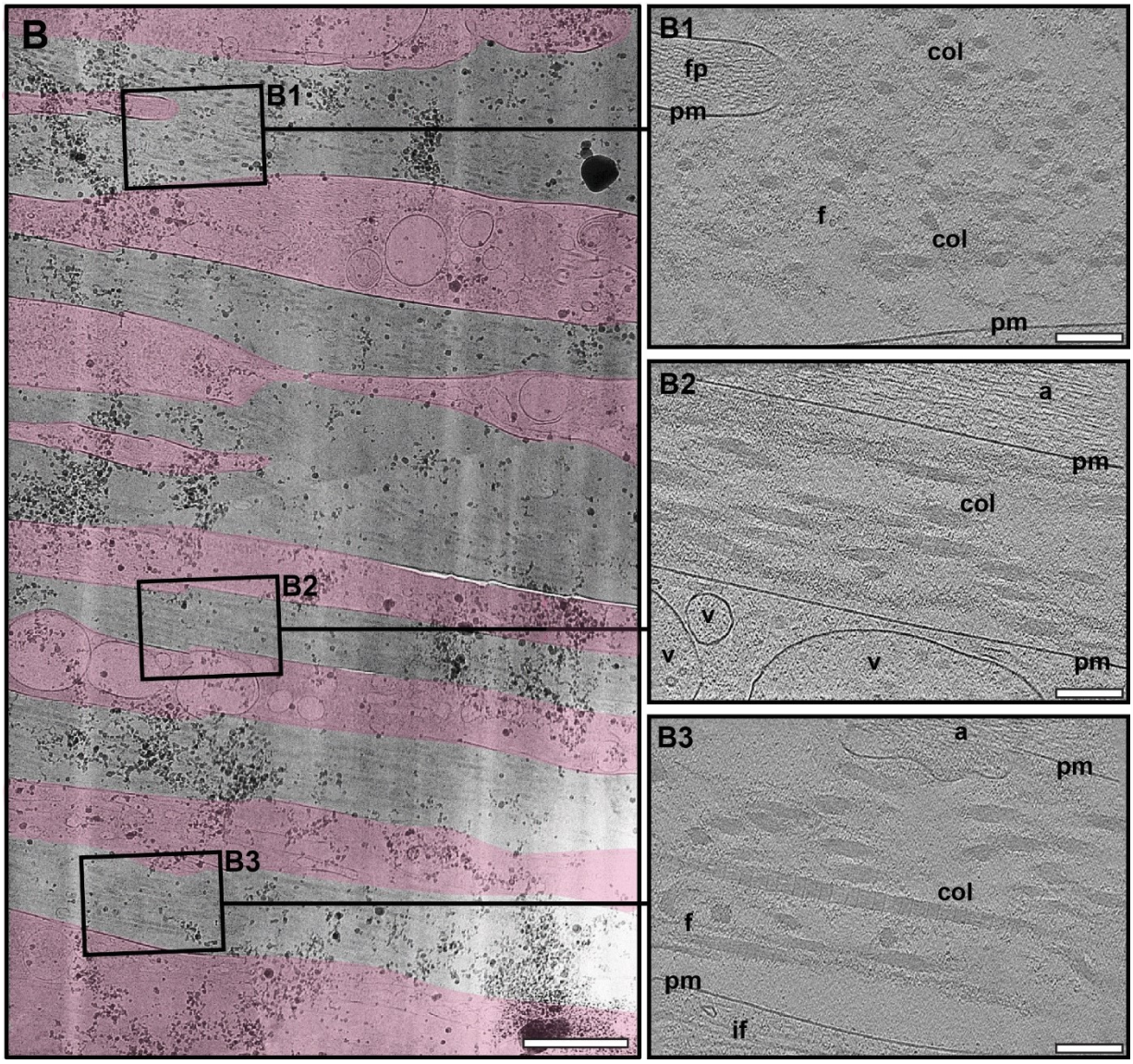

Figure 53 continued.
B) A medium magnification cryo-TEM image of a different lamella on which several tilt series were acquired, marked with black rectangles. Collagen fibers can be seen running in between the cells. In this lamella, the thickness is not as uniform as in A, as evidenced by the difference in contrast toward the lower right corner. The lamella also shows higher contamination; however, tilt series acquisition was not significantly hampered. B1, B2, B3 show a sum of 10 computational slices (= 17 nm) through a tomogram of the specified area. Different intra- and extracellular features are annotated: actin filaments (a), intermediate filaments (if), plasma membranes (pm), vesicles (v), filopodia (fp), microtubules (mt), collagen (col), and unidentified extracellular fibers (f).
Scale bar on A and B = 1 µm. Scale bar on A1-B3 = 200 nm. All tomograms were reconstructed by weighted back-projection and patch tracking.

Below I give a summary of characteristic structural features I could visualize in tomograms of CDM.

Filopodia

High-quality tomograms allowed the identification of several structures, such as cell protrusions that are likely filopodia (fp in Figure 53, Panel A1 and B1). They contain bundled actin filaments running parallel to each other, a hallmark of filopodia (Mattila and Lappalainen, 2008). Other protrusions, such as the one shown in Figure 53, Panel

A3, do not contain these bundled actin filaments and sit very close to cell bodies. These cellular structures could originate from cells just outside the lamella volume and be the edge of a cell body rather than a protrusion into the ECM. It is also possible that they still belong to the cell they are close to and are only separated from the main cell body by an invagination located in the lamella volume. With the given data, this detail remains unclear.

Microtubules

Microtubules (mt in Figure 53, Panel A1) were found in several cells in cryo-lamellae and were most visible in their cross-section view.

In the cross-section view, the 13 protofilaments composing the microtubule (Tilney et al., 1973) can be clearly identified. Interestingly, an inner density can be spotted in all microtubules in this orientation. This inner density was initially described primarily as globular proteins (Coombes et al., 2016; Garvalov et al., 2006), but our data suggest a more filamentous assembly to be present within the microtubule lumen in the majority of side-views (see Figure 54, Panel B). Recently, it was suggested that filamentous F-actin can be present in the lumen of microtubules (Paul et al., 2020). However, (Paul et al., 2020) employed cell treatments that resulted in extensive microtubule network remodeling and extrusion of the microtubules from the cytoplasm. This posed the question of whether the observations were an artifact caused by this very treatment or represented the physiological state of microtubules. Investigating the inner densities I see in my data derived from natively preserved cells could potentially help to answer this question. A closer study of the pitch of the filaments we see in the microtubule lumen could help to elucidate whether it is indeed F-actin that we see here (Hylton et al., 2022). However, currently only a low number of microtubules is available in my data, so the acquisition of more tilt series might be necessary for this.

Actin filaments and intermediate filaments

Actin and intermediate filaments (a and if in Figure 53) are visible in almost all cells in the lamellae. The actin filaments were measured to have a diameter of ~6-8 nm, and intermediate filaments to have a diameter of ~11-12 nm. This fits with the reported dimensions in the literature (Fäßler et al., 2020a; Kirmse et al., 2010). Interestingly, these two populations do not appear to mix and were consistently found to occupy different areas of the cells. Higher magnification images are shown in Figure 54, Panels C and D.

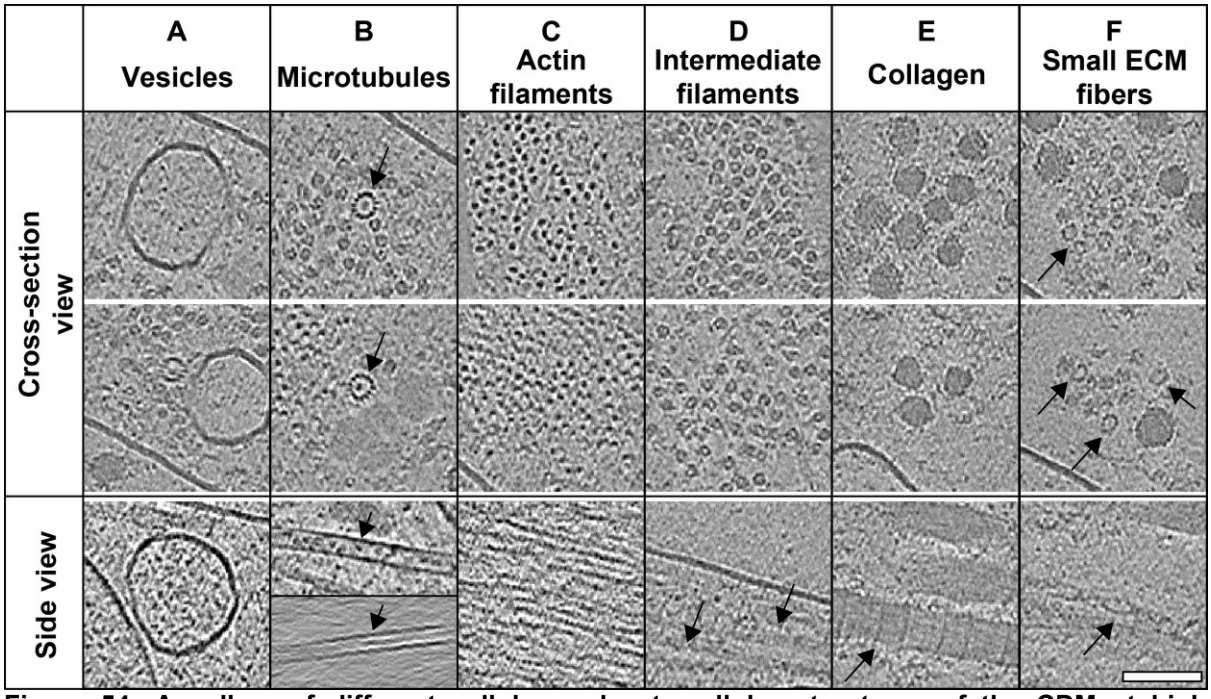

Figure 54: A gallery of different cellular and extracellular structures of the CDM at high magnification.

The images shown above were cropped from the tomograms shown in Figure 53. All images are a sum of 10 slices (=17 nm). Scale bar = 100 nm.

A) Vesicles of different sizes can be found throughout the cells in the CDM. These vesicles are typically bigger and more frequent in cells closer to the top of the CDM. B) Microtubules were seen in several cells on different lamellae, annotated here by arrows. They are easier to spot when they are viewed as a cross-section. The edges of 13 protofilaments can be seen if the microtubules are perfectly parallel to the electron beam. An inner density can be seen in all of these microtubules that are oriented parallel to the electron beam. This density is less apparent in the side view. C) Actin filaments are found throughout the cell. They typically did not mix with intermediate filaments, which are shown in D). E) Collagen fibers of different diameters are the main component of the extracellular space in CDMs. The collagen banding pattern, indicated with an arrow, can be seen in collagen fibers that run perpendicular to the electron beam and relatively parallel to the tomogram volume. F) Smaller ECM fibers are interspersed in between collagen filaments. They are more discernable in their cross-section view and rather hard to spot in their side view. The small ECM fibers are annotated with arrows.

Extracellular matrix fibers

Throughout the depth of the CDMs, collagen fibers (col in Figure 53) were visible. As described before, their orientation changed with the orientation of the cells. This resulted in the acquisition of tomograms with cross-section views closer to the top of the CDM and tomograms with side views of collagen fibers running parallel to the tilt axis toward the bottom of the CDM. Figure 53 shows collagen fibers in different views. Higher magnification images are shown in Figure 54, Panel E. When looking at the collagen fibers in a cross-section view, it becomes evident that they do not have a uniform diameter. The characteristic collagen banding pattern is only evident in a side view of a collagen fiber. Smaller ECM fibers are seen more rarely and are typically interspersed between collagen fibers. They have a beaded appearance (see Figure 54, Panel F) in their cross-section view but tend to be more difficult to discern in their side view.

In these tomograms, the ECM is visualized for the first time in its native state at this unprecedented resolution. The complexity of the data and the wealth of information contained in these tomograms makes it challenging to identify the different structural

features. For many ECM components, no high-resolution information is available yet, and hence, there is no comparative information. Thus, while I can visualize all of these components for the first time *in situ* in their native state and cellular context, I cannot unambiguously assign identities at this point. One of the approaches to overcome this issue was the immunogold labeling discussed in section 3.1.2.2.4. However, it did not result in the successful labeling of specific ECM proteins.
One approach to facilitate determination of the nature of the extracellular filamentous densities was to improve the visualization of ECM further, as discussed below.

3.6. Characterization of native ECM structures by cryo-ET

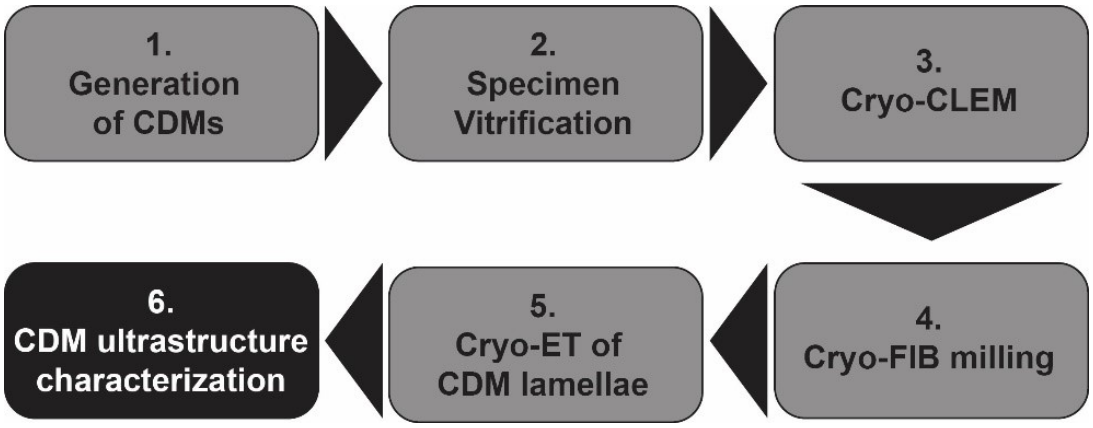

High-quality tomograms were further processed with the deep-learning based tool IsoNet (Liu et al., 2022) to fill in the missing wedge information and improve the SNR. IsoNet processing enhanced the visibility of the different structures (e.g., plasma membranes, vesicles, and ECM fibers) in tomograms and facilitated their identification. This greatly improved the success of manual measurements, automatic fiber tracking, and manual segmentation. The effect of the IsoNet processing strongly depended on the initial quality of the tomograms and was only tested with the best tomograms I had available. Examples of IsoNet-processed tomograms are shown in Figure 55.

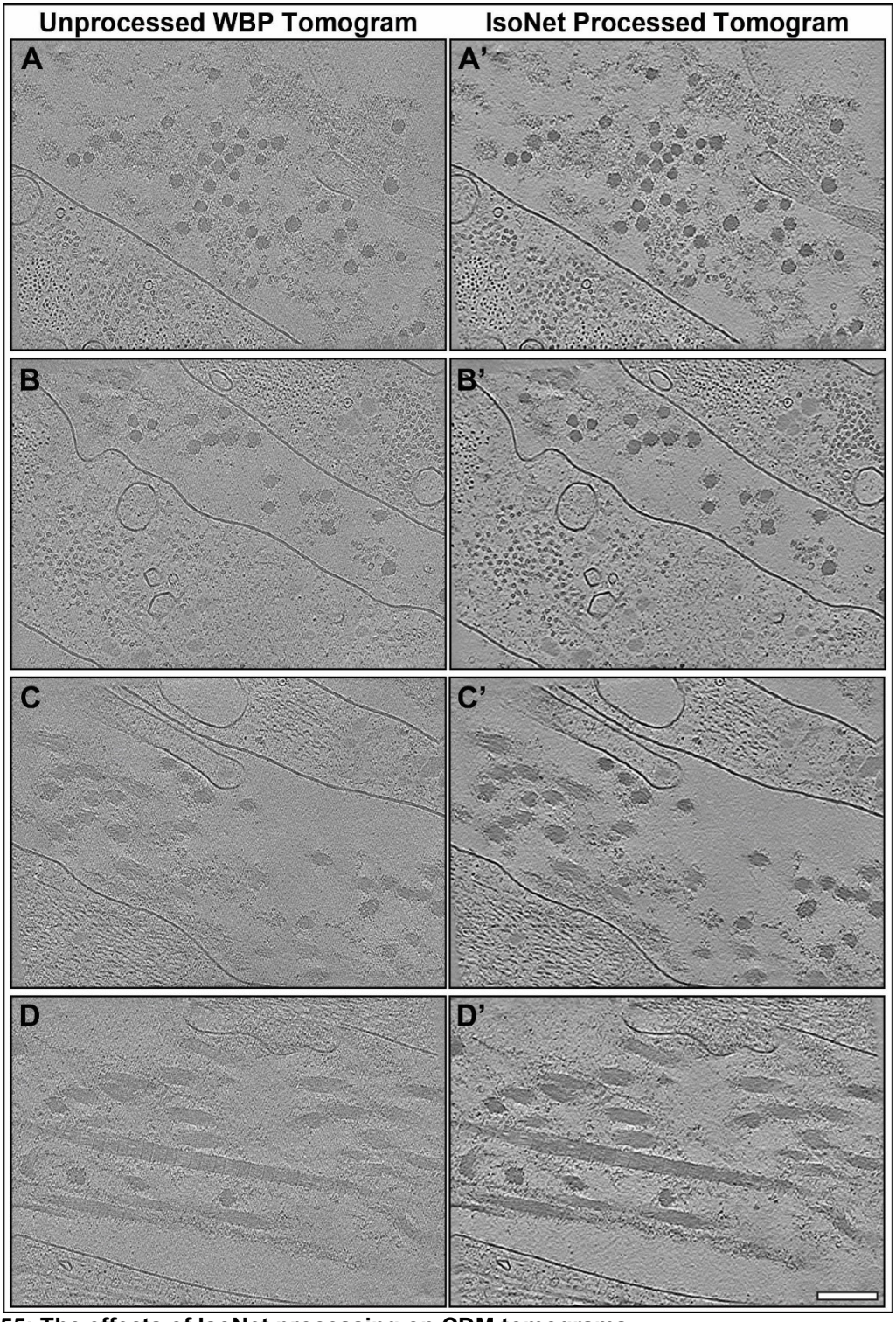

Figure 55: The effects of IsoNet processing on CDM tomograms.
A, B, C, D) Unprocessed tomograms reconstructed by WBP and patch tracking are shown on the left. All these tomograms contain intra- and extracellular structures. Depending on the orientation of the structures in the tomogram, it can be challenging to define their borders and assess small features. These tomograms are the same as those shown in Figure 53. A', B', C', D') IsoNet processing increases the contrast significantly, and all structures have higher visibility. Smaller structures, such as actin filaments and small fibers within the ECM, are easier to discern from their surroundings. Collagen fibers become more evident, but the banding pattern is obscured. Scale bar = 200 nm.

A significant increase, in contrast, can be seen after IsoNet processing compared to the unfiltered and unprocessed tomograms, resulting in more distinguishable features.

I could not detect any introduced artifacts or the removal of any large structures upon IsoNet processing, though the number of processed tomograms is still relatively low (n = 15). However, the main downside of using IsoNet processing on tomograms containing ECM structures is its effect on collagen fibers running parallel to the tilt axis. These collagen fibers show the typical collagen banding pattern in the reconstructed tomogram if they are orientated at the right angle within the tomogram volume. After IsoNet processing, the single bands become less evident and are no longer distinctly visible (Figure 55, Panel D/D').

As an alternative to IsoNet processing, two different filtering options were tested in comparison: Nonlinear Anisotropic Diffusion (NAD) filtering (Frangakis and Hegerl, 1999) on reconstructed tomograms and the application of a Simultaneous Iterative Reconstruction Technique (SIRT)-like filter during tomogram reconstruction. The results are shown in Figure 56.

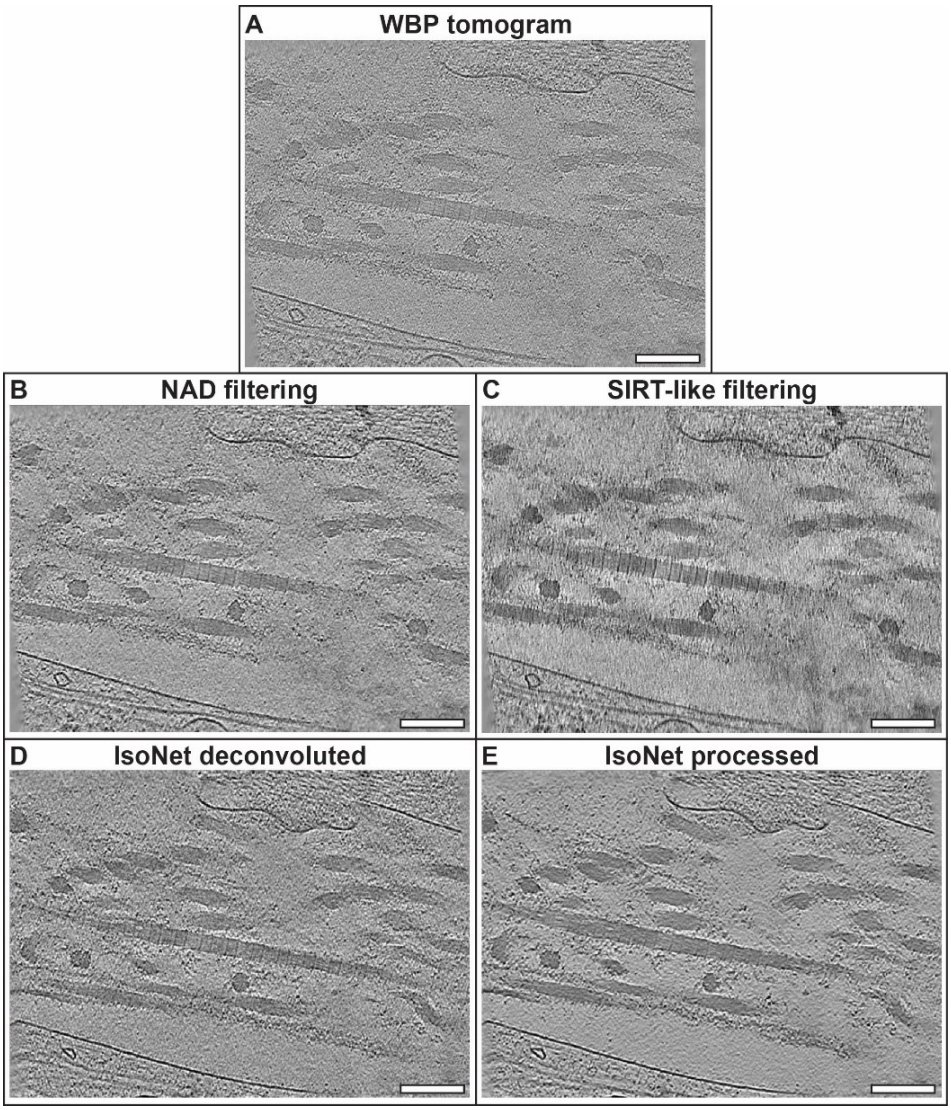

Figure 56: Different processing and filtering methods affect the collagen banding pattern differently.

A) The unfiltered and unprocessed tomogram after reconstruction with WBP and patch tracking. The banding pattern is visible in the collagen fiber that runs horizontally in the tomogram volume. B) An NAD filter (K-value 10, 10 iterations) was applied to the tomogram shown in Panel A. The contrast is increased, resulting in a slightly more visible banding pattern. C) During WBP tomogram reconstruction, a SIRT-like filter (Iterations: 15) was applied, strongly increasing contrast. Moreover, the banding pattern is clearly visible and can easily be measured. D) In an initial step during IsoNet processing, every tomogram gets deconvoluted. This first step already increases the contrast of the structures in the tomogram, and the banding pattern becomes more visible than in the unfiltered and unprocessed tomogram. E) After IsoNet processing, the banding pattern is obscured and less discernable compared to other filtering options.

All images shown are a sum of 10 slices (= 17 nm) of the tomograms. Scale bar = 200 nm. This tomogram is also shown in Figure 55 and Figure 53.

Figure 56 shows how the different processing and filtering methods change the visibility of the collagen I banding pattern. Deconvolution of the tomogram during IsoNet processing as a first step already improves the SNR and the banding pattern becomes more visible (Figure 56, Panel D). However, after IsoNet processing, it is no longer clearly discernable (Figure 56, Panel E). Hence, I concluded that IsoNet-processed tomograms are not suited for the closer inspection and measurement of the collagen banding pattern.

Applying an NAD filter increases the contrast and makes the banding pattern more discernable, similar to the IsoNet deconvolution. The filter that worked best to improve the visibility of the banding pattern is the SIRT-like filter: The contrast is greatly improved, and the banding pattern becomes very evident, facilitating measurements (see Figure 57).
The clear visibility of the banding pattern observed on those fibers running parallel to the lamella allowed unambiguous identification of those fibers to be collagen. The banding pattern was measured to repeat every ~67 nm, with a short band of ~26 nm where all collagen molecules overlap and a wide band of ~41 nm where only a portion of collagen molecules overlap (as explained in the introduction, Figure 2). This is identical to the known banding pattern of collagen I and II (Kadler et al., 2007).
As Mass Spectrometry results show a higher abundance of collagen I than of collagen II (see Table 4), the majority of collagen visible in these tomograms is likely collagen I. However, whether the collagen fibers we see here are a mixed population of collagen I and II remains to be determined.

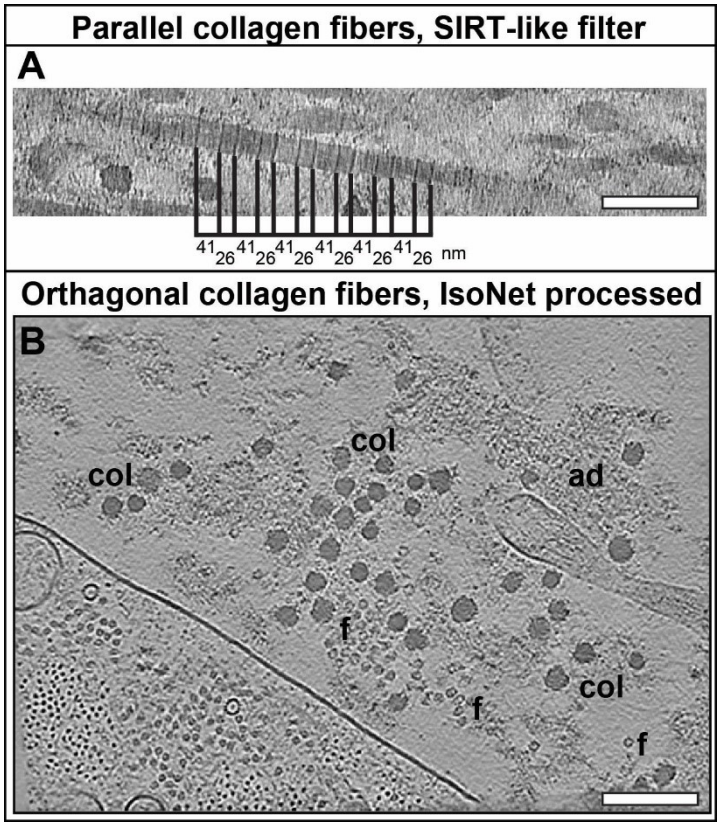

Figure 57: Collagen fibers in filtered tomograms have increased visibility.
A) A cropped area from the tomogram shown in Figure 56. The banding pattern of collagen I (col) fibers running parallel to the tilt axis becomes more evident after applying a SIRT-like filter during reconstruction. Measuring the distances between the single bands is more straightforward, and a repeated band pattern of 41 nm to 26 nm could be confirmed. The banding pattern is indicated in the tomogram, and the distances between the single bands are annotated. B) This tomogram is also shown in Figure 55. Collagen fibers running orthogonal to the tilt axis gain contrast with IsoNet filtering, making the measurements potentially more accurate through sharper border definition. The smaller ECM fibers (f) seem aligned with the collagen fibers and appear hollow. In this orientation, they are far easier to discern. In between the collagen fibers, amorphous density (ad) is evident. All tomograms are shown as a sum of 10 slices.

Initial measurements of collagen fiber cross-sections (as shown in Figure 57, Panel B) show that they range in diameter from 26 to 60 nm (see Figure 58), with an average diameter of ~38 nm (SD = 6.5 µm; n = 79). The majority of collagen fibers have a diameter in the range of 30-45 nm (77%); the distribution within this range is rather even, with 24% of the collagen fibers having a diameter of 30-35 nm, 30% having a diameter of 35-40 nm, and 23% having a diameter of 40-45 nm.

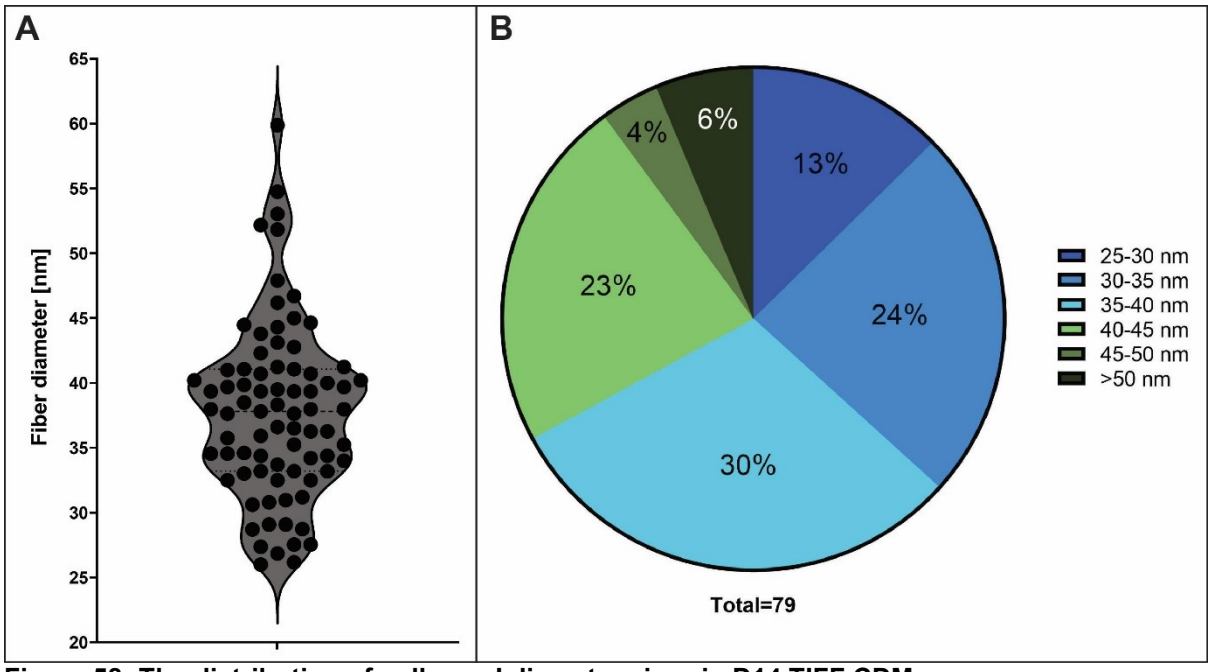

Figure 58: The distribution of collagen I diameter sizes in D14 TIFF CDMs.
A) A violin plot of the distribution of collagen I diameter sizes as measured in IsoNet-processed tomograms. Measurements were taken in IMOD of collagen I cross-sections in tomograms acquired on fully vitrified lamellae. The fibers range in diameter from 25 nm to 60 nm. n = 79. B) A pie chart showing the percentage of collagen I fibers of different size ranges as indicated in the figure legend on the right. Most collagen I fibers have a diameter of 30-45 nm (77 % overall).

In between the collagen fibers, an amorphous density is visible in most tomograms, as shown in Figure 57, Panel B (marked as “ad”). This density is more evident in tomograms where the ECM fibers are seen as cross-sections but is also visible in tomograms with fibers running parallel to the tilt axis. Additional IsoNet processing or tomogram filtering made this density more pronounced.
At this point, the identity of this amorphous density is still unclear. It may contain other ECM proteins that were found to be present in high abundance in our CDMs, such as tenascin, which is known to bind collagen (Lethias et al., 2006; Minamitani et al., 2004). Galectin is another protein that is present in the CDM and is known to bind to sugars, which could also explain the presence of this density. It is even possible that single collagen fibrils are located within the density and in the process of being assembled onto the already existing collagen fibers. However, all this remains speculation at this point.

In several tomograms acquired on fully vitrified lamellae, smaller fibers can be seen interspersed between collagen fibers (see Figure 53 and Figure 54). They become more evident after IsoNet filtering of the tomograms (see Figure 55) and seem aligned with the collagen I fibers: they are seen as cross-sections in the regions closer to the top of the CDMs and running parallel to the tilt axis in the lower regions. These fibers

have a diameter of ~15 nm (±1.5 nm SD) and are more easily discerned when seen in cross-section (see Figure 54, comparison of Panels E and F). In their cross-section view, they look to be hollow. Only when looking at them over the whole volume of the tomogram it becomes evident that these fibers seem to be either beaded or twisting around their axis (see Figure 59).

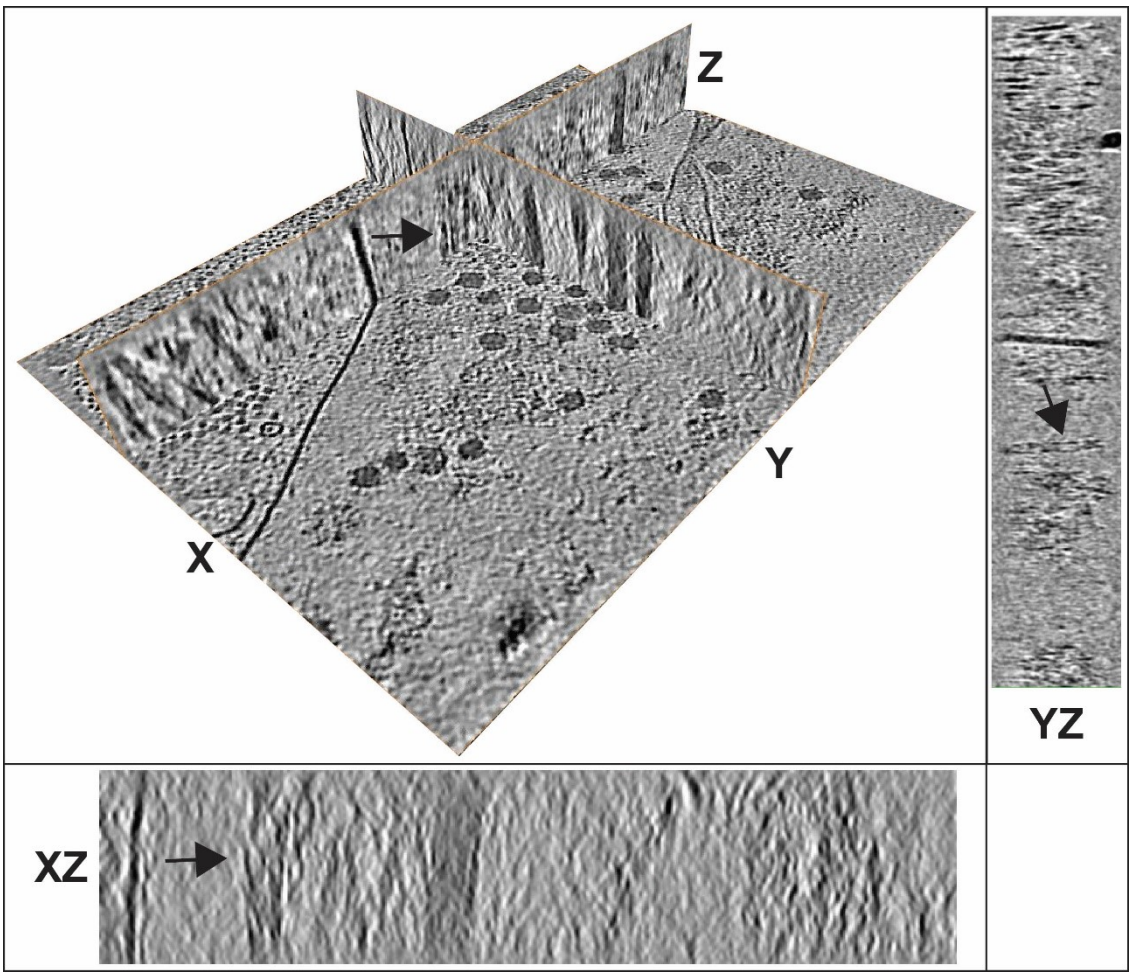

Figure 59: 3D volume of an IsoNet processed tomogram shows small ECM fibers to look beaded. A rendering of the tomogram shown in Figure 57, Panel B, shows all three planes: XY, XZ, and YZ. The cross-sections of collagen I and small ECM fibers are visible in the XY plane. The beaded pattern of the small ECM fibers becomes evident only when looking at them in the YZ or the XZ plane. A black arrow indicates these fibers.

Measuring the distance between the putative beads or twists in the filament proved difficult even in IsoNet-processed tomograms, as only a few filaments are available per tomogram. Moreover, they are often quite challenging to trace, as shown in Figure 59 (see XZ and YZ planes). Preliminary measurements have shown two different bead/twist distances of ~42 nm or ~60 nm (n = 10 filaments). The identity of these fibers remains unclear. However, I think they are likely the same thin ECM fibers visible in TEM of resin-embedded CDM sections (Figure 20, in between the collagen fibers). In both the cryo-ET data shown here and the resin-embedded CDM sections, they were the only other clearly discernable fibers besides the collagen fibers.
According to the Mass Spectrometry results, the two most likely candidates for these fibers would be collagen VI and fibronectin I. However, the structural description of neither of them quite fits what I see in these tomograms.

Collagen VI microfibrils have been described as beaded filaments with a diameter of 4.5 nm, consisting of two large globular domains connected by a 105 nm collagenous domain (Chu et al., 1989; Furthmayr et al., 1983). This does not fit with my measurements, although the bead pattern of ~42 and ~60 nm together would match the described periodicity of 105 nm, and the 15 nm diameter would be a multitude of its reported diameter.
Fibronectin I has been shown to have a periodicity of ~60-130 nm as determined by immunolabelling and super-resolution microscopy (Früh et al., 2015). The diameter of single fibronectin I fibers varies greatly in the literature, similar to collagen. However, (Chen et al., 1997) showed that single fibrils can have different structural arrangements. They found a population with a rope-like structure consisting of nodules with a diameter of 10-13 nm and a second population with a smooth surface. This held true for fibrils formed in cell culture as well as in a cell-free system. Chen et al. report that the majority of the formed fibrils were smooth in nature and always attached to a cell surface. The rope-like fibrils were less abundant and were not necessarily associated directly with cells. The nodules are irregularly spaced and have a diameter of ~12 nm.
These measurements could also roughly fit the unidentified ECM fibers in the CDMs.

At this point, with the given data, identifying the small ECM fibers is not yet possible. Moreover, there is only one population of unidentified ECM fibers. However, both fibronectin I and collagen VI have to be present in the extracellular matrix of TIFF CDMs, according to my proteomics characterization. A further investigation and adapted sample generation approach will be needed to elucidate the location of these proteins.

Segmentation CDM tomograms
The tomogram shown in Figure 59 was segmented as described in section 5, Materials and Methods, to create a 3D visualization of the extra- and intracellular structures. I performed this segmentation to allow for a more straightforward visual assessment of the different structures, their diversity, and their spatial context to each other. Images of this initial segmentation attempt are shown in Figure 60.

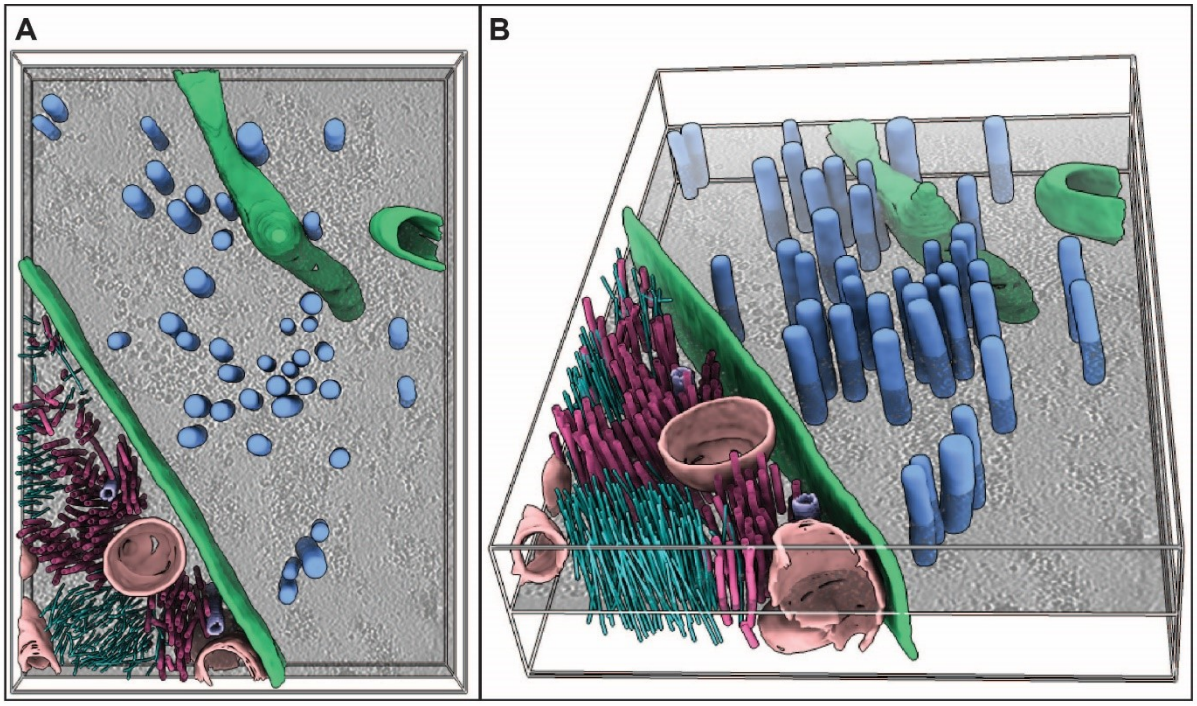

Figure 60: Segmentation of D14 TIFF CDM tomogram containing intra- and extracellular structures.
A) A top-down view of the segmentation with one central slice of the segmented tomogram displayed for additional context. B) An angled side view of the same segmentation for better visualization of the single structures in 3D. A large part of the tomogram contains extracellular matrix with segmented collagen fibers of different diameters (blue) and two cellular protrusions reaching in (green), of which one is a filopodium (upper, longer structure). The small ECM fibers are visible but could not yet be segmented successfully. The amorphous density is visible in between the collagen fibers. On the left lower corner, a part of a cell is visible, separated from the ECM by a plasma membrane (green). Within the cell, vesicles (light pink), microtubules (violet), intermediate filaments (magenta), and actin filaments (turquoise) can be seen.

The segmentation clearly shows the spatial arrangement of collagen fibers of different diameters. They are distributed throughout the ECM, and no grouping according to their diameter or proximity to cells is immediately evident by visual assessment. One filopodium reaches in between the collagen fibers but whether there is any direct interaction remains unclear. The amorphous density previously described can be seen in between the collagen fibers.
Moreover, the small ECM fibers are also present but have not yet been segmented. This is mainly due to their difference in structure to other filaments, which have a primarily even surface. The small ECM fibers, in contrast, have a strongly twisted or beaded structure, which is difficult to segment manually or automated. Further attempts still have to be made.
The tomogram also shows a part of a cell containing several vesicles and a high density of intermediate and actin filaments. As mentioned before, these populations surprisingly do not seem to mix even though they are bordering on each other. Two microtubules sit close to the plasma membrane, interspersed in the intermediate filaments.
This segmentation helps the 3D visualization of the structures and will be improved and also applied to other tomograms with different collagen fiber orientations.

Tomograms from incompletely vitrified lamellae

All tomograms shown in sections 3.5 and 3.6 originated from fully vitrified lamellae. However, tilt series acquired on incompletely vitrified lamellae with only mild ice crystal reflections still resulted in high-quality tomograms. Examples are shown in Figure 61.

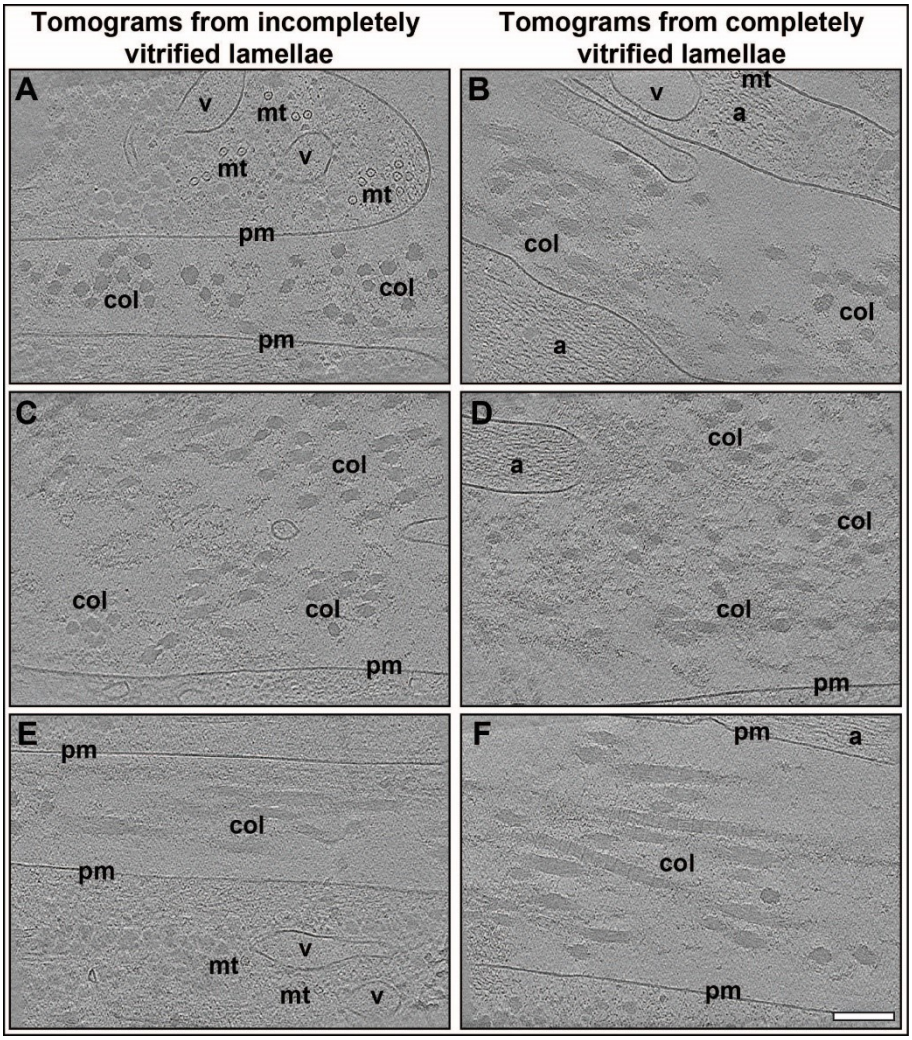

Figure 61: Tomograms collected on incompletely vitrified lamellae are of similar quality to those collected on completely vitrified lamellae.

A, B) Tomograms collected in regions closer to the top of the CDM, where collagen fibers typically run parallel to the electron beam, resulting in a cross-section view. C, D) Tomograms collected in a central region of the CDM. Collagen fibers run at an angle to the tomogram volume and are more difficult to discern. E, F) Tomograms collected closer to the bottom of the CDM. Collagen fibers run parallel to the tomogram volume; the banding pattern is only visible in F due to the angle at which the collagen fibers run in these tomograms. Scale bar = 200 nm. Structural features are annotated. col = collagen; a = actin; pm = plasma membrane; mt = microtubule; v = vesicle. All tomograms were reconstructed by WBP and patch tracking. Tomograms displayed in Panels B, D, and F were also shown in Figure 53 The sum of 10 slices (=17 nm) is shown.

Some of these tomograms reconstructed from tilt series acquired on incompletely vitrified lamellae were of high quality, such as those shown in Figure 62. Here, the single structural features are clearly discernable. The tomograms have an SNR comparable to the best tomograms acquired on vitrified lamellae and could be used for collagen fiber analysis and segmentation. The banding pattern of collagen I was still visible in fibers running at the right angle through the tomogram volume (data not shown). However, it was rarer that the smaller, unidentified ECM fibers could be seen

in these tomograms compared to tomograms from vitrified lamellae, at least during my visual assessment of the tomograms. One possible explanation for this is that, typically, more tilts had to be excluded for the reconstruction of tomograms from incompletely vitrified lamellae. This was reflected in a lower and more anisotropic resolution of the resulting tomogram, potentially obscuring fine details such as the smaller ECM fibers.

Of the tomograms acquired on incompletely vitrified lamellae, ~49% could not be reconstructed due to the exclusion of too many single tilts or incorrect alignment. The remaining ~51% were of sufficient quality to allow tomogram reconstruction, but only ~16% of these resulted in high-quality tomograms with high contrast and good alignment (see Figure 61 for examples). Compared to tomograms acquired on vitrified specimens, the proportion of tomograms that could not be reconstructed is similar. However, the proportion of high-quality tomograms reconstructed from incompletely vitrified specimens is far lower (see Figure 62).

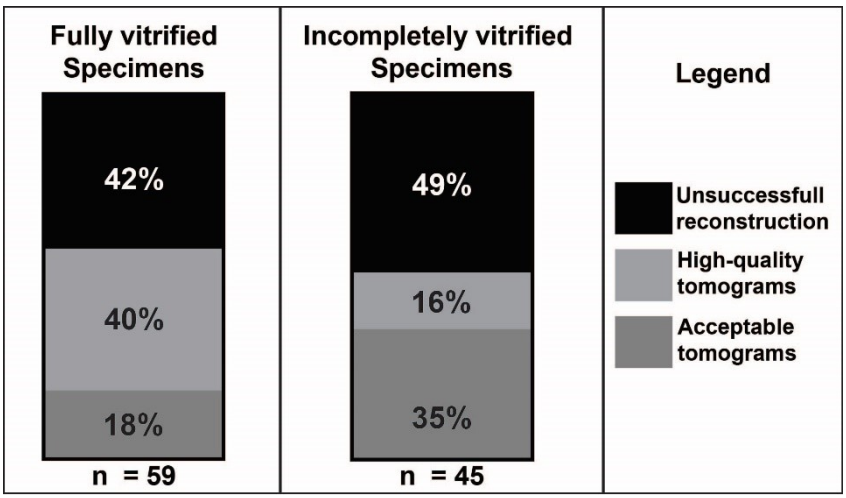

Figure 62: A comparison of the success of tomograms from vitrified specimens vs. incompletely vitrified specimens.
The proportion of unsuccessfully reconstructed tomograms is similar between vitrified and unvitrified specimens. However, vitrified specimens resulted in a much higher proportion of high-quality tomograms than unvitrified specimens.

Moreover, even though the proportion of unsuccessfully reconstructed tomograms is similar, there are several points to consider that relativize the results shown in Figure 62.
To ensure efficient use of available microscope time with the Titan Krios G3i, I prioritized data acquisition on fully vitrified lamellae. On these lamellae, I placed tilt series on all available areas with less consideration to the potential blocking of high tilts by ice contamination and lamella stability. In incompletely vitrified lamellae, the area selection for tilt series acquisition was more stringent. Applying the same stringency to vitrified lamellae when picking tilt series positions might very well reduce the proportion of unsuccessfully reconstructed tomograms in this sample pool.
Moreover, the lamellae and data acquisition improved over time. Fully vitrified lamellae typically could be milled thinner and were more stable, as the milling protocol had already been further optimized.
Using PACE-tomo allows for the collection of a much higher number of tilt series, which allows for also selecting non-optimal areas for acquisition since the time required for

tilt series acquisition is not limiting. This less stringent selection also inevitably results in fewer high-quality tilt series.
It is well possible that lamellae created from incompletely vitrified specimens with the current cryo-lift-out protocol might result in a higher number of high-quality tomograms when imaged with the current cryo-ET acquisition settings.

Overall, it seems that data acquired on incompletely vitrified lamellae can still result in high-quality tomograms, albeit with a lower chance than data acquired on fully vitrified lamellae. With tomograms originating from incompletely vitrified lamellae, one must still be cautious of alterations due to ice crystal formation. While these alterations might not be apparent on an ultrastructural level, they could affect protein structures due to, e.g., dehydration effects. However, with the data obtained from fully vitrified lamellae, I have a control available to ensure that there are no obvious changes on the ultrastructural level. Based on this, I would include high-quality tomograms obtained from incompletely vitrified lamellae in the data pool if necessary.

4. CONCLUSION AND FUTURE OUTLOOK

In this thesis, I describe the development of a novel integrated specimen preparation and cryo-FIBSEM/cryo-ET workflow to study the ultrastructure of native extracellular matrix at an unprecedented resolution. The workflow I developed made the visualization of natively preserved ECM structures in their cellular context at high-resolution possible for the first time. Indeed, the data I have generated has already provided new insights into the ECM ultrastructure and context in a multicellular environment, such as visualizing hitherto unknown structural details of ECM components.
This workflow is highly versatile and thereby provides the opportunity to address a multitude of open questions in ECM biology. One major factor for this is the highly adaptable nature of CDMs, which I believe to be immensely beneficial for future endeavors: Different cell lines, or even primary cells, can be used for CDM generation to address different questions.
For example, osteoblast-derived CDMs can be employed to study the mineralization of ECM, specifically collagen fibers that act as a template for this mineralization process under native conditions.
Epithelial cells can be used to generate CDMs that resemble basement membranes, allowing for a detailed ultrastructural characterization of a tissue component that has not yet been studied by cryo-ET.
Moreover, the employed cells can be genetically modified as needed, and the growth medium can be supplemented with growth factors, inhibitors, or other chemicals. The process of CDM generation can be tailored to the biological questions posed, such as: Which factors are involved in regulating collagen fiber diameter? Is it possible to revert collagen cross-linking? What effect do different growth factors, such as BMP1 and PDGFRα, have on the ultrastructure of the ECM?
Decellularized CDMs seeded with migratory cells such as immune cells, or cancer cells could be used to study cell migration and the structural interactions between the migrating cells and the ECM components. One could even compare CDMs derived from healthy fibroblasts to CDMs derived from cancer-associated fibroblasts. This would allow for studying how the ultrastructure of the ECM changes and alters the reciprocal interactions between migrating cells and ECM components.

I believe the findings of my Ph.D. thesis also benefit users who work on other specimens. The HPF and cryo-lift-out protocol described here can also be used, amongst others, on organoids or tissues, and the sample preparation process can be adjusted as needed. As proof of principle, I have already acquired cryo-lift-out lamellae from deeper CDM layers by adapting the trenches and performing consecutive lift-outs in the same xy position.
Moreover, this method can be adapted to other sample types. Tissue samples of animal models such as skin and muscle tissue can be high pressure frozen directly in HPF carriers and then used to generate cryo-lift-out lamellae. This workflow could also be used to prepare organoids or tissue mimics such as hydrogels used in medicine for (ultra)structural studies by cryo-ET. Even whole organisms, such as zebrafish embryos, *C. elegans* worms, or other small animal models could be studied with this workflow. While optimization for high pressure freezing and cryo-CLEM of these samples would be required, the workflow introduced in this thesis could be adapted for those samples and employed to generate cryo-lift-out lamellae.

This shows that with this workflow, a wide range of sample types can now be prepared for cryo-ET.

Below, the main challenges I had to overcome for the completion of this project are listed. I will also discuss the impact of new technologies on the field of cryo-FIBSEM and how they can help to further facilitate and enhance the workflow I introduce here. Lastly, I will provide an outlook on the future questions that can be addressed with this new workflow.

Challenges

The complexity of the specimen and the tools involved made the development of this workflow challenging for several reasons. Considering these challenges is valuable with respect to future endeavors in developing similar workflows.

One major challenge was the duration of the feedback loop, informing me about the success of a specific condition I tested during specimen preparation. Specifically, cell culture CDM specimen preparation takes at least 16 days. The feedback on the vitrification success takes another 2-6 weeks, depending on the availability of microscopes and the number of conditions tested. For example, cryo-LM only reveals information on the intactness of the CDMs, and cryo-FIBSEM could not be used to gauge the vitrification status. Hence, the effectiveness of the cryoprotectant could only be judged by cryo-TEM at the very end of the entire workflow.

I tested many different cryoprotectant compositions until I found one that resulted in complete vitrification in at least a portion of the CDMs, even though all the used cryoprotectants are routinely used for HPF, followed by freeze-substitution.

This shows that assessing the vitrification success of HPF after freeze-substitution might only work for strong effects on hexagonal ice formation. Incomplete vitrification, such as the one shown in Figure 47, likely remains undetected in freeze-substituted samples, even in slightly more severe cases (see Figure 47, Panel A). In contrast, cryo-TEM immediately reveals the presence of even a few small hexagonal ice crystals.

Another major challenge was the overall novelty of the key technique used in this thesis, which required establishing new experiments without any prior conditions to start from. The Aquilos I arrived at ISTA only in December 2018, when I had already started working on my Ph.D. thesis, making it the only cryo-FIBSEM in Austria. No previous expertise in cryo-FIB milling was available at ISTA. Therefore a considerable amount of time during my first years as a Ph.D. student was spent establishing the Aquilos I instrument and milling protocols. Establishing and optimizing the cryo-lift-out technique was even more challenging, as only a few users worldwide had the necessary equipment for it, and there was very limited information on the procedure and the factors influencing it. Communication and scientific exchange with other cryo-lift-out users was additionally limited due to the impact of the Coronavirus pandemic in the last years.

To my knowledge, this thesis presents the first extensive exploration of the factors influencing the cryo-lift-out success rate and shows the first large cryo-ET dataset acquired on lift-out lamellae.

The influence of new technologies and techniques

Plasma FIBSEMs

One limitation of cryo-FIBSEM instruments using Gallium ions for ablation is the required time to mill thick specimens (as illustrated in this thesis in section 3.3.2.1).
The first dedicated cryo-FIBSEM using plasma instead of Gallium for generating ions is now commercially available: the Arctis Cryo-Plasma-FIB from TFS. There is still only very limited information on the use of plasma ions for cryo-FIB milling. The main argument for using plasma FIB milling instead of Gallium FIB milling is the higher sputtering rate and a higher maximum operating milling current (Dumoux et al., 2022). This could be useful for large-area milling and faster milling rates.
However, whether higher currents and an increased ablation rate damage biological samples or introduce artifacts remains to be seen. Initial experiments have shown that while nitrogen and oxygen plasma might not be well suited due to higher curtaining rates and the production of multiple ion species instead of just one, argon and xenon are promising candidates. Specifically, argon showed low curtaining propensity even at high currents, and at least by SEM imaging, no damage to the sample could be detected (Dumoux et al., 2022). However, whether pFIB instruments are superior to standard gallium FIB instruments remains to be proven in a direct comparison of lamellae by TEM.
A significant advantage of the Arctis instrument is, at the same time, its biggest disadvantage: The chamber size of the Arctis was reduced compared to typical FIBSEMs, such as the Aquilos, which significantly improves vacuum and reduces the contamination rate. However, the contamination rate in our Aquilos II is already relatively low, and, importantly, the small chamber size of the Arctis prevents the performance of the cryo-lift-out technique. This significantly decreases the versatility of this instrument for creating lamellae from different sample types.
However, the next years will show whether the application of Plasma-FIB to bulk samples like CDMs or tissues will facilitate the generation of bulk-lamellae with bigger acquisition areas and higher stability than cryo-lift-out lamellae.

Waffle method

Very recently, a paper by (Kelley et al., 2022) introduced the so-called "Waffle Method". The Waffle Method uses high pressure freezing on suspension samples such as dense yeast cultures in the space between the grid bars, thereby creating a bulk sample of a defined height of around 20 µm. Here, too, milling starts with trenches at high angles and then transitions into a milling protocol like the one I have outlined above in section 3.3.2.1. The authors suggest an orthogonal initial trench milling angle like the one used in the lift-out technique and use significantly higher initial milling currents (15 nA). This confirms that higher milling currents can be used for trench milling, speeding up the milling process considerably. Moreover, adapting the initial trench milling angles to resemble those used for cryo-lift-outs further facilitates this process.
Another factor for the successful generation of bulk lamellae in their publication was the limited sample thickness – their specimens were only around 20 µm high, compared to my high pressure frozen CDMs with an overall height of around 40-45 µm. Their publication states they can create up to 7 lamellae in a single 30 h FIB milling session by combining manual operation and overnight automation.
Kelley et al. show that an adaptation of the bulk milling protocol, using higher milling currents and orthogonal trench milling angles, as suggested in section 3.3.2.1, can

facilitate sample thinning. Moreover, the initial samples I tested for bulk milling were incompletely vitrified, which further hampered FIB milling of bulk samples.
Overall, I believe the Waffle Method is a valuable alternative to the cryo-lift-out technique for some samples, especially in research institutes that do not have access to an Aquilos II. It could even be preferable to use it for suspension samples, such as bacteria or yeast cells, as it potentially results in longer lamellae and, thereby, a larger acquisition area. They state that their method can also be combined with a spacer ring to increase the sample thickness if needed.
However, this method is strongly limited by the sample type used. While it can be adapted to adherent cells to some degree, some adherent cells stop proliferation once they are confluent and might only fill a part of the grid squares. This would result in largely empty lamellae. Samples such as CDMs, on the other hand, would grow over the grid bars and get squeezed against them during HPF. This could result in increased sample damage during HPF and carrier disassembly, resulting in fewer high-quality samples for further processing.
Moreover, it would require the user to avoid compressed regions during HPF and investigate how these compressed areas affect surrounding fibers. While a spacer or a carrier, such as the one I designed for my workflow, could be used to overcome this problem, this would again add sample height and make bulk milling more difficult. The waffle method is also not adaptable for pieces of tissue, as they are unlikely to fit within a grid square.

In comparison, the workflow I describe in this thesis is more adaptable to different types of samples. Initial attempts to use it to investigate skin tissue derived from mice have been successful, requiring only a small adaptation to the HPF process. The throughput stated in the publication from Kelley et al. is comparable to the lift-out approach I have outlined in this thesis. By increasing milling currents to the ones suggested by Kelley et al., I could further reduce the time needed for trench milling and thereby increase the overall throughput.

Automation

Now that the cryo-lift-out technique has been explored in more detail and all parameters for the trench milling are known, the milling of the trenches could be automated. Most likely, even undercutting steps could be automated using automation software such as AutoTEM and AutoScript (TFS) or the open-source SerialFIB (Klumpe et al., 2021). Several cryo-lift-out blocks could be prepared in an automated fashion overnight. The following morning, a user would manually take over the lift-out process and attach the lift-out to the half-moon grid fingers. Such developments are currently ongoing in different research groups. Whether rough and fine milling of the lift-out lamellae can be automated strongly depends on the stability of the lamellae. Based on my experience, I would, at this point, still opt to do at least the fine milling manually.
Instead of the half-moon grids, copper grids (200 mesh) can be sliced in half with a sharp razor blade and then clipped into a FIBSEM AutoGrid™, resulting in a high number of finger-like structures that can be used for attachment.
Using automation software in combination with higher trench milling currents and alternative half-grids could greatly facilitate the throughput of this method and significantly increase the overall throughput and the amount of data that can be collected from a single specimen. Of course, the feasibility of the automation steps has to be tested first but based on the results already shown for automated lamella

milling, I am convinced that the automation of the cryo-lift-out block milling will be implemented in the near future. This would drastically decrease the time required for a user to be present throughout the lift-out process.

Serial cryo-lift-out

This last year, I have also tried to set up serial cryo-lift out in different geometries. As described in section 3.3.2.2, it is possible to mill wider trenches and take lift-out blocks from adjacent positions. In a way, this allows a continuation of the lamella region on the next lamella. However, due to the geometry of the attachment of the needle to the lift-out block and the block to the finger, there is a gap of ~5-7 µm between the single lamellae. This, of course, is too large to trace single structures between the lamellae. Several research groups are currently working on similar developments. Most likely, serial cryo-lift-out will become a realistic possibility within the next few years.

Future Outlook

The data presented in this thesis will be used to write a manuscript for the publication of the workflow introduced here in a peer-reviewed journal in the following months.

The identification of the different ECM fibers characterized in section 3.6. would be my next primary objective.

Further structural investigation into these fibers requires adaptation of tilt series acquisition parameters. Acquiring data with smaller pixel size and closer to focus will enable the use of subtomogram averaging, which could help elucidate the different fibers structures if the structures display sufficient regularity, which remains to be determined. This could help determine whether the small ECM fibers are collagen VI or fibronectin I fibers.

There are three alternative strategies for this determination: First, the immunogold labeling could be further optimized to work on CDMs to confirm the identity of the extracellular structures, particularly fibronectin I and collagen I, where specific primary antibodies are already available in the group. Second, the highly adaptable CDM system I have set up can be used instead: single proteins can be knocked out in fibroblasts (for example, by CRISPR/Cas9), thereby helping to reduce the number of potential candidates for fibers that remain present in the CDMs. Third, the growth medium of CDMs could be adapted to change the relative composition of the CDMs by inhibiting or promoting the expression of specific ECM proteins. This could also help to investigate the amorphous density in close proximity to ECM fibers, to see whether it consists of sugars, single ECM fibrils that are ready for fiber assembly, or other proteins such as fibrillin or fibulin.

The second and third approach would require control experiments, as the removal or reduction of one ECM component can affect the presence and structure of other ECM components. For example, the addition of LOX and BMP1 to the growth medium was shown to result in increased collagen synthesis and deposition (Rosell-Garcia and Rodriguez-Pascual, 2018). Moreover, LOX and BMP1 overexpression result in increased cross-linking of collagen fibers and a drastic reduction of soluble collagen in the ECM (Rosell-Garcia and Rodriguez-Pascual, 2018), mimicking one aspect of fibrosis (Frantz et al., 2010). In contrast, knockdown of fibronectin I and, thereby, the prevention of fibronectin I fiber assembly can directly impact collagen fibrillogenesis (Saunders and Schwarzbauer, 2019).

A high number of proteins have been shown to have an impact on the structure and size of collagen fibrils *in vitro*, such as tenascin, collagen III, and collagen V (Holmes

et al., 2018; Wenstrup et al., 2004), all of which I could show to be present in TIFF CDMs (see Table 4; collagen III is not included in this table as it has a lower expression value and is not among the listed proteins). Knockdown of collagen VI could affect collagen I fibrillogenesis, as it has been shown that collagen I fibers are aberrant in the skin of collagen VI-deficient patients (Minamitani et al., 2004; Theocharidis and Connelly, 2017). Thus, removing one of these ECM components could alter the structure of the remaining collagen fibers.
CDMs could be grown for a prolonged time to see whether the empty spaces in the extracellular space I could observe (see section 3.5) will fill up over time or remain present even in older CDMs.

Next, I would also like to further adapt the cryo-lift-out technique with at least partial automation and incorporate sputter coating the final lamellae with a thin layer (~5-10 nm) of platinum. This has been reported to reduce charging effects significantly (Khavnekar et al., 2022), potentially stabilizing the lamellae and providing a basis for improving the quality of tilt series. While an additional platinum layer would reduce the contrast, which is especially problematic in the thicker areas of the lamellae, increased lamella stability and acquisition area size could be worth the trade-off.

One question I would be particularly interested in addressing is ECM fiber assembly. Until now, studies on the high-resolution structure of collagen fibrils *in situ* are still sparse. The lack of suitable cell culture systems compatible with cryo-EM has hampered progress in the investigation of fibril assembly. The role plasma membrane channels and fibripositors (Canty et al., 2006, 2004) play in collagen fibril assembly and the molecular mechanism of fibronectin-collagen interaction remain unclear.
With the workflow I introduce in this thesis, a physiological 3D system compatible with cryo-ET is now available for studying such questions. ECM fibers are assembled in a cellular context and preserved in their hydrated state *in situ*.
The different layers of the CDM provide a sort of a history of ECM secretion, with fibers in layers closer to the EM substrate being older than those at the top of the CDM, where they are still freshly formed. Finding ECM secretion and assembly sites in these upper layers could be more likely than in lower layers.

Another approach worth following up on is the use of cryo-Scanning Transmission EM (STEM) on lamellae with a thickness of ~600-800 nm. Cryo-STEM is a high-resolution EM technique that can be performed on samples with a thickness of up to 1 µm, as opposed to ET, which requires samples to be ideally ≤250 nm in thickness. Cryo-STEM does not reach the same resolution as cryo-ET but compensates for this by covering a larger volume. This would make it possible to trace the collagen fibers and cells over a greater distance. Data collected by cryo-STEM could help better define the interaction between collagen fibers and cells and increase the chance of finding fibril assembly sites. Lamellae preparation for cryo-STEM is less time intensive than for cryo-ET (as they can be thicker), and lamellae remain more stable.

It would also be interesting to compare the data shown in this thesis to data acquired from tissue. To this end, initial trials with mouse ear skin have already been performed successfully. Following the same protocol I use for my CDMs, mouse ear skin could be vitrified in carriers adapted to the correct sample size. Cryo-lift-out lamellae were successfully created and imaged by cryo-ET. This proves the adaptability of this

protocol to other samples and the number of possibilities it opens up in sample processing.

Aside from these initial steps to continue the work summarized in this thesis, I have discovered several extra- and intracellular structures in my collected data that would be interesting to follow up on. For example, the inner density found in the lumen of microtubules is still not well understood and discussed as an artifact of stressed cells rather than a physiological feature. As shown in section 3.5, I could see this inner density in all microtubule-cross sections. Studying this inner density and its structure could be interesting for the community. This is the first time microtubules and their inner density are visualized in an entirely physiological context in a 3D ECM rather than on potentially highly stressed single cells.
Other structures, such as actin and intermediate filaments, in particular in the context of cell migration, are typically studied in a 2D cell culture setting rather than in 3D. It would be interesting to compare these filaments in migratory cells embedded in the CDM to filaments investigated in a 2D setting in regards to their orientation and arrangement to each other and the cell membrane.

5. MATERIALS AND METHODS

EM substrates

200 or 150 mesh gold holey carbon grids (R 2/2, #N1-C16nAu20-01 and #N1-C16nAu15-01 respectively) and 200 mesh titanium SiO2 grids (R2/2, # N1-S16nTi20-01) were purchased from Quantifoil Micro Tools. 200 mesh gold grids (#G200-AU) and 150 mesh titanium grids (# PY200-TI) were purchased from Science Services, coated with continuous Formvar film (0.75%, Formvar 15/95 powder, Science Services, #E15800) and/or 10 nm of continuous carbon in-house with a floating chamber (made in-house) from mica sheets prepared in-house with a high vacuum sputter coater (Leica ACE600)

Sapphire discs (3 mm diameter, thickness 50 µm) were purchased from Engineering Office M. Wohlwend GmbH (#405). ACLAR® film (thickness 51 µm) was purchased from Science Services, and 3 mm diameter discs were punched out with a standard tissue biopsie puncher. Sapphire discs and ACLAR® discs were coated with 10 nm continuous carbon in-house with high vacuum sputter coater (Leica ACE600). 10 mm diameter glass cover slips (Bartelt, #9.161 063) were acid-washed with HNO_3 (Merck, # 1151871000) for 5 min and sterilized by autoclaving prior to use in cell culture.

Throughout all cell culture experiments Dumont tweezers, medical grade, style 5 and style 7 were used. Prior to seeding of cells, grids were glow discharged in an ELMO glow discharge unit (Cordouan Technologies) for 2 min (holey carbon), or 30 s (Formvar) on Parafilm. Substrates were then prepared for cell seeding as described in section 3.1.2.

3D printing of grid holders

Grid holders are described in detail in (Fäßler F., Zens B., et al., 2020), see section 3.1.1. This text describing the 3D printing of grid holders was originally written for (Fäßler F., Zens B., et al., 2020) by Florian Fäßler and me and modified for this thesis as needed.

“T Square base grid holders were printed using either a PETG (Filament PM) or a Green-TEC Pro filament (3D Jake). Printing resolution was set to a layer height of 0.2 mm for the first layer and 0.15 mm for all additional layers, employing a 0.4 mm nozzle. After printing, all stringing was removed from the grid holders, and any holders showing printing errors were discarded. PETG grid holders were sterilized with perform® classic alcohol EP and UV irradiation prior to first use and again after each use in cell culture experiments. Green-TEC Pro grid holders were sterilized by autoclaving. All grid holders were re-used up to 15 times and stored under sterile conditions until use.”

Cell culture, CDM growth, and CDM decellularization

Wildtype Mus musculus NIH 3T3 cells and wildtype Homo sapiens telomerase immortalized foreskin fibroblasts (TIFF) were kindly provided by Michael Sixt (ISTA). Rattus norvegicus wildtype embryo fibroblasts (REF) were kindly provided by Klemens Rottner (Helmholtz Centre for Infection Research, Braunschweig). NIH 3T3 cells were cultured in Dulbecco's modified Eagle's medium (DMEM GlutaMAX, ThermoFisher Scientific, #31966047), supplemented with 10% (v/v) fetal bovine serum (ThermoFisher Scientific, #10270106) and 1% (v/v) penicillin–streptomycin (ThermoFisher Scientific, #15070063). TIFF cells were cultured in Dulbecco's modified Eagle's medium, supplemented with 20% (v/v) fetal bovine serum, 2% 1 M HEPES

(ThermoFisher Scientific, #15630080), and 1% (v/v) penicillin–streptomycin.

REFs were cultured in Dulbecco's modified Eagle's medium, supplemented with 10% (v/v) fetal bovine serum, 1% (v/v) penicillin–streptomycin, and 1% (v/v) non-essential amino acids (MEM NEAA (100x), Gibco, #11140035).
All cells were incubated at 37 °C and 5% CO2. Phosphate buffered saline (PBS) used for all sterile cell culture work was purchased from ThermoFisher Scientific (#20012019). For all other steps described in the following sections, PBS prepared by the LSF (ISTA) was used.

CDM seeding and growth on EM substrates are described in detail in this thesis in section 3.1.2.

CDM decellularization for plunge-freezing experiments was performed as published in (Kaukonen et al., 2017). Briefly, extraction buffer was prepared by adding 250 µl Triton X-100 (Sigma-Aldrich, #T8787-100M) and 1 ml of NH_4OH (Sigma-Aldrich, #221228-1L-A) to 48.75 ml of PBS and prewarmed to 37°C. CDMs were washed with extraction buffer until the fibroblasts were extracted, as observed by phase contrast microscopy on a standard stereo microscope. This extraction process took ~2 min for NIH 3T3 and REF CDMs, but up to 5 min for TIFF CDMs. Specimens were then washed with PBS and treated with 50 µg/ml DNase I (Roche, #11284932001), 5 mM $MgCl_2$, and 1 mM $CaCl_2$ (LSF, ISTA) for 1 h at 37°C. CDMs were then washed three times with PBS and immediately fixed with PFA.

Antibodies and stainings
For fixation, 4% PFA was diluted in PBS (LSF, ISTA) from a 16% stock solution (Science Services, #E15710) and warmed to 37°C. EM substrates with grown CDMs were recovered from the grid holders, placed on Parafilm stretched over the inside of a 10 cm diameter petri dish, and immediately fixed by the addition of prewarmed 4% PFA in PBS. CDMs were fixed for 20 min at RT and then washed three times with PBS. The specimens were treated with permeabilization solution (0.1% Triton X-100 and 3% BSA in PBS) for 5 min and then washed three times with PBS. They were then treated with blocking solution (3% BSA in PBS) for 1 h at RT. BSA (#10735078001) was purchased from Sigma-Aldrich.
The blocking solution was removed, and the respective primary antibody diluted in blocking solution was added for overnight incubation at 4°C in a wet chamber in the dark.
Primary antibodies for were used in the following concentrations for immunostaining after testing different dilutions: Anti-Fibronectin I from rabbit (Sigma-Aldrich, # F3648), used 1:500; Anti-Collagen I from rabbit (Novus Biologicals, # NB600-408), used 1:500 for immuno-staining as standard collagen I antibody; Anti-Collagen VI from rabbit (Abcam, #ab182744), used 1:500; Anti-Fibrillin 1 antibody from rabbit (Thermo Scientific, #PA5-99225) used 1:500; Anti-Collagen I from rabbit (Thermo Scientific, #PA1-26204), used 1:500.
Specimens were washed three times with PBS before addition of the secondary antibody and other stainings. Anti-Rabbit-IgG-ATTO 594 (Merck, #77671-1ML-F) was used in 1:500 dilution as secondary antibody for immunostaining. Phalloidin-ATTO 488 (ATTO-TEC, #AD488-81) was employed complementary with Anti-Rabbit-IgG-ATTO 594 in 1:500 dilution to visualize actin filaments. 4',6-Diamidino-2-phenylindole dihydrochloride (DAPI, Sigma-Aldrich, #32670-5MG-F) was used in a 1:500 dilution to

visualize DNA and, thereby, the nucleus. Samples were washed three times with PBS and stored at 4°C in a wet chamber in the dark.

CNA35-EGFP

A bacterial expression vector for CNA35-EGFP-6xHis was purchased from Addgene (#61603) (Aper et al., 2014). BL21 bacterial cells were transfected with the vector, and protein expression was induced with 0.1mM IPTG (Thermo Scientific, #R0393) at an OD600 of 0.6. CNA35-EGFP was expressed for 4 h at 37°C, and the cells were pelleted by centrifugation with 6,000g for 15 min at RT. Cells were resuspended in in freshly prepared resuspension buffer containing 20 mM Tris Tris (Lactan, #9090.3), 500 mM NaCl (Lactan, #P029.2), 5% (v/v) Glycerol (Sigma-Aldrich, #G5516-500ML), 2 µM $ZnCl_2$ (Carl Roth, #3533.1), 1 mM PMSF (Sigma-Aldrich, #P7626-1G), 1 mM TCEP (Lactan, #HN95.2), pH 8.0, and snap-frozen in LN_2.

Cell pellets were stored at -80°C until purification. Cells were lysed after thawing by three cycles of freeze/thaw for 20 min at -80°C and 42°C, respectively. Cell debris was removed by centrifugation at 50,000g for 1 h at 4°C. Nucleic acid precipitation was performed by the addition of 10% PEI (Polysciences, #24966-100) to a final concentration of 0.3%. Samples were stirred for 40 min at 4°C and then centrifuged at 6,000g for 10 min at 4°C. Ammonium sulfate (Millipore Sigma, #1012115000) was added to the supernatant to a final concentration of 40% to precipitate proteins, and the solution was stirred overnight at 4°C. Following this, they were centrifuged at 6,000g for 10 min at 4°C. The protein pellet was then dissolved in 20 mM, 500 mM NaCl, 2 mM TCEP, and 20 mM Imidazole (Sigma-Aldrich, #56750), pH 8.0, while stirring at 4°C for 30 min.

The solution was applied to a nickel sepharose column, a HisTrap FF 1mL (Cytiva, #17531901). The column was washed with washing buffer (20 mM T ris, 500 mM NaCl, 2 mM TCEP, 20 mM Imidazol, pH 8.0) and eluted with elution buffer (20 mM Tris, 500 mM NaCl, 2 mM TCEP, 250 mM Imidazol, pH 8.0). Fractions containing protein were pooled and dialyzed against dialysis buffer (20mM Tris, 500mM NaCl, 0.5 mM TCEP, pH 8.0) over night at 4°C while stirring. Aliquots were flash-frozen in LN2 and stored at -80°C.

For live staining, CNA-EGFP was diluted to a final concentration of 1 µM in cell culture medium. CDMs were washed once with this staining solution and then incubated in it for 1-2 hours at 37°C and 5% CO_2. Specimens were then washed three times with cell culture medium and kept at 37°C and 5% CO_2 until imaging and HPF within the next 1-3 hours.

Light Microscopy

Stained CDM specimens were kept on Parafilm in a drop of PBS or cell culture medium and either assessed using an upright widefield microscope or imaged employing an upright confocal microscope. For a quick assessment of sample integrity and quality prior to vitrification, a Zeiss Axioscope with a W N-Achroplan 20x/0.5 water-dipping (WD=2.6 mm) objective was employed.

For confocal imaging, a Zeiss LSM800 microscope with a Plan-Apochromat 20x / NA 1.0 W DIC water-dipping (WD=1.8mm) objective was used. Z-stacks with 1 µm steps over the whole height of the specimen from the EM substrate to the top of the CDM were acquired using the ZEN 2.6 software. Typically, at least 3 positions per specimen were acquired. Live samples were kept at 37°C for the duration of the imaging process and returned to a cell culture incubator after a maximum of 30 min.

Z-stacks were subjected to a maximum intensity Z-projection using Fiji (Schindelin et al., 2012). To improve the visibility of these images for this thesis, contrast and brightness were adjusted as necessary.
All specimens that showed distortions or bending of the EM substrate, any damage to the CDM, or a partial or complete loss of CDM were removed from the sample pool prior to vitrification.

Immunogold antibody labeling

Protocol 1

D14 TIFF CDMs grown on glass cover slips were fixed for 40 min at RT in 4% PFA and 0.05% glutaraldehyde (Science Services, #E16220) in 0.1 M PB (pH 7.4). They were then washed in 0.1M PB and put through a sucrose gradient: Samples were incubated in 5% Sucrose in 0.1M PB for 20 min at RT, then in 10% Sucrose in 0.1M PB for 40 min at RT and finally in 20% Sucrose in 0.1M PB for 40 min. They were then subjected to a freeze-thaw cycle by placing the 24-well plate they were in on top of LN_2 for 45 s. Subsequently, 37°C 0.1M PB buffer was added on top, and the samples were incubated for about five minutes. The specimens were then washed two times with 0.1M PB for 10 minutes and one time with PBS. Blocking solution (3% BSA in PBS) was then added for 1 h before overnight incubation with anti-fibronectin I and anti-collagen I diluted 1:500 in blocking solution. The same primary antibodies as described for light microscopy were used. After overnight incubation, samples were washed with PBS and again incubated overnight with the secondary antibody, anti-rabbit 10 nm nanogold conjugated Fab fragment, diluted 1:30 in blocking solution. Afterward specimens were thoroughly washed in 0.1M PB.

Protocol 2

D14 TIFF CDMs grown on glass cover slips were fixed for 1 h at RT in 2.5% glutaraldehyde and 2% PFA in 0.1 M PB (pH 7.4). Subsequently, specimens were washed with 0.1M PB and put through a sucrose gradient, a freeze-thaw cycle, and antibody staining as described in Protocol 1. The incubation with the primary antibody was expanded to 48 h. As a secondary antibody, anti-rabbit 10 nm nanogold conjugated Fab fragment, diluted 1:20 in blocking solution, was used on one half of the samples. The other half was incubated with a secondary antibody mix of the anti-rabbit 10nm nanogold conjugated Fab fragment (1:20) and an anti-rabbit 5 nm nanogold conjugated Fab fragment (1:20). The incubation time for the secondary antibody was expanded to 72 h. Subsequently, specimens were thoroughly washed in 0.1M PB. The results of this protocol are shown in section 3.1.2.2.4, Figure 21.
Biological replicates were treated as described in Protocol 2, but incubated with anti-rabbit-IgG-ATTO 594 as described for immunofluorescence antibody staining. These served as a control for this protocol.

Resin-embedded sections

Results shown in section 3.1.2.2.4, Figure 20.
D14 TIFF CDMs grown on glass cover slips were fixed for 1 h at RT in 2.5% glutaraldehyde and 2% paraformaldehyde in 0.1 M PB (pH 7.4). They were then washed in 0.1M PB and post-fixed with 1% osmium tetroxide in 0.1M PB for 20 min in the dark. After washing with Milli-Q water, the samples were contrast-enhanced with 1% uranyl acetate in 50% ethanol/water for 30 min in the dark. Samples were dehydrated in a graded ethanol series: 50%, 70%, 90%, 96%, 100% (twice) for 10 min each. Subsequently, the samples are washed twice in propylene oxide for 10 min.

Then, they were infiltrated in a graded series of hard Durcupan™ ACM resin in propylene oxide. The specimens were placed in pure Durcupan overnight. On the next day, the coverslips were put on an **ACLAR®** foil, and a BEEM capsule filled with fresh resin was placed on each cover slip. For polymerization, samples were placed in a 60°C oven for 3 days. To facilitate the removal of the coverslips from the resin block, they were dipped in liquid nitrogen until the coverslip could carefully be removed with a racer blade. Ultrathin sections (70 nm) were sliced using an ultramicrotome (EM UC7, Leica Microsystems) and mounted on formvar-coated copper slot grids. Images were acquired with a Tecnai 10 (FEI/Thermo Fisher) operated at 80 kV and equipped with an OSIS Megaview III camera.

SEM of CDMs

Results shown in section 3.1.2.2.4., Figure 19.

NIH 3T3 CDMs were grown on 200 mesh gold grids with 0.75% continuous formvar and 10 nm continuous carbon coating. They were fixed on day 14 with 2.5% glutaraldehyde in 0.1 M PB (pH 7.4) for 1 h at RT. Subsequently, they were dehydrated in a graded ethanol series (50%, 70%, 90%, 96%, 100% (twice) for 10 min) and dried with a critical point dryer (EM CPD300, Leica Microsystems). The grids with the dried CDMs were coated with platinum to a thickness of 7 nm using an EM ACE600 coating device (Leica Microsystems). The samples were observed with a FE-SEM Merlin compact VP scanning electron microscope (Carl Zeiss AG) at 5kV using a secondary electron detector.

Array Tomography

Results shown in section 3.5., Figure 52.

For Array tomography sample preparation we followed the OTO fixation protocol described in Deerinck et al. (2010) in order to enhance the contrast of sample for SEM (Deerinck et al., 2010).

D14 TIFF CDMs grown on coverslips were fixed with 2% paraformaldehyde and 2.5% glutaraldehyde in 0.1M PB for 1h at RT. The samples were washed in 0.1M PB and then contrast enhanced in 2% aqueous osmium tetroxide and 1.5% potassium ferrocyanide in 0.1M PB for 30 min in the dark. After washing with MilliQ water, the samples were transferred in thiocarbohydrazide for 20 min at RT and then again washed with MilliQ water. Samples were placed in 2% aqueous osmium tetroxide for 30 min at RT in the dark and then washed with MilliQ water. The samples were incubated overnight in 1% aqueous uranyl acetate at 4°C. Then they were washed in MilliQ water, placed in Walton's lead aspartate solution (Sigma-Aldrich) for 30 min at 60°C and washed in MilliQ water. The samples were dehydrated using a graded series of ethanol and then placed in anhydrous acetone. Afterwards they were infiltrated in a graded series of hard DurcupanTM ACM resin in acetone. The samples were placed in pure Durcupan overnight. On the next day, the coverslips were put on an **ACLAR®** foil, and a BEEM capsule, filled with fresh resin, was placed on each coverslip. For polymerization, samples were placed in a 60°C oven for 3 days. To facilitate the removal of the coverslips from the resin block, they were dipped in liquid nitrogen until the coverslip could carefully be removed with a racer blade.

The samples were trimmed with an Ultratrim diamond knife (Diatome) using an ultramicrotome EM UC7. Prior to serial sectioning, a carbon-coated 8 mm wide Kapton tape was plasma treated using an ELMO glow discharge cleaning system, equipped with a homemade reel-to-reel motorized winder, for increasing the hydrophilicity of the tape. Serial ultrathin sections of 70 nm thickness were cut with a 4 mm Ultra 35

diamond knife and picked up with the plasma-treated tape using an automated tape-collecting ultramicrotome ATUMtome. After collecting the sections on the tape, it was cut into strips and mounted on a 4-inch silicon wafer with conductive double sided adhesive carbon tape. The wafer was then coated with a 5 nm carbon layer to ensure conductivity. Sections were imaged on a FE-SEM Merlin compact VP (Zeiss) equipped with the Atlas 5 Array Tomography software. The high-resolution serial images for 3D-SEM reconstruction were taken with 10 nm pixel resolution at 5kV using a backscattered electron detector.

Mass Spectrometry

Results shown in section 3.1.2.2.3., Table 4.

Sample processing

TIFF were seeded into two 10 cm diameter cell culture dishes (Sarstedt, #83.3902) and CDMs were grown following the protocol described in section 3.1.2.1. The cell culture dishes were not coated prior to cell seeding to prevent any influence of surface coating on mass spectrometry results. CDMs were grown for 14 days with ascorbic acid treatment every other day and decellularized as described above (crosslink??).
After decellularization, CDMs were scraped off the cell culture dish surface with a cell scraper (Sarstedt, #83.1830) and placed into 1.5 ml centrifugation tubes.
The samples were centrifuged (13,000 g, 5 min), supernatants were removed, and pellets were re-dissolved by the addition of 100 µl 8 M Urea, 100 mM TEAB (triethylammonium bicarbonate), 25 mM TCEP (tris(2-carboxyethyl)phosphine hydrochloride) followed by sonication (Bioruptor plus, Diagenode, 10 x 30s/30s ON/OFF cycles) and heating up at 37°C for 2 h with shaking (800 RPM, Thermomixer F1.5, Eppendorf). Samples were then alkylated by the addition of 100 µl 50 mM Iodoacetamide and incubated in the dark for 30 min while shaking (800 RPM). Samples were then supplemented with 200 µl 100 mM TEAB and digested with 10 µl PNGase at 50°C for 2 h.
Adapting the protocol published in (Lansky et al., 2019), one sample was diluted by addition of 390 µl 100 mM TEAB, then supplemented with 8 µL Trypsin/LysC (1 µg/µl) and digested overnight at 37°C. The next day, the sample was supplemented with 4 µl Trypsin/LysC (1 µg/µl) and digested for a further 2 h, acidified by addition of 90 µl 10% TFA (trifluoro-acetic acid), then cleaned up on a tC18 SepPak plate (Waters) according to the manufacturer's protocol.
The other sample was precipitated using the methanol/chloroform method, then the protein pellet was trypsin digested and cleaned up using the iST 8x kit (PreOmics) according to the manufacturer's protocol but with overnight digestion.

LC-MS/MS analysis

Samples were dried, re-dissolved in 0.1 % TFA, and analysed by LC-MS/MS on an Ultimate High Performance Liquid Chromatography (HPLC, ThermoFisher Scientific) coupled to a Q-Exactive HF (ThermoFisher Scientific). Each sample was concentrated over a C18 µPAC trapping-column (PharmaFluidics), then bound to a 200 cm C18 µPAC column (micro-Pillar Array Column, PharmaFluidics) and eluted over the following 180 min gradient: solvent A, water + 0.1% formic acid; solvent B, 80% acetonitrile in water + 0.08% formic acid; constant 600 nL/min flow; B percentage: 5 min, 2%; 160 min, 31%; 185 min, 44%. Mass spectra were acquired in positive mode with a Data Dependent Acquisition method: FWHM 120 s, MS1 parameters: Profile, 1 microscan, 120,000 resolution, AGC target 3e6, 50 ms maximum IT, 380 to 1500 m/z; up to 20 MS2s per cycle. MS2 parameters: Centroid mode, 1 microscan, 15,000

resolution, AGC target 1e5, 20 ms maximum IT, 1.4 m/z isolation window (no offset), 380 to 1500 m/z, NCE 28, excluding charges 1+, 8+ and higher or unassigned, 60s dynamic exclusion.

Data analysis

Raw files were searched in MaxQuant 1.6.17.0 against a Homo sapiens reference proteome downloaded from UniProtKB. Fixed cysteine modification was set to Carbamidomethyl. Variable modifications were Oxidation (M), Acetyl (Protein N-term), Deamidation (NQ), Gln->pyro-Glu, Phospho (STY), and Hydroxyproline. Match between runs, dependent peptides, and second peptides were active. All False Discovery Rates (FDRs) were set to 1%. MaxQuant results were further processed in R using in-house scripts, which, starting from MaxQuant's evidence.txt (PSM) table, perform parsimonious protein groups inference and generate an Excel-formatted protein groups table.

Plunge-freezing

Decellularized CDMs on EM grids were vitrified in liquid ethane at -187°C after backside blotting in a Leica GP2 plunger (Leica Microsystems). Blotting conditions were set to 23°C, 90% humidity, and 5-8 s blotting time. Grids were stored in liquid nitrogen conditions and clipped into marked FIBSEM AutoGrids™ prior to further use. These marked FIBSEM AutoGrids™ are described in Figure 24.

High pressure freezing

Carriers were designed by me and produced at the ISTA Miba Machine Shop according to my specifications. Carriers of type A had a 3 mm diameter and a height of 0.5 mm, with a 2 mm diameter recess of a depth of ~20 µm (±5 µm machining inaccuracy). Carriers of Type B had a 3 mm diameter and a height of 0.5 mm without any recess. Every single carrier was measured for its height, and any carrier with more than ±2 µm derivation in height was removed.

Carriers were cleaned in pure ethanol by three rounds of sonication and dried at 60°C on a hot plate. Prior to use, carriers were coated with 1-hexadecene (Sigma, #H2131-100ML).

CDMs were incubated in the used cryoprotectant 30 min prior to vitrification and kept at 37°C, 5% CO_2 during this incubation time. Specimens were also kept at 37°C until HPF sandwich assembly. Every HPF sandwich was assembled directly before HPF and then frozen with a BAL-TEC HPM010. Specimens were stored in cryo-vials in liquid nitrogen until all samples had been high pressure frozen and were then transferred to a freshly cooled, clean clipping station. HPF sandwiches were then disassembled to recover the specimen if they had not already disassembled after HPF. Those specimens that showed obvious signs of distortions, bending, or damage to the EM substrate were removed immediately. All remaining specimens were clipped into marked FIBSEM AutoGrids™ (see Figure 24). Grids were stored in liquid nitrogen conditions until further use.

The used cryoprotectants and the vitrification by HPF are described in detail in section 3.2.2., see Table 5.

Dextran (#31389-100G), Sucrose (#84100-1KG), Polyvinylpyrrolidone (PVP, #PVP10-100G), and BSA (#10735078001) were purchased from Sigma-Aldrich).

Cryo-CLEM
For cryo-light microscopy, clipped grids were imaged on a Leica Cryo CLEM microscope (Leica Microsystems) using the Leica Application Suite 3.7.0. Tile scans were acquired using the LasX navigator or the MatrixScreener function of this software. Details can be found in section 3.3.1. Grids were stored in liquid nitrogen conditions until further use.

Cryo-FIB milling
Bulk lamellae were generated using a first generation TFS Aquilos cryo-FIBSEM (Aquilos I). All lift-out lamellae were created using the second-generation Aquilos (Aquilos II). The GIS system was used at a temperature of 28°C. The Aquilos instrument was operated using the xT user interface and the MAPS 3.14 software (TFS). The FIB was operated at 30kV, and the milling progress was monitored using the SEM beam at 25 pA and 2-5 kV. Grids were stored in liquid nitrogen conditions until further use.
Detailed protocols for the generation of bulk lamellae and lift-out lamellae are described in section 3.3.2.1 and 3.3.2.2.

Cryo-TEM and ET
Cryo-TEM and ET data on lamellae was collected on a TFS Titan Krios G3i operated at 300 kV in nanoProbe energy-filtered transmission electron microscopy mode (EFTEM). Images were acquired using a Gatan K3 BioQuantum direct electron detector with a slit width of 20 eV. For medium magnification images, a nominal magnification of x6,500 with a pixel size of 13.74 Å was used.
For tilt series acquisition, the camera was operated in counting mode using hardware binning and dose fractionation. A total dose of 180 e/Å^2 was used and divided into 61 images (for a 2° increment tilt scheme) or 41 images (for a 3° tilt scheme), while the total exposure was adjusted for each session. Tilt series were acquired with a dose-symmetric scheme starting from the lamella pre-tilt angle in a range of -60° and +60° (Hagen et al., 2017). The exact acquisition parameters are stated in Table 6.
The datasets were acquired using SerialEM (Mastronarde, 2005). More recent datasets were acquired employing PACE-tomo (Eisenstein et al., 2022).
Tomogram reconstruction with weighted back-projection and patch tracking, as well as visualization were done using the IMOD software (Kremer et al., 1996). A SIRT-like filter was applied during tomogram reconstruction for selected tomograms, one of which is shown in Figure 56. The number of iterations was tested and the value giving the best result chosen: for the visualization of the collagen banding pattern, a SIRT-like equivalent to 15 iterations worked best.
AreTomo (Zheng et al., 2022) was additionally used for tomogram reconstruction by weighted back-projection and patch tracking with a binning of 8.
IsoNet (Liu et al., 2022) was used on high-quality tomograms to increase the signal-to-noise ratio (SNR) and reconstruct the missing-wedge information. To this end, raw bin8 tomograms were deconvoluted using IsoNet and then used to train the neural network for 50 iterations. A mask with a patch size of 6 and subtomograms with a cube size of 64 were used for this training. The same tomograms were then used for the reconstruction of the missing-wedge information and improvement of the SNR.
NAD filtering was performed using IMOD on tomograms reconstructed by WBP and patch tracking. A range of values were tested for the K-value and the number of iterations, and the values resulting in the best result were then chosen: 10 iterations with a K-value of 10. One tomogram filtered in this way is shown in Figure 56.

Segmentation

The tomogram shown in Figure 60 was segmented in the Amira-Avizo software, version 2020.2 (Thermo Fisher Scientific). Plasma membranes, vesicles, microtubules, and collagen fibers were tracked manually. Amira filament tracing modules were used to segment filaments (Rigort et al., 2012). Previously established parameters (Dimchev et al., 2021) were used to identify actin filaments. To search for intermediate filaments search parameters were modified iteratively and results were inspected manually until ideal results were achieved. Parameters were optimized for the Cylindrical correlation module (Mask Cylinder Radius, Outer Cylinder Radius, Inner Cylinder Radius, Cylinder Length) and the Trace Correlation Lines module (Minimum Seed Correlation, Minimum Continuation Quality, Minimum Distance, Minimum Length).

Segments and coordinates for each set of segmented filaments were extracted in excel format and converted to a simplified space-separated plain text file (X coord, Y coord, Z coord, tube ID) using a custom made python script. Coordinates were converted from Ångstrom to pixels using Awk, to match the coordinate system in the binned tomogram. This coordinates file was then converted to an imod model file using imod (point2model). The model file was imported into imod (3dmod), superimposed onto the original tomogram, then points were manually curated: false positives were removed and non-automatically identified filaments were manually added. This curated model file was imported into chimeraX for visualization. Points were displayed in chimeraX as connected by lines with approximate diameter of their original size in the tomogram. Manually segmented structures were exported separately from Amira as mrc files which were then imported into chimeraX. For visualization these segmented volumes were smoothed and all segmented densities were colored using chimeraX.

6. REFERENCES

Abhilash, A.S., Baker, B.M., Trappmann, B., Chen, C.S., Shenoy, V.B., 2014. Article Remodeling of Fibrous Extracellular Matrices by Contractile Cells : Predictions from Discrete Fiber Network Simulations. Biophysj 107, 1829–1840. https://doi.org/10.1016/j.bpj.2014.08.029

Al-Amoudi, A., Chang, J.-J., Leforestier, A., McDowall, A., Salamin, L.M., Norlén, L.P.O., Richter, K., Blanc, N.S., Studer, D., Dubochet, J., 2004. Cryo-electron microscopy of vitreous sections. EMBO J. 23, 3583–8. https://doi.org/10.1038/sj.emboj.7600366

Al-Amoudi, A., Dubochet, J., Gnaegi, H., Lüthi, W., Studer, D., 2003. An oscillating cryo-knife reduces cutting-induced deformation of vitreous ultrathin sections. J. Microsc. 212, 26–33. https://doi.org/10.1046/j.1365-2818.2003.01244.x

Al-Amoudi, A., Studer, D., Dubochet, J., 2005. Cutting artefacts and cutting process in vitreous sections for cryo-electron microscopy. J. Struct. Biol. 150, 109–121. https://doi.org/10.1016/j.jsb.2005.01.003

Alberts, B., Heald, R., Johnson, A., Morgan, D., Raff, M., Roberts, K., Walter, P., 2022. Molecular Biology of The Cell, 7th edition., 7th editio. ed, Https://Medium.Com/. W. W. Norton & Company.

Alberts, B., Johnson, A., Lewis, J., Raff, M., Roberts, K., Walter, P., 2002. Looking at the Structure of Cells in the Microscope.

Amirrah, I.N., Lokanathan, Y., Zulkiflee, I., Wee, M.F.M.R., Motta, A., Fauzi, M.B., 2022. A Comprehensive Review on Collagen Type I Development of Biomaterials for Tissue Engineering: From Biosynthesis to Bioscaffold. Biomedicines 10. https://doi.org/10.3390/biomedicines10092307

Aper, S.J.A., Van Spreeuwel, A.C.C., Van Turnhout, M.C., Van Der Linden, A.J., Pieters, P.A., Van Der Zon, N.L.L., De La Rambelje, S.L., Bouten, C.V.C., Merkx, M., 2014. Colorful protein-based fluorescent probes for collagen imaging. PLoS One 9, 1–21. https://doi.org/10.1371/journal.pone.0114983

Arnold, J., Mahamid, J., Lucic, V., De Marco, A., Fernandez, J.J., Laugks, T., Mayer, T., Hyman, A.A., Baumeister, W., Plitzko, J.M., 2016. Site-Specific Cryo-focused Ion Beam Sample Preparation Guided by 3D Correlative Microscopy. Biophys. J. 110, 860–869. https://doi.org/10.1016/j.bpj.2015.10.053

Asano, S., Engel, B.D., Baumeister, W., 2016. In Situ Cryo-Electron Tomography: A Post-Reductionist Approach to Structural Biology. J. Mol. Biol. 428, 332–343. https://doi.org/10.1016/j.jmb.2015.09.030

Assunção, M., Dehghan-Baniani, D., Yiu, C.H.K., Später, T., Beyer, S., Blocki, A., 2020. Cell-Derived Extracellular Matrix for Tissue Engineering and Regenerative Medicine. Front. Bioeng. Biotechnol. https://doi.org/10.3389/fbioe.2020.602009

Ballerini, M., Milani, M., Batani, D., Squadrini, F., 2001. Focused ion beam techniques for the analysis of biological samples: A revolution in ultramicroscopy? Three-Dimensional Multidimens. Microsc. Image Acquis. Process. VIII 4261, 92. https://doi.org/10.1117/12.424523

Beck, K., Boswell, B.A., Ridgway, C.C., Bächinger, H.P., 1996. Triple helix formation of procollagen type I can occur at the rough endoplasmic reticulum membrane. J. Biol. Chem. 271, 21566–21573. https://doi.org/10.1074/jbc.271.35.21566

Bello, Y.M., Falabella, A.F., Eaglstein, W.H., 2012. Tissue-Engineered Skin. Am. J. Clin. Dermatology 2001 25 2, 305–313. https://doi.org/10.2165/00128071-200102050-00005

Ben-Harush, K., Maimon, T., Patla, I., Villa, E., Medalia, O., 2010. Visualizing cellular processes at the molecular level by cryo-electron tomography. J. Cell Sci. 123, 7–12. https://doi.org/10.1242/jcs.060111

Benton, G., Arnaoutova, I., George, J., Kleinman, H.K., Koblinski, J., 2014. Matrigel: From discovery and ECM mimicry to assays and models for cancer research. Adv. Drug Deliv. Rev. 79, 3–18. https://doi.org/10.1016/j.addr.2014.06.005

Bhella, D., 2019. Cryo-electron microscopy: an introduction to the technique, and considerations when working to establish a national facility. Biophys. Rev. 11, 515–519. https://doi.org/10.1007/S12551-019-00571-W/FIGURES/2

Birk, D.E., Trelstad, R.L., 1984. Extracellular compartments in matrix morphogenesis: Collagen fibril, bundle, and lamellar formation by corneal fibroblasts. J. Cell Biol. 99, 2024–2033. https://doi.org/10.1083/jcb.99.6.2024

Bonnans, C., Chou, J., Werb, Z., 2014. Remodelling the extracellular matrix in development and disease. Nat. Rev. Mol. Cell Biol. https://doi.org/10.1038/nrm3904

Bornstein, Paul, 1967. Comparative Sequence Studies of Rat Skin and Tendon Collagen. I. Evidence

for Incomplete Hydroxylation of Individual Prolyl Residues in the Normal Proteins. Biochemistry 6, 3082–3093. https://doi.org/10.1021/BI00862A015/ASSET/BI00862A015.FP.PNG_V03
Bornstein, P., 1967. The Incomplete Hydroxylation of Individual Prolyl Residues in Collagen. J. Biol. Chem. 242, 2572–2574. https://doi.org/10.1016/S0021-9258(18)96002-3
Bozec, L., Van Der Heijden, G., Horton, M., 2007. Collagen Fibrils: Nanoscale Ropes. Biophys. J. 92, 70. https://doi.org/10.1529/BIOPHYSJ.106.085704
Brownell, A.G., Veis, A., 1976. Intracellular location of triple helix formation of collagen. Enzyme probe studies. J. Biol. Chem. 251, 7137–7143. https://doi.org/10.1016/S0021-9258(17)32953-8
Buckley, G., Gervinskas, G., Taveneau, C., Venugopal, H., Whisstock, J.C., de Marco, A., 2020. Automated cryo-lamella preparation for high-throughput in-situ structural biology. J. Struct. Biol. 210, 107488. https://doi.org/10.1016/J.JSB.2020.107488
Canty-Laird, E.G., Lu, Y., Kadler, K.E., 2012. Stepwise proteolytic activation of type I procollagen to collagen within the secretory pathway of tendon fibroblasts in situ. Biochem. J. 441, 707. https://doi.org/10.1042/BJ20111379
Canty, E.G., Kadler, K.E., 2005. Procollagen trafficking, processing and fibrillogenesis. J. Cell Sci. 118, 1341–1353. https://doi.org/10.1242/JCS.01731
Canty, E.G., Lu, Y., Meadows, R.S., Shaw, M.K., Holmes, D.F., Kadler, K.E., 2004. Coalignment of plasma membrane channels and protrusions (fibripositors) specifies the parallelism of tendon. J. Cell Biol. 165, 553. https://doi.org/10.1083/JCB.200312071
Canty, E.G., Starborg, T., Lu, Y., Humphries, S.M., Holmes, D.F., Meadows, R.S., Huffman, A., O'Toole, E.T., Kadler, K.E., 2006. Actin filaments are required for fibripositor-mediated collagen fibril alignment in tendon. J. Biol. Chem. 281, 38592–38598. https://doi.org/10.1074/jbc.M607581200
Chen, Y., Zardi, L., Peters, D.M.P., 1997. High-resolution cryo-scanning electron microscopy study of the macromolecular structure of fibronectin fibrils. Scanning 19, 349–355. https://doi.org/10.1002/SCA.4950190505
Cheng, D., Mitchell, D., Shieh, D., Braet, F., 2012. Practical Considerations in the Successful Preparation of Specimens for Thin-Film Cryo-Transmission Electron Microscopy. Curr. Microsc. Contrib. to Adv. Sci. Technol. 880–890.
Cheng, H.W., Yuan, M.T., Li, C.W., Chan, B.P., 2020. Cell-derived matrices (CDM)—Methods, challenges and applications, in: Methods in Cell Biology. Academic Press Inc., pp. 235–258. https://doi.org/10.1016/bs.mcb.2020.01.001
Chu, M.L., Pan, T., Conway, D., Kuo, H.J., Glanville, R.W., Timpl, R., Mann, K., Deutzmann, R., 1989. Sequence analysis of α1(VI) and α2(VI) chains of human type VI collagen reveals internal triplication of globular domains similar to the A domains of von Willebrand factor and two α2(VI) chain variants that differ in the carboxy terminus. EMBO J. 8, 1939–1946. https://doi.org/10.1002/j.1460-2075.1989.tb03598.x
Cruz-Munoz, W., Khokha, R., 2008. The Role of Tissue Inhibitors of Metalloproteinases in Tumorigenesis and Metastasis. https://doi.org/10.1080/10408360801973244 45, 291–338. https://doi.org/10.1080/10408360801973244
Cui, F.Z., Li, Y., Ge, J., 2007. Self-assembly of mineralized collagen composites. Mater. Sci. Eng. R Reports 57, 1–27. https://doi.org/10.1016/J.MSER.2007.04.001
Curtis, A.S.G., Forrester, J. V., McInnes, C., Lawrie, F., 1983. Adhesion of cells to polystyrene surfaces. J. Cell Biol. 97, 1500–1506. https://doi.org/10.1083/JCB.97.5.1500
Cyrklaff, M., Kühlbrandt, W., 1994. High-resolution electron microscopy of biological specimens in cubic ice. Ultramicroscopy 55, 141–153. https://doi.org/10.1016/0304-3991(94)90165-1
Dahl, R., Staehelin, L.A., 1989. Highpressure freezing for the preservation of biological structure: Theory and practice. J. Electron Microsc. Tech. 13, 165–174. https://doi.org/10.1002/jemt.1060130305
De Beer*, M., Daviran*, D., Roverts*, R., Rutten, L., Macías Sánchez, E., Metz, J.R., Sommerdijk, N., Akiva, A., 2022. Precise targeting for 3D cryo-correlative light and electron microscopy volume imaging of tissues using a FinderTOP. bioRxiv im, 2022.07.31.502212.
Deerinck, T.J., Bushong, E.A., Ellisman, M.H., Thor, A., 2010. NCMIR methods for 3D EM: A new protocol for preparation of biological specimens for serial block face scanning electron microscopy. Protocols.Io. https://doi.org/10.17504/PROTOCOLS.IO.36WGQ7JE5VK5/V2
Dimchev, G., Amiri, B., Fäßler, F., Falcke, M., Schur, F.K., 2021. Computational toolbox for ultrastructural quantitative analysis of filament networks in cryo-ET data. J. Struct. Biol. 213, 107808. https://doi.org/10.1016/J.JSB.2021.107808
Doyle, A.D., Carvajal, N., Jin, A., Matsumoto, K., Yamada, K.M., 2015. Local 3D matrix microenvironment regulates cell migration through spatiotemporal dynamics of contractility-

dependent adhesions. Nat. Commun. 6, 1–15. https://doi.org/10.1038/ncomms9720
Drobne, D., Milani, M., Zrimec, A., Berden Zrimec, M., Tatti, F., Dras, K., Lar, ˇ, 2005. Focused Ion Beam/Scanning Electron Microscopy Studies of Porcellio scaber (Isopoda, Crustacea) Digestive Gland Epithelium Cells 27, 30–34.
Dubochet, J., Lepault, J., Freeman, R., Berriman, J.A., Homo, J. -C, 1982. Electron microscopy of frozen water and aqueous solutions. J. Microsc. 128, 219–237. https://doi.org/10.1111/j.1365-2818.1982.tb04625.x
Dumoux, M., Glen, T., Ho, E.M.L., Perdigão, L.M.A., Klumpe, S., Yee, N.B. -y., Farmer, D., Smith, J.L.R., Lai, P.Y.A., Bowles, W., Kelley, R., Plitzko, J.M., Wu, L., Basham, M., Clare, D.K., Siebert, C.A., Darrow, M.C., Naismith, J.H., Grange, M., 2022. Cryo-plasma FIB/SEM volume imaging of biological specimens. bioRxiv 2022.09.21.508877. https://doi.org/10.1101/2022.09.21.508877
Dunstone, M.A., de Marco, A., 2017. Cryo-electron tomography: an ideal method to study membrane-associated proteins. Philos. Trans. R. Soc. Lond. B. Biol. Sci. 372. https://doi.org/10.1098/rstb.2016.0210
Duval, K., Grover, H., Han, L.-H., Mou, Y., Pegoraro, A.F., Fredberg, J., Chen, Z., 2017. Modeling Physiological Events in 2D vs. 3D Cell Culture. Physiology 32, 266–277. https://doi.org/10.1152/physiol.00036.2016
Dzamba, B.J., Wu, H., Jaenisch, R., Peters, D.M., 1993. Fibronectin Binding Site in Type I Collagen Regulates Fibronectin Fibril Formation. J. Cell Biol. 121, 1165–1172.
Eisenstein, F., Yanagisawa, H., Kashihara, H., Kikkawa, M., Tsukita, S., Danev, R., 2022. Parallel cryo electron tomography on in situ lamellae. bioRxiv 2022.04.07.487557. https://doi.org/10.1038/s41592-022-01690-1
Even-Ram, S., Yamada, K.M., 2005. Cell migration in 3D matrix. Curr. Opin. Cell Biol. 17, 524–532. https://doi.org/10.1016/j.ceb.2005.08.015
Farquhar, M.G., Palade, G.E., 1965. CELL JUNCTIONS IN AMPHIBIAN SKIN. J. Cell Biol. 26, 263. https://doi.org/10.1083/JCB.26.1.263
Fäßler, F., Dimchev, G., Hodirnau, V.V., Wan, W., Schur, F.K.M., 2020a. Cryo-electron tomography structure of Arp2/3 complex in cells reveals new insights into the branch junction. Nat. Commun. 2020 111 11, 1–10. https://doi.org/10.1038/s41467-020-20286-x
Fäßler, F., Zens, B., Hauschild, R., Schur, F.K.M., 2020b. 3D printed cell culture grid holders for improved cellular specimen preparation in cryo-electron microscopy. J. Struct. Biol. 212. https://doi.org/10.1016/j.jsb.2020.107633
Fischer Verlag, G., Brodsky, B., Ramshaw, J.A.M., 1997. The Collagen Triple-Helix Structure. Matrix Biol. 15, 545–554.
Fitzpatrick, L.E., McDevitt, T.C., 2015. Cell-derived matrices for tissue engineering and regenerative medicine applications. Biomater. Sci. https://doi.org/10.1039/c4bm00246f
Frangakis, A.S., Hegerl, R., 1999. Nonlinear anisotropic diffusion in three-dimensional electron microscopy. Lect. Notes Comput. Sci. (including Subser. Lect. Notes Artif. Intell. Lect. Notes Bioinformatics) 1682, 386–397. https://doi.org/10.1007/3-540-48236-9_34/COVER
Frantz, C., Stewart, K.M., Weaver, V.M., 2010. The extracellular matrix at a glance. J. Cell Sci. 123, 4195–4200. https://doi.org/10.1242/jcs.023820
Friedl, P., Wolf, K., 2010. Plasticity of cell migration: A multiscale tuning model. J. Cell Biol. 188, 11–19. https://doi.org/10.1083/jcb.200909003
Früh, S.M., Schoen, I., Ries, J., Vogel, V., 2015. Molecular architecture of native fibronectin fibrils. Nat. Commun. 6. https://doi.org/10.1038/ncomms8275
Furthmayr, H., Wiedemann, H., Timpl, R., Odermatt, E., Engel, J., 1983. Electron-microscopical approach to a structural model of intima collagen. Biochem. J. 211, 303–311. https://doi.org/10.1042/bj2110303
Gelse, K., Pöschl, E., Aigner, T., 2003. Collagens—structure, function, and biosynthesis. Adv. Drug Deliv. Rev. 55, 1531–1546. https://doi.org/10.1016/J.ADDR.2003.08.002
Grant, T., Grigorieff, N., 2015. Measuring the optimal exposure for single particle cryo-EM using a 2.6 Å reconstruction of rotavirus VP6. Elife 4. https://doi.org/10.7554/ELIFE.06980
Gross, J., Schmitt, F.O., 1948. The structure of human skin collagen as studied with the electron microscope. https://doi.org/10.1016/bs.mcb.2017.08.002
Gusnard, D., Kirschner, R.H., 1977. Cell and organelle shrinkage during preparation for scanning electron microscopy: effects of fixation, dehydration and critical point drying. J. Microsc. 110, 51–57. https://doi.org/10.1111/j.1365-2818.1977.tb00012.x
Hagen, W.J.H., Wan, W., Briggs, J.A.G., 2017. Implementation of a cryo-electron tomography tilt-scheme optimized for high resolution subtomogram averaging. J. Struct. Biol. 197, 191–198.

https://doi.org/10.1016/j.jsb.2016.06.007
Hakkinen, K.M., Harunaga, J.S., Doyle, A.D., Yamada, K.M., 2011. Direct Comparisons of the Morphology, Migration, Cell Adhesions, and Actin Cytoskeleton of Fibroblasts in Four Different Three-Dimensional Extracellular Matrices. Tissue Eng. Part A 17, 713. https://doi.org/10.1089/TEN.TEA.2010.0273
Harapin, J., Börmel, M., Sapra, K.T., Brunner, D., Kaech, A., Medalia, O., 2015. Structural analysis of multicellular organisms with cryo-electron tomography. Nat. Methods 12, 634–636. https://doi.org/10.1038/nmeth.3401
Hayles, M.F., de Winter, D.A.M., 2021. An introduction to cryo-FIB-SEM cross-sectioning of frozen, hydrated Life Science samples. J. Microsc. 281, 138–156. https://doi.org/10.1111/JMI.12951
Hayles, M.F., Stokes, D.J., Phifer, D., Findlay, K.C., 2007. A technique for improved focused ion beam milling of cryo-prepared life science specimens. J. Microsc. 226, 263–269. https://doi.org/10.1111/j.1365-2818.2007.01775.x
Ho, M.H., Wang, D.M., Hsieh, H.J., Liu, H.C., Hsien, T.Y., Lai, J.Y., Hou, L.T., 2005. Preparation and characterization of RGD-immobilized chitosan scaffolds. Biomaterials 26, 3197–3206. https://doi.org/10.1016/J.BIOMATERIALS.2004.08.032
Holmes, D.F., Lu, Y., Starborg, T., Kadler, K.E., 2018. Collagen Fibril Assembly and Function. Curr. Top. Dev. Biol. 130, 107–142. https://doi.org/10.1016/BS.CTDB.2018.02.004
Hsieh, C., Schmelzer, T., Kishchenko, G., Wagenknecht, T., Marko, M., 2014. Practical workflow for cryo focused-ion-beam milling of tissues and cells for cryo-TEM tomography. J. Struct. Biol. 185, 32–41. https://doi.org/10.1016/j.jsb.2013.10.019
Hulmes, D.J.S., 2002. Building collagen molecules, fibrils, and suprafibrillar structures. J. Struct. Biol. 137, 2–10. https://doi.org/10.1006/JSBI.2002.4450
Huster, D., 2008. Chapter 4 Solid-State NMR Studies of Collagen Structure and Dynamics in Isolated Fibrils and in Biological Tissues. Annu. Reports NMR Spectrosc. 64, 127–159. https://doi.org/10.1016/S0066-4103(08)00004-5
Hylton, R.K., Heebner, J.E., Grillo, M.A., Swulius, M.T., 2022. Cofilactin filaments regulate filopodial structure and dynamics in neuronal growth cones. Nat. Commun. 13, 1–11. https://doi.org/10.1038/s41467-022-30116-x
Iozzo, R. V., Gubbiotti, M.A., 2018. Extracellular Matrix: The driving force of mammalian diseases. Matrix Biol. 71–72, 1. https://doi.org/10.1016/J.MATBIO.2018.03.023
Jacquemet, G., Hamidi, H., Ivaska, J., 2015. Filopodia in cell adhesion, 3D migration and cancer cell invasion. Curr. Opin. Cell Biol. 36, 23–31. https://doi.org/10.1016/J.CEB.2015.06.007
Jin, L., Milazzo, A.C., Kleinfelder, S., Li, S., Leblanc, P., Duttweiler, F., Bouwer, J.C., Peltier, S.T., Ellisman, M.H., Xuong, N.H., 2008. Applications of Direct Detection Device in Transmission Electron Microscopy. J. Struct. Biol. 161, 352. https://doi.org/10.1016/J.JSB.2007.10.007
Kadler, K.E., Baldock, C., Bella, J., Boot-Handford, R.P., 2007. Collagens at a glance. J. Cell Sci. 120, 1955–1958. https://doi.org/10.1242/JCS.03453
Kadler, K.E., Hill, A., Canty-Laird, E.G., 2008. Collagen fibrillogenesis: fibronectin, integrins, and minor collagens as organizers and nucleators. Curr. Opin. Cell Biol. 20, 495–501. https://doi.org/10.1016/J.CEB.2008.06.008
Karuppasamy, M., Karimi Nejadasl, F., Vulovic, M., Koster, A.J., Ravelli, R.B.G., 2011. Radiation damage in single-particle cryo-electron microscopy: Effects of dose and dose rate. J. Synchrotron Radiat. 18, 398–412. https://doi.org/10.1107/S090904951100820X/XH5022SUP1.AVI
Kaukonen, R., Jacquemet, G., Hamidi, H., Ivaska, J., 2017. Cell-derived matrices for studying cell proliferation and directional migration in a complex 3D microenvironment. Nat. Protoc. 12, 2376–2390. https://doi.org/10.1038/nprot.2017.107
Keene, D.R., Oxford, J.T., Morris, N.P., 2017. Ultrastructural localization of collagen types II, IX, and XI in the growth plate of human rib and fetal bovine epiphyseal cartilage: type XI collagen is restricted to thin fibrils. http://dx.doi.org/10.1177/43.10.7560887 43, 967–979. https://doi.org/10.1177/43.10.7560887
Keene, D.R., Tufa, S.F., 2018. Ultrastructural analysis of the extracellular matrix, 1st ed, Methods in Cell Biology. Elsevier Inc. https://doi.org/10.1016/bs.mcb.2017.08.002
Kelley, K., Raczkowski, A.M., Klykov, O., Jaroenlak, P., Bobe, D., Kopylov, M., Eng, E.T., Bhabha, G., Potter, C.S., Carragher, B., Noble, A.J., 2022. Waffle Method: A general and flexible approach for improving throughput in FIB-milling. Nat. Commun. 2022 131 13, 1–13. https://doi.org/10.1038/s41467-022-29501-3
Khavnekar, S., Vrbovská, V., Zaoralová, M., Kelley, R., Beck, F., Klumpe, S., Kotecha, A., Plitzko, J., Erdmann, P.S., 2022. Optimizing Cryo-FIB Lamellas for sub-5Å in situ Structural Biology.

bioRxiv 2022.06.16.496417.
Kirmse, R., Page, C., Hoenger, A., 2010. Three-Dimensional Cryo-Electron Microscopy on Intermediate Filaments. Methods Cell Biol. 96, 565–589. https://doi.org/10.1016/10.1016/S0091-679X(10)96023-8
Kisseleva, T., Brenner, D.A., 2008. Mechanisms of fibrogenesis. Exp. Biol. Med. (Maywood). 233, 109–122. https://doi.org/10.3181/0707-MR-190
Kloareg, B., Badis, Y., Cock, J.M., Michel, G., 2021. Role and Evolution of the Extracellular Matrix in the Acquisition of Complex Multicellularity in Eukaryotes: A Macroalgal Perspective. https://doi.org/10.3390/genes12071059
Klumpe, S., Fung, H.K.H., Goetz, S.K., Zagoriy, I., Hampoelz, B., Zhang, X., Erdmann, P.S., Baumbach, J., Müller, C.W., Beck, M., Plitzko, J.M., Mahamid, J., 2021. A Modular Platform for Automated Cryo-FIB Workflows. Elife 10, 1–29. https://doi.org/10.7554/eLife.70506
Kolovou, A., Schorb, M., Tarafder, A., Sachse, C., Schwab, Y., Santarella-Mellwig, R., 2017. A new method for cryo-sectioning cell monolayers using a correlative workflow, Methods in Cell Biology. Elsevier Ltd. https://doi.org/10.1016/bs.mcb.2017.03.011
Kremer, J.R., Mastronarde, D.N., McIntosh, J.R., 1996. Stahlberg, H. &Walz, T. ~2008!.Molecular electron microscopy: State of the art and current challenges. ACS Chem Biol 3, 268–281. J. Struct. Biol. 116, 71–6.
Krohn, V.E., Ringo, G.R., 1975. Ion source of high brightness using liquid metal. Appl. Phys. Lett. 27, 479–481. https://doi.org/10.1063/1.88540
Kuba, J., Mitchels, J., Hovorka, M., Erdmann, P., Berka, L., Kirmse, R., König, J., De Bock, J., Goetze, B., Rigort, A., 2021. Advanced cryo-tomography workflow developments – correlative microscopy, milling automation and cryo-lift-out. J. Microsc. 281, 112–124. https://doi.org/10.1111/JMI.12939
Kukulski, W., Schorb, M., Welsch, S., Picco, A., Kaksonen, M., Briggs, J.A.G., 2012. Precise, Correlated Fluorescence Microscopy and Electron Tomography of Lowicryl Sections Using Fluorescent Fiducial Markers, Methods in Cell Biology. Elsevier. https://doi.org/10.1016/B978-0-12-416026-2.00013-3
Kukulski, W., Schorb, M., Welsch, S., Picco, A., Kaksonen, M., Briggs, J.A.G., 2011. Correlated fluorescence and 3D electron microscopy with high sensitivity and spatial precision 192, 111–119. https://doi.org/10.1083/jcb.201009037
Kutys, M.L., Doyle, A.D., Yamada, K.M., 2013. Regulation of cell adhesion and migration by cell-derived matrices. Exp. Cell Res. https://doi.org/10.1016/j.yexcr.2013.05.030
Lansky, Z., Mutsafi, Y., Houben, L., Ilani, T., Armony, G., Wolf, S.G., Fass, D., 2019. 3D mapping of native extracellular matrix reveals cellular responses to the microenvironment. J. Struct. Biol. X 1, 100002. https://doi.org/10.1016/j.yjsbx.2018.100002
Ledger, P.W., Uchida, N., Tanzer, M.L., 1980. Immunocytochemical localization of procollagen and fibronectin in human fibroblasts: effects of the monovalent ionophore, monensin. J. Cell Biol. 87, 663–671. https://doi.org/10.1083/JCB.87.3.663
Lee, S., Solow-Cordero, D.E., Kessler, E., Takahara, K., Greenspan, D.S., 1997. Transforming Growth Factor-Î² Regulation of Bone Morphogenetic Protein-1/Procollagen C-proteinase and Related Proteins in Fibrogenic Cells and Keratinocytes*. J. Biol. Chem. 272, 19059–19066. https://doi.org/10.1074/jbc.272.30.19059
León-López, A., Morales-Peñaloza, A., Martínez-Juárez, V.M., Vargas-Torres, A., Zeugolis, D.I., Aguirre-Álvarez, G., 2019. Hydrolyzed Collagen—Sources and Applications. Molecules 24. https://doi.org/10.3390/MOLECULES24224031
Lethias, C., Carisey, A., Comte, J., Cluzel, C., Exposito, J.Y., 2006. A model of tenascin-X integration within the collagenous network. FEBS Lett. 580, 6281–6285. https://doi.org/10.1016/J.FEBSLET.2006.10.037
Lin, X., Patil, S., Gao, Y.G., Qian, A., 2020. The Bone Extracellular Matrix in Bone Formation and Regeneration. Front. Pharmacol. 11. https://doi.org/10.3389/FPHAR.2020.00757
Liu, Y.T., Zhang, H., Wang, H., Tao, C.L., Bi, G.Q., Zhou, Z.H., 2022. Isotropic reconstruction for electron tomography with deep learning. Nat. Commun. 13, 1–17. https://doi.org/10.1038/s41467-022-33957-8
Lu, H., Hoshiba, T., Kawazoe, N., Koda, I., Song, M., Chen, G., 2011. Cultured cell-derived extracellular matrix scaffolds for tissue engineering. Biomaterials 32, 9658–9666. https://doi.org/10.1016/J.BIOMATERIALS.2011.08.091
Lucero, H.A., Kagan, H.M., 2006. Lysyl oxidase: an oxidative enzyme and effector of cell function. Cell. Mol. Life Sci. C. 2006 6319 63, 2304–2316. https://doi.org/10.1007/S00018-006-6149-9
Lučić, V., Förster, F., Baumeister, W., 2005. Structural studies by electron tomography: From cells to

molecules. Annu. Rev. Biochem. 74, 833–865. https://doi.org/10.1146/annurev.biochem.73.011303.074112
Mader, A., Elad, N., Medalia, O., 2010. Cryoelectron Tomography of Eukaryotic Cells. Methods Enzymol. 483, 245–265. https://doi.org/10.1016/S0076-6879(10)83012-5
Mahamid, J., Schampers, R., Persoon, H., Hyman, A.A., Baumeister, W., Plitzko, J.M., 2015. A focused ion beam milling and lift-out approach for site-specific preparation of frozen-hydrated lamellas from multicellular organisms. J. Struct. Biol. 192, 262–269. https://doi.org/10.1016/j.jsb.2015.07.012
Malek, S., Köster, D. V., 2021. The Role of Cell Adhesion and Cytoskeleton Dynamics in the Pathogenesis of the Ehlers-Danlos Syndromes and Hypermobility Spectrum Disorders. Front. Cell Dev. Biol. 9, 883. https://doi.org/10.3389/FCELL.2021.649082/BIBTEX
Marko, M., Hsieh, C., Moberlychan, W., Mannella, C.A., Frank, J., 2006. Focused ion beam milling of vitreous water: Prospects for an alternative to cryo-ultramicrotomy of frozen-hydrated biological samples. J. Microsc. 222, 42–47. https://doi.org/10.1111/j.1365-2818.2006.01567.x
Marko, M., Hsieh, C., Schalek, R., Frank, J., Mannella, C., 2007. Focused-ion-beam thinning of frozen-hydrated biological specimens for cryo-electron microscopy. Nat. Methods 4, 215–217. https://doi.org/10.1038/NMETH1014
Martinez-Hernandez, A., Amenta, P.S., 1993. The hepatic extracellular matrix - II. Ontogenesis, regeneration and cirrhosis. Virchows Arch. A Pathol. Anat. Histopathol. 423, 77–84. https://doi.org/10.1007/BF01606580
Mastronarde, D.N., 2005. Automated electron microscope tomography using robust prediction of specimen movements. J. Struct. Biol. 152, 36–51. https://doi.org/10.1016/j.jsb.2005.07.007
Mattila, P.K., Lappalainen, P., 2008. Filopodia: molecular architecture and cellular functions. Nat. Rev. Mol. Cell Biol. 2008 96 9, 446–454. https://doi.org/10.1038/nrm2406
McDonald, J.A., Kelley, D.G., Broekelmann, T.J., 1982. Role of fibronectin in collagen deposition: Fab' to the gelatin-binding domain of fibronectin inhibits both fibronectin and collagen organization in fibroblast extracellular matrix. J. Cell Biol. 92, 485–492. https://doi.org/10.1083/JCB.92.2.485
METEOR: an integrated top down cryo-CLEM imaging system. [WWW Document], 2022. . Online Homepage. URL https://blog.delmic.com/meteor-an-integrated-top-down-cryo-clem-imaging-system (accessed 11.20.22).
Miller, A., Parry, D.A.D., 1973. Structure and packing of microfibrils in collagen. J. Mol. Biol. 75, 441–447. https://doi.org/10.1016/0022-2836(73)90035-1
Miller, A., Wray, J.S., 1971. Molecular Packing in Collagen. Nat. 1971 2305294 230, 437–439. https://doi.org/10.1038/230437a0
Minamitani, T., Ikuta, T., Saito, Y., Takebe, G., Sato, M., Sawa, H., Nishimura, T., Nakamura, F., Takahashi, K., Ariga, H., Matsumoto, K.I., 2004. Modulation of collagen fibrillogenesis by tenascin-X and type VI collagen. Exp. Cell Res. 298, 305–315. https://doi.org/10.1016/j.yexcr.2004.04.030
Mohan, V., Das, A., Sagi, I., 2020. Emerging roles of ECM remodeling processes in cancer. Semin. Cancer Biol. 62, 192–200. https://doi.org/10.1016/J.SEMCANCER.2019.09.004
Mott, J.D., Werb, Z., 2004. Regulation of matrix biology by matrix metalloproteinases. Curr. Opin. Cell Biol. 16, 558. https://doi.org/10.1016/J.CEB.2004.07.010
Mouw, J.K., Ou, G., Weaver, V.M., 2014. Extracellular matrix assembly: a multiscale deconstruction. Nat. Rev. Mol. Cell Biol. 2014 1512 15, 771–785. https://doi.org/10.1038/nrm3902
Muir, H., 1995. The chondrocyte, architect of cartilage. Biomechanics, structure, function and molecular biology of cartilage matrix macromolecules. BioEssays 17, 1039–1048. https://doi.org/10.1002/bies.950171208
Murgoci, A., Duer, M., 2021. Molecular conformations and dynamics in the extracellular matrix of mammalian structural tissues: Solid-state NMR spectroscopy approaches. Matrix Biol. Plus 12. https://doi.org/10.1016/J.MBPLUS.2021.100086
Myllyharju, J., Kivirikko, K.I., 2004. Collagens, modifying enzymes and their mutations in humans, flies and worms. Trends Genet. 20, 33–43. https://doi.org/10.1016/J.TIG.2003.11.004
Naba, A., Clauser, K.R., Hoersch, S., Liu, H., Carr, S.A., Hynes, R.O., 2012. The Matrisome: In Silico Definition and In Vivo Characterization by Proteomics of Normal and Tumor Extracellular Matrices. Mol. Cell. Proteomics 11. https://doi.org/10.1074/MCP.M111.014647
Nogales, E., 2016. The development of cryo-EM into a mainstream structural biology technique. Nat. Methods 13, 24. https://doi.org/10.1038/NMETH.3694
Nyström, H., 2021. Extracellular matrix proteins in metastases to the liver – Composition, function and potential applications. Semin. Cancer Biol. 71, 134–142.

https://doi.org/10.1016/J.SEMCANCER.2020.06.004
Ockenga, W., 2015. A Brief History of Light Microscopy – From the Medieval Reading Stone to Super-Resolution.
Orgel, J.P.R.O., Miller, A., Irving, T.C., Fischetti, R.F., Hammersley, A.P., Wess, T.J., 2001. The in situ supermolecular structure of type I collagen. Structure 9, 1061–1069. https://doi.org/10.1016/S0969-2126(01)00669-4
Orloff, J., 2001. Focused Ion Beam Characterization Techniques. Encycl. Mater. Sci. Technol. 3226–3231. https://doi.org/10.1016/b0-08-043152-6/00574-x
Orloff, J., 1996. Fundamental limits to imaging resolution for focused ion beams. J. Vac. Sci. Technol. B Microelectron. Nanom. Struct. 14, 3759. https://doi.org/10.1116/1.588663
Persikov, A. V., Ramshaw, J.A.M., Brodsky, B., 2005. Prediction of collagen stability from amino acid sequence. J. Biol. Chem. 280, 19343–19349. https://doi.org/10.1074/JBC.M501657200
Petrie, R.J., Yamada, K.M., 2016. Multiple mechanisms of 3D migration: The origins of plasticity. Curr. Opin. Cell Biol. 42, 7–12. https://doi.org/10.1016/j.ceb.2016.03.025
Piez, K.A., 1997. History of Extracellular Matrix : A Personal View 1.
Ploetz, C., Zycband, E.I., Birk, D.E., 1991. Collagen fibril assembly and deposition in the developing dermis: Segmental deposition in extracellular compartments. J. Struct. Biol. 106, 73–81. https://doi.org/10.1016/1047-8477(91)90064-4
Prabhakar, N., Belevich, I., Peurla, M., Heiligenstein, X., Chang, H.C., Sahlgren, C., Jokitalo, E., Rosenholm, J.M., 2021. Cell volume (3D) correlative microscopy facilitated by intracellular fluorescent nanodiamonds as multi-modal probes. Nanomaterials 11, 1–10. https://doi.org/10.3390/nano11010014
Raey, W.S., Hertl, W., Nowlan, E.D., Binkowski, N.J., 1984. Surface treatments and cell attachment. Vitr. J. Tissue Cult. Assoc. 20, 802–808. https://doi.org/10.1007/BF02618296
Ricard-Blum, S., 2011. The Collagen Family. Cold Spring Harb. Perspect. Biol. 3, 1–19. https://doi.org/10.1101/CSHPERSPECT.A004978
Richter, K., 1994. Cutting artefacts on ultrathin cryosections of biological bulk specimens. Micron 25, 297–308. https://doi.org/10.1016/0968-4328(94)90001-9
Rigort, A., Bäuerlein, F.J.B., Leis, A., Gruska, M., Hoffmann, C., Laugks, T., Böhm, U., Eibauer, M., Gnaegi, H., Baumeister, W., Plitzko, J.M., 2010. Micromachining tools and correlative approaches for cellular cryo-electron tomography. J. Struct. Biol. 172, 169–179. https://doi.org/10.1016/j.jsb.2010.02.011
Rigort, A., Günther, D., Hegerl, R., Baum, D., Weber, B., Prohaska, S., Medalia, O., Baumeister, W., Hege, H., 2012. Automated segmentation of electron tomograms for a quantitative description of actin filament networks. J. Struct. Biol. 177, 135–144. https://doi.org/10.1016/j.jsb.2011.08.012
Robins, S.P., 2007. Biochemistry and functional significance of collagen cross-linking. Biochem. Soc. Trans. 35, 849–852. https://doi.org/10.1042/BST0350849
Rosell-Garcia, T., Rodriguez-Pascual, F., 2018. Enhancement of collagen deposition and cross-linking by coupling lysyl oxidase with bone morphogenetic protein-1 and its application in tissue engineering. Sci. Rep. 8, 1–12. https://doi.org/10.1038/s41598-018-29236-6
Rubi-Sans, G., Castaño, O., Cano, I., Mateos-Timoneda, M.A., Perez-Amodio, S., Engel, E., 2020. Engineering Cell-Derived Matrices: From 3D Models to Advanced Personalized Therapies. Adv. Funct. Mater. https://doi.org/10.1002/adfm.202000496
Sandvold Beckwith, M., Sandvold Beckwith, K., Sikorski, P., Tostrup Skogaker, N., Helen Flo, T., Halaas, Ø., 2015. Seeing a Mycobacterium-Infected Cell in Nanoscale 3D: Correlative Imaging by Light Microscopy and FIB/SEM Tomography. https://doi.org/10.1371/journal.pone.0134644
Saunders, J.T., Schwarzbauer, J.E., 2019. Fibronectin matrix as a scaffold for procollagen proteinase binding and collagen processing. Mol. Biol. Cell 30, 2218–2226. https://doi.org/10.1091/MBC.E19-03-0140/ASSET/IMAGES/LARGE/MBC-30-2218-G007.JPEG
Schaffer, M., Mahamid, J., Engel, B.D., Laugks, T., Baumeister, W., Plitzko, J.M., 2017. Optimized cryo-focused ion beam sample preparation aimed at in situ structural studies of membrane proteins. J. Struct. Biol. 197, 73–82. https://doi.org/10.1016/J.JSB.2016.07.010
Schaffer, M., Pfeffer, S., Mahamid, J., Kleindiek, S., Laugks, T., Albert, S., Engel, B.D., Rummel, A., Smith, A.J., Baumeister, W., Plitzko, J.M., 2019. A cryo-FIB lift-out technique enables molecular-resolution cryo-ET within native Caenorhabditis elegans tissue. Nat. Methods 16, 757–762. https://doi.org/10.1038/s41592-019-0497-5
Schellenberger, P., Kaufmann, R., Siebert, C.A., Hagen, C., Wodrich, H., Grünewald, K., 2014. High-precision correlative fluorescence and electron cryo microscopy using two independent alignment markers. Ultramicroscopy 143, 41–51. https://doi.org/10.1016/J.ULTRAMIC.2013.10.011

Schertel, A., Snaidero, N., Han, H.M., Ruhwedel, T., Laue, M., Grabenbauer, M., Möbius, W., 2013. Cryo FIB-SEM: Volume imaging of cellular ultrastructure in native frozen specimens. J. Struct. Biol. 184, 355–360. https://doi.org/10.1016/j.jsb.2013.09.024
Schiller, J., Huster, D., 2012. New methods to study the composition and structure of the extracellular matrix in natural and bioengineered tissues. Biomatter 2, 115. https://doi.org/10.4161/BIOM.20866
Schindelin, J., Arganda-Carreras, I., Frise, E., Kaynig, V., Longair, M., Pietzsch, T., Preibisch, S., Rueden, C., Saalfeld, S., Schmid, B., Tinevez, J.Y., White, D.J., Hartenstein, V., Eliceiri, K., Tomancak, P., Cardona, A., 2012. Fiji: An open-source platform for biological-image analysis. Nat. Methods 9, 676–682. https://doi.org/10.1038/nmeth.2019
Schorb, M., Briggs, J.A.G., 2014. Correlated cryo-fluorescence and cryo-electron microscopy with high spatial precision and improved sensitivity. Ultramicroscopy 143, 24–32. https://doi.org/10.1016/j.ultramic.2013.10.015
Schorb, M., Gaechter, L., Avinoam, O., Sieckmann, F., Clarke, M., Bebeacua, C., Bykov, Y.S., Sonnen, A.F.P., Lihl, R., Briggs, J.A.G., 2017. New hardware and workflows for semi-automated correlative cryo-fluorescence and cryo-electron microscopy/tomography. J. Struct. Biol. 197, 83–93. https://doi.org/10.1016/j.jsb.2016.06.020
Schultz, G.S., Wysocki, A., 2009. Interactions between extracellular matrix and growth factors in wound healing. Wound Repair Regen. 17, 153–162. https://doi.org/10.1111/J.1524-475X.2009.00466.X
Shoulders, M.D., Raines, R.T., 2009. COLLAGEN STRUCTURE AND STABILITY. Annu. Rev. Biochem. 78, 929. https://doi.org/10.1146/ANNUREV.BIOCHEM.77.032207.120833
Singh, P., Carraher, C., Schwarzbauer, J.E., 2010. Assembly of Fibronectin Extracellular Matrix. Annu. Rev. Cell Dev. Biol. 26, 397. https://doi.org/10.1146/ANNUREV-CELLBIO-100109-104020
Small, J. V., Auinger, S., Nemethova, M., Koestler, S., Goldie, K.N., Hoenger, A., Resch, G.P., 2008. Unravelling the structure of the lamellipodium. J. Microsc. 231, 479–485. https://doi.org/10.1111/j.1365-2818.2008.02060.x
Smith, J.W., 1968. Molecular Pattern in Native Collagen. Nat. 1968 2195150 219, 157–158. https://doi.org/10.1038/219157a0
Starborg, T., Lu, Y., Meadows, R.S., Kadler, K.E., Holmes, D.F., 2008. Electron microscopy in cell-matrix research. Methods 45, 53–64. https://doi.org/10.1016/j.ymeth.2008.01.004
Tacke, S., Erdmann, P., Wang, Z., Klumpe, S., Grange, M., Plitzko, J., Raunser, S., 2021. A streamlined workflow for automated cryo focused ion beam milling. J. Struct. Biol. 213. https://doi.org/10.1016/j.jsb.2021.107743
Theocharidis, G., Connelly, J.T., 2017. Minor collagens of the skin with not so minor functions. https://doi.org/10.1111/joa.12584
Theocharis, A.D., Manou, D., Karamanos, N.K., 2019. The extracellular matrix as a multitasking player in disease. FEBS J. 286, 2830–2869. https://doi.org/10.1111/FEBS.14818
Theocharis, A.D., Skandalis, S.S., Gialeli, C., Karamanos, N.K., 2016. Extracellular matrix structure. Adv. Drug Deliv. Rev. https://doi.org/10.1016/j.addr.2015.11.001
Torchia, D.A., 1982. [6] Solid state NMR studies of molecular motion in collagen fibrils. Methods Enzymol. 82, 174–186. https://doi.org/10.1016/0076-6879(82)82063-6
Toro-Nahuelpan, M., Zagoriy, I., Senger, F., Blanchoin, L., Théry, M., Mahamid, J., 2020. Tailoring cryo-electron microscopy grids by photo-micropatterning for in-cell structural studies. Nat. Methods 17, 50–54. https://doi.org/10.1038/s41592-019-0630-5
Untergasser, G., Madersbacher, S., Berger, P., 2005. Benign prostatic hyperplasia: age-related tissue-remodeling. Exp. Gerontol. 40, 121–128. https://doi.org/10.1016/J.EXGER.2004.12.008
Wagner, F.R., Watanabe, R., Schampers, R., Singh, D., Persoon, H., Schaffer, M., Fruhstorfer, P., Plitzko, J., Villa, E., 2020. Preparing samples from whole cells using focused-ion-beam milling for cryo-electron tomography. Nat. Protoc. 15, 2041–2070. https://doi.org/10.1038/s41596-020-0320-x
Wagner, J., Schaffer, M., Fernández-Busnadiego, R., 2017. Cryo-electron tomography—the cell biology that came in from the cold. FEBS Lett. 591, 2520–2533. https://doi.org/10.1002/1873-3468.12757
Wendt, U., Nolze, G., 2007. FIB Milling and Canneling. Imaging Microsc. 9, 34–36. https://doi.org/10.1002/imic.200790176
Wenstrup, R.J., Florer, J.B., Brunskill, E.W., Bell, S.M., Chervoneva, I., Birk, D.E., 2004. Type V collagen controls the initiation of collagen fibril assembly. J. Biol. Chem. 279, 53331–53337. https://doi.org/10.1074/jbc.M409622200
Wess, T.J., Hammersley, A., Wess, L., Miller, A., 1995. Type I collagen packing, conformation of the

triclinic unit cell. J. Mol. Biol. 248, 487–493. https://doi.org/10.1016/s0022-2836(95)80065-4
Wilgus, T.A., 2012. Growth Factor–Extracellular Matrix Interactions Regulate Wound Repair. Adv. Wound Care 1, 249. https://doi.org/10.1089/WOUND.2011.0344
Williams, E.C., Janmeyl, P.A., Ferrylll, J.D., Masher, D.F., 1982. Conformational states of fibronectin. Effects of pH, ionic strength, and collagen binding. J. Biol. Chem. 257, 14973–14978. https://doi.org/10.1016/S0021-9258(18)33379-9
Wolff, A., 2020. Focused ion beams: An overview of the technology and its capabilities [WWW Document]. Wiley Anal. Sci. URL https://analyticalscience.wiley.com/do/10.1002/was.00070009/ (accessed 11.10.22).
Wolff, G., Limpens, R.W.A.L., Zheng, S., Snijder, E.J., Agard, D.A., Koster, A.J., Bárcena, M., 2019. Mind the gap: Micro-expansion joints drastically decrease the bending of FIB-milled cryo-lamellae. J. Struct. Biol. 208, 107389. https://doi.org/10.1016/J.JSB.2019.09.006
Young, R.J., Moore, M. V., 2005. Dual-Beam (FIB-SEM) Systems. Introd. to Focus. Ion Beams 247–268. https://doi.org/10.1007/0-387-23313-x_12
Zachs, T., Schertel, A., Medeiros, J., Weiss, G.L., Hugener, J., Matos, J., Pilhofer, M., 2020. Fully automated, sequential focused ion beam milling for cryo-electron tomography. Elife 9. https://doi.org/10.7554/ELIFE.52286
Zeug, A., Stawarski, M., Bieganska, K., Korotchenko, S., Wlodarczyk, J., Dityatev, A., Ponimaskin, E., 2014. Current microscopic methods for the neural ECM analysis. Prog. Brain Res. 214, 287–312. https://doi.org/10.1016/B978-0-444-63486-3.00013-X
Zheng, S., Wolff, G., Greenan, G., Chen, Z., Faas, F.G.A., Bárcena, M., Koster, A.J., Cheng, Y., Agard, D.A., 2022. AreTomo: An integrated software package for automated marker-free, motion-corrected cryo-electron tomographic alignment and reconstruction. J. Struct. Biol. X 6. https://doi.org/10.1016/j.yjsbx.2022.100068
Zhong, C., Chrzanowska-Wodnicka, M., Brown, J., Shaub, A., Belkin, A.M., Burridge, K., 1998. Rho-mediated Contractility Exposes a Cryptic Site in Fibronectin and Induces Fibronectin Matrix Assembly. J. Cell Biol. 141, 539–551. https://doi.org/10.1083/JCB.141.2.539
Zhong, X., Wade, C.A., Withers, P.J., Zhou, X., Cai, C., Haigh, S.J., Burke, M.G., 2021. Comparing Xe+pFIB and Ga+FIB for TEM sample preparation of Al alloys: Minimising FIB-induced artefacts. J. Microsc. 282, 101. https://doi.org/10.1111/JMI.12983